Modeling and Understanding Supernova Signals in the IceCube Neutrino Observatory

By
Benedikt Riedel

A dissertation submitted in partial fulfillment of
the requirements for the degree of

Doctor of Philosophy

(Physics)

at the
UNIVERSITY OF WISCONSIN–MADISON
2014

Date of final oral examination: October 17, 2014

The dissertation is approved by the following members of the Final Oral Committee:
Francis Halzen, Professor, Physics
Reina Maruyama, Assistant Professor, Yale University, Physics
Albrecht Karle, Professor, Physics
Kael Hanson, Professor, Physics
Michael Duvernois, Senior Scientist, Wisconsin IceCube Particle Astrophysics Center
Paolo Desiati, Scientist, Wisconsin IceCube Particle Astrophysics Center

MODELING AND UNDERSTANDING SUPERNOVA SIGNALS IN THE ICECUBE NEUTRINO OBSERVATORY

Benedikt Riedel

Under the supervision of Professor Francis Halzen
At the University of Wisconsin-Madison

Exploding stars, or supernovae, are among the most cataclysmic events observed. The detection of supernova neutrinos from SN1987A marked the beginning of a new type of astronomy–neutrino astronomy. The observation of $\mathcal{O}(10\,\mathrm{MeV})$ neutrinos from the next galactic core-collapse supernova will provide invaluable insight into the supernova explosion process and may provide information about the elusive nature of neutrinos.

The IceCube Neutrino Observatory is a cubic-kilometer neutrino detector designed to detect astrophysical neutrinos with energies $\geq 100\,\mathrm{GeV}$. With its supernova analysis timing resolution ($2\,\mathrm{ms}$) and high event statistics ($\mathcal{O}(10^5\text{–}10^6)$) per galactic supernova, it takes a central part in the current efforts to detect neutrinos from the next galactic supernova.

Understanding the detector response to the signal and the backgrounds is essential to detect and analyze the supernova neutrino signal. This is especially true for a signal where the neutrinos have orders of magnitude lower energy than the detector is designed for. For this reason, supernova neutrinos in IceCube are detected as a statistically significant deviation in the detector noise rate over the course of $\mathcal{O}(1\text{–}10\,\mathrm{s})$.

The large number of individual events and the length of the signal makes the signal and background simulation of supernova neutrinos in IceCube a daunting endeavor. The simulation needs to be computationally efficient, easy adaptable to the wide variety of available theoretical neutrino emission models, and able to accommodate the significantly lower energies, higher fluxes, and longer time span. For this reason, IceCube's detector response to supernova neutrinos has, so far, only been modeled using a statistical simulation.

A new simulation framework is presented here. This implementation is able to provide the full detector response in the case of a galactic core-collapse supernova. It is based on principles already employed in other IceCube simulation.

A pre-generated sample of neutrino events with a given energy spectrum and sample size is produced. From this pre-generated neutrino sample, multiple subsets are selected depending on the given input parameters (theoretical model, distance to source, *etc.*). A statistical weight to adjust for differences between the pre-generated sample and the expected signal are applied to the subsets. A separate statistical weight will be applied according to the chosen neutrino oscillation scenario. It is the first time that simulation of both the primary and supernova data stream are done simultaneously and can be used to study individual events that produce a detector readout.

The low energy and transient nature of the signal requires a thorough understanding of the detector backgrounds over the long-term. Over the course of the last three years of operations of the completed IceCube detector, an increasing sensitivity to the atmospheric muon background has been observed. This has been observed through a 48.2% increase in the number of false positive triggers induced by the atmospheric muon background in the first two years of the completed detector. The increasing sensitivity is caused by a systematic decay in the detector baseline noise rate. The observed ∼3.5% decrease in the noise rate produces a ∼2% increase in sensitivity to atmospheric muons. This in turn causes an increasing number of false positive triggers.

The decay in the baseline noise is attributed to effects of the re-freezing process of the ice after the detector has been constructed. The re-freezing process appears to cause light emission, which decreases over time as the ice settles after the re-freezing over time. The exact cause of the decay has not been established. There is a strong indication that it is related to triboluminescence of the ice.

As part of the investigation into the increasing sensitivity of atmospheric muons, the stability of the atmospheric muon background independent of the observed seasonal effects was analyzed. This showed that the atmospheric muon background is roughly constant with time for given atmospheric properties. The measurement is highly dependent on detector and atmospheric property systematics.

The current atmospheric muon subtraction method relies on a trigger that has an energy bias towards higher energy muons than IceCube is sensitive to. The impact of using data with a lower threshold is investigated from a small subset of the data. Using the lower energy trigger, this increases the estimate of the number of DOM triggers caused by atmospheric muons by ∼6.5%. This will not affect current atmospheric muon subtraction methods employed in the analysis running at the South Pole. It would affect the direct subtraction method employed in the current search for supernovae in five years of data. This method cannot be employed in this search, as the data is not available for all supernova triggers.

The new simulation framework provides an additional tool to study and understand the detector response to supernova neutrinos and their backgrounds. It provides, for the first time, a means to tie the simulation directly into the analysis and test the effect of background reduction techniques.

The long-term studies of the detector background has revealed that a relatively small change in the baseline noise rate affects the supernova analysis greatly and that these changes appear to be related to the construction of the detector. A future study using the data sets employed can be used to determine the stability of the atmospheric muon background with time and thereby study the properties of the atmosphere. Additionally, the data sets can be used to study phenomena that would typically be below the trigger threshold for IceCube.

Francis Halzen

ACKNOWLEDGMENTS

This work was made possible with the help of numerous people. First, I would like to thank my advisors Prof. Francis Halzen and Prof. Reina Maruyama for their advise, support, and help. A special thanks to Michael DuVernois for always being there when I needed an open ear and providing endless help and support.

I would like to thank Claudio Kopper for being willing to listen to my (albeit mostly crazy and unorganized) ideas, and creating CLSim. My thanks goes to Michael Larson for taking the time and energy to improve the noise simulation.

Numerous people at WIPAC have helped me during this endeavor. Particular thanks goes to Jakob van Santen and Christopher Weaver for tolerating my questions (may it be statistics, programming, or just general particle physics) and patiently explaining IceCube software. Paolo Desiati for listening to my problems and providing valuable insight into cosmic ray physics and CORSIKA. I would like to thank Naoko Kurahashi Neilson for her input and insight. I also extend my thanks to Antonia Hubbard, Walter Pettus, Zachary Pierpoint, and Laura Gladstone for their edits to my thesis.

To my partner Laurel Norris a very big thank you. Her tireless support provided me with the strength I needed to finish.

Finally, I want to dedicate this work to my parents, Sieglinde and Martin. Their willingness to let me follow my own path has allowed me to get where I am today. Words cannot express how grateful I am their unwavering support, motivation, and love over the past 26 years.

TABLE OF CONTENTS

Page

Page

LIST OF TABLES

LIST OF FIGURES

Figure Page

Figure Page

Figure Page

Figure Page

Figure Page

Chapter 1

Introduction

Exploding stars or supernovae[1] play an essential role in astronomy and astrophysics, as they are one of the most cataclysmic events observed by mankind. Starting with one of the first recorded events by the Chinese in 185 C.E. [52] to the Dark Ages in 1054 and 1181 [53], the Renaissance in 1572 [54] and 1604 [55], and the birth of x-ray astronomy in 1962 [56], the observation of supernovae and their remnants across the millennia has marked milestones in astronomical and human history.

Figure 1.1: Observation of Supernova 1987A before (left) and during (right) the explosion. Credit: Anglo-Australian Observatory [8, 9]

---

[1] The focus of this work will be core-collapse supernovae, *i.e.* the explosion of massive stars at the end of their life. When mentioning supernovae this work is generally referring to core-collapse supernovae.

Supernovae take a central role in explaining a number of astrophysical phenomena and making known life possible. They are thought to take essential roles in stellar formation, as their shockwaves may cause gravitational collapse of interstellar clouds [57, 58]. Their remnants are thought to be the sources of galactic cosmic rays [59, 60]. Their occurrences in a galaxy can be a measure of the age or shape of a galaxy [61]. Without the nucleosynthesis of elements, such as oxygen, in supernovae, life on earth would look very different or may not be possible [62].

The most recent close-by supernova, Supernova 1987A (SN1987A), marked the beginning of a new type of astronomy–neutrino astronomy. For the first time, minuscule nearly undetectable particles called "neutrinos," originating from outside the solar system, were definitively observed in Kamiokande-II [63] and Irvine-Michigan-Brookhaven (IMB) [64]. It took nearly a quarter century to again detect neutrinos from outside the solar system [32].

SN1987A provided a confirmation that neutrinos originate from supernovae, and revealed information about the nature of neutrinos themselves [65]. The arrival times of the 19 events (24 including the events in BAKSAN detector [66]) provided the means to set limits on the mass, the charge, and lifetime of neutrinos. A limit on the number of possible neutrino flavors was derived as well from the expected neutron star formation.

An important aspect of the neutrinos from SN1987A was that they arrived at Earth hours before the light emission. Supernova neutrinos are an early warning of a galactic supernova. For this reason, a number of neutrino experiments have formed the Supernova Early Warning System (SNEWS)[2] [67].

Neutrinos are a unique way to observe the universe. Their special nature makes it possible for them to penetrate through matter that traditional astronomical messengers, mainly photons, cannot overcome readily or at all, travel directly from their source to the detector unaffected by magnetic fields or large dust clouds, and provide a measurable signal [65, 68]. As such they make it possible to probe, for example the origin of high energy cosmic rays [69, 70] and more relevant for this work the internal nature of the supernova explosion [15, 23, 71, 72]. These clear advantages come with a significant disadvantage. The minute interaction probabilities of neutrinos with matter require detectors with massive volumes.

The IceCube Neutrino Observatory was constructed to meet these requirements. By instrumenting $1\,\mathrm{km}^3$ of the Antarctic ice cap at the geographic South Pole with extremely sensitive light sensors, IceCube is able to observe the interactions of neutrinos in the ice. This large volume as well as the excellent optical properties [73] and radioactive purity [74] of the Antarctic ice makes it possible to observe neutrinos with an energy of $\mathcal{O}(10\,\mathrm{MeV}\text{–}1\,\mathrm{PeV})$ [30, 32].

---

[2] Current members include: Borexino, Super-Kamiokande, LVD, KamLAND, Mini-BooNE, and IceCube Neutrino Observatory

This work focuses on the possibility of detecting the signal of the next galactic supernova with the IceCube Neutrino Observatory; mainly on improving the current simulation of signal and backgrounds as well as gaining a better understanding of the backgrounds involved in the supernova search. This work is split into three parts: Theory, Simulation, and Analysis.

The theory section comprises Chapter 2, 3, and 4. A summary on the nature of neutrino and neutrino oscillations is presented in Chapter 2. The supernova process with a focus on the neutrino signal of the core-collapse supernovae is summarized in Chapter 3. Chapter 4 focuses on the IceCube Neutrino Observatory, its functions, operations, and response to supernova neutrinos.

The simulation section consists of Chapter 5. This chapter presents a new simulation framework that aims to produce simulation of supernova neutrinos and their backgrounds and tie them into the supernova neutrino analysis.

The analysis section, Chapter 6, provides an explanation of the increasing effect of atmospheric muon contamination on the supernova neutrino analysis. A study of possible improvements to the supernova analysis to reduce the effect of atmospheric muons on the analysis is also presented.

The next observation of a galactic supernova will be another milestone in astronomical history. With the increasing number, size, and precision of neutrino detectors, the community will observe thousands if not millions of events. This could open the door to understanding the supernova process and thereby a host of other astrophysical phenomena. This observation may take decades of waiting. The wait is well worth it.

Chapter 2

Neutrinos

Neutrinos play a crucial role in the explosion mechanism of core-collapse supernovae (CCSN). They also have fundamental properties that can be studied with CCSN. This chapter explores neutrino properties and their importance within particle physics, with a focus on supernova neutrinos.

2.1 History

Neutrinos were first postulated by Wolfgang Pauli in 1930 in his famous "Dear Radioactive Ladies and Gentlemen..." letter as a "desperate" explanation of the observation of a continuous energy spectrum of electrons emitted during β-decay [75, 76]:

$$n \rightarrow p + e^- + \bar{\nu}_e$$

Unlike the discrete kinetic energy spectrum observed in α-decay [10, 74], the continuous β-decay spectrum requires a three-body final state in order to conserve both energy and momentum; see Figure 2.1 for an example of the difference in the energy spectra. In 1934, Enrico Fermi formulated his β-decay theory given Pauli's postulate of a third particle by including a massless and chargeless particle to conserve the energy and momentum [77]. Fermi named the particle *neutrino*, *i.e.* little neutral one.

Neutrinos, specifically electron anti-neutrinos, were first detected by Frederick Reines and Clyde Cowan in 1956 at the Savannah River Nuclear Plant via inverse β-decay process [78]

$$\bar{\nu}_e + p \rightarrow n + e^+$$

The process occurring in a cadmium-chloride-doped water scintillation detector, produced three γs. Two from electron-positron annihilation

$$e^- + e^+ \rightarrow \gamma + \gamma$$

A delayed third from the neutron absorption on the cadmium:

$$n + {}^{108}\mathrm{Cd} \rightarrow {}^{109}\mathrm{Cd}^{\star} \rightarrow {}^{109}\mathrm{Cd} + \gamma$$

Two more flavors of neutrinos the muon [79–81] and tau [82, 83], corresponding to their lepton partners, were discovered in 1962 at the Alternating Gradient Synchrotron at Brookhaven National Laboratory and in 2001 by the DONUT experiment at the Fermi National Accelerator Laboratory, respectively. The muon neutrino had been postulated since the 1957 [84]. The tau neutrino was hypothesized after the discovery of the tau lepton in 1975 [82, 85].

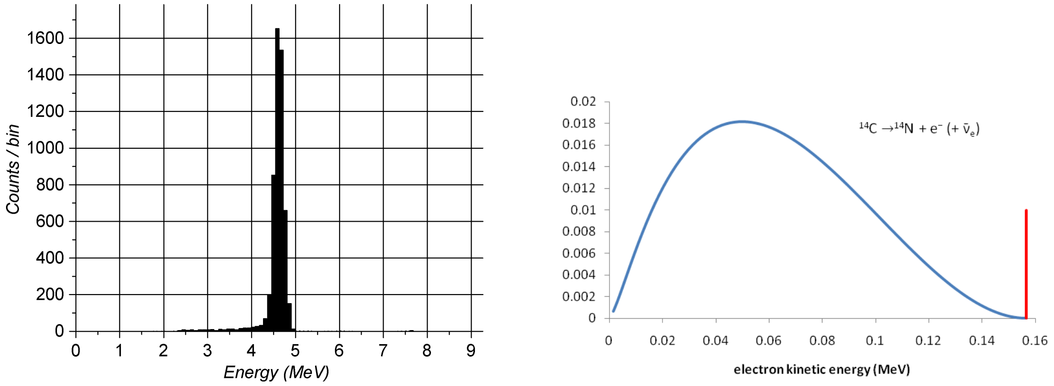

(a) Energy spectrum of α particles emitted by ^{230}Th. Credit: [10]

(b) Energy spectrum of positrons emitted by the β-decay of ^{14}C. The blue line is the actual spectrum. The red line is the expected signal if β-decay only emitted electrons. Credit: [11]

Figure 2.1: Energy Spectrum for α (left) and β-decay (right) products. Credit: Left: [10]; Right: [11]

Neutrinos have been the main player in one of the most intriguing conundrums in physics–the "solar neutrino problem." Ray Davis and John Bahcall measured a lower than expected flux of (electron) neutrinos from the standard solar model [86]. A solution of the solar neutrino problem is to consider "neutrino oscillations," *i.e.* neutrino flavors can interchange; see Section 2.3 for details [12, 87, 88]. Neutrinos have been shown to oscillate by observing the solar flux of other neutrino flavors, specifically the transition from electron neutrinos to muon and tau neutrinos, in 2001 by the Sudbury Neutrino Observatory [89]. Characterizing neutrino oscillation and neutrino properties is still on the forefront of neutrino physics [90].

2.2 Properties

In the Standard Model of particle physics neutrinos take a central role as “elementary particles” because they do not possess substructure; see Figure 2.2 and [12]. Neutrinos are expected to be chargeless and have a spin of 1/2 [12].

Compared to other particles in the Standard Model, they are special in that they only interact via the weak force, *i.e.* they couple to other particles via the $\mathrm{W}^{\pm}$- and Z-bosons in case of charged-current (CC) and neutral-current (NC) couplings, respectively. These couplings require the particles to have a certain handedness [12, 91–95]. This means that neutrinos are the origin of maximal parity violation as only left-handed neutrinos and right-handed anti-neutrinos can interact with matter [12, 84, 94, 95]. Neutrinos with opposite handedness are theoretically possible. They can not to be observed directly as they do not interact with matter [96].

As neutrinos are chargeless, they are able to have two Lorentz-invariant mass terms in relativistic Schrödinger Equation, *e.g.* a Dirac [97, 98] and a Majorana mass term [97, 99]. In case the neutrino has a Majorana mass term, the neutrino is its own antiparticle [97,100]. Alternatively, a Dirac mass term means that the neutrino and anti-neutrino are two distinct particles [12, 35, 101–104].

The neutrino interaction eigenstates, or flavor eigenstates (ν_α, where α = e, μ, τ), are a superposition of the mass eigenstates (ν_i, where i = 1, 2, and 3). This superposition is represented by

$$\begin{pmatrix} \nu_e \\ \nu_\mu \\ \nu_\tau \end{pmatrix} = U \begin{pmatrix} \nu_1 \\ \nu_2 \\ \nu_3 \end{pmatrix} \tag{2.1}$$

U is the Pontecorvo-Maki-Nakagawa-Sakata (PMNS) matrix:

$$\begin{aligned} U &= \begin{pmatrix} U_{e1} & U_{e2} & U_{e3} \\ U_{\mu 1} & U_{\mu 2} & U_{\mu 3} \\ U_{\tau 1} & U_{\tau 2} & U_{\tau 3} \end{pmatrix} \\ &= \begin{pmatrix} c_{12}c_{13} & s_{12}c_{13} & s_{13}e^{-i\delta} \\ -s_{12}c_{23} - c_{12}s_{23}s_{13}e^{i\delta} & c_{12}c_{23} - s_{12}s_{23}s_{13}e^{i\delta} & s_{23}c_{13} \\ s_{12}s_{23} - c_{12}c_{23}s_{13}e^{i\delta} & -c_{12}s_{23} - s_{12}c_{23}s_{13}e^{i\delta} & c_{23}c_{13} \end{pmatrix} \begin{pmatrix} 1 & 0 & 0 \\ 0 & e^{i\alpha_1/2} & 0 \\ 0 & 0 & e^{i\alpha_2/2} \end{pmatrix} \end{aligned} \tag{2.2}$$

with $\mathrm{c}_{ij} = \cos\theta_{ij}$, $\mathrm{s}_{ij} = \sin\theta_{ij}$, δ being a phase factor due to CP-violation, and α_i are the Majorana phase angles in case the neutrino is a Majorana particle [12,87,88,99,105]; see Table 2.1a for the individual values.

The superposition of neutrino mass and flavor eigenstates causes neutrinos to change or “oscillate” their flavor, as discussed in Section 2.1 and Section 2.3. Besides the angles in the PMNS matrix, the mixing and

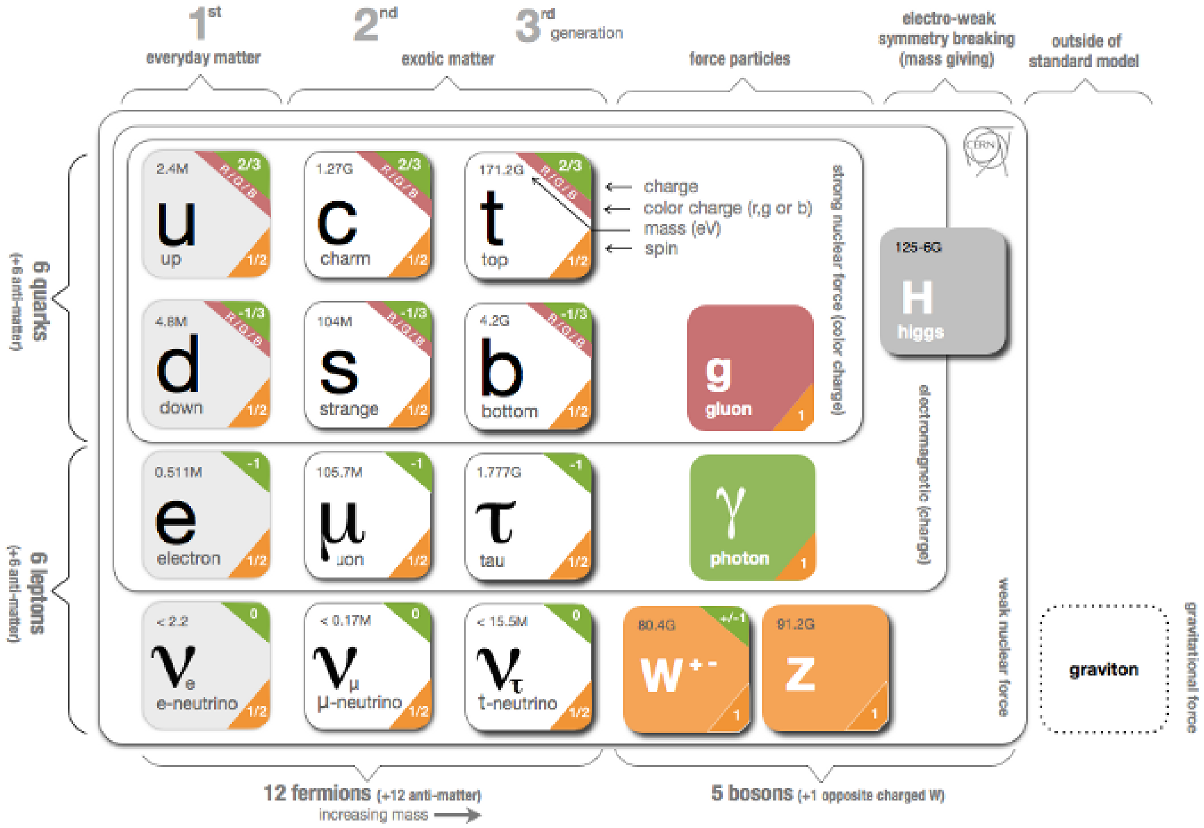

Figure 2.2: Particles of the Standard Model of Particle Physics. Credit: CERN Webfest, David Galbraith, Carsten Burgard [12, 13]

Parameter	Experimental Value
$\sin^2\theta_{12}$	3.08×10^{-1}
$\sin^2\theta_{23}$	$4.37\text{–}4.55 \times 10^{-1}$
$\sin^2\theta_{13}$	$2.34\text{–}2.40 \times 10^{-2}$
δ	$\cong 1.08\pi$
α_i	Unknown

(a) Parameters for the PMNS matrix

Parameter	Experimental Value
Δm^2_{21}	$7.5 \times 10^{-5}\,\mathrm{eV}^2$
$\Delta m^2_{31} \approx \Delta m^2_{32}$	$2.4 \times 10^{-3}\,\mathrm{eV}^2$

(b) Mass squared splittings

Table 2.1: Parameters for the PMNS matrix and the mass squared splittings from the mass hierarchy [1, 2].

oscillation between flavor eigenstates depends on the mass differences between the mass eigenstates. The squared mass differences have been measured from solar neutrino and atmospheric neutrino experiments [1, 2];

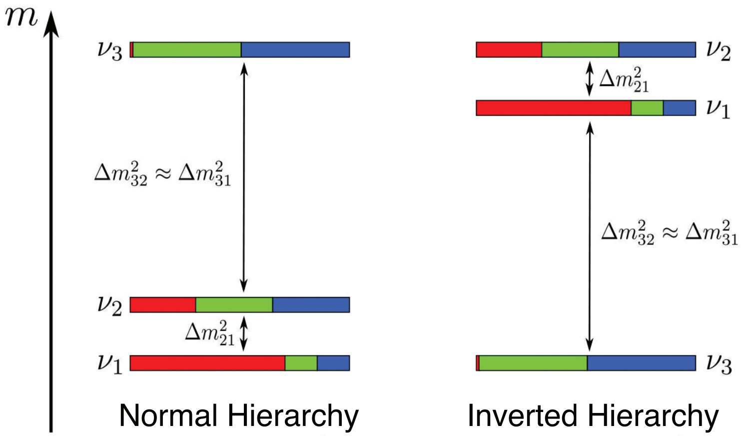

Figure 2.3: Illustration of the normal ($\nu_3 > \nu_2 > \nu_1$) and inverted ($\nu_2 > \nu_1 > \nu_3$) mass hierarchy for neutrinos. $\nu_{1,2,3}$ mass eigenstates are labeled, with the color showing how much each flavor eigenstate (ν_e: red, ν_μ: green, and ν_τ: blue) contributes to the individual mass eigenstates [12,14].

see Table 2.1b. The exact ordering of the neutrino masses ($\nu_3 > \nu_2 > \nu_1$ versus $\nu_2 > \nu_1 > \nu_3$), the so-called neutrino mass hierarchy, has yet to be experimentally constrained; see Figure 2.3.

The small mass differences make it very difficult to constrain the absolute masses of the individual neutrino flavors. Some constraints on the sum of neutrino masses have been made from cosmological models and observations of the cosmic microwave background. The Planck collaboration has published a best limit using data from the Planck and Wilkinson Microwave Anisotropy Probe (WMAP) satellites and assuming baryonic acoustic oscillations [106]:

$$\sum m_\nu < 0.23\,\mathrm{eV}$$

Attempts at absolute measurements have only yielded limits so far:

$$\mathrm{m}_{\nu_e} < 2\,\mathrm{keV} \text{ at } 90\% \text{ C.L. } [12,107]$$

$$\mathrm{m}_{\nu_\mu} < 190\,\mathrm{keV} \text{ at } 90\% \text{ C.L. } [12,108]$$

$$\mathrm{m}_{\nu_\tau} < 18.2\,\mathrm{MeV} \text{ at } 95\% \text{ C.L. } [12,109]$$

2.3 Neutrino Oscillations

Neutrinos can oscillate between flavor eigenstates. The flavor eigenstates are a superposition of mass eigenstates, as discussed in Section 2.2. The nature of the oscillations has to be differentiated by the medium through which the neutrinos are traveling, *i.e.* vacuum and matter. For an more detailed overview of the concepts outlined in this section see [12,31,94,95,110].

2.3.1 General Considerations

Neutrinos traveling through a medium can be generalized as using the Schrödinger Equation

$$i\frac{\partial}{\partial t}\left|\nu_i(t)\right\rangle = H\left|\nu_i(t)\right\rangle \tag{2.3}$$

The mass eigenstate at a given time, t, is represented by $|\nu_i(t)\rangle$, and H is the Hamiltonian given by the medium the neutrino is traveling through [12,31,110]. This means that the mass eigenstates travel as a plane wave through the medium, such that

$$\left|\nu_i(t)\right\rangle = e^{iHt}\left|\nu_i\right\rangle \tag{2.4}$$

The evolution of the mass eigenstates due to traveling through the medium causes the original flavor eigenstate to be altered according to

$$\left|\nu_\alpha\right\rangle = \sum_i U_{\alpha i}\left|\nu_i\right\rangle \tag{2.5}$$

where U is the PMNS matrix from Equation 2.2. The flavor eigenstate at a later time, $|\nu_\alpha(t)\rangle$, is

$$\left|\nu_\alpha(t)\right\rangle = \sum_i U_{\alpha i}\left|\nu_i(t)\right\rangle = \sum_i U_{\alpha i}e^{iHt}\left|\nu_i\right\rangle = \sum_i U_{\alpha i}e^{iE_i t}\left|\nu_i\right\rangle \tag{2.6}$$

The probability that given neutrino remains in its flavor, $p_{\nu_\alpha\rightarrow\nu_\alpha}$, is called “survival probability,”

$$p_{\nu_\alpha\rightarrow\nu_\alpha} = \left|\left\langle \nu_\alpha \,\middle|\, e^{iHt} \,\middle|\, \nu_\alpha \right\rangle\right|^2 \tag{2.7}$$

while the probability of a transition between flavors, $p_{\nu_\alpha\rightarrow\nu_\beta}$, is called “transition probability”

$$p_{\nu_\alpha\rightarrow\nu_\beta} = \left|\left\langle \nu_\beta \,\middle|\, e^{iHt} \,\middle|\, \nu_\alpha \right\rangle\right|^2 \tag{2.8}$$

where $|\nu_\beta\rangle$ is the eigenstate for a different flavor.

The oscillation scenario can be simplified further by considering two flavor eigenstates instead of three. This assumption can be made as most core-collapse supernova neutrino models assume a two flavor system; see Section 3.4 and [23,30,71,111,112]. Muon and tau (anti-)neutrinos can only undergo NC interactions in case of supernova neutrinos with $\mathcal{O}(10\,\mathrm{MeV})$; see Section 4.5.1. These interactions exhibit flavor symmetry, *i.e.* the interactions of two flavors are in indistinguishable [12]. For example, the Daya Bay Experiment is specialized to detect electron anti-neutrinos through inverse β-decay [113,114]. It cannot distinguish between the interactions of ν_μ and ν_τ in the detector. In IceCube the two flavor assumption can be made since the detector cannot distinguish the nature (CC or NC) of individual neutrino events [30]. This means that the oscillation effects are observed as an enhancement or weakening of the signal. The two flavor assumption simplifies the PMNS matrix to

$$U = \begin{pmatrix} \cos\theta & \sin\theta \\ -\sin\theta & \cos\theta \end{pmatrix} \tag{2.9}$$

In an experimental setting, one generally deals with an initial flux of a given flavor, $\Phi^0_{\nu_\alpha}$. This initial flux will change as the neutrino travels through the medium. The oscillated flux, Φ_{ν_α}, of the initial flavor can be generalized to

$$\Phi_{\nu_\alpha} = p_{\nu_\alpha \to \nu_\alpha}\Phi^0_{\nu_\alpha} + p_{\nu_\beta \to \nu_\alpha}\Phi^0_{\nu_\beta} + p_{\nu_\gamma \to \nu_\alpha}\Phi^0_{\nu_\gamma} \tag{2.10}$$

where $p_{\nu_{\alpha,\beta,\gamma} \to \nu_\alpha}$ are the oscillation probabilities the flavor eigenstates ($\nu_{\alpha,\beta,\gamma}$) into the initial flavor eigenstate.

2.3.2 Vacuum Oscillations

The oscillation of neutrinos in vacuum is due to the time evolution of mass eigenstates in free space, *i.e.* the mass eigenstate travels without being affected by other particles or potentials, which alters the respective flavor eigenstates. Since the mass eigenstate is a free relativistic particle, the energy, E_i, in Equation 2.6 can be approximated by

$$E_i \approx E + \frac{m_i^2}{2E} \tag{2.11}$$

This means that the flavor eigenstate evolves according to

$$|\nu_\alpha(t)\rangle = \sum_i U_{\alpha i} e^{i\frac{m_i^2}{2E}t} |\nu_i\rangle \tag{2.12}$$

and, under the assumption that energy is conserved during the flavor transitions, the transition probability is given by

$$\begin{aligned}\bar{p}_{\nu_\alpha\rightarrow\nu_\beta} &= \left|\langle\nu_\beta \,|\, \nu_\alpha(t)\rangle\right|^2 \\ &= \left|\sum_i U_{\alpha i}U^\star_{\beta i}e^{i\frac{m_i^2}{2E}t}\,|\nu_i\rangle\right|^2 \\ &= \sum_i \left|U_{\alpha i}\right|^2 \left|U_{\beta i}\right|^2 - 2\mathfrak{Re}\sum_{i>j} U_{\alpha i}U^\star_{\beta i}U^\star_{\alpha j}U_{\beta j}e^{-i\frac{\Delta m_{ij}^2}{2E}t}\end{aligned} \tag{2.13}$$

where Δm_{ij}^2 is the squared mass difference between the neutrino mass eigenstates. In the two neutrino approximation Equation 2.13 can be simplified to

$$\bar{p}_{\nu_\alpha\rightarrow\nu_\beta} = \sin^2(2\theta)\sin^2\left(\frac{\Delta m^2}{4E}t\right) = \sin^2(2\theta)\sin^2\left(\frac{\Delta m^2}{4E}L\right) \tag{2.14}$$

where time of flight, t, and length of travel, L, are interchangeable in natural units[1]. The oscillation probability therefore only varies with time of flight, the neutrino energy, and the mixing parameters, *i.e.* mixing angle and squared mass difference. On average the oscillation probability converges to

$$\bar{p}_{\nu_\alpha\rightarrow\nu_\beta} = \sum_i \left|U_{\alpha i}\right|^2 \left|U_{\beta i}\right|^2$$

2.3.3 Matter Oscillations

Traveling through matter alters the oscillation pattern as shown by the Mikheyev-Smirnov-Wolfenstein (MSW) effect. The neutrino is being forward scattered off the constituents of the matter, in case electron (e^-), proton (p), and neutron (n). The scattering effect is similar to traveling through an effective potential [115–117].

This will alter the Hamiltonian that the neutrino flavor eigenstates experience as they travel through the medium as the Hamiltonian gains an additional term from the vacuum oscillation case

$$H = H_0 + H_1 \tag{2.15}$$

where H_0 is the Hamiltonian due to vacuum oscillations, *i.e.* free particle, and H_1 is the Hamiltonian due to the effective matter potential, V_{eff}. Only flavor eigenstates can interact with other particles. The addition of H_1 alters the mass differences and mixing angles. This makes it possible that the flavor conversion probability for certain mixing parameters flips from nearly impossible to maximal [118].

Equation 2.3 for the flavor eigenstates for the matter oscillation is given by

---

[1] $c = \hbar = 1$

$$\begin{aligned} i\frac{\partial}{\partial t}\left|\nu_\alpha(t)\right\rangle &= \left(H_0 + H_1\right)\left|\nu_\alpha(t)\right\rangle \\ &= \left(\frac{UM^2U^\dagger}{2E} + V\right)\left|\nu_\alpha(t)\right\rangle \\ &= \frac{\Delta m^2}{4E}\begin{pmatrix} -\cos 2\theta + 2EV_{\text{eff}} & \sin 2\theta \\ \sin 2\theta & \cos 2\theta \end{pmatrix}\left|\nu_\alpha(t)\right\rangle \end{aligned} \tag{2.16}$$

where V_{eff} is the potential to due interactions with the matter such that [31,111,118]

$$V_{\text{eff}} = \pm\sqrt{2}G_F N_e \tag{2.17}$$

where G_F $(= 1.667 \times 10^{-5}\,\text{GeV}^{-2}$ [12]) is the Fermi constant, N_e is the electron density of the matter, and ± is needed neutrinos and anti-neutrinos, respectively. This extra potential thus produces an effective mass difference [12,31,111]:

$$\Delta m^2_{\text{eff}} = \sqrt{(\Delta m^2 \cos 2\theta - 2EV_{\text{eff}})^2 + (\Delta m^2 \sin 2\theta)^2} \tag{2.18}$$

and effective mixing angle:

$$\sin 2\theta_{\text{eff}} = \frac{\Delta m^2 \sin 2\theta}{\Delta m^2_{\text{eff}}} \tag{2.19}$$

$$\cos 2\theta_{\text{eff}} = \frac{\Delta m^2 \cos 2\theta - 2EV_{\text{eff}}}{\Delta m^2_{\text{eff}}} \tag{2.20}$$

From these conditions one can determine MSW resonance regions, in which the electron density is given by:

$$N_e^R = \frac{\Delta m^2 \cos 2\theta}{2\sqrt{2}G_F E} \tag{2.21}$$

where Equation 2.17 becomes

$$V_{\text{eff}} = \frac{\Delta m^2 \cos 2\theta}{2E} \tag{2.22}$$

At this point maximal mixing occurs as $\cos 2\theta_{\text{eff}} \to 0$ and Δm^2_{eff} is minimal. The resonances are different for neutrinos and anti-neutrinos and depend on θ, while the resonance occurs for neutrinos if $\theta \leq \pi/4$ and for anti-neutrinos if $\theta > \pi/4$ [31].

The addition of terms to the Schrödinger Equation for the flavor eigenstates and the change of the mixing parameters will alter the Schrödinger Equation for the mass eigenstates. The PMNS matrix becomes

$$U = \begin{pmatrix} \cos\,\theta_{\mathrm{eff}} & \sin\,\theta_{\mathrm{eff}} \\ -\sin\,\theta_{\mathrm{eff}} & \cos\,\theta_{\mathrm{eff}} \end{pmatrix} \tag{2.23}$$

The Hamiltonian for the mass eigenstate is transformed such that [12,14,112,119,120]

$$i\frac{\partial}{\partial z}\begin{pmatrix} \nu_1 \\ \nu_2 \end{pmatrix} = \begin{pmatrix} -\frac{\Delta m^2_{\mathrm{eff}}}{4E} & -i\frac{d\theta_{\mathrm{eff}}}{dz} \\ i\frac{d\theta_{\mathrm{eff}}}{dz} & \frac{\Delta m^2_i}{4E} \end{pmatrix}\begin{pmatrix} \nu_1 \\ \nu_2 \end{pmatrix} \tag{2.24}$$

where ${}^{d\theta_{\mathrm{eff}}}/_{dz}$ is the change of the effective mixing angle as the neutrino travels through the medium.

In most current neutrino oscillation experiments, a constant matter density profile along the propagation axis, *i.e.* ${}^{d\rho}/_{dx} = 0$, is assumed. The transition probability is therefore a modification of Equation 2.14 using the effective mixing parameters

$$\bar{p}_{\nu_\alpha \to \nu_\beta} = \sin^2\left(2\theta_{\mathrm{eff}}\right)\sin^2\left(\frac{\Delta m^2_{\mathrm{eff}}}{4E}t\right) \tag{2.25}$$

In the case of solar or supernova neutrinos, this assumption falls apart as the matter surrounding the neutrino source is non-homogenous, *i.e.* ${}^{d\rho}/_{dx} \neq 0$. Most of the oscillation behavior in this case can be approximated using Equation 2.21 in two resonance regions, one for the $|\Delta m^2_{32}|$ (H-resonance) and another for the $|\Delta m^2_{12}|$ (L-resonance) mass splittings. The density in these resonance regions is given by [119]

$$\rho_{Res} \approx 1.4 \times 10^6 \left(\frac{\Delta m^2}{1\,\mathrm{eV}^2}\right)\left(\frac{10\,\mathrm{MeV}}{E}\right)\left(\frac{0.5}{Y_e}\right)\cos\,2\theta\,\mathrm{g\ cm}^{-3} \tag{2.26}$$

The strength of the mixing is now a function of m^2_{eff} as well as ${}^{d\rho}/_{dx}$. One can define an adiabaticity parameter, γ, to describe the relationship of diagonal to off-diagonal elements of Equation 2.24 such that [111,119]

$$\gamma = \frac{\Delta m^2_{\mathrm{eff}}}{4E|\frac{d\theta_{\mathrm{eff}}}{dz}|} = \frac{(\Delta m^2_{\mathrm{eff}})^2}{4E^2\sin\,2\theta_{\mathrm{eff}}|\frac{d}{dx}V_{\mathrm{eff}}|} \tag{2.27}$$

which provides a measure for the density gradient in terms of the change in V_{eff} and hence a measure of the change in the mixing parameters.

The conversion probability for neutrino mass eigenstates, P_c, for a given γ is given by the Landau-Zener formula [119,121,122]:

$$P_c = \frac{\exp(-{}^{\pi}/_{2}\gamma F) - \exp(-{}^{\pi}/_{2}\gamma({}^{F}/_{sin^2\theta}))}{1 - \exp(-{}^{\pi}/_{2}\gamma({}^{F}/_{sin^2\theta}))} \tag{2.28}$$

where F is a function that varies with the functional form of the density profile. For a baseline model for the density profile of a star such as simplified power-law

$$\rho \propto r^{-n} \tag{2.29}$$

Equation 2.28 simplifies to [14,122]:

$$P_c \approx \exp\left(-5.73 \times 10^6 \left(\frac{\Delta m_{13}^2}{E}\right)^{\frac{2}{3}} \frac{\sin^2 \theta_{13}}{(\cos 2\theta_{13})^{\frac{1}{3}}}\right) \tag{2.30}$$

For $\gamma \ll 1$, *i.e.* a non-adiabatic density gradient, there will be a non-zero probability for the transition in spectra of ν_1 and ν_2, given by $P_{\nu_1 \to \nu_2}$. This transition can be translated into a survival probability for ν_e, $P_{\nu_e \to \nu_e}$, as follows:

$$P_{\nu_e \to \nu_e} = \frac{1}{2} + \frac{1}{2}(\cos 2\theta_{\text{eff}} \cos 2\theta) - P_{\nu_1 \to \nu_2} \cos 2\theta_{\text{eff}} \cos 2\theta \tag{2.31}$$

On the other hand, for $\gamma \gg 1$, *i.e.* adiabatic density gradient, one will see a flat density gradient, for which $P_c \approx 0$.

The adiabaticity parameter is a function of the mass splitting, therefore we can define

$$\gamma_H = 2.6 \times 10^4 \frac{\sin^2 2\theta_{13}}{(\cos^2 2\theta_{13})^{4/3}} \left(\frac{\Delta m_{31}^2}{10^{-3}\,\text{eV}^2}\right)^2 \left(\frac{\text{MeV}}{E}\right)^{2/3} \tag{2.32}$$

for the $|\Delta m_{32}^2|$-resonance considering the Daya Bay result and

$$\gamma_L = 1.2 \times 10^3 \frac{\sin^2 2\theta_{12}}{(\cos^2 2\theta_{12})^{4/3}} \left(\frac{\Delta m_{21}^2}{10^{-5}\,\text{eV}^2}\right)^2 \left(\frac{\text{MeV}}{E}\right)^{2/3} \tag{2.33}$$

for the $|\Delta m_{12}^2|$-resonance. Both γ_H and γ_L are $\gg 1$, which means that both transition region will follow an adiabatic regime and the transition probabilities in both regions, P_H and P_L, respectively, will ≈ 0.

2.3.4 Neutrino Oscillation in Supernova

Inside a supernova, the high density and density gradient of the stellar matter surrounding the core-collapse can enhance and complicate the matter oscillation effect. In the high density regime inside the neutrino source, the so-called "neutrinosphere," see Section 3.3 and 3.3.3 for details, the mixing flavor and mass eigenstates shown in Figure 2.3 is suppressed and a one-to-one mapping occurs [111,112,119]. In the normal mass hierarchy ($\nu_1 < \nu_2 < \nu_3$), the mapping is [119]

$$\nu_e = \nu_3,\ \nu_{\mu'} = \nu_1,\ \nu_{\tau'} = \nu_2$$

$$\bar{\nu}_e = \nu_1,\ \bar{\nu}_{\mu'} = \nu_2,\ \bar{\nu}_{\tau'} = \nu_3$$

For the inverted hierarchy ($\nu_2 > \nu_1 > \nu_3$) the mapping is [119]

$$\nu_e = \nu_2,\ \nu_{\mu'} = \nu_1,\ \nu_{\tau'} = \nu_3$$

$$\bar{\nu}_e = \nu_3,\ \bar{\nu}_{\mu'} = \nu_2,\ \bar{\nu}_{\tau'} = \nu_1$$

where $\nu_{\mu'}$, and $\nu_{\tau'}$ are proxies for superpositions of ν_μ and ν_τ that are mostly the respective flavor.

The flux emerging from the neutrinosphere. $\Phi^0_{\nu_e}$ and $\Phi^0_{\nu_x}$ are the initial fluxes for ν_e and ν_x (a superposition of ν_μ and ν_τ) and $\Phi^0_{\bar{\nu}_e}$ and $\Phi^0_{\bar{\nu}_x}$ for the anti-neutrino counterparts, respectively, such that

$$\Phi^0_{\nu_e} = \Phi^0_{\nu_3},\ \Phi^0_{\nu_x} = \Phi^0_{\nu_2},\ \Phi^0_{\nu_x} = \Phi^0_{\nu_1}$$

$$\Phi^0_{\nu_e} = \Phi^0_{\nu_2},\ \Phi^0_{\nu_x} = \Phi^0_{\nu_1},\ \Phi^0_{\nu_x} = \Phi^0_{\nu_3}$$

for the normal hierarchy

$$\Phi^0_{\nu_e} = \Phi^0_{\nu_2},\ \Phi^0_{\nu_x} = \Phi^0_{\nu_1},\ \Phi^0_{\nu_x} = \Phi^0_{\nu_3}$$

$$\Phi^0_{\nu_e} = \Phi^0_{\nu_3},\ \Phi^0_{\nu_x} = \Phi^0_{\nu_2},\ \Phi^0_{\nu_x} = \Phi^0_{\nu_1}$$

for the inverted hierarchy. The fluxes that at the surface of the star undergoing core-collapse can therefore be characterized, as [111,112]

$$\Phi_{\nu_e} = p\Phi^0_{\nu_e} + (1-p)\Phi^0_{\nu_x} \tag{2.34}$$

$$\Phi_{\bar{\nu}_e} = \bar{p}\Phi^0_{\bar{\nu}_e} + (1-\bar{p})\Phi^0_{\bar{\nu}_x} \tag{2.35}$$

for electron (anti-)neutrino fluxes, while the μ and τ (anti-)neutrino flux is given by

$$\Phi_{\nu_\mu} + \Phi_{\nu_\tau} = 2\Phi_{\nu_x} = (1-p)\Phi^0_{\nu_e} + (1+p)\Phi^0_{\nu_x} \tag{2.36}$$

$$\Phi_{\bar{\nu}_\mu} + \Phi_{\bar{\nu}_\tau} = 2\Phi_{\bar{\nu}_x} = (1-\bar{p})\Phi^0_{\bar{\nu}_e} + (1+\bar{p})\Phi^0_{\bar{\nu}_x} \tag{2.37}$$

where p ($\bar{p}$ for anti-neutrinos) is the contribution to the initial fluxes to the final fluxes. Given that the transition probabilities for both resonance regions is 0, p and $\bar{p}$ are given by

Hierarchy	p	$\bar{p}$
Normal	$\lvert U_{e3}\rvert^2$	$\cos^2\theta_{12}$
Inverted	$\sin^2\theta_{12}$	$\lvert U_{e3}\rvert^2$

when considering the Daya Bay results [123].

This is an idealized picture of neutrino oscillations in stellar matter in the case of a supernova. The density gradients may vary significantly depending on the explosion mechanism, the position and nature of the shock, *etc.* [23,71,72]; see Section 3.3. The high matter and neutrino densities inside the neutrinosphere and surrounding matter may cause new oscillation scenarios due to neutrino-neutrino interactions to appear. For possible extensions of this picture see [14,110,124–134] and references therein.

Chapter 3

Supernovae

Core-collapse supernova are one of the most energetic astrophysical explosions observed today. This chapter will explore the origin of the neutrino signal from core-collapse supernovae and the supernova rate and distribution starting with the stellar evolution of massive stars, and the core-collapse supernova process.

3.1 Stellar Evolution

Similar to organisms, stars are born, live, and die. Unlike organism though, the lifespan of a star is solely dependent on its initial mass and elemental composition [135–137]. The various stages of stars are visually summarized in Figure 3.1 and on a Hertzsprung-Russell Diagram (HRD) [138–140] in Figure 3.2. The HRD relates the surface temperature, T, the color of the star from a cool red to a hot blue, to the luminosity, L, across all wavelengths of the star, the energy output or brightness of the star. For an overview of stellar evolution see [141, 142].

A star begins to form when a gas cloud becomes gravitationally instable, *i.e.* the gravitational force overcomes the thermal pressure, and causes the cloud to contract [142]. The precise reason for the "spontaneous" collapse of a cloud are unknown. Various theories such as the shock waves from nearby stellar explosions compressing the material exist [57, 58]. A more typical reason for a cloud to collapse is that the cloud has accumulated sufficient mass that the thermal pressure can no longer support the gravitational pull and begins to collapse. The result of the collapse is a "protostar" [137]. A star will result from the protostar, if the protostar develops temperatures high enough to disassociate molecular hydrogen ($\sim$2000 $-$ 3000 K) [143,144], ionize hydrogen ($\sim$10000 K) [145–147], and its core can ultimately reaches $\approx\mathcal{O}(10^7\,\mathrm{K})$ to ignite the hydrogen fusion that powers the star [142, 148].

After its birth, the star will undergo multiple different stages, or burning-phases for massive stars ($M \gg M_\odot$, where $M_\odot$ denotes one solar mass), in its life; see Figure 3.1. The star will spend most of its life on the "main-sequence" burning hydrogen in its core; see Figure 3.2. Stars will start at different points on the main-sequence depending on their mass and composition [142]; see Figure 3.2. It will move along this "trunk" until it has used up most of the hydrogen in its core. It will subsequently turn off the trunk and

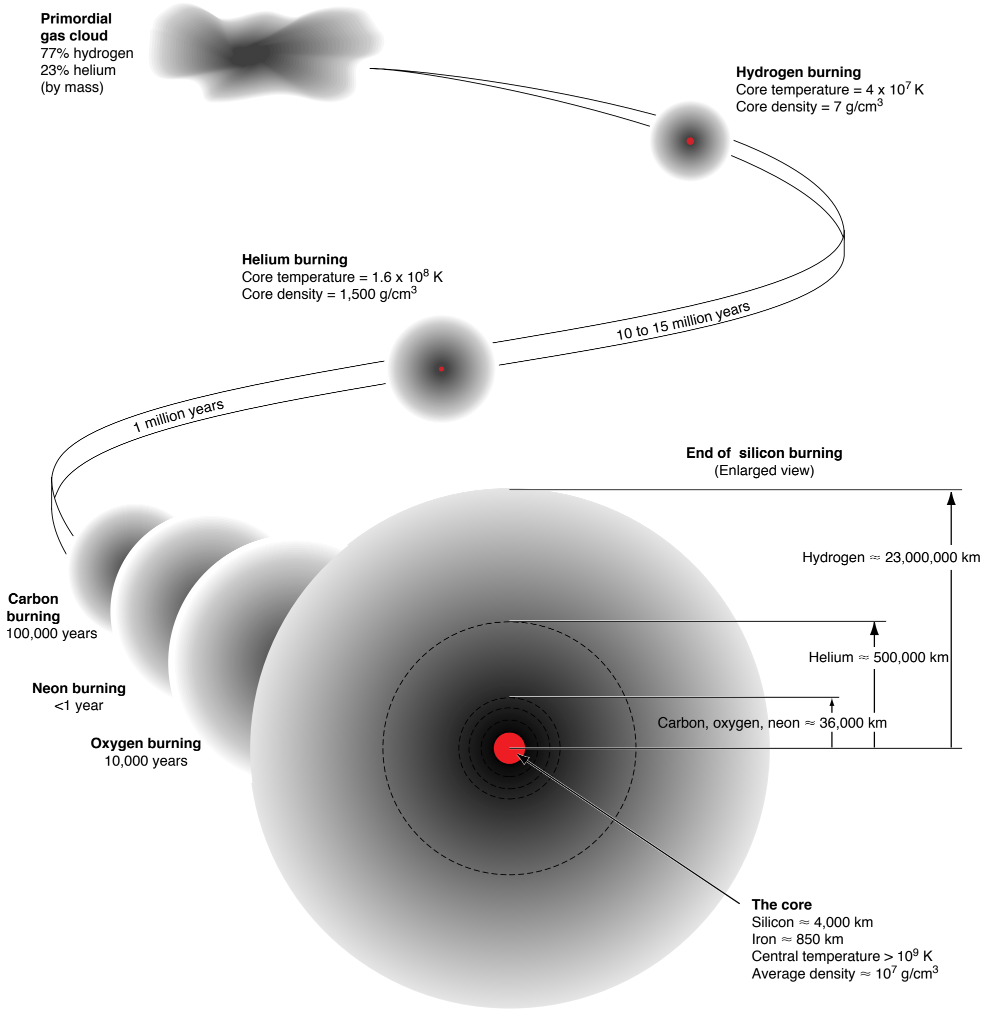

Figure 3.1: The different phases of a massive stars life. The star begins as a gas cloud that collapses sufficiently to form a main-sequence star that burns hydrogen burning. After the hydrogen is depleted in the core, the star beings to fuse helium. As the star continues to age, it will begin to fuse heavier and heavier elements until it reaches iron. In this process, the areas surrounding the core will start fusing elements as well, ultimately producing an onion-like elemental structure. Taken from [15]

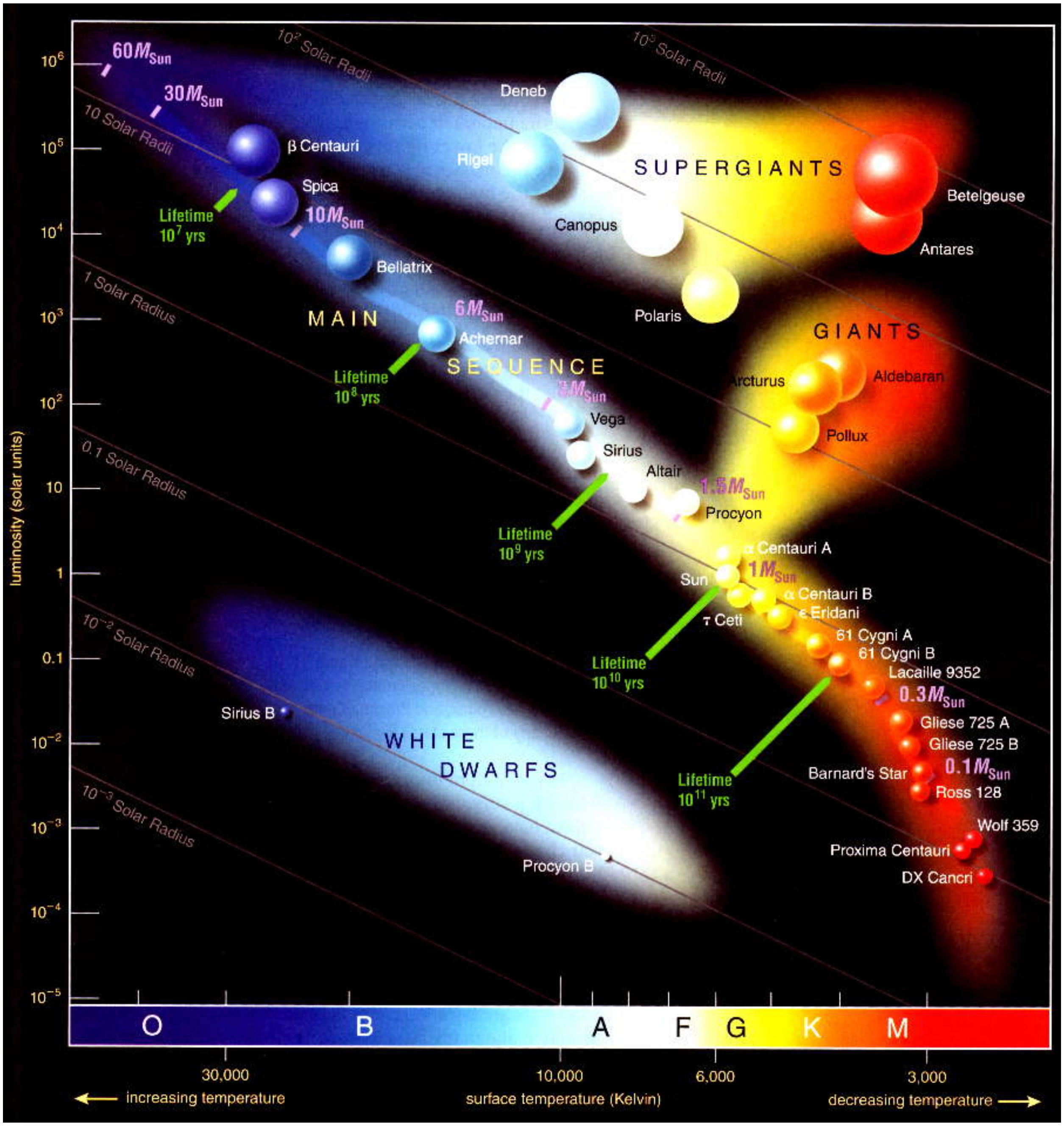

Figure 3.2: Hertzsprung-Russell Diagram with some Milky Way stars representing the various stellar masses along the main-sequence and different stages of stellar life. Credit: European Southern Observatory [16, 17]

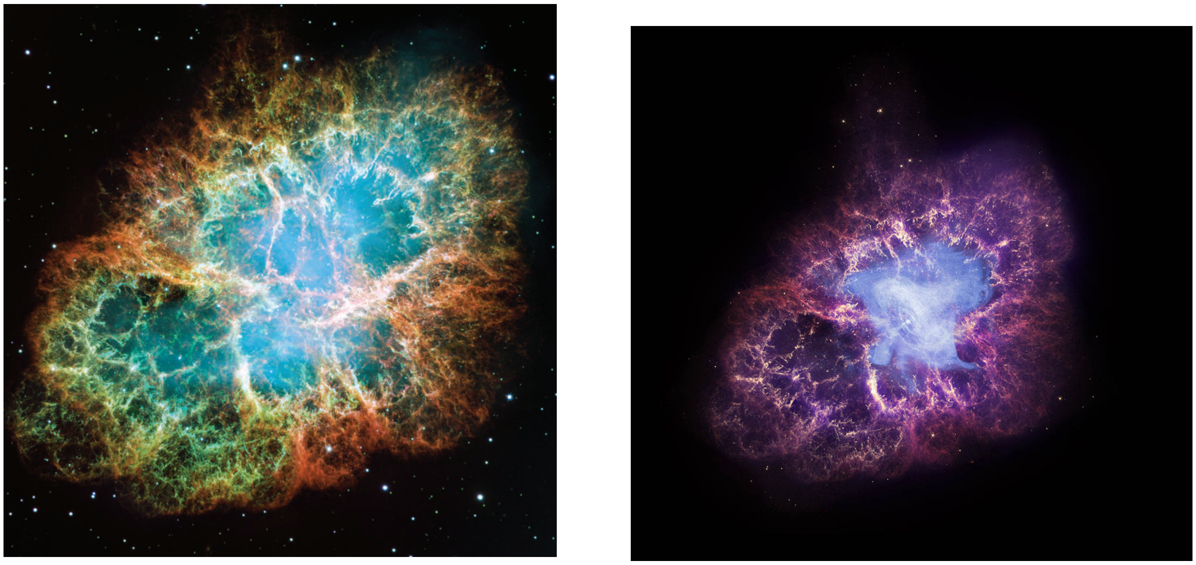

(a) Composite image of the Crab Nebula from observations of the Hubble Space Telescope at different optical wavelengths indicating the presence of different elements. Credit: NASA, ESA, J. Hester and A. Loll (ASU) [18,19]

(b) Composite image of the Crab Nebula from observations of the Hubble Space Telescope (optical), Chandra X-Ray Observatory (x-ray), and Spitzer Space Telescope (infrared). Credit: X-Ray: NASA/CXC/J.Hester (ASU); Optical: NASA/ESA/J.Hester/A.Loll (ASU); Infrared: NASA/JPL-Caltech/R.Gehrz (Univ. Minn.) [20]

Figure 3.3: Composite images of the Crab Nebula (M1, NGC 1952, Taurus A), a supernova remnant of core-collapse supernova in 1054, in optical wavelengths (left) and in optical, x-ray, and infrared (right) wavelengths. The layered cloud of debris is visible in both images. The different layers of the debris cloud shows that the cloud is expanding. The spinning neutron star (pulsar) is clearly visible in the left image as a strong x-ray source. For an overview of observations of the Crab Nebula see [18]. Credit: [19, 20]

onto one of the "branches". Below the trunk, white dwarfs form special group on the HRD because they are no longer actively burning [142].

The mass is the main determinant of a stars fate (white dwarf, neutron star, or black hole [23, 111, 142, 149–151]). For a star too massive to form a white dwarf, a so-called "core-collapse" occurs, as the core cannot withstand the gravitational pull of its own mass and collapses. If the star is simply too heavy to form a stable neutron star the collapse will result in a black hole [152–154]. Otherwise, the star will explode in a "core-collapse supernova" and form a neutron star surrounding by an expanding cloud of stellar debris; see Figure 3.3.

The progenitor star for a core-collapse supernova is a massive star (typically $\geq 8\,M_{\odot}$ [23, 26, 111]) that has moved off the main-sequence to the giant phase of its life on the HRD; see Figure 3.2. The star progresses through helium, carbon, neon, oxygen, and ultimately silicon burning (for a heavy enough star [24]) phases inside the core; see Figure 3.1 [23,26,111]. As the core progresses through these different burning phases, the layers outside the core will evolve similarly. This ability to have multiple distinct fusion processes occurring at the same time produces an onion-like elemental structure inside the star; see Figure 3.1. When and how this occurs during the life span of the star is heavily dependent on the initial mass and composition [111].

The core becomes inactive as the fusion conditions for heavier elements (namely temperature and pressure) are not given or the process becomes endothermic, as happens when iron is being produced [23, 26, 111, 142]. The core forms a white dwarf-like system, as it supports itself with electron degeneracy pressure from the inward pull of gravity. Outside of the inactive core, distinct fusion processes continue. The resulting products move inward and continue to fuse to ever heavier elements until they reach the core. This adds to the overall mass of the core. When the core reaches the Chandrasekhar mass limit [111,155,156], the electron degeneracy pressure is no longer sufficient to counteract gravity and the core collapse of the progenitor commences [23, 26, 111]; see Section 3.2.

3.2 Types of Supernovae

Typically, supernovae are classified by their optical spectra using Minkowski-Zwicky system [60,157,158]; see Figure 3.4 for a visual summary. Optical spectra of Type I supernovae do not exhibit hydrogen lines. Type Ia are also missing helium lines, but exhibit strong silicon absorption lines. Spectra of Type Ib and Ic, on the other hand, do not exhibit silicon absorption lines, while Type Ic spectra are also missing helium lines. Spectra of Type II supernovae show spectral lines for hydrogen, and helium [157]. In the neutrino regime, these classification are no longer valid since the signal depends on the nature of the explosion mechanism. Type Ia supernovae can be most aptly described as thermonuclear supernovae. Type Ib, Ic, and II are core-collapse supernovae and the focus of this work. Type II supernovae have additional sub-categories that will not discussed here; see [159–161] for more details

Type Ia supernovae are produced in binary systems between a white dwarf and star or two white dwarfs [162,163]. In case of a white dwarf–star system, the star is close enough to its companion that the white dwarf accretes mass from its companion. For the white dwarf–white dwarf system, a merger will occur. In both cases, the white dwarf becomes unstable if it reaches the Chandrasekhar mass limit ($\sim 1.39\,M_{\odot}$ [162]). At $M \gtrapprox M_{\text{Chandrasekhar}}$, the white dwarf will be able fuse heavier elements from its constituents, mostly carbon and oxygen. The carbon and oxygen fusion reaction continues unhindered. Unlike heavier stars, the low-mass stellar remnant cannot produce sufficient gravitational pressure to counteract the pressure generated by the nuclear fusion reaction. The white dwarf is torn apart by the run-away fusion reaction, *i.e.* a thermonuclear

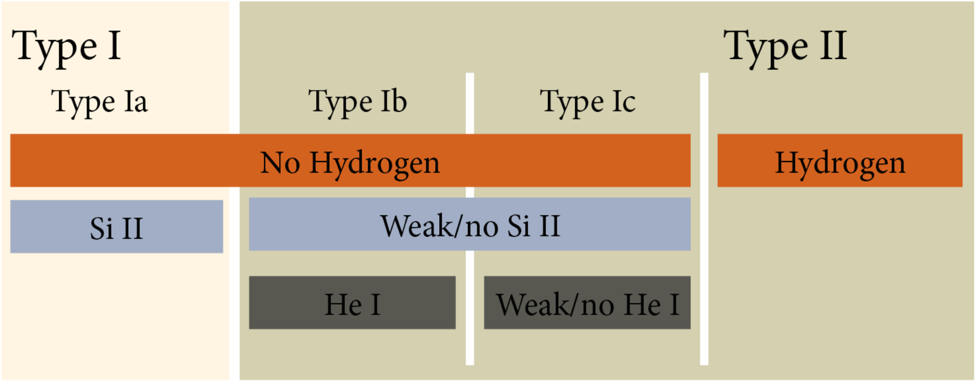

Figure 3.4: Schematic diagram of the Minkowski-Zwicky system for supernova classification. The types of supernovae are grouped by emission and absorption lines rather than physical mechanism of the explosion. Type I are do no exhibit hydrogen lines, while Type II do. The separation between Ia, Ib and Ic are due to silicon (Si II) absorption and helium emission (He I) lines, respectively. If one were to group these by explosion mechanism, Type Ib, Ic, and II are core-collapse supernova (the focus of this work). Type Ia are thermonuclear supernovae.

explosion. The emission is dominated by electromagnetic radiation. A comparatively short-lived and small neutrino luminosity has been proposed; see Figure 3.5a compared to Figure 3.5b [21,163].

Counter-intuitively, the Chandrasekhar limit indicates at which mass the electron degeneracy pressure can no longer compensate for the inward gravitational pull; initiating the stellar collapse. The collapse is what causes the run-away fusion reaction. Chandrasekhar limit is not a fixed quantity. It depends on the mean electron fraction per baryon, $\bar{Y}_e$, and $\bar{s}_e$ being mean electron entropy [111,155,156]; see Equation 3.1.

$$M_{\text{Chandrasekhar}} = 5.38\bar{Y}_e^2\left[1+\left(\frac{\bar{s}_e}{\pi\bar{Y}_e}\right)^2\right]M_\odot \tag{3.1}$$

Type Ib, Ic, and II supernovae are produced by an inward collapse of the core of a massive star at the end of its life span [23,31,111]. In this process, the core will accrete matter from the ongoing fusion processes in the areas outside of the core until the core reaches the Chandrasekhar mass limit and starts to collapse; see Equation 3.1. Unlike a Type Ia supernova, the core collapses under its own weight until it reaches nuclear densities and produces a Proto-Neutron Star (PNS) or a black hole, in case of a mass $> 25\,M_\odot$ or composition with relatively small amount of "metals," *i.e.* elements heavier than hydrogen [111,142]. Matter continues to fall onto the rigid PNS, bounces off the PNS, and produces an outward moving shock. This process will ultimately lead to an explosion. The electromagnetic emission is subdominant to the neutrino emission. The distinctive pattern of the neutrino emission given by the different phases of the explosion,

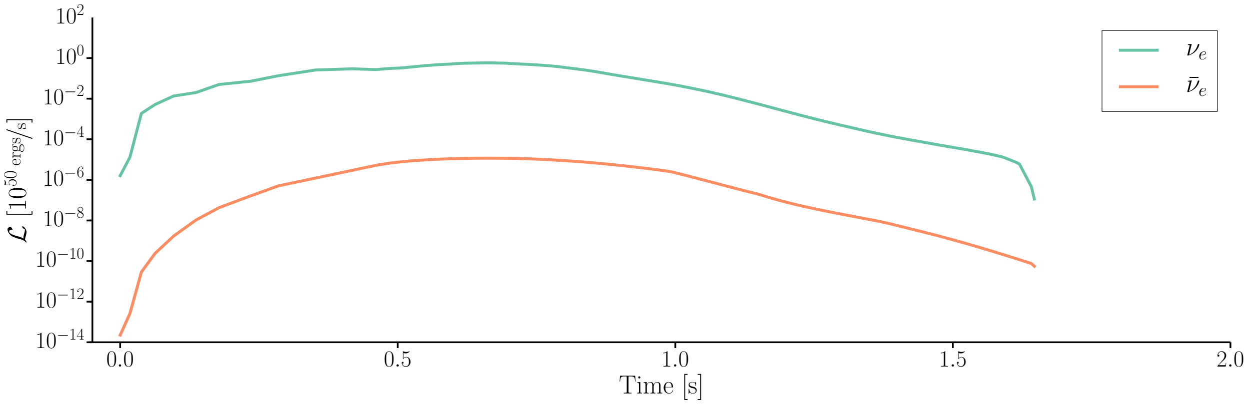

(a) Neutrino luminosity for Type IA Supernova as published by [21]

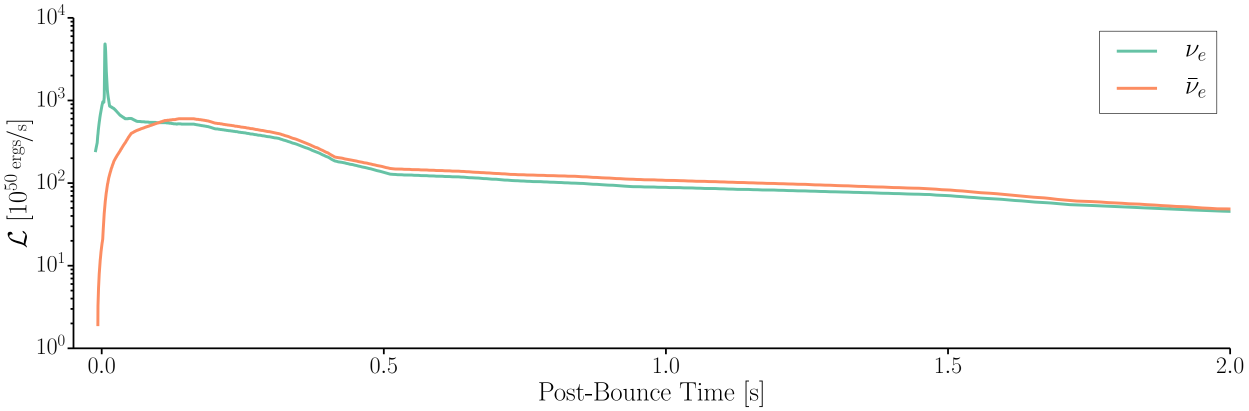

(b) Neutrino luminosity for a core-collapse supernova according to the Lawrence–Livermore Model [22], which has been cut off after 2 s out ≈15 s for comparison.

Figure 3.5: Comparison of neutrino luminosity for a thermonuclear and core-collapse supernova. The values are taken from [21] and [22], respectively.

make core-collapse supernovae extremely important in neutrino astronomy; see Section 3.3 and Section 3.4 for more details [23, 31, 111].

3.3 Core-Collapse Supernova Process

Neutrinos play a fundamental role in the nature, and progression of the core-collapse, and the ultimate explosion [164,165]. For an overview of the core-collapse supernova process and the relevant physical concepts see [23,26,71,72,111,166] and references therein. Neutrinos provide the necessary energy to drive the explosion shock front outward and are the main energy release mechanism for the explosion. 99% of the gravitational binding energy of the progenitor star is being released in form of neutrinos at thermal energies ($\mathcal{O}(10\,\mathrm{MeV})$).

The type and progression of the explosion is highly dependent on the properties (mass, elemental composition, *etc.*) of the progenitor star. In a simplified model, the collapse and explosion itself consists of distinct phases (collapse onset, core collapse, neutrino trapping, core bounce, delayed shock, and Kelvin-Helmholtz neutrino cooling) and that can be identified through their neutrino signatures.

3.3.1 Collapse Onset

The continual mass accretion will cause the Fermi energy of electrons to be higher than the mass difference between ^{56}Mn and ^{55}Fe; see Figure 3.6 Panel 1. This causes electron-capture on iron nuclei

$$^{55}\mathrm{Fe} + e^- \rightarrow {}^{56}\mathrm{Mn} + \nu_e$$

This reduces the number of electrons in the core and consequently decreases $\bar{Y}_e$ and $M_{\text{Chandrasekhar}}$; see Equation 3.1. The star contracts until electron degeneracy pressure can counteract gravity again. The contraction causes an increase in pressure and temperature. The higher pressure and temperature leads to photo-dissociation of iron

$$\gamma + {}^{56}\mathrm{Fe} \rightarrow 13\alpha + 4n - 124.4\,\mathrm{MeV}$$

This decreases $\bar{s}_e$, thermal pressure, and $\bar{Y}_e$, as the photo-dissociation is endothermic and increases the number of baryons. Meanwhile, electrons will also capture on baryons and other nuclei

$$e^- + p \rightarrow n + \nu_e$$
$$e^- + N(Z, A) \rightarrow N(Z-1, A) + \nu_e$$

inside the core. This will produce an additional decrease in $\bar{s}_e$ and hence $M_{\text{Chandrasekhar}}$. A stable balance between electron-degeneracy pressure and gravity can no longer be achieved and the collapse ensues temporarily unchecked [23, 111].

The neutrinos that were produced so far are free to flow outward. The electron-capture on iron produces electron neutrinos, which are the first part of the collapse signature. With increasing density, electron-capture on nucleons becomes a stronger electron neutrino source.

3.3.2 Core Collapse

The collapse itself is split between the inner and outer regions of the core. Initially, the outer regions are unaffected by the contraction deeper inside the core; see Figure 3.6 Panel 2. This changes with increasing density and pressure. The velocity of the infalling matter becomes a function of radius, as the density profile

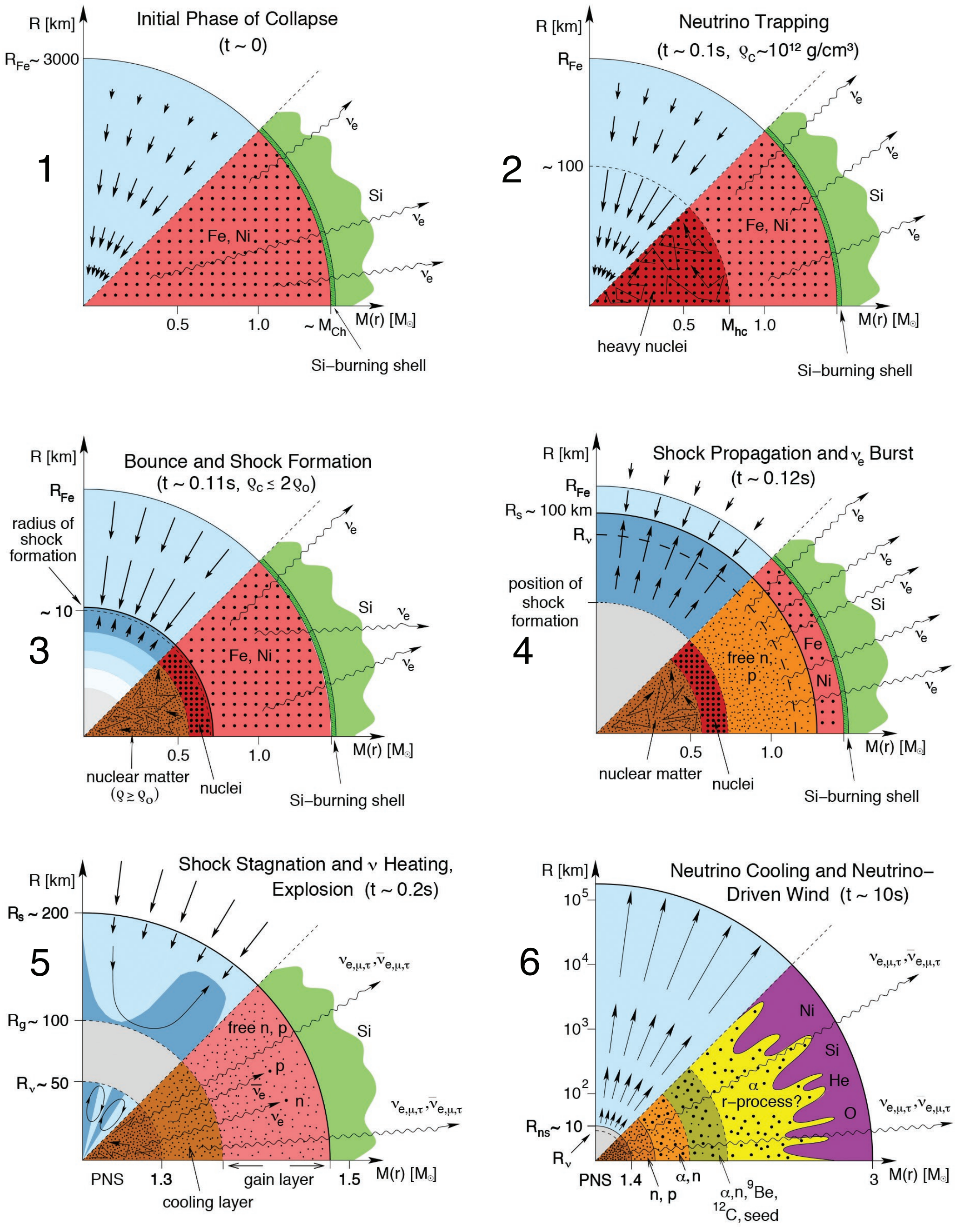

Figure 3.6: Schematic diagrams of the core collapse. In each diagram, the upper half shows the dynamical conditions with the length of arrows indicating velocities of infalling matter. The lower half shows the composition. R_{Fe}, R_s, R_ν, and R_{ns} are the radius for iron core, location of the shock front, neutrinosphere, and the radius of the neutron star, respectively. Credit: [23]

has a large gradient in this area. The outer regions of the core are no longer supported and begin to free fall towards the already compressed inner regions of the core. This process creates even larger densities that leads to neutrino trapping [23, 111].

3.3.3 Neutrino Trapping

As the core compresses, the neutrino optical depth reaches values >1, *i.e.* the mean neutrino diffusion time is longer than the time it takes for matter to fall into the core's center; see Figure 3.6 Panel 2. The neutrinos are now trapped inside the core and are even being pushed further inward by the infalling matter. This happens because neutrinos scatter on nucleons and nuclei at a high rates

$$\nu_e + p/n/N(Z,A) \rightarrow \nu_e + p/n/N(Z,A)$$

at these extreme densities ($10^{12}\,\mathrm{g\,cm^{-3}}$) and produce a β-equilibrium with electrons, *i.e.* electron neutrino and electron numbers continually swap [23, 111]

$$e^- + p \leftrightarrow n + \nu_e$$

The density is dependent on the radius, therefore at some radius the core will become transparent to neutrinos again. This "neutrinosphere" is defined as the radius where neutrino optical depth drops below 2/3. This radius is energy-dependent and creates a filter for low-energy neutrinos. The decrease in optical depth also leads to the first rise in neutrino luminsoity due to the core collapse process [23, 111].

3.3.4 Core Bounce

Unless the core keeps collapsing and forms a black hole, the core collapse will halt when the core reaches nuclear densities; see Figure 3.6 Panel 3. The matter that is now falling onto this object is being repelled and starts to move outward, *i.e.* bouncing off the core. This produces an outward shock wave. As the shock moves outward towards the neutrinosphere it will lose energy due to electron-capture on protons with the still infalling matter.

As soon as the shock front reaches the neutrinosphere, the trapped electron neutrinos can escape. A large increase in the electron neutrino luminosity ensues for 5-10 ms, the so-called "deleptonization burst"; see Figure 3.6 Panel 4 and spike ν_e luminosity in Figure 3.7a, 3.8a, and 3.9a

The electron-capture process decrease the electron-degeneracy making it possible for electron-positron pair production to occur. This makes positron capture on neutrons possible:

$$e^+ + n \rightarrow p + \bar{\nu}_e$$

At the same time, electron-positron annihilation and nucleon-nucleon scattering

$$e^+ + e^- \rightarrow \nu_{e,\mu,\tau} + \bar{\nu}_{e,\mu,\tau}$$

$$N + N' \rightarrow N + N' + \nu_{e,\mu,\tau} + \bar{\nu}_{e,\mu,\tau}$$

are able to increase the neutrino luminosity of all flavors [23, 111].

3.3.5 Delayed Explosion

The energy loss of the shock due to the electron-capture will cause it to stall at radius of $\sim 100 - 200\,\mathrm{km}$, thus delaying the explosion; see Figure 3.6 Panel 5. Infalling matter still moves inward past the stalled shock, accreting matter on the PNS. The PNS begins to cool through $\nu_{e,\mu,\tau}$–$\bar{\nu}_{e,\mu,\tau}$ pair production, which will diffuse outward through the shock and the infalling matter. Neutrinos moving through the stalled shock will deposit energy into the shock via

$$\nu_e + n \rightarrow e^- + p$$

$$\bar{\nu}_e + p \rightarrow e^+ + n$$

If the neutrinos are able to deposit $\sim 10\%$ of their energy into the shock, the shock will be reignited and the explosion continues [23, 111, 167].

3.3.6 Kelvin-Helmholtz Cooling

As the PNS forms, it becomes gravitationally decoupled from the exterior shells of the progenitor star; see Figure 3.6 Panel 6. Neutrino cooling after the core bounce has shrunk the PNS by roughly an order of magnitude. The matter accretion continues and heats up the exterior of the PNS. This heat travels inward and makes it possible for neutrinos that are still trapped inside the PNS to escape, which leads to a secondary deleptonization during the cooling. This ultimately leads to a cooled PNS that is transparent to neutrinos [23, 111, 168, 169].

3.4 Core-Collapse Supernova Neutrino Signal

The individual stages of the explosion greatly depend on neutrinos and their interactions with matter. The neutrino emission follows distinctive patterns depending on the stage of the explosion. Initially, only the emission from the optically thin regions is seen. With the start of the deleptonization peak the electron neutrino emission rises significantly. As the accretion phase takes over, the luminosity of all neutrino flavors rises. This luminosity decreases again as the shock drives outward and slowly levels off as the PNS is cooling [23, 111].

The precise nature of the neutrino signal from core-collapse supernova is still a mystery. The lack of observations as well as the enormous computational resources needed for core-collapse supernova simulations are major obstacles to resolve the problem in the near future.

The advances in simulations since the publication of the Lawrence-Livermore model in 1998 by [22] have brought the community significantly closer to understand the supernova explosion mechanism; see [72] for an overview. The group of the Max-Planck-Institute in Munich and Garching, for example, has explored the explosion of stars just above the explosion threshold ($\sim 8\,M_\odot$) [24, 27]. The core-collapse supernova simulations community has been moving towards ever better simulations with the introduction of higher dimensional simulations, and improvements in the understanding and simulation of physical features of the supernova system (equation of state of nuclear matter, magnetohydrodynamics, neutrino transport, *etc.*) by groups, for example, located at aforementioned Max-Planck-Institute [170–176], California Institute of Technology [177–180], Princeton [181–184], Oak Ridge National Laboratory(-Basel) [185–190], and in Japan [191–195]. With these improvements in simulation have also brought a significant increase in the resources required to run these simulations; see [194, 196] for examples.

To simulate the detector response to neutrinos from a core-collapse supernova in IceCube, one typically uses the Lawrence-Livermore model [22] and one model from the Garching group [24, 27]; see Figure 3.7, 3.8, and 3.9, respectively. These models are chosen because they are one of the few simulations that model the whole neutrino emission process including luminosities during and after the explosion, and the cooling phase of the star. The Lawrence-Livermore model is old and is lacking most of the microphysics (magnetohydrodynamic simulation, neutrino transport, *etc.*) that are including in newer models. It still provides a baseline to compare other models to as it is one of the first to show the whole explosion. The Garching models provide the means to study the response to the most abundant class of stars that could produce supernovae, *i.e.* 8–10 $M_\odot$. Most other models terminate before or just after a possible explosion; as shown in Figure 3.9. This only provides a partial picture of the IceCube response, as the supernova emission could last ten times longer, as observed during SN1987A [63, 64]. Additionally, other experiments, such as Super-Kamiokande, use these models for their comparisons as well [197].

Supernova simulations have shown that there are distinct features in the neutrino signal for each of the phases described in Section 3.3. Observing any of these features would yield a wealth of information with regard to the processes occurring within the core-collapse supernova, *e.g.* the nature of the hot nuclear matter [27, 198], neutrino transport in hot nuclear matter [185, 195], matter convection during the explosion [176, 199], rotation of the star [200], *etc.* The direct observation of black hole formation is also possible in

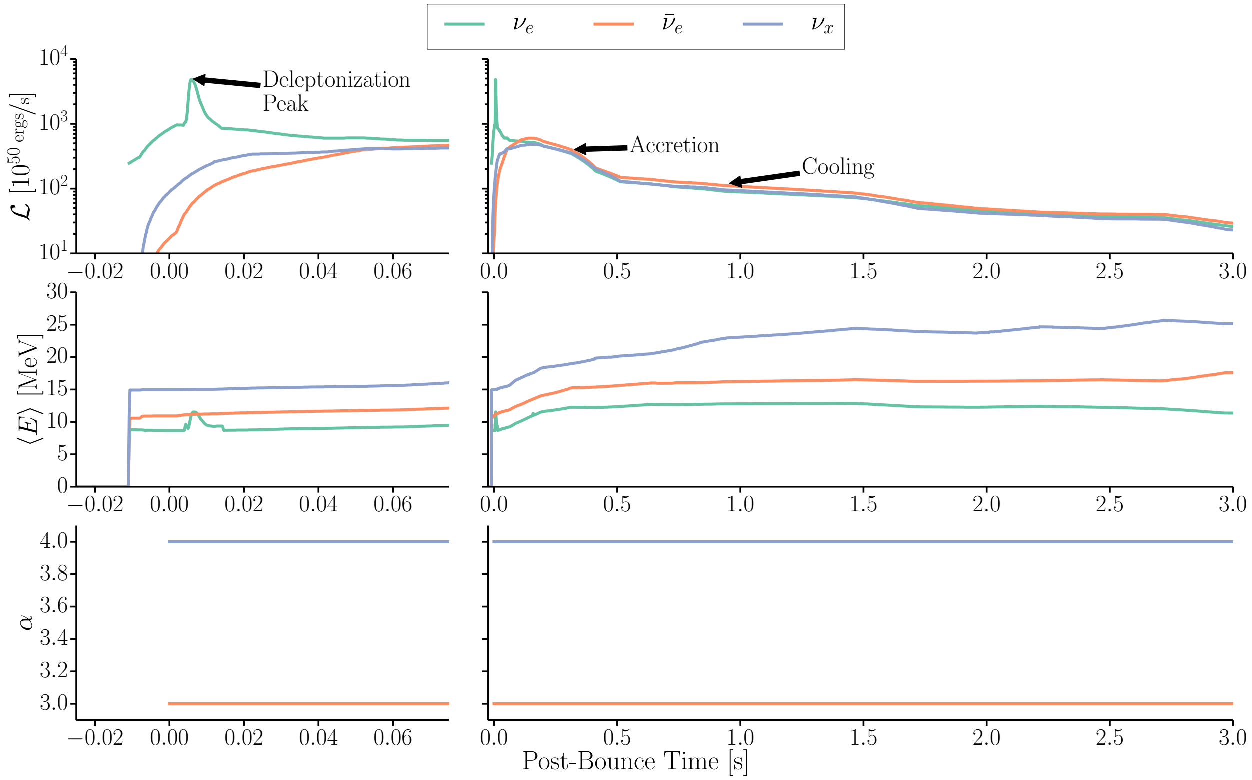

(a) Luminosity, mean energy, and pinch parameter (α) of the Lawrence-Livermore Model [22] for a $20\,M_\odot$ star modeled after SN1987A. The model shows all relevant stages of the CCSN explosion that are also seen in newer models. It was one of the first to show the full cooling phase over the course of ≈15 s. NOTE: Timescale was shortened for better representation of different phases of explosion.

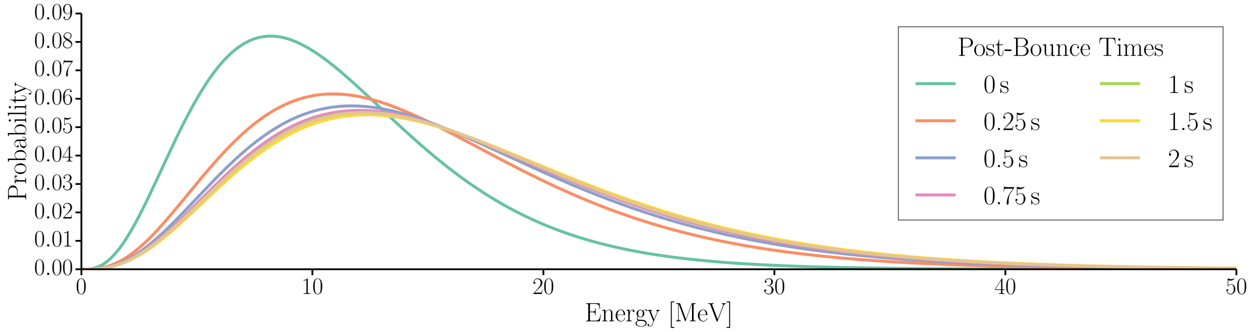

(b) Energy spectrum for the Lawrence-Livermore Model for a $20\,M_\odot$ star modeled after SN1987A at various post-bounce times.

Figure 3.7: Luminosity, spectral parameters, and energy spectrum versus time for the Lawrence-Livermore model [22] for a star with $20\,M_\odot$. The emission is modeled after the neutrino detection of SN1987A and provides the full PNS cooling phase.

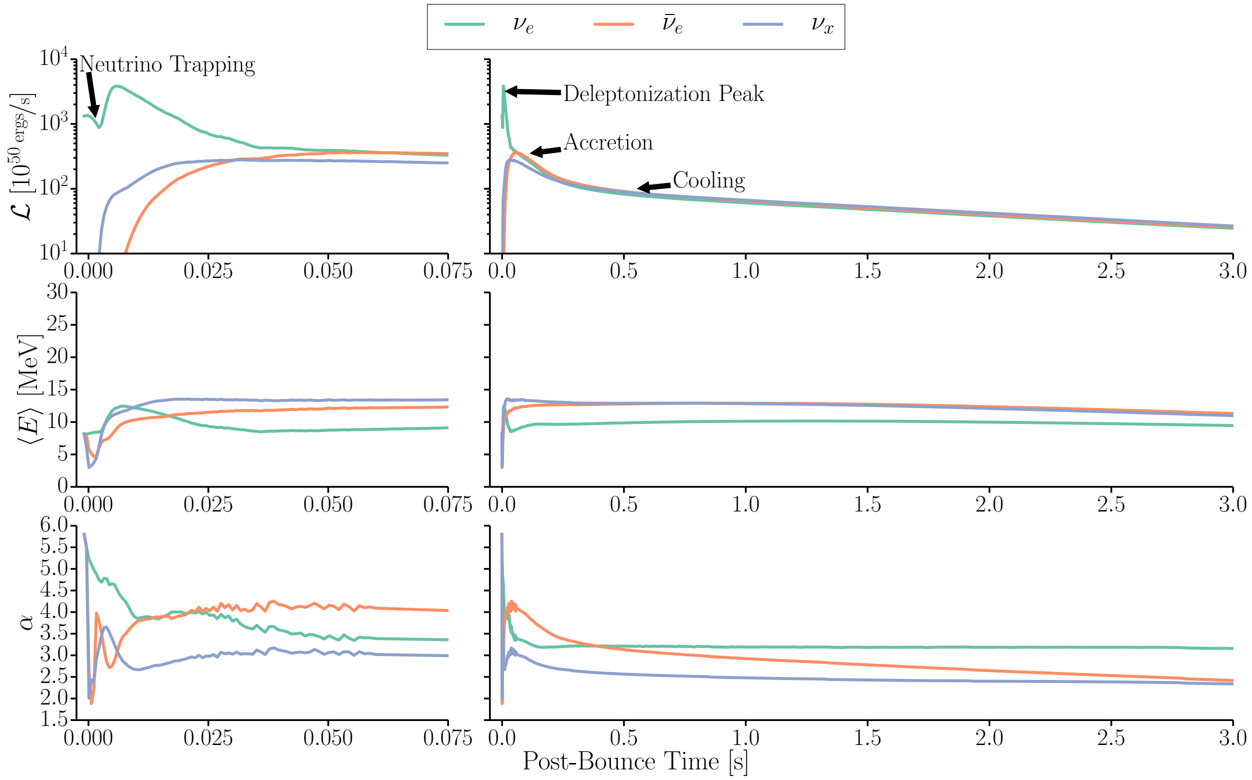

(a) Luminosity, mean energy, and pinch parameter (α) for a model by the Garching group simulation of a star with $8.8\,M_\odot$ and an O-Ne-Mg core with the full Shen equation of state [25] undergoing an electron-capture supernova [26]. This simulation runs until $\sim 9\,\mathrm{s}$. NOTE: Timescale was shortened for better representation of different phases of explosion.

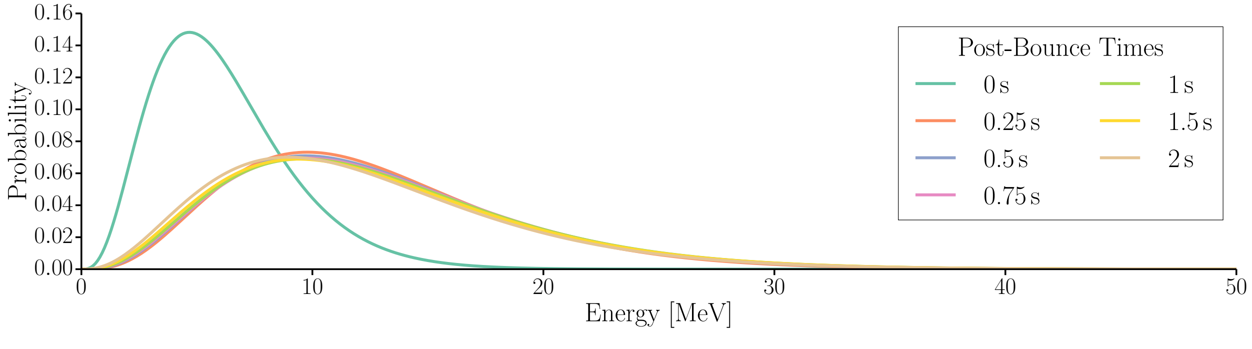

(b) Energy spectrum for the model by the Garching group of a star with $8.8\,M_\odot$ and an O-Ne-Mg Core at various post-bounce times.

Figure 3.8: Luminosity, spectral parameters, and energy spectrum versus time for Garching group simulation of a star with $8.8\,M_\odot$ and an O-Ne-Mg core [24] with the full Shen equation of state [25] undergoing an electron-capture supernova [26]. This provides a baseline for possible supernova from stars just above the explosion threshold that do not even form iron in their cores.

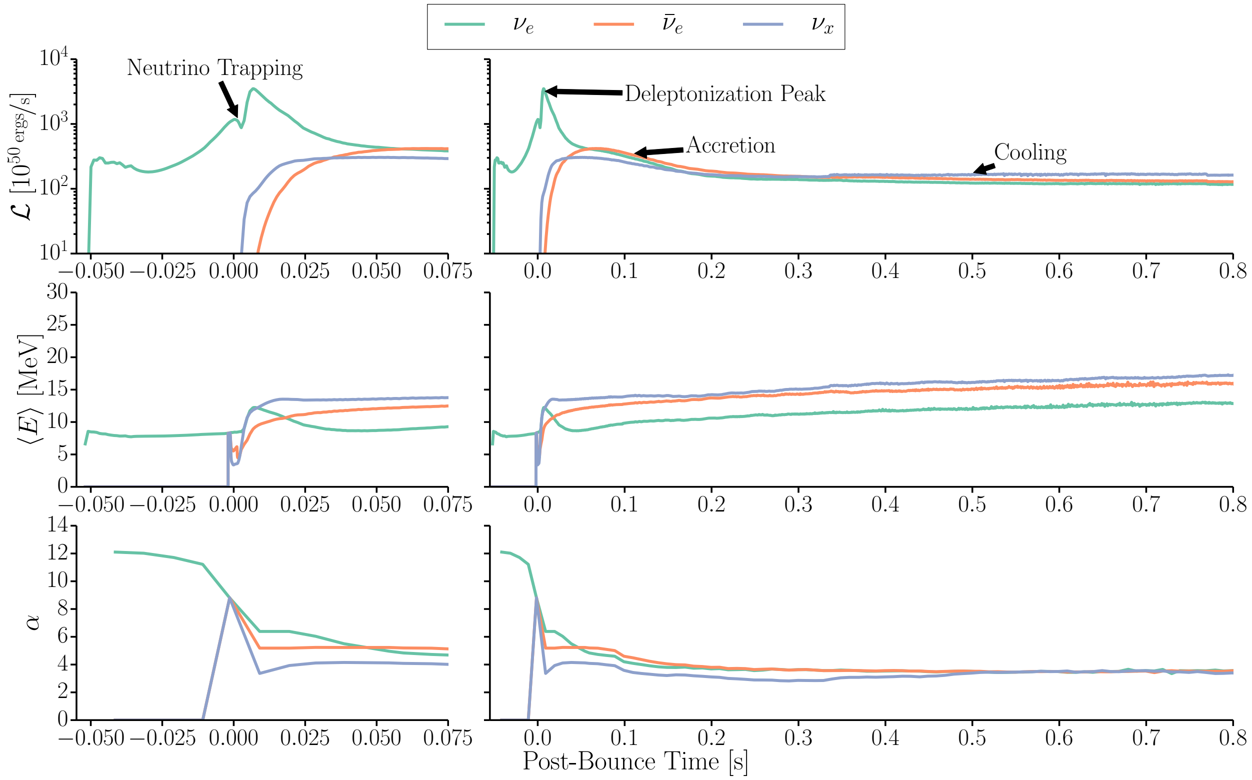

(a) Luminosity, mean energy, and pinch parameter (α) for a model by the Garching group simulation of a star with 8–10 $M_\odot$. This simulation was terminated after 0.8 s.

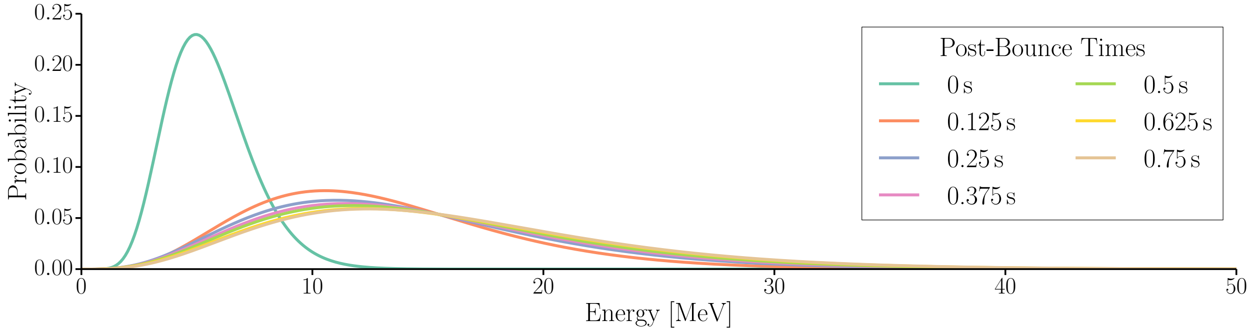

(b) Energy spectrum for the model by the Garching group of a star with 8–10 $M_\odot$ at various post-bounce times.

Figure 3.9: Luminosity, spectral parameters, and energy spectrum versus time for Garching group simulation of a star with 8–10 $M_\odot$ [27]. This is an example of a simulation that was terminated prematurely because of computational constraints. It is still used as a baseline model in IceCube simulation as it shows the possible response for a large number of stars that are supernova candidates because of their mass.

case the signal abruptly ends as the neutrinos cannot escape the gravitational pull of the black hole; see Figure 3.10. Fundamental neutrino properties such as the mass hierarchy could be probed as well [30].

Taking a closer look at the neutrino luminosity and energy spectrum with time, one can separate the signal into four distinct time frames: neutrino trapping, deleptonization, accretion, and cooling; see Figure 3.7a, 3.9a, and 3.8a. Even before the collapse occurs, the high rate of electron-capture on free nucleons causes a measurable electron neutrino flux. Neutrino trapping is characterized by a sudden decrease in the electron neutrino luminosity. As the collapse sets in and increases the density to the point that the matter becomes opaque to neutrinos, the electron neutrino luminosity will dip down; see Figure 3.9a and 3.8a.

The deleptonization of the stellar matter causes a sudden burst in electron neutrinos independent of the chosen model; see Figure 3.7a, 3.8a, and 3.9a. This burst is caused by the shock propagating through infalling matter and disassociating matter to free nucleons, thereby converting gravitational into thermal energy. With a sudden increase in free nucleons, the electron-capture rate will be boosted as well. This produces electron neutrinos, which are free to diffuse towards the neutrinosphere and leave the supernova uninhibited causing an order of magnitude increase in electron neutrino luminosity for 5-10 ms. It is worth noting that the sudden hardening of the electron neutrino energy spectrum during the deleptonization peak; see Figure 3.7b, 3.8b, and 3.9b.

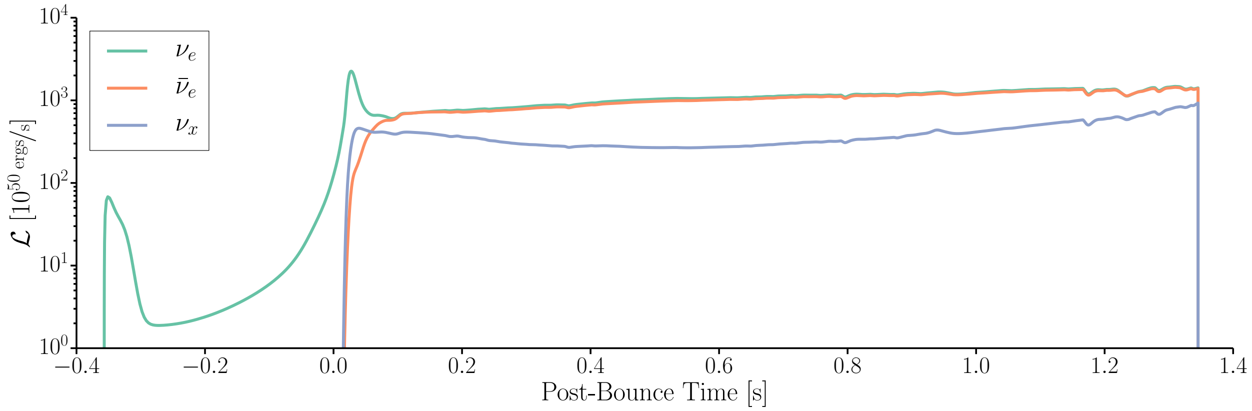

Figure 3.10: Supernova neutrino luminosity from a 40 $M_\odot$ non-rotating star that forms a black hole [28]. A portion of the neutrino signal can escape before the black hole is formed. The characteristic feature of these signals is the sudden drop off in luminosity and hence in the rate in IceCube.

The deleptonization of the matter also causes the electron degeneracy to decrease, which makes it possible to convert γ-rays to electron-positron pairs more frequently. This in turn increases the amount of electron- and positron-capture on free nucleons. In addition, electron-positron annihilation and nucleon bremsstrahlung will produce neutrinos of all flavors. These processes adds electron anti-neutrinos, $\bar{\nu}_e$, and

ν_x to spectrum, where ν_x is a chosen representation for muon and tau (anti-)neutrinos. The luminosity of ν_x is about half that of electron (anti-)neutrinos for the Lawrence-Livermore and double for the Garching models; see Equation 3.4 as well as Figure 3.7 3.8, and 3.9 [23, 111].

The neutrino signature of the PNS cooling process takes over the signal after ~0.5 s. Neutrinos of all flavors are being produced in pair production processes in the core of the star. The cooling is an inward moving process, which means that the PNS will not be completely transparent to neutrinos for $\mathcal{O}(10\,\mathrm{s})$ after the collapse [23].

Besides the overall flux, the detectability of the different phases of the collapse depend heavily on the respective neutrino energy spectrum. The spectral function for the models discussed above can be most aptly described as a "pinched" thermal spectrum [201, 202]:

$$p(E, \langle E_\nu \rangle(t), \alpha(t)) = \frac{E^{\alpha(t)}}{\Gamma(1+\alpha(t))} \left(\frac{1+\alpha(t)}{\langle E_\nu \rangle(t)} \right)^{1+\alpha(t)} \exp\left(-\frac{(1+\alpha(t)) \cdot E}{\langle E_\nu \rangle(t)} \right) \tag{3.2}$$

where $\langle E_\nu \rangle(t)$ is the time-dependent average neutrino energy, and $\alpha(t)$ is a time-dependent ("pinch") spectral parameter that varies between 2 and 14, depending on the model and neutrino flavor. The overall flux for a given neutrino energy at given time can be summarized as

$$\Phi_\nu(t, E_\nu) = \frac{\mathcal{L}_\nu(t)}{\langle E_\nu \rangle(t)} \cdot p(E_\nu, \langle E_\nu \rangle(t), \alpha(t)) \tag{3.3}$$

where $\mathcal{L}_\nu(t)$ is the time-dependent neutrino luminosity.

The mean energy for muon and tau (anti-)neutrinos is expected to be higher than that of electron (anti-) neutrinos. The neutrinosphere for these flavors is deeper inside the PNS [201, 202] and they escape with an average higher energy. Contrary to expectations, muon and tau (anti-)neutrinos interact strongly with matter. Considering all possible interaction channels, the muon and tau (anti-)neutrinos energy spectrum is within 10-20% of the electron anti-neutrino spectrum. The neutron-rich matter inside the supernova softens the electron neutrino spectrum, which leads to an average energy relationship of [23, 26, 31, 111, 112, 201, 202]

$$\langle E_{\nu_e} \rangle < \langle E_{\bar{\nu}_e} \rangle \lessapprox \langle E_{\nu_x} \rangle \tag{3.4}$$

The effect of stellar mass on the neutrino luminosity and energy spectrum is discussed in [72, 112, 203]. Up to $20\,M_\odot$, the neutrino luminosity and energy spectrum are roughly the same as a function of stellar mass. For stars with mass $> 20\,M_\odot$, the luminosity and energy spectrum change significantly during the accretion phase. The luminosity varies by a factor of $\lesssim 2$. This discrepancy can be explained due to the neutrino production during the accretion phase. The luminosity is a function of mass

$$\mathcal{L}_\nu \propto \frac{G M_{R_\nu} \dot{M}}{R_\nu} \tag{3.5}$$

where R_ν is the radius of the neutrinosphere, M_{R_ν} is the mass enclosed in the neutrinosphere, $\dot{M}$ is the mass accretion rate, and G $(= 6.67 \times 10^{-11}\,\mathrm{m^3\,kg^{-1}\,s^{-2}})$ is the gravitational constant. This relationship explains the discrepancy to zeroth-order, as $\dot{M}$ increases for heavier stars.

3.5 Supernova Rate and Distribution

Determining the rate and distribution of supernovae is one of the most challenging tasks in astronomy. A large portion of supernovae are obscured in the optical regime by interstellar dust [204]; making their optical detection nearly impossible. The host galaxy also has to be able to produce high mass stars. Elliptical galaxies, for example, are old and only have small star forming regions that are unable to produce high mass stars [31, 61]. Even though ~66% of supernovae are Type-II, their optical signature is significantly smaller than Type-I. This makes Type-I much easier to detect with current techniques [205, 206].

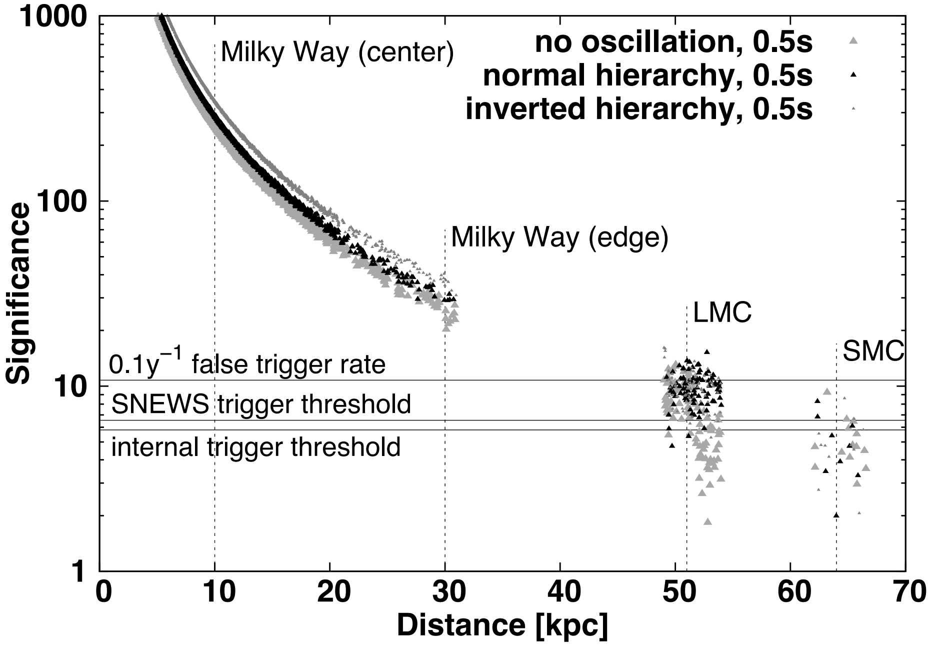

Figure 3.11: Sensitivity of IceCube to core-collapse supernovae for three different oscillation scenarios in terms of supernova analysis significance of detection versus distance for the Lawrence-Livermore model [22] using the progenitor distribution in [29] and the current simulation described in Section 5.1.1; see Section 4.9 for the definition of the supernova analysis significance. The background is taken from data. Credit: [30]

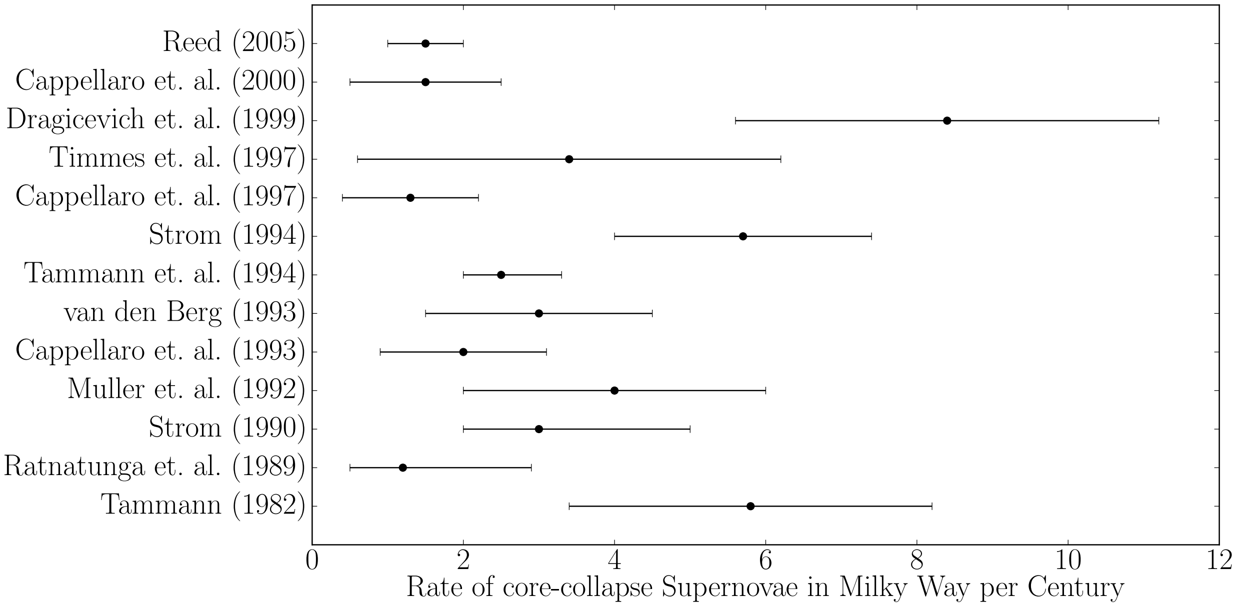

Figure 3.12: Various predictions for the core-collapse supernova rate in the Milky Way given different tracer methodology. Plot is based on values given in [31] and references there in.

The distribution of supernovae within a galaxy is unknown. A possible model can be formulated by considering the distribution of tracers for past supernovae [207–211], the distribution of star forming regions [211, 212], the distribution of massive stars in the galaxy [211, 212], and the distribution of supernovae in galaxies of similar type [213]. Past supernovae are a tracer for future supernova activity as they follow the distribution of massive stars in the galaxy. Star forming regions will yield fewer supernovae, as the stars in this region are predominantly young, which lowers the possibility of a supernova occurring. The distribution of massive stars yields the distribution of possible future supernova as a massive star is required for a core-collapse supernova.

The detection of supernova neutrinos in IceCube requires the knowledge of the core-collapse supernova rate in the Milky Way, Large Magellanic Cloud, and Small Magellanic Cloud; see Figure 3.11. From a study of 330 galaxies in [213], one can predict that 82-91% (depending on the exact geometry of the galaxy) of the supernova in the Milky Way are core-collapse supernovae. From Figure 3.12, one can find a supernova rate of 1.7-2.5 supernovae per century within 3σ. In addition, the BAKSAN observatory has set a limit of < 13 core-collapse supernovae per century [214]. The energy requirements to produce galactic cosmic rays point to a rate of one galactic supernova per ~30 years, if all remaining kinetic energy were given to cosmic rays [215]. This of course leads to an over-predication as not all the kinetic energy will be transferred to cosmic rays.

3.6 Current Supernova Neutrino Detectors

There are several neutrino experiments currently operating that can detect the signal from a galactic supernova. The most promising possible detectors are: IceCube Neutrino Observatory [30, 216], Super-Kamiokande (Super-K) [217], Borexino [218], Helium and Lead Observatory (HALO) [216,219], Large Volume Detector (LVD) [220, 221], Imaging Cosmic And Rare Underground Signals (ICARUS) [222–224], and in the near future SNO+ [225]. All of these detectors, except for HALO and LVD, are not dedicated supernova neutrino search experiments. Their physics capabilities for supernova neutrinos complement each other. IceCube's contribution to this global network of supernova neutrino experiments will be discussed in detail in Chapter 4.

Super-K, besides IceCube is the only other water Cherenkov neutrino experiment currently operating that could detect a signal from the next galactic supernova. It consists of a stainless steel cylinder holding 50 ktons of purified water (of which 22.5 ktons are the fiducial mass) with 40% coverage from 11,146 20 inch PMTs. The main science focus is the study of neutrino oscillations [226, 227], atmospheric neutrinos at $\mathcal{O}(1\text{–}10\,\mathrm{GeV})$ [228], solar neutrinos [229, 230], and proton decay [231]. Super-K will be able to measure the energy spectrum of supernova neutrinos at high statistics, which is essential to understand the supernova process and neutrino oscillations in supernova matter [197]. Additionally, it will be able to provide directional information about incoming neutrino front (within $\sim 25°$) [197, 232]. No other experiment can provide this information.

LVD, Borexino and SNO+ are organic liquid scintillator based experiments. LVD is dedicated supernova neutrino search experiment [221] that has been used to measure the atmospheric muon flux at the Gran Sasso lab [233, 234]. Borexino is focused on the study of solar neutrinos [235, 236]. SNO+ is looking for neutrino-less double beta decay from tellurium [237, 238]. Liquid scintillator-based detectors have the advantage that they have a low energy threshold and can explore lower energy neutrinos. They also provide very precise calorimetry of the events. The typically smaller active mass compared to Super-K and IceCube reduce the statistics.

HALO stands out in two ways [216]. It is a dedicated supernova neutrino search experiment and uses lead as its neutrino detection medium. Supernova neutrino interaction will cause neutrons to be liberated from the lead. These will then be detected using ^{3}He proportional counters [239]. The relative high energy threshold of ν–Pb interactions compared to water or scintillator produce low statistics. It is sensitive to certain spectral features [219] and adds another dedicated experiment to the mix.

ICARUS is largest currently operating liquid argon-based neutrino experiment. It consists of a 600 ton liquid argon time projection chamber [240]. The relatively small target mass produce relative few neutrino events from a galactic core-collapse supernova. The use of liquid argon make it very sensitive experiments to the ν_e flux [222, 241], which most of the other experiments are not. ICARUS can therefore detect the deleptionization burst and possible neutrino trapping better any of the other detectors.

Chapter 4

IceCube Detector

The work presented in this thesis is based on data collected by, and simulated for, the IceCube Neutrino Observatory. This chapter will explore its design, as well as operating and detecting principles with a focus on the detection of supernova neutrinos and the infrastructure in place to do so.

4.1 IceCube Detector

The IceCube Neutrino Observatory is a cubic-kilometer-scale neutrino detector designed for the detection of high energy (>100 GeV) astrophysical neutrinos at the geographic South Pole; see Figure 4.1a. The observatory itself consists of three sub-detectors: IceCube [242–244], DeepCore [245], and IceTop [246]. Each sub-detector uses the same instrumentation design with embedded Digital Optical Module (DOM) and associated surface readouts DOM Readout (DOR) modules; see Figure 4.1c, Section 4.7, and Section 4.8 for more details. The photomultiplier tubes (PMTs) inside the DOMs are all oriented downward to bias the detection efficiency towards events that originate below the horizon. Only neutrino events can cause events that originate below the below the horizon.

The "in-ice" portion of the detector consists of 86 strings with 60 DOMs each in a hexagonal pattern embedded in the South Polar icecap. 80 of these strings are main in-ice array with an inter-DOM spacing of 17 m and inter-string spacing of ∼125 m between 1450 m and 2450 m below the surface; see Figure 4.1b. The remaining 6 strings are DeepCore strings with a 7 m inter-DOM spacing, ∼62.5 m inter-string spacing, and 401 DOMs with ∼35% higher quantum efficiency PMTs; see Figure 4.1b. The DeepCore DOMs are also located deeper in detector at a depth of 1760 to 2450 m (there are no DOMs between 1850 and 2107 m due to dust layers; see Section 4.6). The smaller inter-DOM and -string space lowers the energy threshold to 10 GeV in the infill region.

IceTop is a surface array consisting of 162 tanks with 2 DOMs each placed in 81 stations on top of IceCube strings. It is designed to observe the electromagnetic components of cosmic ray air showers from cosmic ray primaries with energies between ∼100 TeV and 1 EeV, which can be used for vetoing air shower events with a zenith <30° in IceCube.

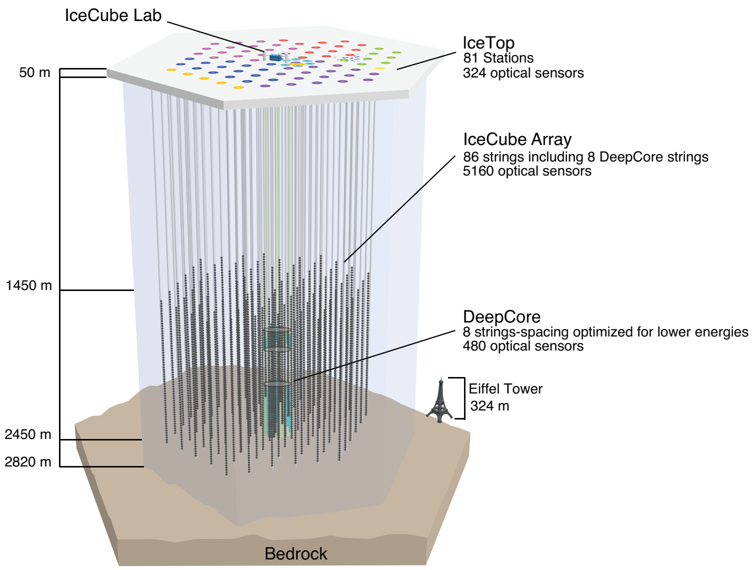

(a) Schematic diagram of the IceCube Neutrino Observatory. The colors at the surface indicate the different seasons when respective strings were deployed. The small black dots that are inside the glacier represent individual DOMs; see Figure 4.1c. The Eiffel tower is added as a dimensional reference.

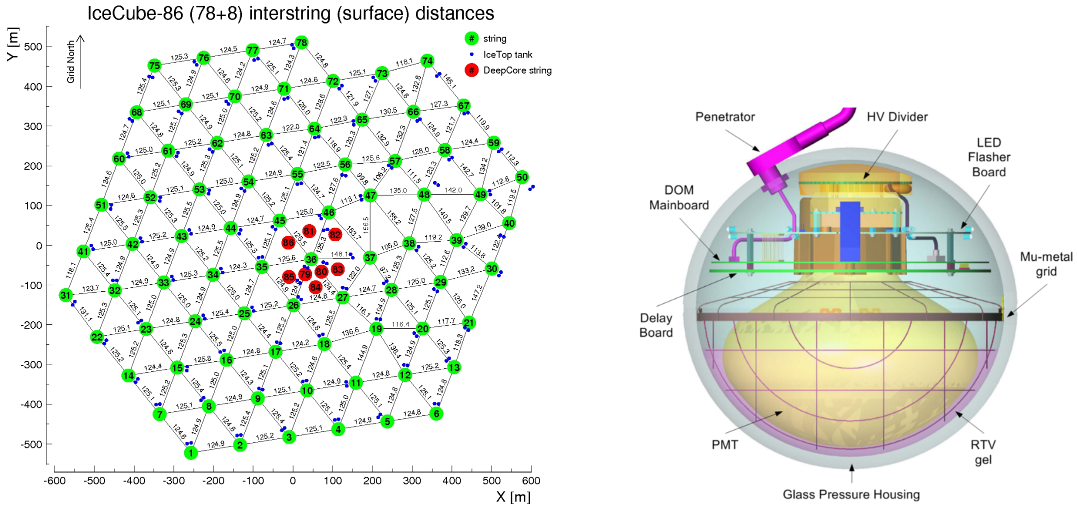

(b) Top view of the IceCube Neutrino Observatory showing the hexagonal geometry and inter-string spacing in meters for both the main in-ice array (in green) and DeepCore (in red) infill. The blue dots indicate the location of IceTop tanks.

(c) Schematic diagram of a Digital Optical Module.

Figure 4.1: Schematic diagrams of IceCube Neutrino Observatory, a top view of the detector, and a Digital Optical Module

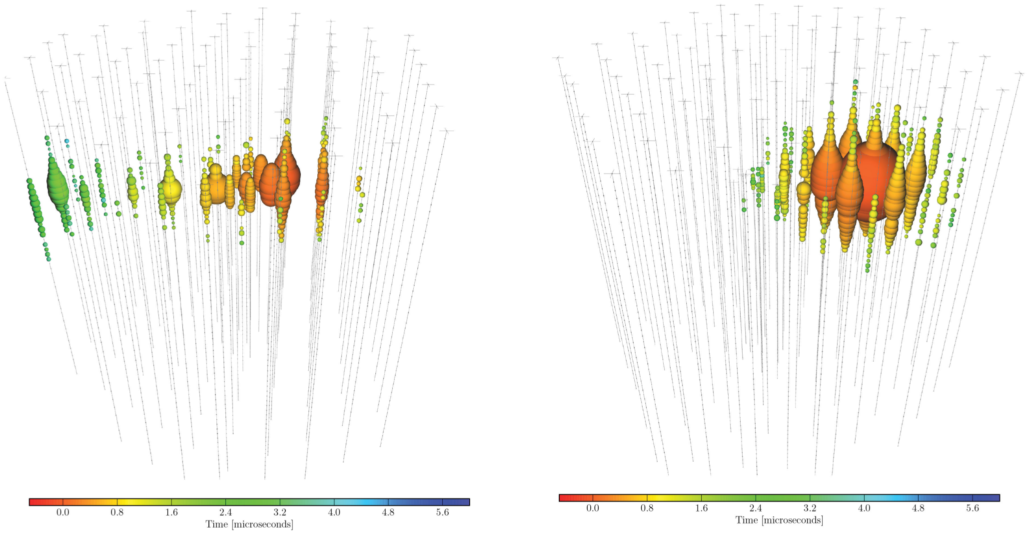

(a) A ~71 TeV "track" event found in [32]. This event posses the neutrino interaction vertex is inside the detector and the resulting muon travels out of the detector.

(b) A ~1 PeV "cascade" event found in [32]. A hadronic shower occurs inside the detector leaving a nearly spherical light deposition pattern.

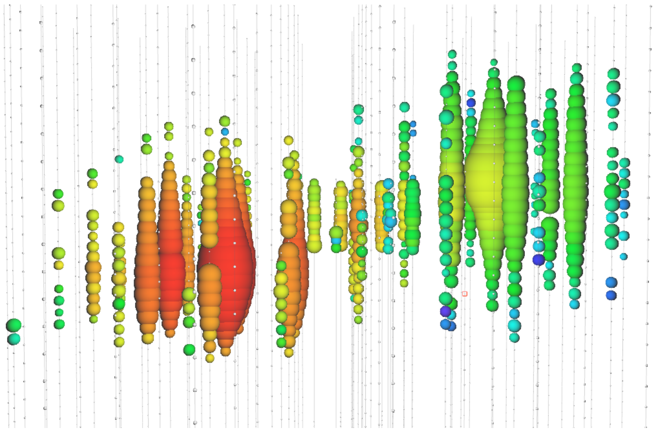

(c) A $\mathcal{O}$(PeV) "double-bang" simulated event in IceCube. A hadronic shower occurs from the initial CC interaction in the detector leaving a nearly spherical light deposition pattern. A τ emerges from the interaction and will rapidly decay leaving another spherical pattern. Note: The τ decay length is set to be artificially high to give it the double bang structure.

Figure 4.2: Examples of the three main classes of events in IceCube. The rainbow color scheme represent the time dimension where red is early and blue/purple is late. The size of the spheres are the amount of charge that was deposited on a given DOM. NOTE: These events have had noise and possible coincident events removed.

4.2 IceCube Neutrino Events

The neutrino energies that IceCube was designed for, *i.e.* atmospheric and astrophysical neutrino with energies $\geq 10\,\text{GeV}$, will present a distinctive geometric pattern in the detector over the course of $\mathcal{O}(1\text{–}10\,\mu\text{s})$; see Figure 4.2. The different geometric patterns are caused by the interaction of different neutrino flavors and types of interaction, *i.e.* charged-current (CC) through the exchange of a $\text{W}^{\pm}$-boson or neutral-current (NC) through the exchange of a Z-boson. The "track" events are caused by CC interactions of ν_μ; see Figure 4.2a. For these events the interaction may occur outside the detector and the resulting muon penetrates the detector or, as in Figure 4.2a, the interaction occurs inside the detector and the product muon travels outward [247]. A "cascade" event is caused by the CC interaction of ν_e or ν_τ or NC interaction of all neutrino flavors [247]; see Figure 4.2b. The spherical structure of the cascade the manifestation of a hadronic shower inside the sparsely populated detector [247]. Events from high-energy ($\geq \mathcal{O}(500\,\text{TeV})$) ν_τ will have a double cascade or "double-bang" structure, *i.e.* two cascades separated by some distance in the detector due to rapid decay of the resulting τ inside the detector. This class of events has not been observed so far; see Figure 4.2c.

4.3 IceCube Supernova Neutrino Events

The supernova neutrino signal in IceCube is very distinct from a typical IceCube signal event outlined above. The supernova signal will manifest as a statistically significant increase of the detector noise rate over the course of $\mathcal{O}(0.1\text{–}10\,\text{s})$; see Figure 4.3. This increase is dependent on the theoretical supernova model and distance between the supernova and IceCube.

Supernova neutrino detection in IceCube is considered a counting experiment with all in-ice DOMs acting as independent detectors. The increase in the DOM noise can be represented succinctly on a per DOM basis

$$R(t) = \epsilon \cdot n_{\text{Ice}} \int_0^\infty dE_\nu \Phi_\nu^{\text{Detector}}(E_\nu, t) \int_0^\infty dE_e \frac{d\sigma}{dE_e}(E_\nu, E_e) V_{\text{eff}}^{e^\pm}(E_e) \tag{4.1}$$

where ϵ is an efficiency factor, n_{Ice} is the number of targets for ice per unit volume, E_e is the lepton energy, $\frac{d\sigma}{dE_e}(E_\nu, E_e)$ is the differential cross-section for the interaction of interest, and $V_{\text{eff}}^{e^\pm}(E_e)$ is the effective detection volume for leptons with a given energy as described in Section 4.6.1.

$$\Phi_\nu^{\text{Detector}}(E_\nu, t) = \frac{\Phi_\nu(E_\nu, t)}{4\pi d^2} = \frac{\mathcal{L}_\nu(t)}{4\pi d^2 \langle E_\nu \rangle(t)} \cdot p(E_\nu, \langle E_\nu \rangle(t), \alpha(t)) \tag{4.2}$$

is neutrino flux for a given neutrino energy, E_ν, at the detector [30].

As IceCube is not a dedicated supernova neutrino experiment and the event topology differs greatly from a typical IceCube events. IceCube's supernova neutrino detection capabilities are limited when solely considering IceCube. IceCube will produce a very high statistics sample ($\mathcal{O}(0.1\text{–}1 \times 10^6)$) events for the whole

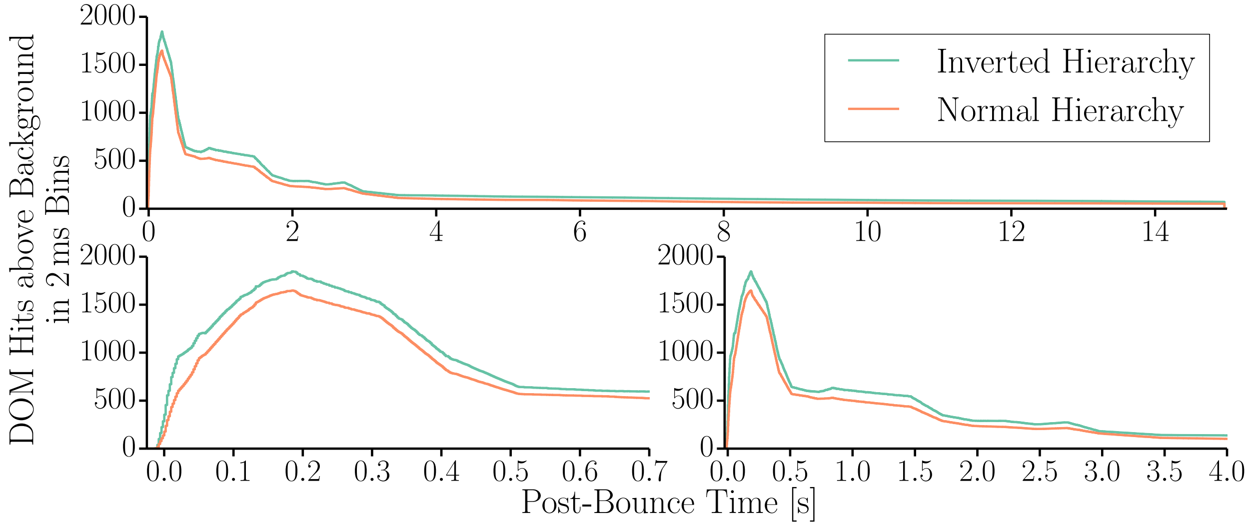

(a) Expected integrated detector response for a supernova according to the Lawrence-Livermore model at 10 kpc [22, 30]; see Figure 3.7 for details on model.

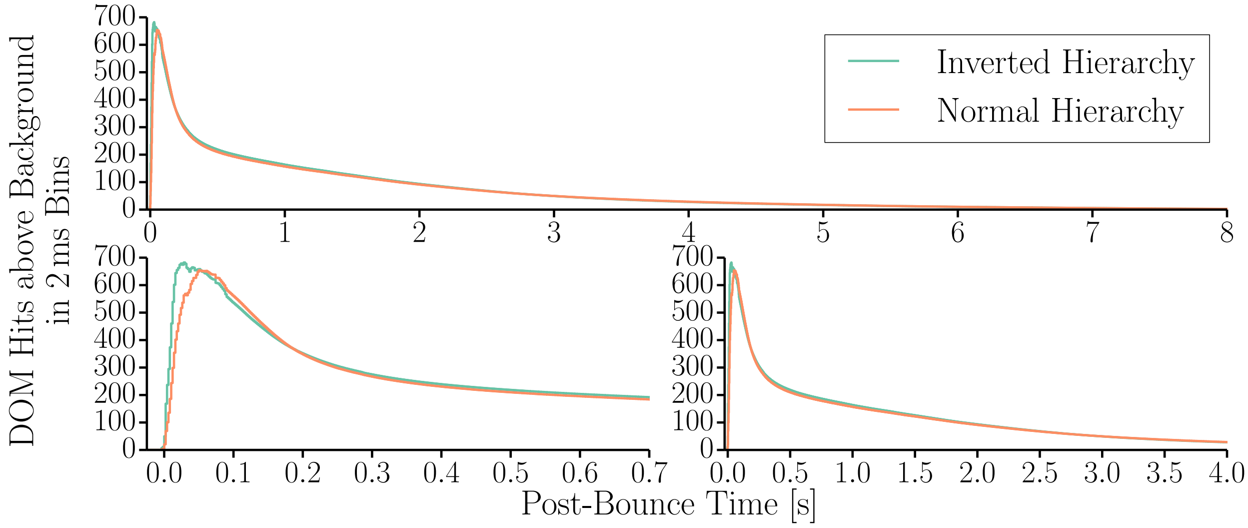

(b) Expected integrated detector response for a supernova according to the 8.8 $M_\odot$ with an O-Ne-Mg core with the full Shen equation of state model at 10 kpc [24, 30]; see Figure 3.8 for details on model.

Figure 4.3: Expected detector response above background for two supernova models, one for a ∼20 $M_\odot$ mass star [22] in Figure 4.3a and for a 8.8 $M_\odot$ mass star [24] in Figure 4.3b. The background is ∼3000 hits per 2 ms bins for the whole detector.

supernova event. It will also provide information with a time resolution of 2 ms with high statistics (up to $\mathcal{O}(10^2\text{–}10^3)$) per time bin; see Figure 4.3 as well as Section 4.7.2 and 4.9 for details. No other experiment can provide these high statistics with the same time resolution. The large spacing between the strings and DOMs make it hard to extract additional information, such as pointing information, spectral features, *etc.*, from the signal. More information about the neutrino signal, such as the average neutrino energy, can be extracted from double or triple DOM triggers, *i.e.* two or more DOM triggers produced by the same neutrino interaction [248].

Considering the advantages and disadvantages of all the different detectors and detector technologies discussed in Section 3.6 and above, the community is well-prepared for the next galactic core-collapse supernova. There are a number of experiments that can perform calorimetry of the events (Super-K and liquid scintillator experiments), while others can be used to measure spectral parameters (HALO). IceCube fits well into this setup as it provides a detailed view of the progression of the supernova signal in time with high statistics. The different locations of the detectors, for example Antarctica, Japan, and Italy, could yield a deeper insight into neutrinos independent of the supernova model [249].

4.4 Source of Detector Backgrounds

A thorough understanding of the detector backgrounds is important for any particle physics experiment. The comparatively faint signal that supernova neutrinos produce makes it necessary to understand the inherent DOM noise and the atmospheric muons that contribute to the overall supernova signal in detail as well as produce false positive supernova signals; see Section 6.1.

The stability of the detector backgrounds is an important aspect for detecting faint and transient signals from a galactic supernova. This requires monitoring the detector backgrounds continuously; see Section 4.7.2 and 4.9. This means that besides an understanding of physical sources of the backgrounds, the stability of the backgrounds over $\mathcal{O}(1\text{–}10\,\mathrm{s})$ is a fundamental aspect for the supernova analysis. IceCube is ideally setup for this kind of search as the backgrounds are mostly stable over these time periods.

4.4.1 DOM Noise

The DOM noise consists of multiple interdependent components: thermal noise from the electronics [250, 251], thermionic noise from the PMT [252], and statistically correlated noise component; see [253] for a detailed overview. The thermal noise from the electronics is Johnson-Nyquist noise [250, 251] that is inherent to any electronic system due to thermal disturbance of the electrons in the system. The thermionic noise from the PMT is caused by emission of electrons from a (hot) metal surface. The source of the correlated noise is largely unknown at this point.

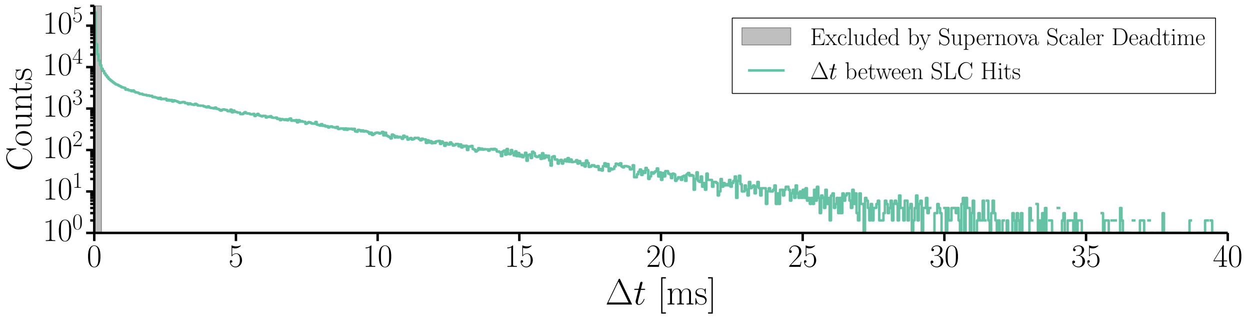

(a) Distribution of time difference, Δt, between individual photoelectron detections on DOM 21-01 up to a time difference of 40 ms.

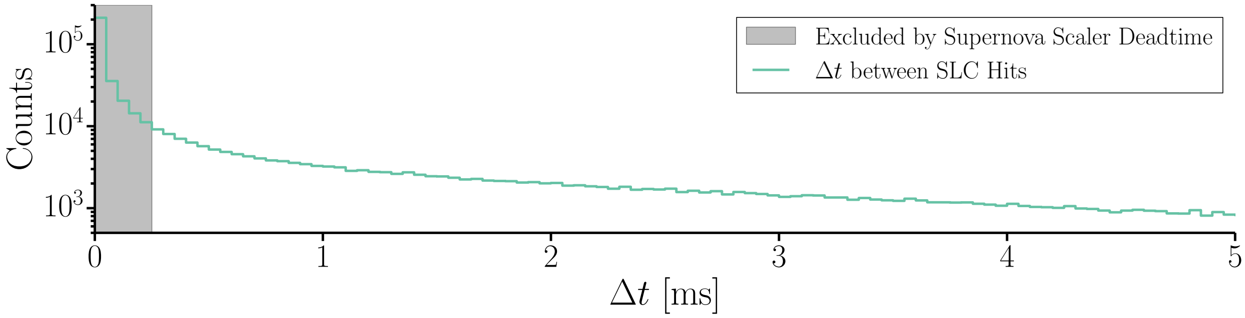

(b) Distribution of time difference, Δt, between individual photoelectron detections on DOM 21-01 up to a time difference of 5 ms.

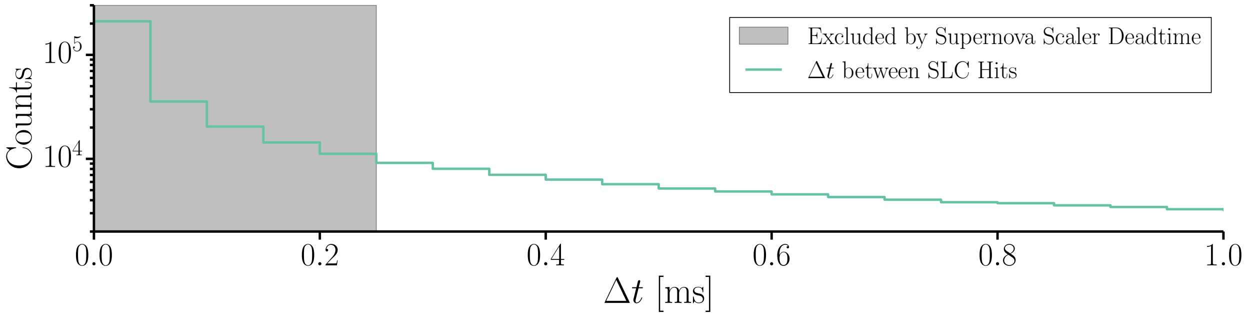

(c) Distribution of time difference, Δt, between individual photoelectron detections on DOM 21-01 up to a time difference of 1 ms.

Figure 4.4: Distribution of time difference, Δt, between individual photoelectron detections on DOM 21-01. For a purely Poissonian noise behavior, the Δt distribution would follow an exponential, which would be a straight line, where the slope represents the rate, in this representation. The grey area indicates the DOM triggers that are excluded from the supernova analysis due to artificial deadtime applied to the supernova scalers; see Section 4.7.2. The supernova scaler deadtime excludes most of the DOM triggers that are caused by the non-Poissonian behavior of the DOM noise.

The effect of correlated noise can be seen in two ways: the distribution of the time difference, Δt, between noise triggers (predominantly single photoelectrons) on a DOM and temperature dependence of the noise rate. The Δt distribution in Figure 4.4 shows that the data does not follow a purely Poisson process. The time difference between individual events does not follow a exponential fall off for $\Delta t \lessapprox 0.6\,\mathrm{ms}$. For $\Delta t \gtrapprox 0.6\,\mathrm{ms}$, the Poissonian noise dominates. To reduce the effect of the correlated noise in the supernova analysis, a deadtime removes a significant portion of the correlated noise triggers; indicated by the grey area in Figure 4.4.

The electronics and thermionic noise rate are a function of temperature. In this case, as the temperature decreases the noise rate decreases. This is relationship is not observed in IceCube as the noise rate increased with decreasing temperature; see Figure 4.5 and [242]. A similar temperature trend in other PMTs has been observed in [254, 255].

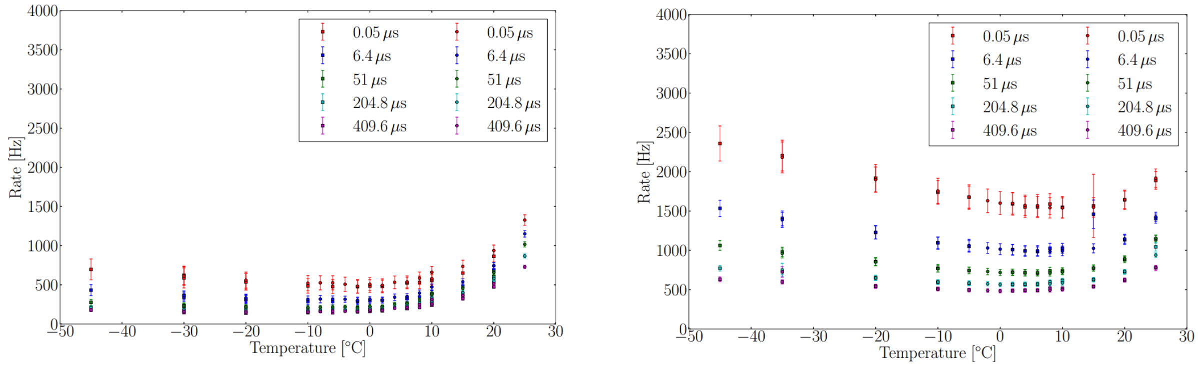

(a) Noise rate measurements of a bare IceCube PMT at different temperatures and deadtime settings.

(b) Noise rate measurements of a IceCube DOMs at different temperatures and deadtime settings.

Figure 4.5: Noise rate measurements of a bare IceCube PMT (left) and DOM (right) at various temperatures and deadtime settings. The addition of the pressure sphere glass causes an increase in the overall noise rate. The relative increase in the non-Poissian noise is larger than that of the Poissonian noise. This can be seen by the much larger relative change in the noise rate for temperatures $\leq -10\,^{\circ}\mathrm{C}$.

The correlated noise is believed to be caused by scintillation effects in the PMT and pressure sphere glass following a radioactive decay in either. There are several studies that support this hypothesis. The radioactive decay-induced scintillation is expected to cause a burst-like behavior, *i.e.* an initial Poisson-distributed noise event followed by one or more subsequent events on a short timescale. This effect was seen in IceCube and [254]; see Figure 4.6. Similarly, the rate should increase as a function of the amount of glass surrounding the PMT. This has been observed in the laboratory; see Figure 4.5. The pressure sphere

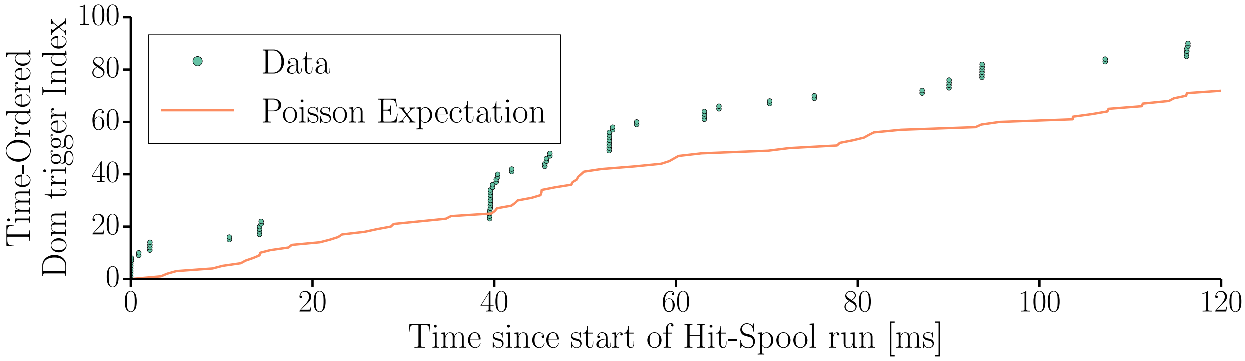

Figure 4.6: DOM trigger times versus DOM trigger index for DOM 21-01 for the first 120 ms of data. The data shows a burst behavior, especially around 40 ms, while the Poisson expectation with the same rate (535.98 Hz) follows a more linear behavior.

emits light when exposed to a radioactive source. This has been observed for the pressure housings of the predecessor to IceCube, the Antarctic Muon And Neutrino Detector Array (AMANDA), in [256]. The PMT manufacturer Hamamatsu notes in [257, 258] that scintillation in the glass can occur. It has been shown in [259, 260] that light yield from scintillation in a different scintillation material, NaI(Tl), increases with lower temperature. This supports the trend towards higher dark noise rate at lower temperatures. The glass could also have higher scintillation efficiency at lower temperatures. Alternative reasons for the correlated noise can be found in [254, 255, 261].

4.4.2 Atmospheric Muons

Atmospheric muons constitute a major background source for any IceCube analysis as they can easily the mimic the signal; compare Figure 4.7 with Figure 4.2a. The supernova analysis is also affected because of the relatively large integration periods used in the analysis compared to the crossing time of individual muons, *i.e.* 2 ms versus ∼6 µs, and assumptions made in the analysis; see Section 4.9. For a more detailed overview of the effect of atmospheric muons see Section 6.1. In order to understand their effect on the supernova signal, one needs to understand the origin and their characteristics once they reach the detector.

4.4.2.1 Origin of Atmospheric Muons

High energy atmospheric muons are created from decay of charged mesons (primarily $\pi^{\pm}$ and $K^{\pm}$) generated in interaction of cosmic rays with air molecules in the upper atmosphere; see Figure 4.8. These charged mesons decay to (anti-)muons and muon (anti-)neutrinos:

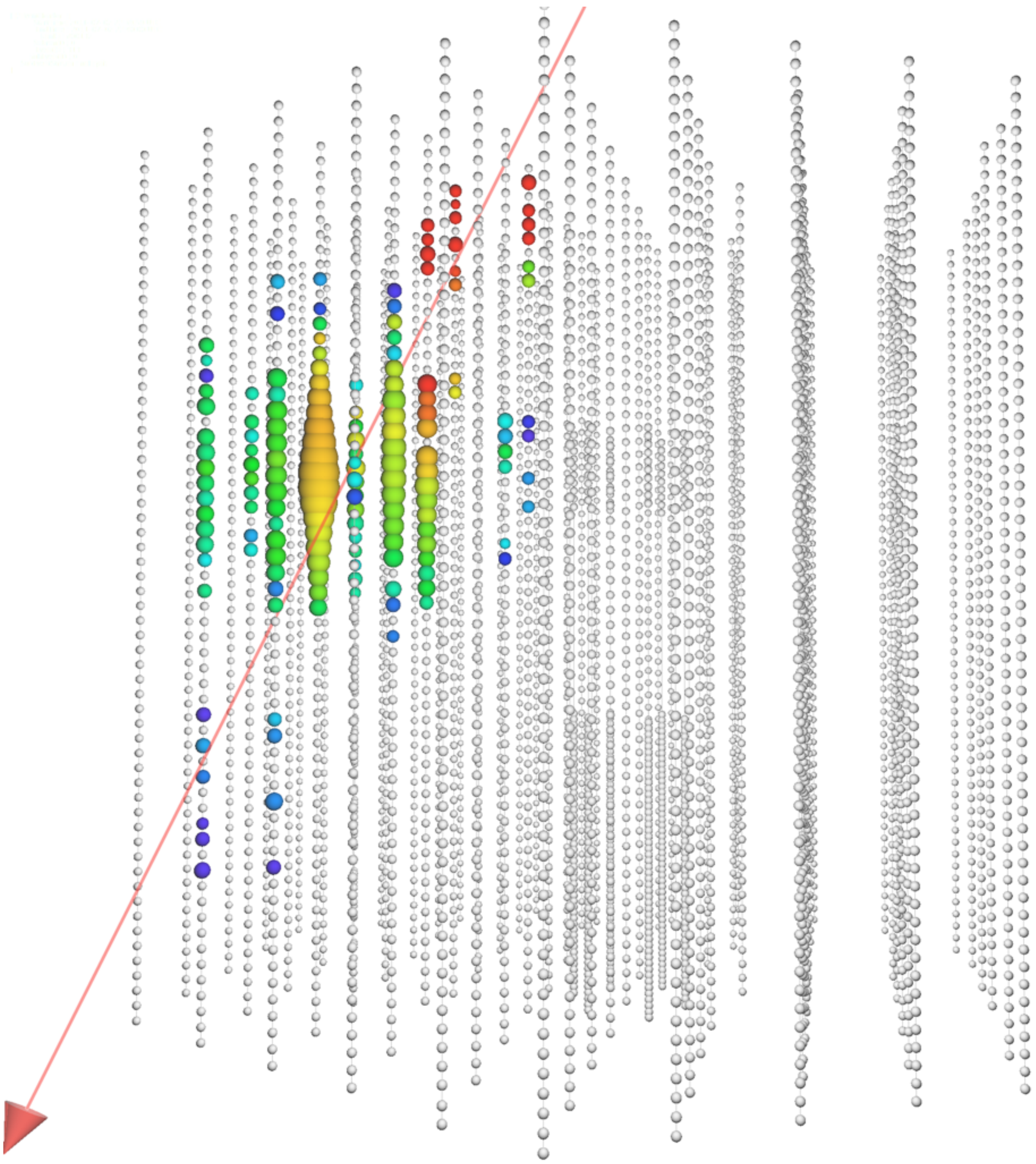

Figure 4.7: Example of a penetrating atmospheric muon event in IceCube. The rainbow color scheme represent the time dimension where red is early and blue/purple is late. The size of the spheres are the amount of charge that was deposited on a given DOM. The red line indicates the direction of the event. This event shows that stochastic nature of the muon energy deposition and possible misidentification as a cascade event; see Figure 4.2b. NOTE: This event has had noise and possible coincident events removed.

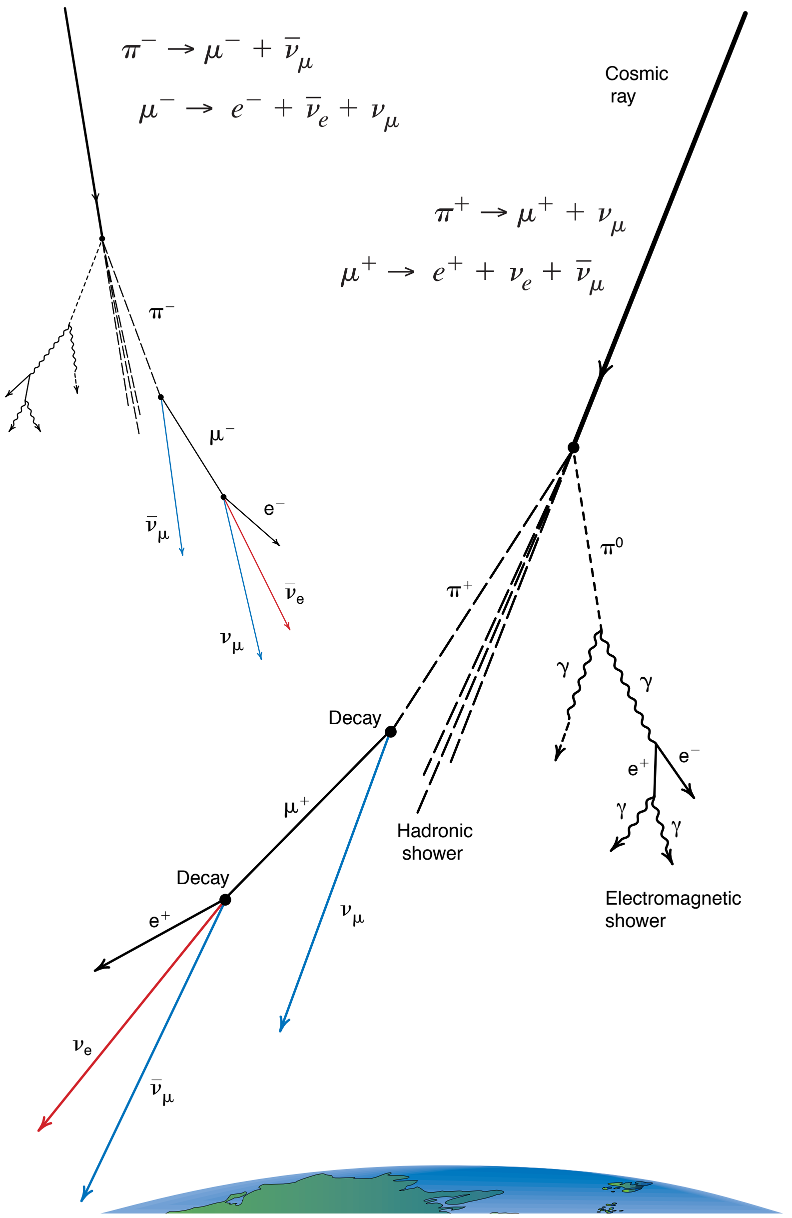

Figure 4.8: Schematic diagram of a cosmic ray air shower. The incoming cosmic rays interacts with a molecule in the atmosphere and produce pions. These pions (π) decay into μs, γs, and νs. These products can subsequently decay into other particles to create a large number of particles [12, 33, 34]. Credit: [35]

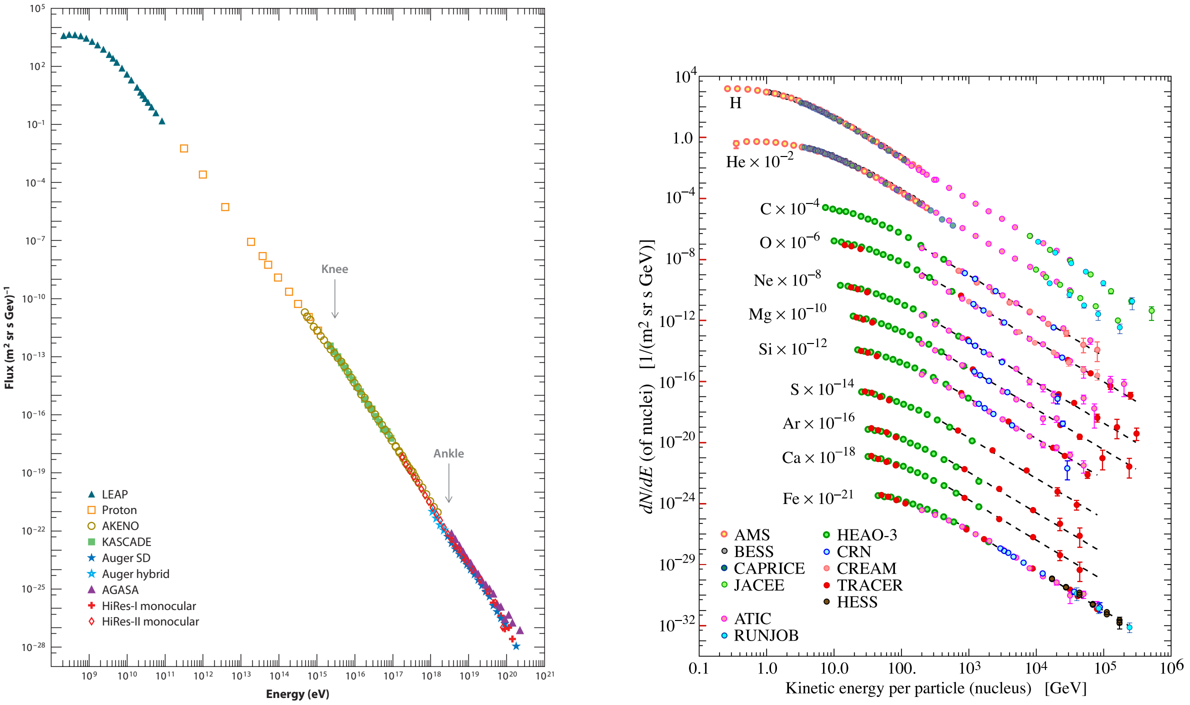

(a) Energy spectrum of cosmic rays. Credit: [34]

(b) Composition of cosmic rays. Cosmic rays are predominantly hydrogen, but particle interactions up to iron have been measured. Credit: [12] and references therein

Figure 4.9: Energy spectrum (left) and composition of cosmic ray primaries as measured near Earth (right). Credit: Left: [34]; Right: [12] and references therein

$$\pi^+ \rightarrow \mu^+ + \nu_\mu \qquad\qquad K^+ \rightarrow \mu^+ + \nu_\mu$$

$$\pi^- \rightarrow \mu^- + \bar{\nu}_\mu \qquad\qquad K^- \rightarrow \mu^- + \bar{\nu}_\mu$$

For an overview of cosmic ray air shower physics see [12, 33, 34]. The predominant interaction is that of high energy cosmic ray protons, which produce a hadronic shower in the atmosphere; see Figure 4.9.

The muons from the charged meson decay are highly relativistic, which means that their lifetime will be extended considerably due to relativistic time dilation given by the Lorentz factor, γ. This means that a muon with $\gamma = 15.2$ can on average travel 10 km through the atmosphere. In addition to the muonic component, an electromagnetic component is generated in the interaction of the cosmic ray and the atmosphere. This component is absorbed at the surface and can only be detected by IceTop for high energy cosmic ray interactions at a certain zenith angle.

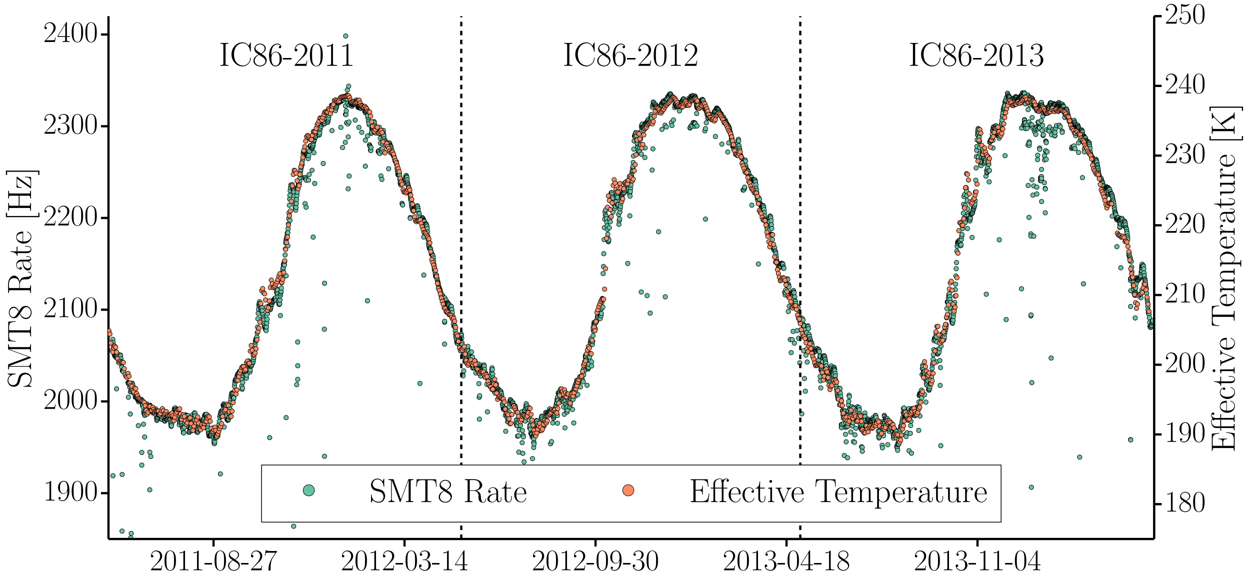

Figure 4.10: Overlay of effective atmospheric temperature as measured by satellite and integrated over atmospheric temperature profile and the SMT8 trigger rate, as a proxy for the atmospheric muon rate. The correlation between the two quantities is clearly visible. The periodic behavior of both the rate and the temperature is due to seasonal changes of the weather and therefore the atmospheric properties above the South Pole.

The overall rate of atmospheric muons, varies seasonally, as the temperature of the upper atmosphere changes throughout the seasons; see Figure 4.10. With decreasing temperature the average density of the atmosphere increases which decreases the mean free path for pions and kaons. This means that the pions or kaons have a higher probability to interact with air molecules and therefore will not decay as frequently hence decreasing the rate of muon production. The opposite is true for the case of increasing temperature.

The relationship between the muon rate, R_μ, and the effective temperature of the atmosphere, T_{eff} is given by:

$$\frac{\Delta R_\mu}{\langle R_\mu \rangle} = \alpha_T \frac{\Delta T_{\text{eff}}}{\langle T_{\text{eff}} \rangle} \tag{4.3}$$

where $\langle R_\mu \rangle$ and $\langle T_{\text{eff}} \rangle$ are the respective averages for the given time frame of the two quantities, ΔR_μ and ΔT_{eff} are the deviation from the mean value, and α_T is the *effective temperature coefficient* [262]. An effective temperature has to be defined because the atmospheric temperature varies significantly with height; see Figure 4.11. The seasonal variation in temperature can also be traced out in the atmospheric muon rate; see Figure 4.10 and Figure 4.11.

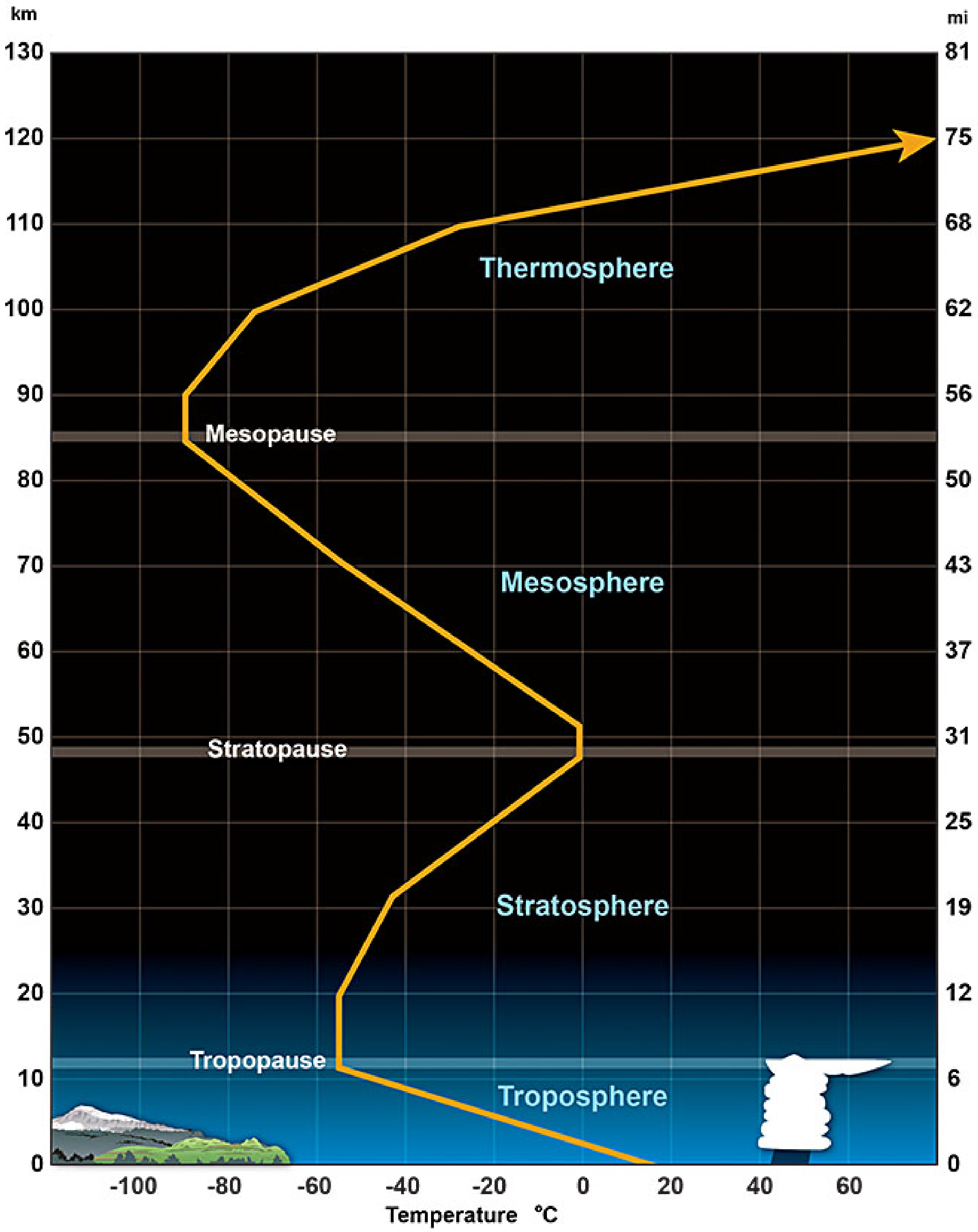

Figure 4.11: Atmospheric temperature profile. Cosmic ray interactions typically occur at $\mathcal{O}(10\,\mathrm{km})$ height [33, 36, 37]. This means that the air shower that produces the muons observed with IceCube has to traverse a large temperature and density gradient as it reaches the surface. An effective atmospheric temperature has to be used. The measurement of which could have large systematic errors. Credit: [38]

4.4.2.2 Atmospheric Muons in IceCube

Atmospheric muons are able to mimic the supernova signal in several different ways. The largest contributors are assumptions made in the supernova analysis, the high atmospheric muon trigger rate (≈2.0 − 2.4 kHz for atmospheric muons ¿1 TeV depending the season; see Figure 4.10), and the disconnect between the supernova data stream and the primary data stream; see Section 4.9 and 6.1 for more details. The supernova analysis operates on timescales of $\mathcal{O}(1\,\mathrm{s})$; see Section 4.9. This means that a large number of cosmic ray air showers are sampled and there is a significant variations in the number of muons produced in each air shower. This means that during some time periods, more energy is deposited in the detector and a false positive supernova alert may occur.

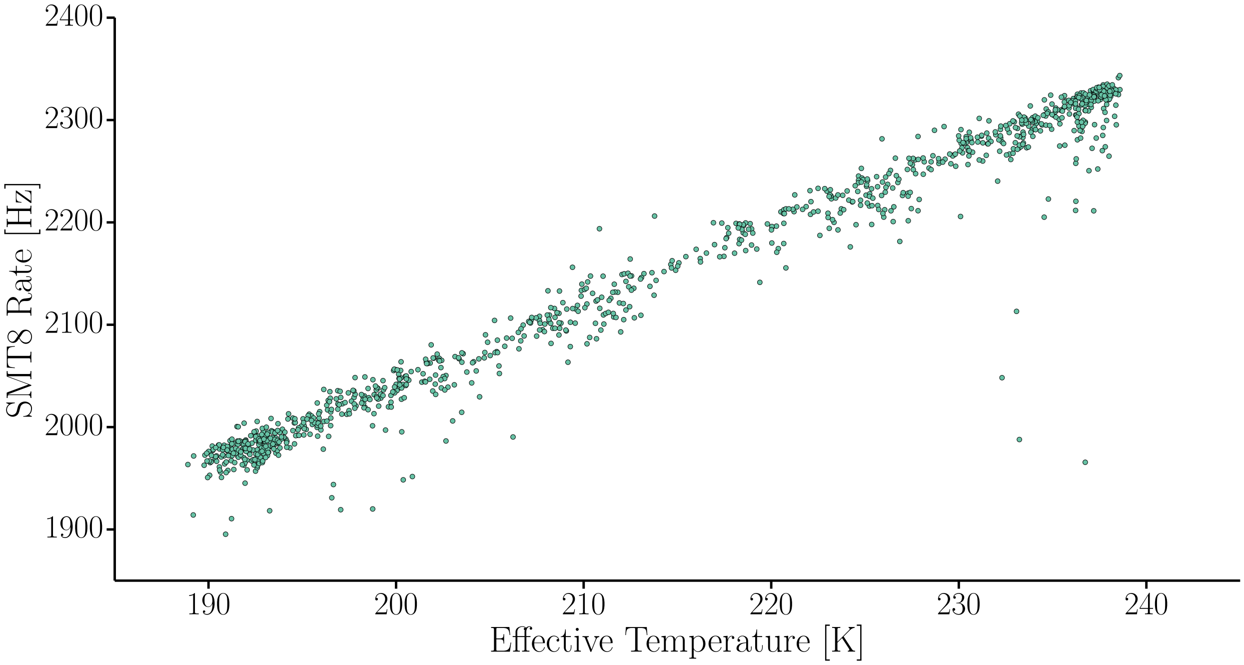

Figure 4.12: Correlation of atmospheric temperature and atmospheric muon rate as measured by IceCube over the course of the first three years of the completed detector. The correlation has a Pearson's r [39] of ∼0.98. The points are centered around low temperature/rate and high temperature/rate due to the sinusoidal-like trend in both quantities leading to more dwell time in those periods.

Simulation has shown that 5.1–5.4 kHz [263] (the number varies with assumed optical properties of the ice, hadronic interaction model [264–267], *etc.*) of atmospheric muons or muon bundles will have at least one DOM trigger; see Section 4.6. This means that during the 2 ms integration window an average of ∼9 atmospheric muons or muon bundles will pass through the detector. Every DOM is its own detector for the supernova analysis this will cause $\mathcal{O}(100)$ DOMs to trigger in this time frame; see Section 4.9 and Figure 6.4. Given that the online analysis uses even longer time windows of up 10 s this will produce a very high background floor for the analysis; see Section 4.9 and 6.1 for more details.

4.4.3 Triboluminescence

Triboluminescence is light emission caused by the application of mechanical stress [268]. As the ice re-solidifies, the so-called “freeze-in” process, an orders of magnitude higher noise rate was detect for the first ∼2.5 weeks after deployment; see [269] for details. The freeze-in process continues for several weeks to months after ice has been formed around the DOM, as the ice in the drill hole begins to become clearer. The impurities, mainly trapped gas, that were introduced into the water from the drill process are being pushed inward into a column at roughly the center of the drill hole. This most likely occurs due to the large pressure that the ice is subject to [270]. This process requires the breaking of bonds in the ice, which in turn can cause triboluminescence. For a majority of IceCube analyses, this effect is subdominant as they rely on much higher energy events where noise can easily be removed by requiring coincidence among DOMs; see Section 4.7.1. For the supernova analysis, this effect may cause a change of sensitivity for the first couple years for the newly deployed strings; see Section 6.1.

4.5 Detection Principle

Neutrinos, unlike photons used in traditional astronomy, cannot be detected directly, but rather through their interaction with matter. The main interaction types across all energy can be generalized as follows:

$$\begin{aligned} \nu_l + p/n &\rightarrow p/n + \nu_l \quad \text{(NC)} & \bar{\nu}_l + p &\rightarrow n + l^+ \quad \text{(CC)} \\ \bar{\nu}_l + p/n &\rightarrow p/n + \bar{\nu}_l \quad \text{(NC)} & \nu_l + e^- &\rightarrow e^- + \nu_l \quad \text{(CC, NC)} \\ \nu_l + n &\rightarrow p + l^- \quad \text{(CC)} & \bar{\nu}_l + e^- &\rightarrow e^- + \bar{\nu}_l \quad \text{(CC, NC)} \end{aligned}$$

where l is the lepton flavor, ± denotes the positive and negative charge respectively, p are protons, and n are neutrons. The exact nature of neutrino interactions in the glacial ice depends greatly on the neutrino energy [12, 49, 271]. The resulting charged leptons and hadronic showers will travel at relativistic speeds through the medium and emit Cherenkov photons that are detected by photomultiplier tubes (PMT) inside the DOMs that are deployed inside the glacial ice; see Section 4.5.3.

4.5.1 Supernova Neutrino Interactions in Ice

The nature and cross-section of neutrino interactions in ice depends greatly on the neutrino energy [12, 49, 271]. For the case of supernova neutrinos, the overall calculation is simplified because supernova neutrinos are of $\mathcal{O}(10\,\mathrm{MeV})$. The interactions can only produce electrons (e^-) and positrons (e^+) because the energy threshold, *i.e.* their mass, to produce muons ($m_\mu = 105.65\,\mathrm{MeV}$) and taus ($m_\tau = 1776.82\,\mathrm{MeV}$) are not surpassed [12, 112]. The three main interactions for $\mathcal{O}(10\,\mathrm{MeV})$ neutrinos in ice are inverse β-decay, ν–e^- scattering, and ν–O interactions. Inverse β-decay dominates for supernova neutrino interactions in IceCube contributing 91-93% of the signal. The remaining signal arises from the ν–e^- scattering (3-3.5%) and ν–O interactions (3.5-6%) [112]. The range in contributions of each interaction type is dependent on the neutrino oscillation scenario.

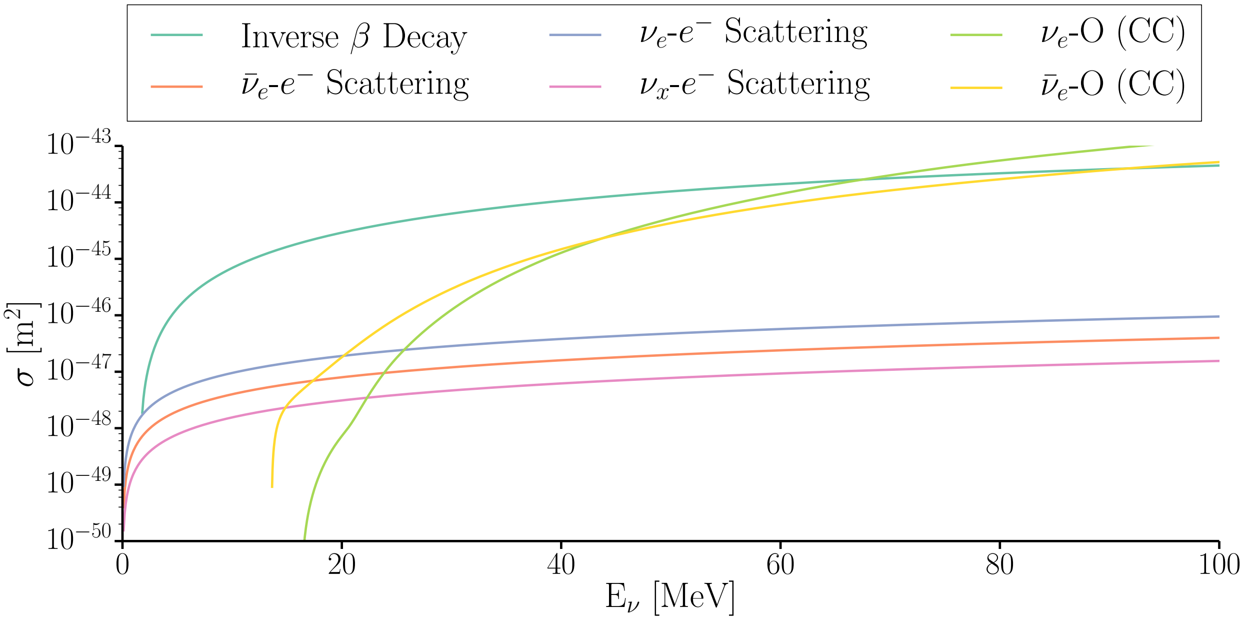

Figure 4.13: Comparison of cross-sections for interactions relevant to the detection of supernova neutrinos in IceCube. Inverse β-decay is the dominant interaction channel as it has the highest cross-section for neutrinos with 10-30 MeV, where the largest fraction of supernova neutrinos will be; see Figure 3.7b, 3.9b, and, 3.8b. The electron scattering interactions are relevant to detect neutrino trapping and the deleptonization peak; see Section 3.4. Oxygen interaction are important in case the energy spectrum shifts to higher energies due to oscillation or the production of higher energy neutrinos by the supernova.

4.5.1.1 Inverse β-decay

Inverse β-decay is the interaction of electron anti-neutrinos ($\bar{\nu}_e$) and the protons (p) of the hydrogen atoms in H_2O to produce a positron (e^+) and neutron (n):

$$\bar{\nu}_e + p \to e^+ + n \quad \text{(CC)}$$

The large contribution of ∼91% to the overall supernova signal arises from the low threshold ($m_e + m_n - m_p = 1.806\,\text{MeV}$) and the cross-section rises quickly at low energies; see Figure 4.13. The cross-section used in IceCube and whose derivation is summarized below is based on [272].

The differential cross-sections at the lowest order (or *Tree-Level*) in terms of the Mandelstam variable– Lorentz-invariant numerical quantities of four momenta in a scattering process–

$$\begin{aligned} t &= (p_{\bar{\nu}_e} - p_{e^+})^2 = (p_p - p_n)^2 \\ s &= (p_{\bar{\nu}_e} + p_p)^2 = (p_{e^+} + p_n)^2 \\ u &= (p_{\bar{\nu}_e} - p_n)^2 = (p_p - p_{e^+})^2 \end{aligned}$$

is given by:

$$\frac{d\sigma}{dt}(E_\nu, E_e) = \frac{G_F^2 \cos^2\theta_C}{2\pi} \frac{1}{(s - m_p^2)^2} |\mathfrak{M}|^2 \tag{4.4}$$

where G_F is the Fermi constant, cos θ_C (= 0.89) is the cosine of the Cabbibo angle (the relative probability that a down and strange quark will change into an up quark), and m_p (= $0.938\,\text{GeV}$) is the mass of the proton [12]. The scattering matrix, $\mathfrak{M}$, is given by:

$$\mathfrak{M} = \bar{v}_e \gamma^a (1 - \gamma_5) v_e \cdot \bar{u}_n \left(f_1 \gamma_a + g_1 \gamma_a \gamma_5 + \frac{i f_2}{2M} \sigma_{ab} q^b + \frac{g_2}{M} q_a \gamma_5 \right) \tag{4.5}$$

where $q = p_\nu - p_e = p_n - p_p$ and $M = \frac{(m_n + m_p)}{2} \approx 938.9\,\text{MeV}$. For neutrinos of $\mathcal{O}(10\,\text{MeV})$, $|\mathfrak{M}|^2$ only has to be calculated up to third order in E_ν/m_p to an error <1%. $|\mathfrak{M}|^2$ is therefore:

$$\begin{aligned} |\mathfrak{M}|^2 \simeq\ & M^2(f_1^2 - g_1^2)(t - m_e^2) - \\ & M^2 \Delta_{np}^2 (f_1^2 + g_1^2) - \\ & 2 m_e^2 M \Delta_{np} g_1 (f_1 + f_2) - \\ & (s - u) t g_1 (f_1 + f_2) + \\ & (s - u)^2 (f_1^2 + g_1^2)/4 \end{aligned} \tag{4.6}$$

where $f_1 \simeq 1.778$, $f_2 \simeq 6.588$, $g_1 \simeq -1.270$, and $\Delta_{np} = m_n - m_p \approx 1.293\,\text{MeV}$.

To determine the total number of events in the detector and the number of events as a function of lepton energy, E_e, one will need both the total, $\sigma(E_\nu)$, and differential cross-section, $\frac{d\sigma}{dE_e}(E_\nu, E_e)$, respectively. Using the proton rest frame, one can determine the Mandelstam variables s, t, and u:

$$s - m_p^2 = 2m_p E_\nu$$
$$s - u = 2m_p(E_\nu + E_e) - m_e^2$$
$$t = m_n^2 - m_p^2 - 2m_p(E_\nu - E_e)$$

From this, one can determine $\frac{d\sigma}{dE_e}(E_\nu, E_e)$ by finding $\frac{dt}{dE_e}$ and multiplying with Equation 4.4, such that:

$$\frac{d\sigma}{dE_e}(E_\nu, E_e) = 2m_p \frac{d\sigma}{dt}(E_\nu, E_e) \tag{4.7}$$

The total cross-section is given by:

$$\sigma(E_\nu) = \int_{E_{\min}}^{E_{\max}} dE_e \frac{d\sigma}{dE_e}(E_\nu, E_e) \tag{4.8}$$

E_e is still unknown at this point for a given E_ν. E_e can be given in terms of E_ν and the cosine of the scattering angle, $\cos\theta$:

$$E_e = \frac{(E_\nu - \delta)(1+\epsilon) + \epsilon \cdot \cos\theta \sqrt{(E_\nu - \delta)^2 - m_e^2 \kappa}}{\kappa} \tag{4.9}$$

where $\epsilon = \frac{E_\nu}{m_p}$, $\kappa = (1+\epsilon)^2 - (\epsilon \cdot \cos\theta)^2$ and $\delta = \frac{m_n^2 - m_p^2 - m_e^2}{2m_p}$. The precise angular distribution of $\cos\theta$ is not relevant in IceCube and can be approximated by a flat distribution in $\cos\theta$, as the light deposition is only within a minuscule volume compared to the overall detector volume, which makes tracing individual events impossible. For a more detailed study of the distribution of $\cos\theta$; see [272, 273]

Besides the Cherenkov light from the positrons, the neutron will capture on the hydrogen atom, which produces a gamma-ray [114, 274, 275]:

$$n + {}^1\text{H} \rightarrow {}^2\text{H} + \gamma$$

The emitted γ-ray has an energy of 2.225 MeV (binding energy of the deuterium nucleus). The γ-ray will Compton scatter on electrons in ice and produce relativistic electrons with an energy distribution of [14, 276]

$$\begin{aligned} p(E_{e^-}) \sim\ & (E_\gamma - E_{e^-})^{-2} E_\gamma^{-2} - \\ & \left(2 + 2\frac{E_\gamma}{m_e} - \left(\frac{E_\gamma}{m_e}\right)^2\right)(E_\gamma - E_{e^-})^{-1} E_\gamma^{-3} + \\ & \left(1 + \frac{E_\gamma}{m_e}\right) E_\gamma^{-4} - m_e^{-2} E_\gamma^{-3} E_{e^-} \end{aligned} \tag{4.10}$$

These electrons are energetic enough to pass the Cherenkov threshold (0.753 MeV) and produce Cherenkov photons as well.

4.5.1.2 Neutrino-Electron Scattering

A 3 to 3.5% contribution to the overall signal, depending on the oscillation scenario, arises from the scattering of neutrinos of all flavors on the orbital electrons of the ice.

$$\begin{aligned} &\nu_e + e^- \rightarrow \nu_e + e^- \quad (\mathrm{CC}, \mathrm{NC}) \qquad && \nu_{\mu,\tau} + e^- \rightarrow \nu_{\mu,\tau} + e^- \quad (\mathrm{NC}) \\ &\bar{\nu}_e + e^- \rightarrow \bar{\nu}_e + e^- \quad (\mathrm{CC}, \mathrm{NC}) \qquad && \bar{\nu}_{\mu,\tau} + e^- \rightarrow \bar{\nu}_{\mu,\tau} + e^- \quad (\mathrm{NC}) \end{aligned}$$

Electron (anti-)neutrinos experience both CC and NC interactions, while muon and tau (anti-)neutrinos only experience NC interactions. The muon and tau neutrinos can only experience NC interactions because the respective leptons cannot be produced at $\mathcal{O}(10\,\mathrm{MeV})$. The cross-section used in IceCube and summarized below are taken from [277].

The cross-section for neutrino-electron scattering can only be quantified when considering small momentum transfer ($|q| \ll m^2_{W^\pm, Z^0}$). The total cross-section at lowest order is given by:

$$\sigma(E_\nu) = \frac{2G_F^2 m_e E_\nu}{\pi} \left[\epsilon_\mp^2 + \frac{1}{3}\epsilon_\pm^2 - \frac{1}{2}\epsilon_+\epsilon_- \frac{m_e}{E_\nu} \right] \tag{4.11}$$

and the differential cross-section is given by:

$$\frac{d\sigma}{dy}(E_\nu, E_e) = \frac{2G_F^2 m_e E_\nu}{\pi} \left[\epsilon_\mp^2 + \epsilon_\pm^2 (1-y)^2 - \epsilon_+\epsilon_- \frac{m_e}{E_\nu} y \right] \tag{4.12}$$

Neutrino	ϵ_+	ϵ_-
ν_e, $\bar{\nu}_e$	$-\sin^2\theta_W$	$-\frac{1}{2} - \sin^2\theta_W$
$\nu_{\mu,\tau}$, $\bar{\nu}_{\mu,\tau}$	$-\sin^2\theta_W$	$\frac{1}{2} - \sin^2\theta_W$

Table 4.1: Values for the ϵ_+ and ϵ_- for all possible neutrino-electron scattering interactions in Equation 4.11 and 4.12.

where $\epsilon_\pm$ is a flavor-dependent quantity given in Table 4.1, and $y = (E_e - m_e)/E_\nu$ is the amount of impulse transferred to the electron and has a range from 0 to $1/(1 + m_e/2E_\nu)$. Neither cross-section formulas require radiation or neutrino dipole correction, as the energy is too low for these corrections to have an effect >1%.

Inverse β-decay does have a significantly larger overall effect. The possibility to trace the electron neutrino signal and detect neutrino trapping and the deleptonization peak are important aspects to understanding the core-collapse supernova process; see Section 3.3.3 and 3.3.4.

4.5.1.3 Neutrino-Oxygen Interactions

The contribution of 3.5 to 6% from the neutrino-oxygen cross-sections arises because the interactions relatively high energy threshold; see Figure 4.13 [3, 4, 112, 278–280]. If the neutrinos had higher average energy ($\gtrapprox 60\,\mathrm{MeV}$), the oxygen cross-sections would be the predominant interaction. The cross-sections for certain oxygen isotopes are higher than those for ^{16}O. Their small relative abundance (0.038% for ^{17}O, 0.2% for ^{18}O [278]) reduces their importance significantly. The interactions themselves are mathematically complex as they involve the shell structure of the nucleus. The main detectable interactions in IceCube are solely charged-current interactions:

$$\begin{gathered}
\nu_e + {}^{16}\mathrm{O} \to {}^{15}\mathrm{O} + e^- + p \quad \text{(CC)} \\
\bar{\nu}_e + {}^{16}\mathrm{O} \to {}^{15}\mathrm{N} + e^+ + n \quad \text{(CC)} \\
\nu_e + {}^{16}\mathrm{O} \to {}^{14}\mathrm{N}^\star + e^- + 2p \quad \text{(CC)} \\
\nu_e + {}^{16}\mathrm{O} \to {}^{15}\mathrm{O}^\star + e^- + p + \gamma \quad \text{(CC)}
\end{gathered}$$

$$\begin{gathered}
\bar{\nu}_e + {}^{16}\mathrm{O} \to {}^{16}\mathrm{N} + e^+ \quad \text{(CC)} \\
\bar{\nu}_e + {}^{16}\mathrm{O} \to {}^{15}\mathrm{N}^\star + e^+ + n + \gamma \quad \text{(CC)} \\
\nu_e + {}^{18}\mathrm{O} \to {}^{18}\mathrm{F} + e^- \quad \text{(CC)}
\end{gathered}$$

Neutrino Interactions	A	B	C	D
ν_e CC [3]	$4.7 \times 10^{-44}\,\mathrm{m}^2$	0.25	15	6
$\bar{\nu}_e$ CC [4]	$3.1 \times 10^{-44}\,\mathrm{m}^2$	0.223	8.0	5.9
ν NC [4]	$6.7 \times 10^{-44}\,\mathrm{m}^2$	0.203	8.0	6

Table 4.2: Values for A, B, C, and D for Equation 4.13 as given by [3, 4].

The energy threshold for ν_e interactions is 13 MeV and 18 MeV for $\bar{\nu}_e$. There are also neutral-current interactions that only produce photons and protons. These particles cannot be easily detected in IceCube, as the protons are below the Cherenkov threshold and the photons have to be captured.

$$\nu + {}^{16}\mathrm{O} \to {}^{15}\mathrm{O} + \nu' + p \quad \text{(NC)} \quad \nu + {}^{16}\mathrm{O} \to {}^{15}\mathrm{N}^\star + \nu' + p + \gamma \quad \text{(NC)}$$

but are not detectable in IceCube because the energy threshold for Cherenkov radiation from protons is not met. This cross-section can be fit using

$$\sigma(E_\nu) = A \cdot \left[\left(\frac{E_\nu}{\mathrm{MeV}} \right)^B - C^{1/4} \right]^D \tag{4.13}$$

as prescribed by [3]. The parameters for the interactions above are given in Table 4.2. Similarly, the cross-section for ^{17}O and ^{18}O can be parametrized [4]; see Equation 4.14.

$$\sigma(E_\nu) = \left(0.17\left(\frac{E}{\mathrm{MeV}}\right)^2 + 1.6\left(\frac{E}{\mathrm{MeV}}\right) - 0.92\right) \times 10^{-49}\,\mathrm{m}^2 \tag{4.14}$$

4.5.2 Neutrino Interaction Products in Ice

The predominant energy loss mechanism of $\mathcal{O}(10\,\mathrm{MeV})$ leptons traveling through the ice is ionization. The leptons ($e^{\pm}$) produced in neutrino interactions elastically collide with electrons of the water molecules. With increasing E_e, the bremsstrahlung on the Coulomb field of the molecules grows proportionally with energy and becomes an increasing contributor to the energy loss. The total energy loss can be described using the equation [12]:

$$-\frac{dE_{\pm}}{dx} = \kappa_1 \frac{n_e}{\beta^2} \ln\left(\frac{\kappa_2\beta^2}{(1-\beta 2)I} - \beta^2 - \delta\right) + \kappa_3 E_e \tag{4.15}$$

where

$$\kappa_1 \frac{n_e}{\beta^2} \ln\left(\frac{\kappa_2\beta^2}{(1-\beta 2)I} - \beta^2 - \delta\right) \tag{4.16}$$

is the Bethe-Bloch formula, where n_e is the electron density, I is the mean excitation potential of the medium, $\beta = v/c$, δ is a correction factor to account for the electromagnetic shielding of the matter, $\kappa_3 E_e$ is the energy loss due to bremsstrahlung, and κ_i are matter-independent constants [12].

The low energies of the produced $e^{\pm}$ traveling through the ice restricts the photon production to the Cherenkov effect and the production of e^+e^--pairs from virtual photons; see Section 4.5.3 for details. Using the GEANT4 simulation toolkit described in [281, 282], the average track length for $e^{\pm}$ with $E_e < 100\,\mathrm{MeV}$ is a linear relationship with energy and given by [4, 112]:

$$\bar{x}(E_e) = (0.579 \pm 0.017)\,\mathrm{cm} \cdot \frac{E_e}{\mathrm{MeV}} \tag{4.17}$$

The major contributor to the overall error of Equation 4.17 is the manner in which e^+ and e^- interact with the ice.

4.5.3 Cherenkov Effect

The Cherenkov effect describes the production of electromagnetic radiation from relativistic charged particles travel through a dielectric medium, in this case ice [12, 283, 284]. The charged particle polarizes the medium it travels through. This induces a time-varying dipole field along the path of the particle. In case the charged particle travels through the dielectric medium with a velocity, v, greater than the speed of light in the medium, the dipole field interferes constructively and produces electromagnetic radiation. The speed

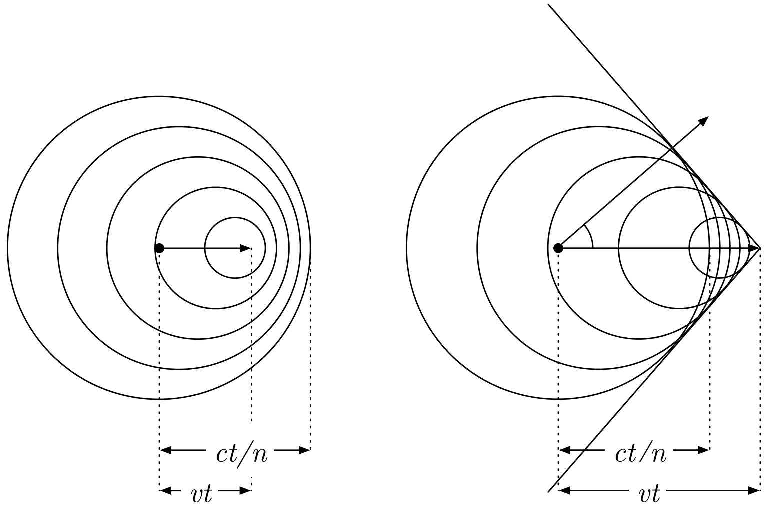

Figure 4.14: Graphical depiction of the Cherenkov effect using Huygen's construction. If a charged particle moves through a medium with $\beta < \mathrm{c}/\mathrm{n}_{\mathrm{Med}}$ the wavefronts from the dipole field are slightly shifted in the direction of travel but do not constructively interfere; see left illustration. If $\beta > \mathrm{c}/\mathrm{n}_{\mathrm{Med}}$, the dipole field wavefronts start to constructively interfere with each other producing electromagnetic emission; see right illustration. For ice, n $\simeq$ 1.32, the angle of emission will be $\approx$42°, as depicted here. Credit: Jakob van Santen [40]

of light in the medium is given by $\mathrm{c}/\mathrm{n}_{\mathrm{Med}}$, where c is the speed of light in vacuum and $\mathrm{n}_{\mathrm{Med}}$ is the refractive index of the medium.

Characteristic of Cherenkov radiation is the emission of light in a cone with an opening angle θ_{ch} [12]; see Figure 4.14 and Equation 4.18.

$$\cos\theta_{ch} = \frac{1}{\beta n} \tag{4.18}$$

This means that an electron with a minimum kinetic energy of 0.242 MeV while traveling through the ice ($n \approx 1.32$) will produce a light cone with an opening angle of $\theta_{ch} \approx 42°$. The total photon yield, N_γ, is dependent on the wavelength, λ, and lepton path length, x, as is given by the Frank-Tamm equation [12,285]:

$$\frac{dN}{dxd\lambda} = \frac{2\pi\alpha Z^2}{\lambda^2}\left(1 - \frac{1}{\beta^2 n^2(\lambda)}\right) \tag{4.19}$$

where α ($\approx\frac{1}{137}$) is the fine-structure constant, Z ($= 1$ for $e^{\pm}$) is the charge of the particle traveling through the medium in units of electron charge, e, and $n(\lambda)$ is the refractive index as function of wavelength. For a given wavelength range of 300 to 675 nm, an average value for the refractive index in ice ($\bar{\mathrm{n}}_{\mathrm{Ice}} = 1.32$), and using Equation 4.17, the average number of Cherenkov photons per MeV can be determined.

$$\bar{N}_\gamma = 2\pi\alpha\left(1 - \frac{1}{\beta^2 \bar{n}_{Ice}}\right)\bar{x}\int_{300\,\mathrm{nm}}^{675\,\mathrm{nm}}\frac{d\lambda}{\lambda^2} = 361.5\,\frac{\bar{x}}{\mathrm{cm}} = 209.3 \pm 6.1\,\frac{E_e}{\mathrm{MeV}} \tag{4.20}$$

The average number of Cherenkov photons is directly proportional to the energy of the product, as long as $0.753\,\mathrm{MeV} < E < 100\,\mathrm{MeV}$.

4.6 Optical Properties of the Ice

The ability to detect the faint photon signal from the interactions of supernova neutrinos in the ice directly depends on the optical properties of the ice; see Equation 4.1. For details on the optical properties of the ice see [41–43, 73]. The glacial ice at the South Pole is an extremely pure optical medium with an effective absorption length of $\mathcal{O}(100\,\mathrm{m})$ longer than any man-made optical medium [73]; see Figure 4.15. This enables IceCube to operate over multiple orders of magnitude in neutrino energy, to produce high quality data as well as energy and directional reconstruction, and to do so with a relatively sparsely populated detector compared to other neutrino detectors [286, 287].

Using a naturally-occurring detector medium for precision measurements brings challenges with it. Unlike a man-made material, where the optical properties of the material can be manufactured to specification and measured prior to detector construction, the properties and features of the glacial ice can only be extrapolated from ice core samples, measuring the dust concentration during construction [288], determined from *in situ* calibration [42], and verified using atmospheric muon data [289]. To be able to perform the *in situ* calibration, every DOM is deployed with a calibration device in form of a LED flasher board that consists of 12 LEDs in total, six pointed horizontally and six slightly upward. Flasher studies make it possible to derive a model of the glacial ice in terms of effective absorption and scattering length that can be used in simulation as well as reconstruction [42].

Calibration studies reveal that there is significant depth-dependent structure in both effective absorption and effective scattering length; see Figure 4.15. This is an effect due to the age of the ice. At the top of the detector where the ice is more recently formed, there has not been sufficient time and pressure to dissolve larger air bubbles in the ice, which increases the scattering length. The ice at the bottom of the detector has had sufficient time to dissolve these bubble into the ice [42]. Throughout the whole detector comparatively large dust particles are embedded into the ice from volcanic eruptions. The concentration is so sparse that they do not effect the optical properties significantly. In the $\approx 200\,\mathrm{m}$ below the center of the detector there is a so-called *dust layer*. It has a very high concentration of these dust particles. This is characterized by

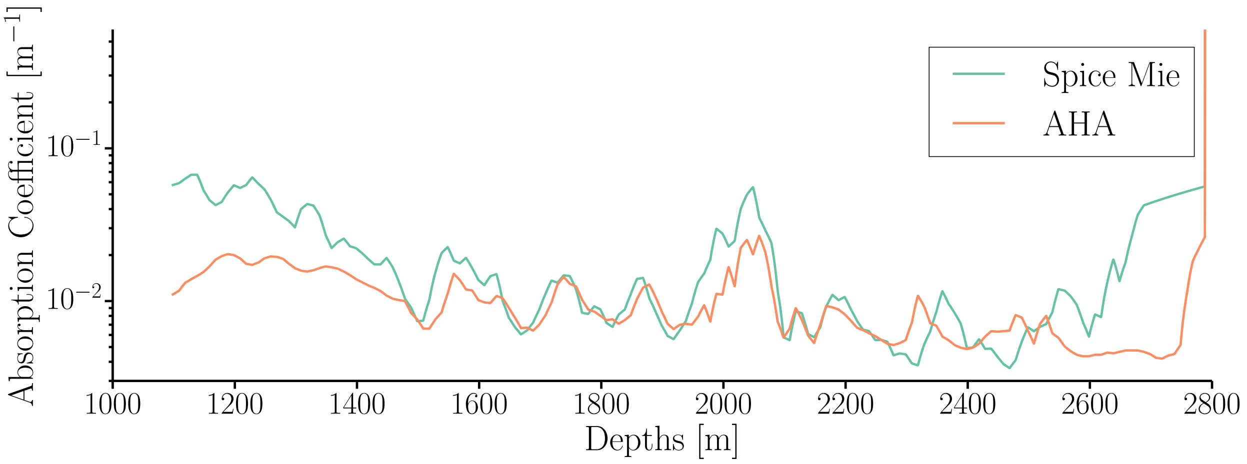

(a) Absorption coefficient as a function of depth for photons with $\lambda = 400\,\mathrm{nm}$ for the AHA and SpiceMie ice model. The effective absorption length is given by the inverse of the of the absorption coefficient, *i.e.* the lower the coefficient the clearer the ice.

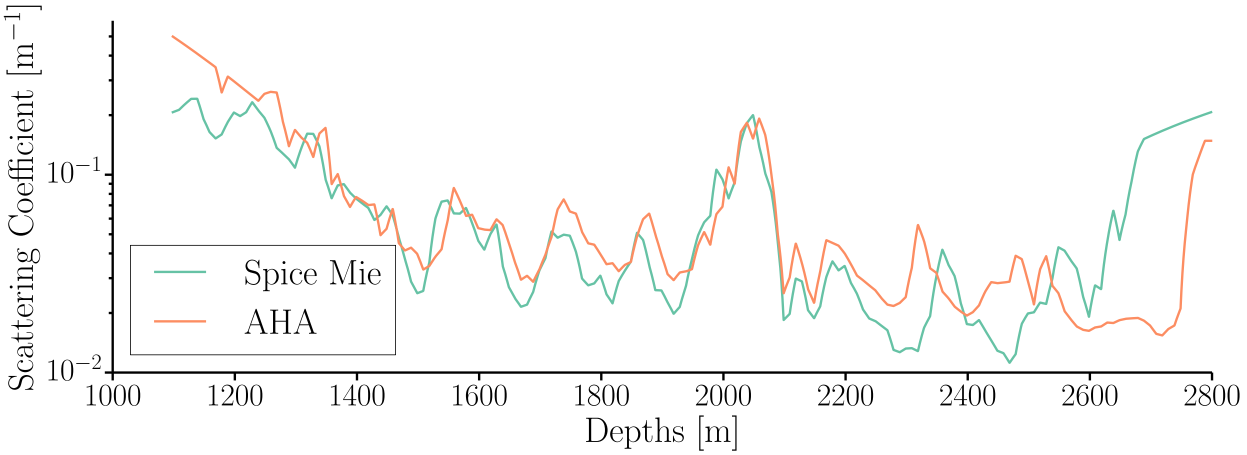

(b) Scattering coefficient as a function of depth for photons with $\lambda = 400\,\mathrm{nm}$ for the AHA and SpiceMie ice model. The effective scattering length is given by the inverse of the of the scattering coefficient, *i.e.* the lower the coefficient the longer photons will travel through the ice without scattering.

Figure 4.15: Absorption and scatting coefficient for two ice models: Additionally Heterogeneous Absorption (AHA) [41] and SpiceMie [42]; see text for more details.

increase in absorption and scattering coefficient in Figure 4.15 at a depth ≈2100 m. The layer is the result increased volcanic activity when those layers where precipitating [288, 290–292].

The ice models currently mostly describe the “bulk” ice, *i.e.* the optical properties of most of the detector medium in terms of layers. There are however certain features that these models have to handle. One of

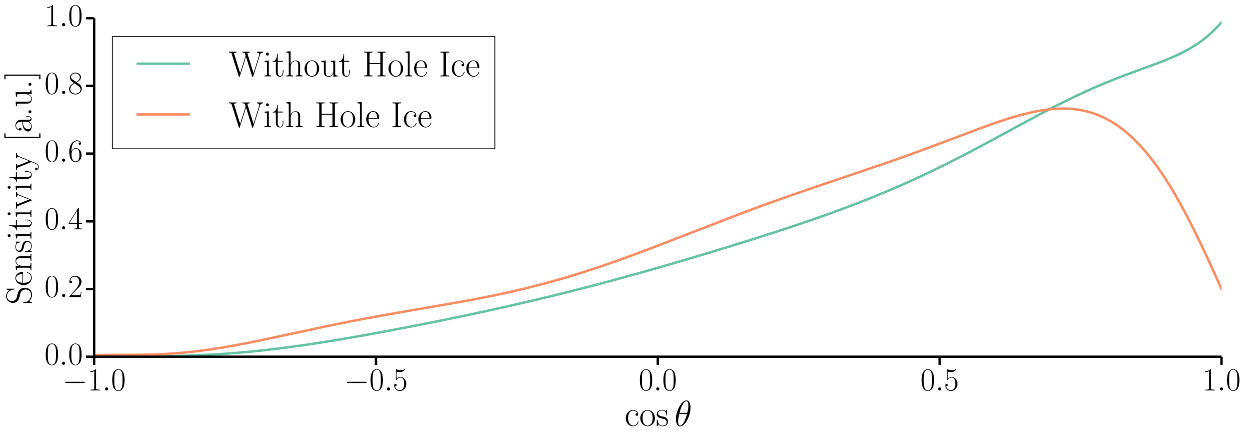

Figure 4.16: Angular sensitivity function for a standard IceCube PMT. The effect of the "hole ice" is a decrease in the sensitivity of the DOM for photons originating from a cos $\theta \gtrapprox 0.75$.

these is the so-called "tilt," a systematic shift of the ice layers due to elevation changes of the bedrock [42]. This shifts the position of the layers with respect to their expected position. A feature that is not yet fully incorporated in the ice models is the effect of the re-freezing on the ice surrounding the DOMs, the so-called "hole ice;" see Figure 4.16. When the water refreezes around the DOMs, a column of ice with large number of air bubbles form and a different dust distribution to form. This in turn causes more absorption and scattering in this area.

4.6.1 Effective Volume for Supernova Neutrino Products

Besides the cross-sections mentioned in Section 4.5.1, the effect of the optical properties of the ice on the detectability of supernova neutrinos in ice has to be determined. The low brightness of supernova neutrino events requires an understanding of the ice properties close to a DOM. In order to test the ice properties close to an individual DOM, one needs to determine the effective volume for this DOM, *i.e.* the volume surrounding the DOM in which the detection efficiency for an interaction is ∼100%. For most events in IceCube, the effective size of the detector is larger than the instrumented volume. This is a function of the clarity of the detection medium and the energy of the interacted neutrino. For supernova neutrinos with $\mathcal{O}(10\,\mathrm{MeV})$ in IceCube, this means that the effective volume is a relatively small volume around a given DOM; see Figure 4.17.

In order to determine the effective volume for the various ice models, one needs to simulate a fixed number of positrons of a given energy range into a given volume and determine the number of particles that were detected compared to the total number and the injection volume. For this reason, 1.4×10^9 positrons with

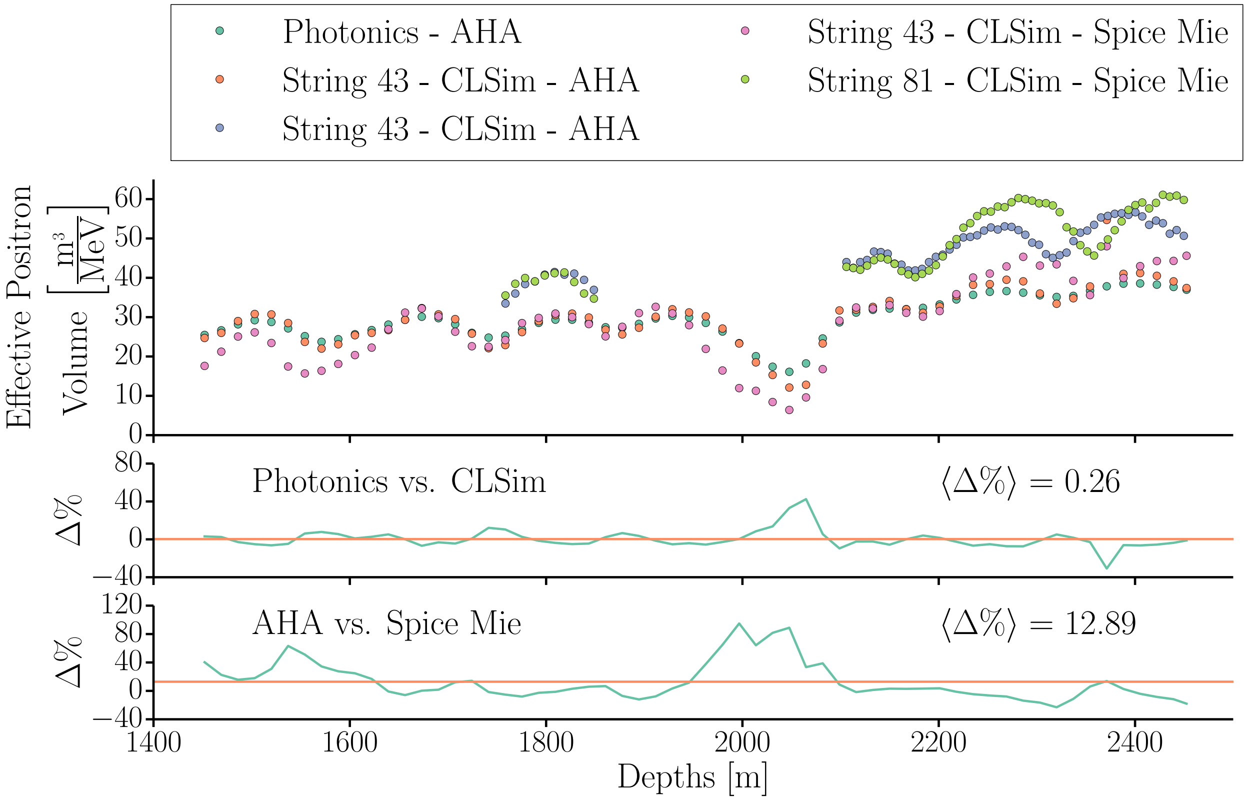

Figure 4.17: Effective Volume for an IceCube and DeepCore string for the AHA and SpiceMie ice model as determined for String 43 and 81. The top plot shows a comparison between the different propagation methods (Photonics versus CLSim) [42–44], ice models (AHA versus SpiceMie), and quantum efficiencies for a given PMT. The middle and bottom plot are residuals between the propagation methods (middle) and ice models (bottom). The propagation methods are comparable and the difference is dominated by different handling of the dust layer and DOM 43-55. The difference between ice models is mostly due to differences in the dust layer and the shallower depths. The effect between different quantum efficiencies can be seen by comparing DOM 43-55 to values of String 81. NOTE: DOM 43-55, aptly re-named “Breach of Protocol,” is a high quantum efficiency DOM that was placed on an non-DeepCore string.

10 MeV kinetic energy were injected into a 250 m sphere around every DOM on String 43 and String 81 for a given ice model. String 43 is chosen because it was far away from DeepCore and effects from shadowing from nearby strings would be included. String 81 was chosen because there are fewer DeepCore strings close by and the string has only high quantum efficiency DOMs. The large volume was necessary because of the

long absorption length. This is an energy-independent study as the number of Cherenkov photons scales linear with energy in the MeV-energy regime; see Equation 4.20 and [4].

The comparison between different propagation methods was used to assess the possible systematic errors that may arise; see Section 5.1. The different propagation methods are summarized in [43] for Photonics and [42, 44] for CLSim[1]. In general, these methods are comparable outside of the dust layers. For higher energies, the CLSim propagation methods yields better comparison between data and simulation; see [293, 294]. The photons from these simulations typically originate $\mathcal{O}(10–100\,\mathrm{m})$ from the individual DOM. This means that the ice surrounding the DOMs or the detection efficiency are not accurately described in the IceCube simulation or that the detection efficiency of the DOMs is not accurate for close-by events. This is a known issue as the hole ice is only parametrically described; see Figure 4.16. This is not surprising as the ice surrounding the DOMs still only parametrized as decrease in the angular sensitivity rather than studied on a per-DOM or per-string basis; see Figure 4.16.

Differences between ice models, *i.e.* Additionally Heterogeneous Absorption (AHA) [41] and SpiceMie [42], presents the systematic effect in the simulation due to detector medium. The largest difference between the ice models has mostly to do with the width of the dust layer and the decreased clarity at shallower depths, $\lessapprox 1700\,\mathrm{m}$. Otherwise the two ice models are comparable at the $\sim$5% level.

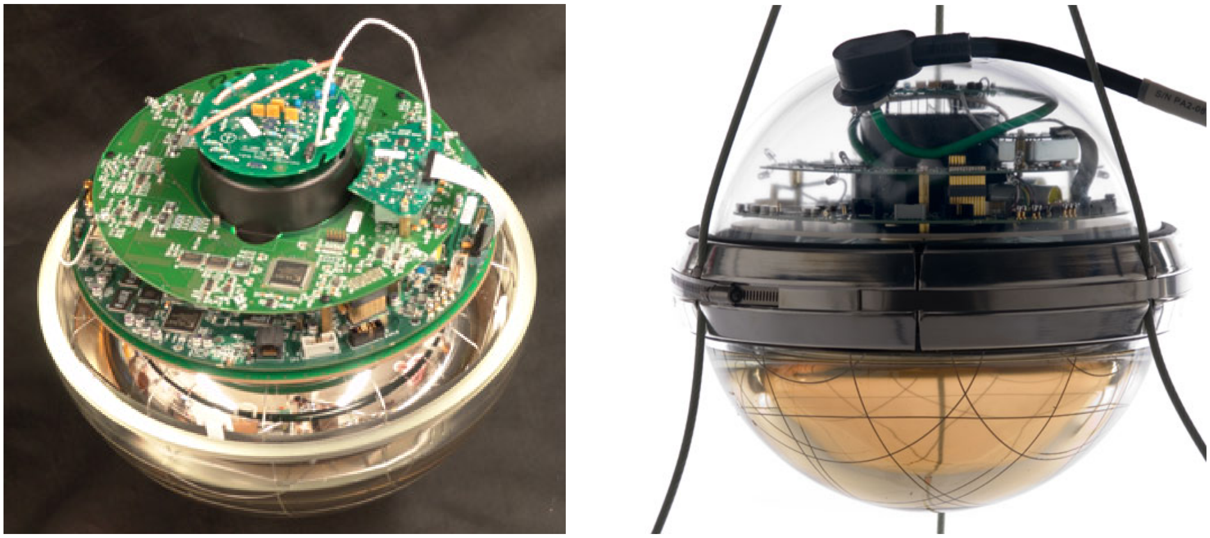

(a) Picture showing the mainboard, flasher, and high voltage controller for the PMT. Credit: [45]

(b) Picture showing the fully assembled DOM. Credit: [46]

Figure 4.18: Pictures showing the mainboard, flasher, and high voltage controller for the PMT (right) and the fully assembled DOM (left). Credit: Left: [45]; Right: [46]

---

[1] CLSim is a re-implementation of the Photon Propagation Code (ppc) used in [42]

4.7 Digital Optical Module

The 5484 DOMs that constitute the IceCube observatory can be thought of as independent data collection and data acquisition systems; see Figure 4.1c and 4.18. An individual DOM consists of a 25.4 cm photomultiplier tube (PMT) with a power supply, readout and digitization electronics, and LED calibration electronics housed inside a 33 cm glass pressure vessel, designed to withstand 68.9 MPa pressure from a 2500 m long column of ice and the ice forming around the DOMs. The PMTs are Hamamatsu R7081-02 with a quantum efficiency of 25% at 390 nm, and a spectral response ranging between 300 and 675 nm [242, 258]; see Figure 4.19. It is optically coupled to the pressure sphere using an optical silicone gel. To compensate for the effects of the Earth's magnetic field on the collection efficiency of the PMT, a mu metal wire grid of nickel-iron alloy surrounds the PMT.

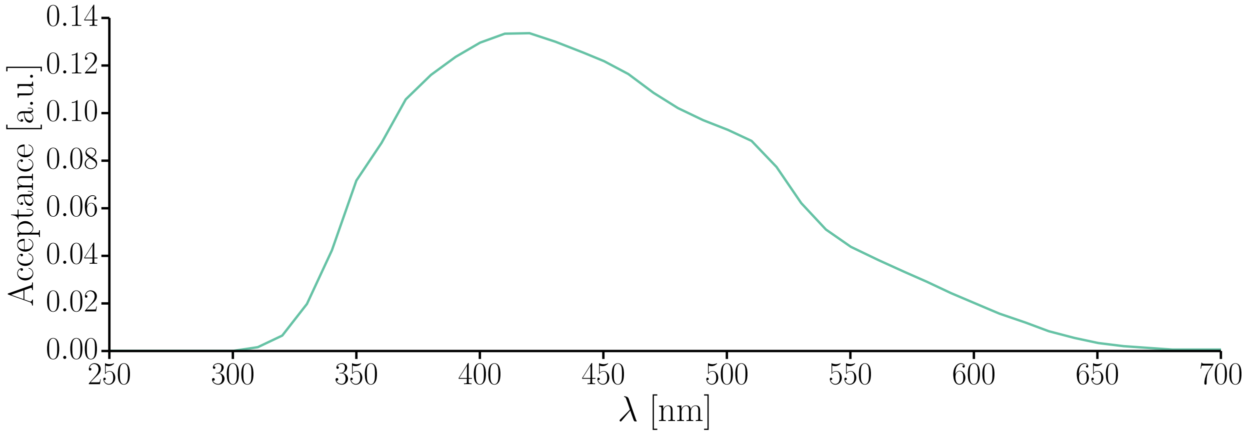

Figure 4.19: Wavelength response function for a standard IceCube DOM. The response curves takes the effect of the pressure vessel, optical gel, mu-metal cage, and the cable into account. The data is taken from the CLSim acceptance parametrization.

4.7.1 Digitization and Triggering

The readout and digitization electronics are responsible for independent data acquisition and transmission; see Figure 4.20 and [243] for more details. A field-programmable gate array (FPGA) predominantly handles the readout of the on-board digitizers–two Analog Transient Waveform Digitizers (ATWD) and a Flash Analog-to-Digital Converter (FADC)–and data transmission. ATWD is a custom-designed low power chip sampling at ≈300 MHz that collects up to 128 samples every 3.3 ns for a total of 426 ns from three separate amplification stages (16×, 2×, and 0.25×). There are two separate ATWDs on the mainboard to minimize the deadtime, as 29 μs are required to digitize, readout, and reset an individual ATWD. The FADC is a commercial chip using a 20 MHz clock that is sampled at both edges of the clock gate for a total sampling rate of 40 MHz. It has a readout window of 6.4 µs storing a total of 256 samples. The coarser readout is a trade-off between lower deadtime (50 ns) compared to the ATWD and much longer readout window. There is a 70 ns delay line in order to read out the triggering pulse.

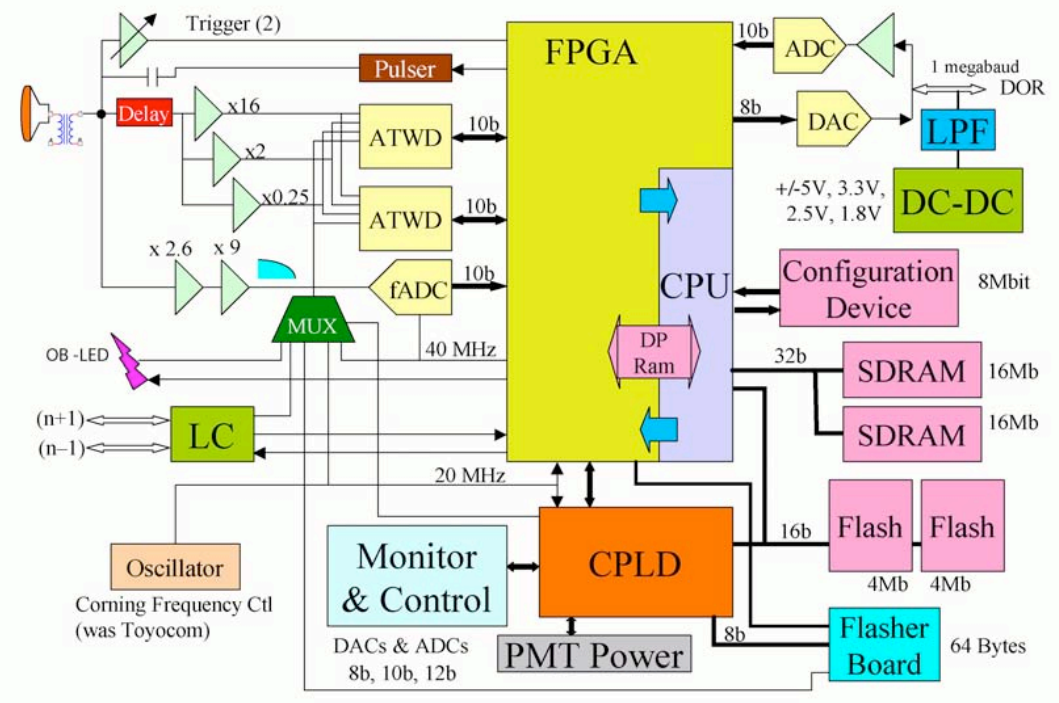

Figure 4.20: Schematic diagram of the IceCube DOM mainboard electronics. Only the FPGA, the discriminator, and the PMTs are the relevant components for the supernova scalers discussed in Section 4.7.2.

A DOM triggers independently if its discriminator threshold, ≈0.25 photoelectrons (PE), has been met or exceeded and begins to readout its digitizers. A DOM trigger is internally referred to as a “hit” or “launch.” Concurrently to the DOM trigger, the DOM checks the state of its closest two neighbors above and below on a string for *Local Coincidence* (LC). If any of these neighbors also triggers within a ±1 µs window, the *Hard Local Coincidence* (HLC) condition is met and the DOMs stores their full waveform readout and sends it to the counting house on the surface of the ice shelf when queried. In case HLC is not met, *Soft Local Coincidence* (SLC) is invoked and only 3 FADC samples centered on the highest amplitude bin are transmitted. HLC was introduced to reduce the effect of the PMT and DOM noise. An atmospheric muon, for example, is much more likely to trigger the HLC condition than a random coincidence. The HLC noise rate, *i.e.* rate of random coincidence, is 2–5 Hz, while the average HLC rate for detector is ∼13 Hz; see Figure 4.21. The average SLC rate is ∼585 Hz; see Figure 4.22

Most DOM triggers in case of a supernova will be SLC. This because of the diffuse nature of the signal in time and space and as mostly single photoelectrons being detected. The probability that a supernova neutrino interaction will produce triggers on two DOMs is $< 1\%$. An increase in the HLC can still occur as an increasing SLC rate will cause an increasing rate of random coincidence.

4.7.2 Supernova Scalers

The distinctive event signature of supernova neutrinos and the transient source requires the continual monitoring of the noise rate of individual DOMs; see Section 4.3 and 4.9. The normal event stream does not allow this. A certain trigger threshold has to be met to consider the data and the readout window is significantly shorter; see Section 4.8. The data rate would be too high for a single DOM and the majority of light from a given supernova neutrino interaction is expected to only trigger one DOM. For this reason a separate physics data stream–Supernova Scalers–was created alongside primary waveform-based data stream; see Section 4.7.1.

The supernova scalers are the result of a routine implemented in the FPGA that is independent of the LC condition and digitization electronics; see [30,243] for details. The FPGA counts the number of discriminator crossings in 2^{16} clock cycles and applies a 250 µs non-paralyzing deadtime [295] to the signal for background reduction; see Section 4.4.1 for details. With a 40 MHz sampling rate, this means that the integration window is $2^{16}/40\,\text{MHz}$ or 1.6384 ms. A single DOM is capable of storing the scaler counts in 1.6384 ms for ∼10 s. The DOM transmits them to the surface when queried by the DAQ system every ∼1 s for further processing by the online analysis; see Section 4.8 and 4.9 for details.

4.8 Data Acquisition System

IceCube's data acquisition (DAQ) software *pDAQ* handles the data taking, detector configuration, and event construction. As part of the DAQ, the *StringHub* is the communication and monitoring relay between the individual DOMs on a string. The StringHub constantly requests data from the DOMs. The received data stream is split off into four components: DOM triggers, monitoring data, time calibration data, and supernova scaler data. These data sets are then transmitted to the relevant components, *i.e.* DOM triggers are transferred to software triggers and the supernova scaler data is sent to supernova analysis. The supernova scalers are the primary data stream for the supernova analysis; see Section 4.9 for more details.

In addition to relaying the received DOM triggers to pDAQ's trigger and event construction system, the StringHub also writes these into a time-ordered ring buffer on disk, named *Hit-Spooling*; see [296, 297] for details. For the purposes of supernova data acquisition and physics analysis, the supernova scalers and the

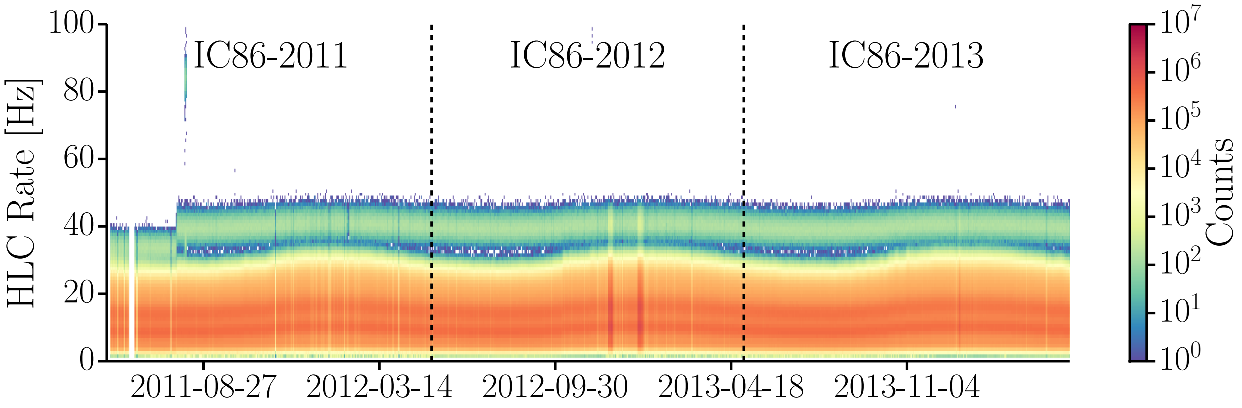

(a) HLC rate distribution of the course of the first three years of the completed detector. There is a separation visible because of depth dependence of the atmospheric muon contamination. The jump several months into IC86-2011 is due to a change in the DOM deadtime by 10%.

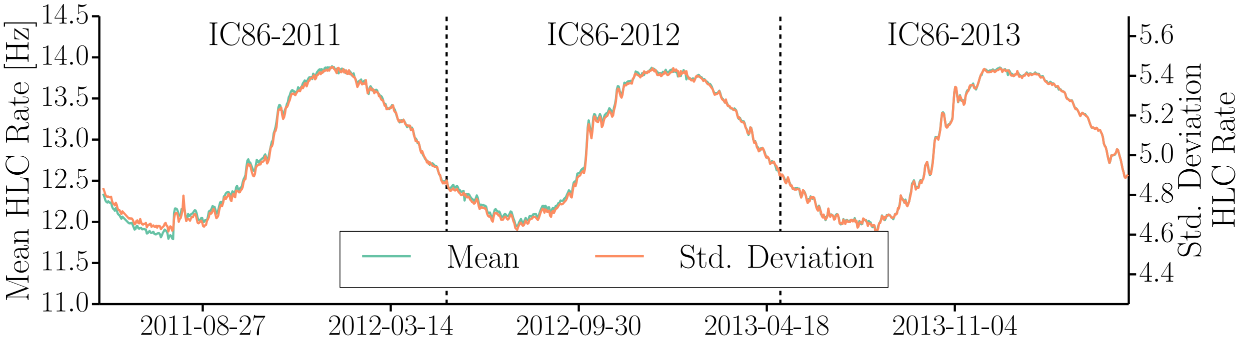

(b) Mean and standard deviation of the HLC rate distribution shown in Figure 4.21a

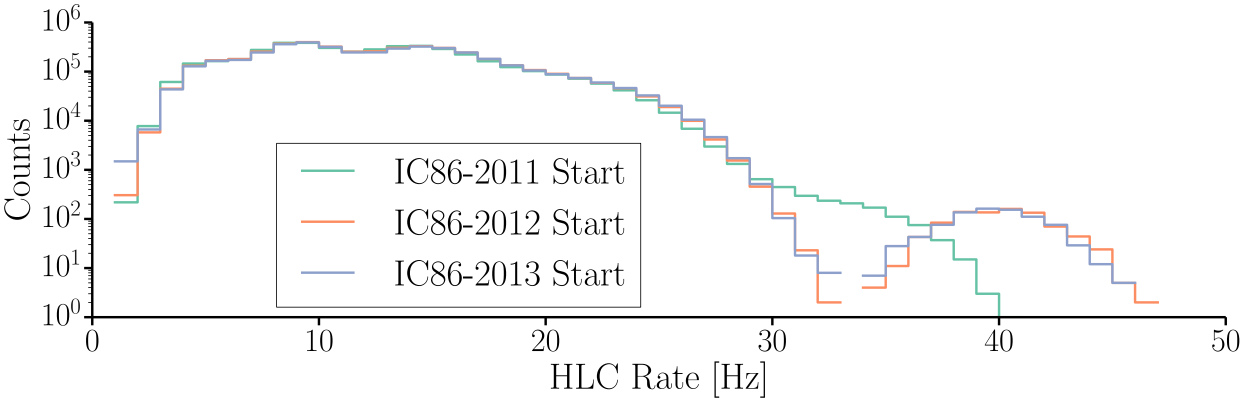

(c) Slices of the HLC rate distribution in Figure 4.21a at the start of physics runs in this data set. There is a separation visible because of depth dependence of the atmospheric muon contamination.

Figure 4.21: HLC rate distribution and its statistical properties over the course of the first three years of the completed IceCube detector.

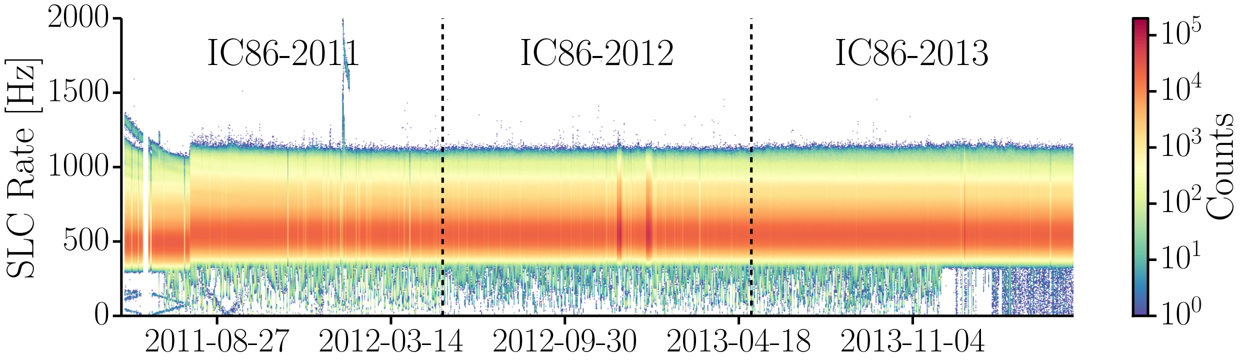

(a) SLC rate distribution of the course of the first three years of the completed detector. A decay is visible in the width of the distribution is clearly visible. The source of the decay is explored in Section 6.1. The jump several months into IC86-2011 is due to a change in the DOM deadtime by 10%.

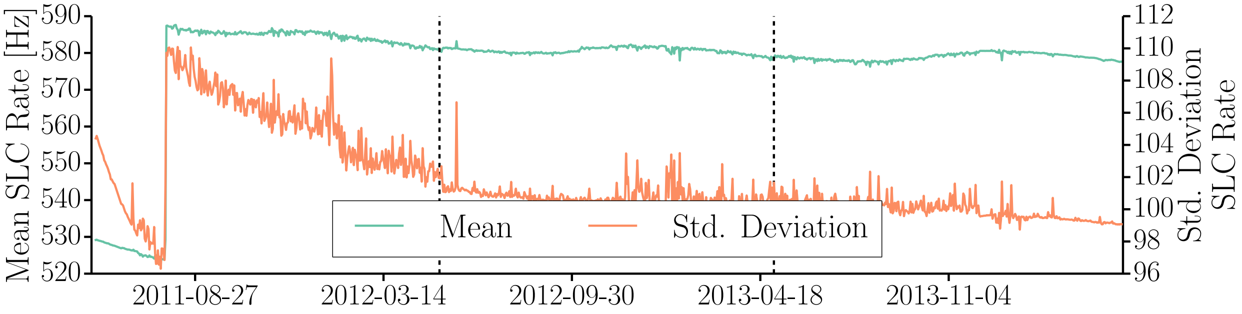

(b) Mean and standard deviation of the SLC rate distribution shown in Figure 4.22a. The decay and jump are clearly visible in both quantities.

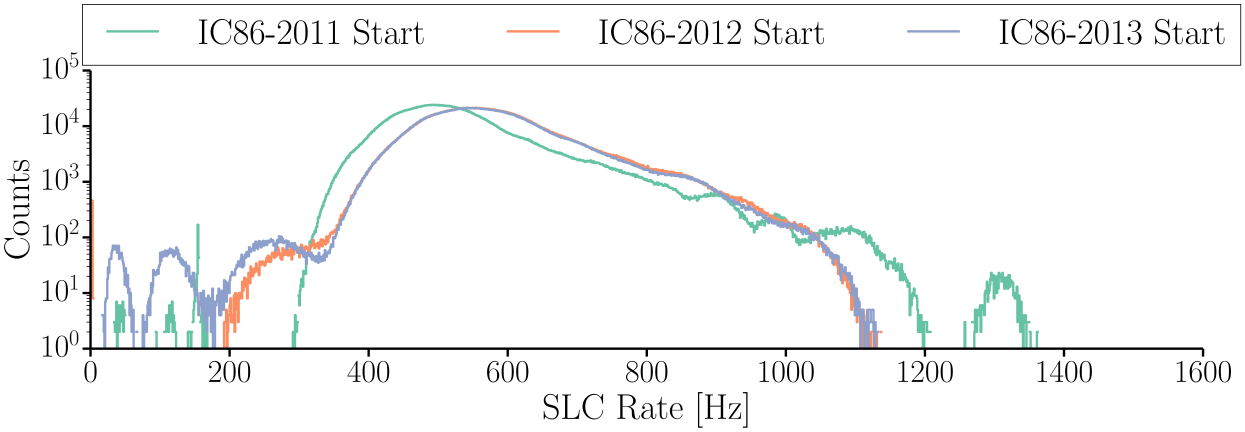

(c) Slices of the SLC rate distribution in Figure 4.22a at the start of physics runs in this data set. A shift in the distribution is visible. This is related to the decay seen in Figure 4.22b

Figure 4.22: SLC rate distribution and its statistical properties over the course of the first three years of the completed IceCube detector.

Hit-Spooling data are of importance, as it provides access to all available detector information. *Hit-Spooling*, currently, constitutes a view at the data without any software triggers applied and a short-term ($sim8[hours]$) backup of the detector data. The removal of any cuts due to software triggers is very important because software triggers would generally ignore the supernova signal as it is too diffuse in time and location inside the detector. Additionally, *Hit-Spooling* provides a view of noise behavior of the detector, which is necessary for background studies; see [253] for details.

Trigger	Trigger Condition	Trigger Window (µs)	Readout Window (µs)
VT	4 DOMs with HLC in a cylinder with radius 175 m and height 75 m or 8 DOMs with HLC	1	-4, +6
ST	5 out of 7 vertically adjacent DOMs	1.5	-4, +6
SMT3	3 DOMs with HLC on DeepCore Strings	2.5	-6, +6
SMT8	8 DOMs with HLC	5	-4, +6

Table 4.3: Summary of trigger conditions, trigger window, and readout window for String, Volume, and Simple Multiplicity triggers. The readout window indicates the time before (-) the first and after (+) the last HLC DOM triggerin the trigger window the detector is being readout for. Values taken from [5] and the pDAQ configuration [6].

The most important aspect of pDAQ is the integration of the individual strings and DOMs into a single detector. The respective DOM readouts are being sorted time-wise in real time and passed through a software trigger system. The main trigger types are the *String Trigger* (ST), *Volume Trigger* (VT), and *Simple Multiplicity Trigger* (SMT). The trigger conditions, trigger windows, and readout windows are summarized in Table 4.3. The supernova scalers, as described in Section 4.7.2, are handled independently of triggers. pDAQ queries the DOMs for the data and the DOMs sent the data to pDAQ. pDAQ writes the data out into a binary data format that is then processed online. Information about other triggers can be found in [5].

4.9 Supernova Online Analysis–Supernova DAQ

The search for supernova neutrinos inside IceCube relies on supernova neutrino burst illuminating the detector approximately uniformly; see Section 4.3. The uniform illumination will cause a significant increase in the DOM noise rates compared their respective mean values. In other words, there would be a global or DOM-to-DOM correlated increase in the noise rate. To use neutrinos as a early messenger for supernova explosions, the analysis has to be done online, *i.e.* at the South Pole. For an overview of the analysis see [30, 112, 298].

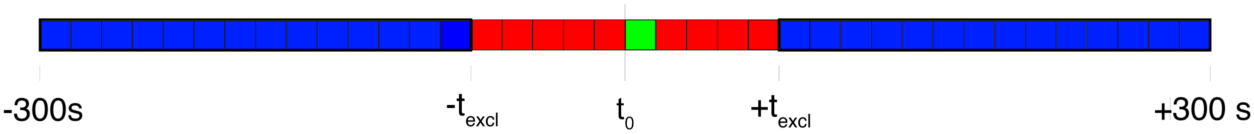

Figure 4.23: Graphic representation of the 600 s analysis window used in SNDAQ. The green bin is the signal bin, the red bins are the buffer region, and the blue bins are the background region. Modified from a version in [47]

The online analysis of the supernova scaler data is performed by the Supernova DAQ (SNDAQ). The SNDAQ is an analysis suite that is focused on continually monitoring of detector noise rate to search for a collective increase in the detector noise rate. The search is performed using a log-likelihood analysis under the assumption that there is no DOM-to-DOM correlation in the noise and DOM noise is Gaussian distributed with mean, μ_i, where i is the index of a DOM, and standard deviation, σ_i. The assumption of Gaussian distributed noise is valid because the analysis is integrating over at least 250 2 ms bins. If one were to use smaller binning, *i.e.* 2 ms binning, the Gaussian noise assumption is no longer valid and would be replaced with a Poisson distribution. The Poisson distribution can not be solved analytically in this case.

To determine a collective deviation in the noise across the detector, $\Delta\mu$, from individual noise rates the following likelihood is used:

$$\mathcal{L}(\Delta\mu) = \prod_{i=1}^{N_{\mathrm{DOM}}} \frac{1}{\sqrt{2\pi}\sigma_i} \exp\left\{-\frac{1}{2}\left(\frac{r_i - (\mu_i + \epsilon_i \Delta\mu)}{\sigma_i}\right)^2\right\} \tag{4.21}$$

where r_i is the per DOM rate in the signal bin, ϵ_i is a DOM-specific efficiency parameter associated with the detection properties, *i.e.* ice and PMT acceptance, of the individual DOM, as well as μ_i and σ_i are the mean and standard deviation, respectively, estimated from the background window. Maximizing the log-likelihood

$$-2\ln(\mathcal{L}(\Delta\mu)) + \text{constant} = \chi^2(\Delta\mu) = \sum_{i=1}^{N_{\mathrm{DOM}}} \left(\frac{r_i - (\mu_i + \epsilon_i \Delta\mu)}{\sigma_i}\right)^2 \tag{4.22}$$

with respect to $\Delta\mu$ will result in an analytic form of $\Delta\mu$ in terms of the measurable quantities; r_i, ϵ_i, μ_i, and σ_i:

$$\Delta\mu = \sigma_{\Delta\mu}^2 \sum_{i=1}^{N_{\mathrm{DOM}}} \left(\frac{r_i - \mu_i}{\sigma_i}\right)\left(\frac{\epsilon_i}{\sigma_i}\right) \tag{4.23}$$

where $\sigma^2_{\Delta\mu}$ derives from the requirement that $\mathcal{L}(\Delta\mu \pm \sigma_{\Delta\mu}) = \mathcal{L}(\Delta\mu) \pm 1$, *i.e.* that the likelihood grows by one if the to-be-determined parameter changes by its standard deviation. $\sigma^2_{\Delta\mu}$ is therefore given by

$$\sigma^2_{\Delta\mu} = \left(\sum_{i=1}^{N_{\mathrm{DOM}}} \frac{\epsilon_i^2}{\sigma_i^2} \right)^{-1} \tag{4.24}$$

The significance, ξ, of the illumination of the detector, and thereby $\Delta\mu$ is given by

$$\xi = \frac{\Delta\mu}{\sigma_{\Delta\mu}} \tag{4.25}$$

The values of ξ is expected to be a unit normal distribution (Gaussian-distributed with $\mu = 0$ and $\sigma = 1$). Under the assumption of a unit normal distribution ξ, the numerical value of ξ will correspond to units of σ, as it is normalized to the error of $\Delta\mu$. The log-likelihood value also provides a measure of the uniformity of the illumination. The $\chi^2(\Delta\mu)$ from Equation 4.22 is a measure of the goodness-of-fit of $\Delta\mu$ to the individual rates, r_i, of the DOMs, which provides a measure of how many DOMs contributed to the signal and therefore the uniformity of the illumination.

Analysis Bin Size (s)	Exclusion Window (s)	Left Background Window (s)	Right Background Window (s)
0.5	-15, +15	-300, -15	+15, +300
1.5	-15, +15	-300, -15	+15, +300
4	-12, +16	-300, -12	+16, +300
10	-10, +20	-300, -10	+20, +300

Table 4.4: Summary of analysis window for the various SNDAQ analysis bin sizes. The times are given relative to signal bin with time, t_0, where the signal bin is from $t_0 \rightarrow t_0$ + Analysis Bin Size [7].

To determine the measurable quantities, the supernova scalers from individual DOMs are initially rebinned into time-synchronized 2 ms per-DOM bins and subsequently rebinned into 0.5 s per DOM bin for analysis. A 600 s long rolling window centered on the r_i or signal bin (green bin in Figure 4.23) is applied to the data. The signal bin is the center of a $\sim\pm$ 15 s (red bins in Figure 4.23) buffer region. The signal and buffer region are surrounded by two background regions (blue bins in Figure 4.23) from which μ_i and σ_i are determined.

The size of the signal bin has to be adjusted for the expected signal. The shape of the supernova signal in time can be generalized as a sharp rise in the rate with an exponential fall off with a time constant, τ, see Figure 3.7a and 3.9a. The significance is related to the analysis bin size, Δt, and τ as follows

$$\xi \propto \int_0^{\Delta t} dt \frac{e^{-t/\tau}}{\sqrt{\Delta t}} \tag{4.26}$$

This dependence on the analysis bin size and the differences in supernova models, requires that the online analysis is being conducted in four time bins: 0.5 s, 1.5 s, 4 s, and 10 s. The bin sizes were chosen to optimize the detection sensitivity for several scenarios:

- 0.5 s: Shortest time scale available. Looking for short bursts associated with black hole formation from core-collapse supernova.
- 1.5 s: Most models, such as Lawrence-Livermore, have a large flux in the first 1-2 seconds.
- 4 s: Proto-neutron star cooling follows an exponetial decay with $\tau \approx 3$ s, which has an optimal detection value of $\Delta t \approx 3.8$ s.
- 10 s: Time scale of all neutrinos events detected for SN1987A.

The changing analysis bin sizes will also produce differently sized buffer and background regions, see Table 4.4.

The limited satellite connection and bandwidth from the South Pole to the northern hemisphere allows SNDAQ to only send a limited amount of information. At the moment this includes:

- "SN_Streaming_All_t" ("sn_all"): 500 ms bins of supernova scalers for individuals DOMs
- "SN_ORoutEvent_t" ("sn_rout"): Result of the analysis class bins stored in "sn_all"
- "SN_OCandEvent_t" ("sn_cand")': Additional information for significant triggers
    - 90 s (-30 s, +60 s) of time-synchronized per-DOM 2 ms bins
    - r_i, μ_i, σ_i, ϵ_i for every channel

For more details on the data format see [47, 112, 298].

Chapter 5

Simulation

Simulating the detector response to signal and background is a necessary step in any particle physics experiment. This chapter outlines the IceCube simulation framework, the current supernova neutrino simulation, and the implementation of new simulation framework for supernova neutrinos in IceCube.

5.1 Methodologies

Supernova neutrino simulation in IceCube is a daunting endeavor. There are a large number of possible theoretical neutrino emission models and progenitor distributions yielding a large number of possible signal hypotheses; for examples see [22,24,179,180,183,187] and [29,211,299], respectively. The detector geometry is optimized for the detection of individual neutrinos and their interaction products at energies 1 TeV and above. Besides the nearly 10^6 eV disparity in energy, the large number of neutrino interactions combined with the low probability of detecting these interactions, and the long time span of the event causes many different challenges compared to typical IceCube signals, such as certain backgrounds become significantly more important, see Section 4.4. There are a variety of possible approaches to simulate the detector response to supernova neutrinos, which are discussed below.

5.1.1 Parametric Simulation

Prior to this work, IceCube used and still uses a "parametric" approach based on Equation 4.1 for its supernova simulation, in form of the software framework named *Unified Supernova Simulation Routine* (USSR). The USSR uses parameterizations of independent simulations of the optical properties of the ice, DOM efficiency, and cross-sections to determine the detector-specific response, *i.e.* the expected number of DOM hits above the background, for a given supernova signal; see Section 4.3. The ice and DOM optical properties are modeled using IceCube's light propagation tool *Photonics*, see [43] for details. The cross-sections are from [3, 4, 272, 277, 280]. This implementation provides a fast and efficient way to simulate various different models, neutrino oscillation scenarios, and number of DOMs.

The parametric approach used in USSR lacks the ability to perform a more detailed study of signal and backgrounds. From the simulation one can estimate the response of the SNDAQ analysis to an expected signal. There is no per event information in this simulation; rather a statistical representation of the expected signal. This means that one cannot study the events that are detected and reveal possible biases between detected and simulated signal. This could lead to misinterpretation of signal characteristics when considering features in the detector, *i.e.* dust layers, geometry changes in DeepCore, *etc.*, and the per-DOM backgrounds, *i.e.* individual DOM rates, sensitivity of individual DOMs to atmospheric muons, *etc.*

The backgrounds for individual DOMs can be accounted for from data, as the background is measured from supernova scalers. To be able to reproduce the same background in simulation, one would have to account for the correlation between DOMs caused by atmospheric muons. The supernova scaler records are stored in 0.5 s long bins in the SNDAQ output files. This makes it impossible to measure the effect of individual muons. One can only measure an ensemble of atmospheric muon and for relatively long integration periods. This latter is especially problematic as one would like to study the effect of the atmospheric muons effect on the signal on shorter time scales. This could be done by examining the 2 ms supernova scaler bins that SNDAQ stores for “interesting” events. This data set cannot be used for simulation studies as it is biased towards background events that produce a false positive supernova trigger, and hence are biased sample of the background.

USSR is also separate from any of the other IceCube simulation software. This makes it difficult to establish possible analysis techniques for other data streams in IceCube, such as *Hit-spooling* or triggered data; see Section 4.8. Methods to extract more information about the signal, as presented by [248], cannot be explored. Such studies would also require the information about how many DOMs detect a given neutrino interactions and to generate individual neutrino events. Similarly, atmospheric muon background reduction techniques cannot be studied from a parametric simulation. There is no way to create “typical” IceCube events with the same amount of information and the effect on the primary data stream cannot be simulated in this case.

5.1.2 Event Simulation

The event approach, from a supernova point of view, performs the simulation by injecting neutrino interactions sampled from a distribution given by the input parameters, *i.e.* selected models, distance between source and detector, oscillation scenario, and detector size and geometry. This approach provides the per neutrino interaction information, can produce pure background simulation including atmospheric muons, relies on already tested, and confirmed lepton propagation and light production, and can be implemented in the IceCube Simulation Framework, *IceSim*.

This increased output and abilities comes at a high computational cost. The large flux from a supernova causes a large number of interactions in IceCube's detector volume. A predominant fraction of these interactions occur too far away from any DOM for the Cherenkov light from the products to reach them. On average, only ≈0.1% of neutrino interactions that occur in the detector are actually detected. From a computational standpoint, this means that a lot of resources used for particle and light propagation are wasted. This makes it infeasible to perform a study of the detector response for the large number of possible input parameters.

A test version of the event-based simulation has been implemented for this work. It is meant for comparison studies between the new implementation of the supernova simulation and the USSR, especially to establish the source of possible differences between the parametric and weighted simulation. To do so, this event-based simulation uses the same cross-sections, and technique to determine the number of interacted neutrinos and interaction product energies as the USSR. The geometry, light propagation, medium properties, and lepton propagation are simulated using standard IceCube tools; see Section 5.2.1 for details. The result provides the means to study the difference in detector simulation that would otherwise be hard to disentangle, for example changes in the cross-sections calculation or the energy of products.

5.1.3 Weighted Simulation

A "weighted" approach was developed to harness the advantages and minimize the disadvantages of the other two approaches presented above. In IceCube, weighted simulation is used extensively in both background and signal simulation and is required in most cases; see Section 5.2.1. This approach is employed because it saves computational resources, for example the neutrino events can used as an atmospheric or astrophysical depending on their statistical weight, and is easily applicable when interested in individual events rather than ensembles of thousands of events.

Weighted simulation splits influences on the simulated detector response between "source" and "detector" effects. A source effect produces changes in the signal and background independent of the detector. In case of supernovae, source effects are associated with the origin of the signal, such as stellar mass, distance to source, or neutrino oscillation scenario. A detector effect would be changes in the signal produced by detector systematics, *i.e.* the ice or geometry. Source effects can be compensated for using statistical weights that accounts for the differences between different supernova scenarios and a simulated signal hypothesis. Detector effects can only be mitigated by simulating different detector systematics using the same signal hypothesis, for example the same signal with difference ice models.

For the supernova simulation, the number of possible signal hypotheses greatly outweigh the possible variations in the detector features as the number of theoretical models, distance between source and detector, and neutrino oscillation scenarios produce a significant number of possibilities. Given that the supernova signals extends over $\mathcal{O}(0.1\text{–}10\,\mathrm{s})$ and involves ensembles of individual events one typically would not be able to use this approach. The weighted approach can be used since the SNDAQ analysis is looking for a statistical effect in the noise rate; see Section 4.9. A scaling factor can therefore be determined to account for the differences in the expected number of events and those in the sample; see Section 5.2.2, and 5.3. The weight can also compensate for differences in the energy spectrum, which can be used to explore, for example the mean energy of supernova neutrinos [248, 300].

For the supernova simulation, one first has to generate signal events, *i.e.* neutrino interactions, according to a given hypothesis, *i.e.* sample size, energy spectrum, *etc.* A supernova event from given input parameters is then constructed by selecting several subsets from the pre-generated neutrino interaction set. The difference in statistics and spectral shape between the pre-generated sample and input parameter-dependent neutrino sample are compensated for by calculating a statistical weight, see Section 5.2.2.1 for details.

Selecting events and calculating the statistical weight is computationally more expensive than a purely parametric simulation as employed by the USSR. It requires significantly less resources than an event-based approach. This method still has the disadvantage of requiring a large amount of computational resources to generated the ensemble. The computational effort is only required once for different detector geometries and ice models instead of for every set of input parameters.

5.2 Supernova Simulation in IceCube

The first section will give an overview of simulation of signal and background events in IceCube. The subsequent sections are an overview of the new supernova neutrino simulation framework, *sni3sim*, that integrates the supernova signal simulation into the IceCube simulation framework, *IceSim*.

5.2.1 IceCube Simulation Environment–IceSim

IceSim is the simulation framework build on top of the IceCube software framework, *IceTray*. It is used for simulating the detector response of IceCube to neutrino and background events. Background events are generated by four software packages: *vuvuzela*, *Cosmic Ray Simulations for Kascade* (CORSIKA) [301, 302], *MuonGun* [48, 303], and *neutrino-generator* (for producing atmospheric neutrino background for astrophysical neutrinos analyses) [304]. *vuvuzela* simulates the backgrounds inherent to the DOM; see Section 4.4.1 for details.

CORSIKA is a tool for the simulation of cosmic ray interaction in the upper atmosphere and propagating particles through the atmosphere to the surface, in the case of IceCube the ice shelf; see Section 4.4.2. *MuonGun* is an in-house development based on work previously done by the Astronomy with a Neutrino Telescope and Abyss Environmental Research (ANTARES) collaboration in [305]. Instead of simulating the cosmic ray interactions and propagating the muons through the atmosphere and ice, the atmospheric single muon flux that penetrates the detection volume[1] of IceCube is parametrization from CORSIKA simulation in the deep ice [48, 303]. This parametrization is then sampled to produce atmospheric muons according to this distribution and a statistical weight is applied according to the comic ray interactions model, cosmic ray energy spectrum, *etc.* [264–267]

Neutrino events are generated using *Generates Events for Neutrino Interaction Experiments* (GENIE) [306–308] for $E_\nu \lesssim 200\,\mathrm{GeV}$ and *neutrino-generator* for $E_\nu \gtrsim 200\,\mathrm{GeV}$. *neutrino-generator* is used to produce both atmospheric and astrophysical neutrino interactions in the detector and uses statistical weights to to compensate for the difference in the source of the neutrinos, *i.e.* atmospheric or astrophysical origin, and the probability of interacting in the detector. *neutrino-generator* is based on ANIS described in [304]. GENIE is a neutrino interaction simulation framework focused on energy ranges for atmospheric- and accelerator-based neutrino oscillation experiments, $\mathcal{O}(1\text{–}10\,\mathrm{GeV})$ [306–308]. Instead of forcing a neutrino interaction and calculating the interaction probability, GENIE produces neutrinos and calculates whether or not this neutrino would interact. If the neutrino does not interact, GENIE repeats the cycle until an interaction occurs. Given the total number of sampled neutrinos and the number of interacted neutrinos a probability of such an event occurring is calculated. Extensions down to $\mathcal{O}(1\,\mathrm{MeV})$ by the GENIE collaboration are planned, see [309].

Besides the background and signal generation, *IceSim* includes the simulation for particle and light propagation, DOM functionality, and the DAQ. Particle propagation is performed depending the energy and type of the product lepton. For low energy neutrino interaction products, such as in case of supernova neutrinos, GEANT4 is used for particle propagation and light production [281, 282]. For the majority of other cases either *Muon Monte Carlo* (MMC) [310] or *Propagator with Optimized Precision and Optimized Speed for All Leptons* (PROPOSAL) [311] is used for high energy lepton propagation and light production.

The light can be propagated using statistical approach as used in *Photonics* [43], or direct propagation using *Photon Propagation Code* (PPC) or *OpenCLSim* (CLSim) [42, 44, 312]. The simulated light that reaches a given DOM and would create a photoelectron is converted into a *IceCube Monte Carlo Photoelectron* (I3MCPE). These are converted into *IceCube Monte Carlo Pulse*s (I3MCPulses) using *PMTResponseSimulator*, which also simulates the PMT response as well as pre- and afterpulsing behavior of PMTs. These pulses are than converted into *DOMLaunch*es, *i.e.* digitized waveforms and timing information, similar to the data transmitted to the DAQ by the DOMs, using *DOMLauncher*. The DAQ simulation is performed using *trigger-sim*. For a visual summary of the simulation chain see Figure 5.1.

This software framework is setup under the assumption that an injected background or signal particle produces a physically relevant signal, *i.e.* a trigger or *DOMLaunch*. The simulation splits individual events

---

[1] The detection volume is a cylinder with radius of 800 m and height of 1600 m centered on the IceCube detector. It was chosen to accommodate the length light could travel through the ice and the location of the bedrock.

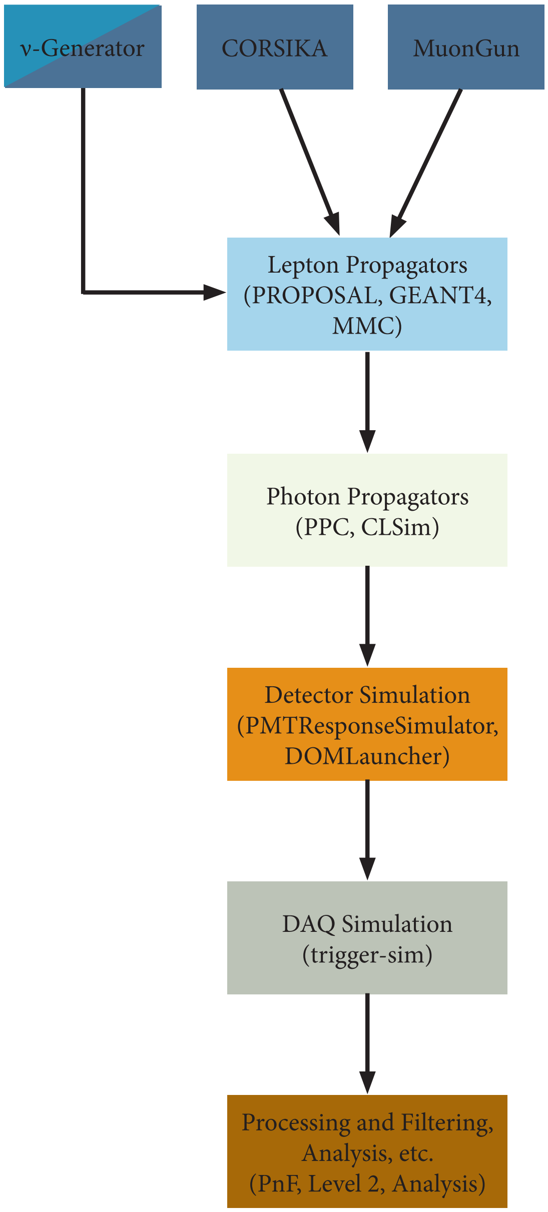

Figure 5.1: Summary of the typical IceCube signal and background simulation chain without the new supernova simulation. The simulation begins with either generating atmospheric muon background events using CORSIKA/*MuonGun* or either signal or background neutrino events using *neutrino-generator*. The resulting leptons and their Cherenkov light are are propagated through the medium. The photons that reach the DOMs and produce I3MCPEs and subsequently into *DOMLaunch*es. These *DOMLaunch*es are fed through a DAQ simulation and ultimately through the IceCube processing chain.

prior to triggering, *i.e.* the atmospheric muon background is being produced on a per-event basis rather than a stream of background. Individual events and triggers are stored in so-called "frames." In *IceTray*, frames from data store information (trigger conditions met, time, direction, *etc.*) for individual or a set of triggers depending on the event. Frames from simulation store data about individual injected particles that produce a detector readout, either on the individual DOM level or as a trigger. The typical length of a frame in simulation and data is $\mathcal{O}(10\text{–}100\,\mu\text{s})$. An exception being events that pass the slow particle trigger (SLOP) that are on $\mathcal{O}(0.1\,\text{ms})$ per event in length [5]. These are used in the search for non-relativistic magnetic monopoles [313].

This means that supernova neutrino-like events, *i.e.* events lasting $\mathcal{O}(100\,\text{ms})$ to $\mathcal{O}(10\,\text{s})$, have not been considered when setting up the general simulation framework. Separately, the SNDAQ analysis requires at least 600 s of supernova scaler data to do the analysis; see Section 4.9. The software cannot readily accommodate events that last orders of magnitude longer and reaches the limit of current computational constraints of the software and the collaboration as whole. The new supernova simulation has to accommodate these assumptions, as outlined in the subsequent sections.

5.2.2 Supernova IceCube Simulation–sni3sim

Implementing a weighted supernova simulation inside of *IceSim* requires a number of separate steps. Generating the ensemble, selecting a subset, and applying the statistical weight is handled by *Supernova Physics Simulation* (SNPS). The detector-specific portion of the simulation, such as producing unweighted simulation and converting discriminator crossings to supernova scalers, is handled by *Supernova Detector Simulation* (SNDS).

5.2.2.1 Supernova Physics Simulation–SNPS

SNPS splits its tasks into independent software instances, so-called "modules" in *IceTray.* Each module in this case handles a separate step of the process: ensemble generation, model creation, and neutrino oscillations. For a visual summary see Figure 5.2.

Ensemble Generation The injection module, *SNInjection*, generates neutrino interactions according to a given interaction, such as inverse β-decay or ν-e^- scattering, for $\mathcal{O}(1\text{–}100\,\text{MeV})$ neutrinos inside a predefined cylindrical volume. The volume is typically chosen to be a cylinder with a radius of 800 m and height of 1600 m encompassing the instrumented volume. It is the same effective volume of the detector as used for the atmospheric muon background generation. The choice is related to the maximum distance that light can travel in the ice and the position of the bedrock. It can be changed to smaller and large volumes if so desired.

The neutrino energy of the injected neutrinos follows either a Γ-distribution with a shape parameter, α, and rate parameter, β, a Gaussian distribution with a given mean and variance, or a flat spectrum. By default, the Γ-distribution is used as it is the energy spectrum used in the Garching models; see Equation 3.2. The Gaussian input spectrum is implemented to be able to generate ensembles for models without a given energy spectrum. The product energies are calculated from the given interaction; see Section 4.5.1.

The generated neutrino interactions are split into subsets across several frames. The size of the subset is an input to *SNInjection*, by default 1000 neutrino interactions are saved in an individual frame. The value was chosen to produce at least one detected interaction per frame and not select too many interactions when assembling a neutrino signal.

The interactions are forced, as done in *neutrino-generator*, to be able to generate a large ensemble much faster than continuously drawing neutrinos from a distribution until they interact, as done in GENIE. For each neutrino interaction an "interaction" weight is calculated to determine the probability that this neutrino would have actually interacted in this spot in the ice for a given interaction volume and direction; see [304] for details. This weight is not needed for the SNPS supernova neutrino simulation. The interaction weight would be needed in case the cross-sections were not considered in subsequent steps. Without this assumption, the ensemble would be orders of magnitude larger. This mode of operations was therefore not implemented.

A significant portion of the neutrino interactions are not detected by DOMs. To save disk storage space and improve speed when assembling a model, any neutrino interaction that is not detected is removed using *SNFilePruner*. The module keeps frames without any detected interactions. They are needed for bookkeeping purposes when generating an ensemble, as one cannot calculate the number of detected neutrino interactions independent of detector effects.

Model Creation Once a sufficiently large ensemble is generated, a supernova event can be constructed using *SNPickEvents(Queue)*. *SNPickEvents(Queue)* calculates the number of interacted neutrinos for a given time bin of the model and input parameters. It then selects the required number of neutrinos from the ensemble as function of the number of frames and the number of particles per frame. This is necessary as frames cannot be readily split; especially after having been pruned. The choice of number of interactions per frame should be as small as possible as not to waste parts of the ensemble. The required number of frames are then added to a queue awaiting further processing. For a visual summary of this process see Figure 5.3.

To accommodate for the differences in the spectrum of the ensemble and that of the model in the given time bin, the ensemble has to be oversampled, by default by a factor of 10. Currently, only models that have a Garching energy are supported; see Equation 3.2. Future extension are easily accommodated.

Once the frame queue has reached its required size, the frames are processed and combined into a single frame that contains all events for the model time bin. For each particle a "generation" weight, $w_{\text{Generation}}$,

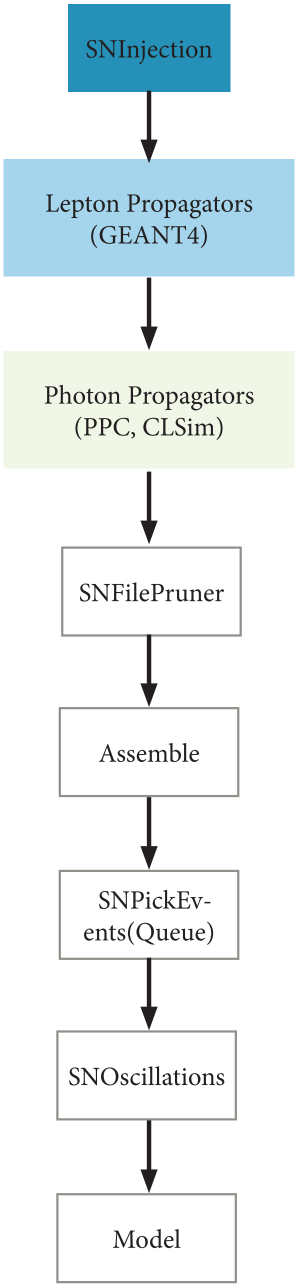

Figure 5.2: Summary of the SNPS simulation chain. After the generation of neutrino interactions using *SNInjection* the particle propagation is performed using GEANT4 and light propagation using CLSim. To construct a supernova event a subset of the pre-generated ensemble is selected by *SNPickEvents(Queue)* and a statistical weight is applied according to the model. Subsequently, *SNOscillations* calculates an additional weight according to the selected oscillation scenario.

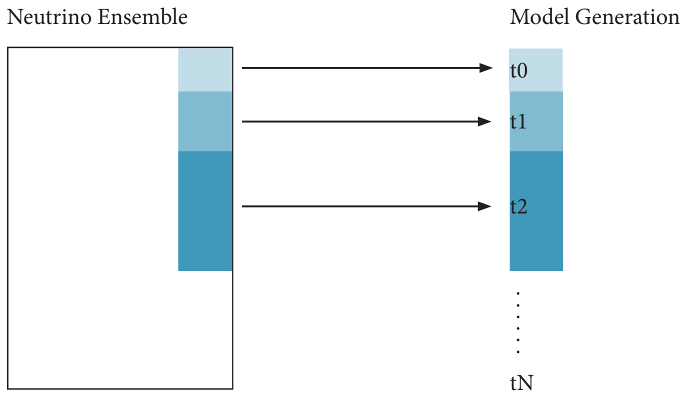

Figure 5.3: Schematic of model creation. The ensemble is divided according to required number of neutrino interactions for each time bin. The interactions in each sub-division are assigned times and weights according to the time bin they have been assigned to. The information for each individual parcels are stored in single frames. The oscillation weight can then be applied separately.

is calculated and a timestamp within the time bin is applied. $w_{\text{Generation}}$ accommodates for the shape and sampling differences between the input and model spectra and the probability that such an interaction would actually occur. The generation weight is the ratio between the number of expected interacted neutrinos from the given model with a given neutrino energy and the number of neutrinos with that energy expected in the selected subset of the neutrino ensemble. The expected number of interacted neutrinos has to be used because the interactions are forced and, as mentioned above, the ensemble would be significantly larger when using the interaction weight. In short, the generation weight requires the cross-section weighting to compensate for the fact that forced interactions are used.

Mathematically, the generation weight can be summarized as:

$$w_{\text{Generation}}(E,t) = \frac{p^{\text{Phys}}_{\text{Weighted}}(E_\nu,t)N_{\text{Int}}(t)}{p_{\text{Ensemble}}(E_\nu)N_{\text{Subset}}} \tag{5.1}$$

where

$$p^{\text{Phys}}_{\text{Weighted}}(E_\nu,t) = \frac{\sigma(E_\nu)p^{\text{Phys}}(E_\nu,\langle E_\nu\rangle(t),\alpha_\nu(t))}{\int_{E_\nu^{\text{min}}}^{E_\nu^{\text{max}}} dE_\nu \sigma(E_\nu)p^{\text{Phys}}(E_\nu,\langle E_\nu\rangle(t),\alpha_\nu(t))} \tag{5.2}$$

is the model's physics spectrum weighted according to the total cross-section for a given interaction, $\sigma(E_\nu)$, with $\langle E_\nu\rangle(t)$ being the average neutrino energy in the time bin and $\alpha_\nu(t)$ being the shape or pinch parameter in the time bin; see Section 3.4 and 4.5.1.

$$N_{\text{Int}}(t) = \frac{\mathcal{L}_\nu(t)(\Delta t) n \pi r^2 h}{4\pi d^2 \langle E_\nu \rangle(t)} \int_{E_\nu^{\text{min}}}^{E_\nu^{\text{max}}} dE_\nu \sigma(E_\nu) p^{\text{Phys}}(E_\nu, \langle E_\nu \rangle(t), \alpha_\nu(t)) \tag{5.3}$$

is the total number of interacted neutrinos given from the model and time bin, where $\mathcal{L}_\nu(t)$ is the neutrino luminosity at source, Δt is the width of the time bin, n is the particle density of the target, $\pi r^2 h$ is the volume of the selected cylinder, and d is the distance between detector and source, N_{Subset} is the total number of interactions taken from the ensemble, typically

$$N_{\text{Subset}} = \text{oversampling factor} \times N_{\text{Int}}(t) \tag{5.4}$$

and $p_{\text{Ensemble}}(E_\nu)$ being the spectral function with which the ensemble was generated. The timestamp is chosen from a uniform distribution according to the width of the time bin. This is possible because no information is provided about the time structure of the signal during that time bin. *SNPickEvents(Queue)*, by default, adjusts the time in the output frame to reflect the time that has passed since the beginning of the signal, *i.e.* the time is incremented by size of the time bin.

To produce a similar output as the USSR, *i.e.* a histogram of the total number of DOM hits in a given time bin width, several steps have to be undertaken. Initially, the time of the DOM hits (and all other times that may be relevant to an analyzer) have to be incremented by the time difference of the absolute time and time of the frame. This is necessary as the DOM hit times, particle start times, *etc.* are stored relative to the frame time. The absolute time is, by default, the start time of the first frame of the model. The total number of DOM hits for the model as a whole or in some time binning can now determined by multiplying the I3MCPE per detected event by its $w_{\text{Generation}}$ and histogram the time difference between the hit and the absolute time in the desired time binning.

The output of the USSR and *sni3sim* for a given supernova model will not be the same for several reasons. Time is defined differently in each simulation. USSR defines time as the start of the overall signal, *i.e.* when the ν_e flux begins in most models, and bins the output accordingly. Time in *sni3sim* is defined by the respective model binning. This means that for a given neutrino interaction the model output timing distribution is driven by that interactions relevant particle, for example for inverse-β decay this is $\bar{\nu}_e$.

Separate from timing differences, the ensemble is generated with neutrino oscillations in mind. For any of the relevant interactions, this means that neutrino spectrum may have a higher or lower average energy than expected from the model. The higher average energy of muon and tau (anti-)neutrinos (grouped together as ν_x in the models) compared to electron (anti-)neutrinos is the reason for this; see Section 3.4. Some of the supernova's muon and tau (anti-)neutrinos will oscillate into electron (anti-)neutrinos at the detector. This increases the average neutrino energy of electron (anti-)neutrinos. The opposite will of course also occur, *i.e.* lower average energy for the muon and tau (anti-)neutrinos at the detector. This means that ensemble for a given neutrino interaction will over predict the signal when not considering oscillations.

Oscillations Different oscillation scenarios can also be handled using an "oscillation" weight, $w_{\mathrm{Oscillation}}$. The weight compensates for the probability that a given interacted neutrino actually survived traveling through stellar matter or has oscillated to this flavor. $w_{\mathrm{Oscillation}}$ is given by

$$w_{\mathrm{Oscillation}}(E,t) = p_{\mathrm{Survival}}(E,t) + (1 - p_{\mathrm{Survival}}(E,t))\frac{\Phi^0_{\nu_\beta}(E,t)}{\Phi^0_{\nu_\alpha}(E,t)} \tag{5.5}$$

where $\Phi^0_{\nu_\alpha}(E,t)$ is the initial flux of the neutrino flavor that interacted in the detector, $\Phi^0_{\nu_\beta}(E,t)$ is the initial flux of the neutrino flavor that the detected flavor can oscillate into, and p_{Survival} is the survival probability of the interacting neutrino flavor. For an example of p_{Survival} and $\Phi^0_{\nu_\alpha}(E,t)$ see Equation 2.7 and Equation 3.3, respectively. There are only two terms necessary compared to Equation 2.10, as two neutrino approximation can be used. This is possible because IceCube cannot distinguish between individual interactions and the flux of ν_μ and ν_τ are summarized as single flavor in most models; see Section 3.4.

p_{Survival} for stellar matter is greatly dependent on the assumed density profile; see Section 2.3.3 for details. The matter shock patterns seen in theoretical supernova explosion simulations show a significantly more tumultuous matter profile, making p_{Survival} time-dependent, see [14,110,125–127] and references therein for details. Neutrino oscillations due to ν-ν interactions could occur, which alter oscillation scenario immensely. Due to these effects and possible variety of oscillation scenarios, the current implementation only considers a power-law density profile, as shown in Section 2.3.3.

5.2.2.2 Supernova Detector Simulation–SNDS

To simulate the supernova-specific detector readout, SNDS provides a conversion from the weighted per-DOM I3MCPE to supernova scalers and generation of SNDAQ-compatible input files. These tools are split into two modules, *SNUnweighter* and *SNi3ScalerWriter*. For a visual summary see Figure 5.4.

Weight Translation The weighted I3MCPEs are a statistical representation of the expected signal and not the signal itself. This statistical representation has to be converted into an expected physical signal, in short an unweighted I3MCPE, to be able to produce supernova scalers.

The translation method outlined below has to assume that the detected neutrino interactions do not produce signal on more than one DOM. This is required as every DOM has to act as an independent detector to be able to convert from a statistical construct of the expected signal to the actual signal, *i.e.* number of supernova scalers. This assumption can be made since $< 1\%$ of the signal is expected to produce more than one I3MCPE and it is a central assumption in the SNDAQ analysis.

SNUnweighter converts the weighted I3MCPEs into unweighted I3MCPEs by summing the weighted I3MCPEs in a given time bin and DOM. The sum is the Poisson average, λ, of the expected number of counts on a given DOM and time bin; see Equation 5.6.

$$\lambda_i = \sum_{j=1}^{N_{\text{I3MCPE}}} \text{I3MCPE}_j \times \left(w^j_{\text{Oscillation}}(E,t) \times w^j_{\text{Generation}}(E,t) \right) \tag{5.6}$$

Given this Poisson average per DOM, a random number of events is drawn per DOM. These events are than assigned random times uniformly within the time bin and added to a new set of I3MCPEs. The absolute timing and source information are lost. Given that the supernova scalers have a larger time bin than most supernova models, the absolute timing information is not necessary for studies with the supernova scalers. Moreover, the time binning of available theoretical models have, by IceCube standards, very large time binning which makes it impossible to establish absolute timing for neutrino interactions.

Conversion to Supernova Scalers To convert the unweighted I3MCPEs into discriminator crossings with a given timestamp, a special mode–*Discriminator Overthreshold*–was added to the IceCube DOM electronics simulation, *DOMLauncher*. It provides a time-sorted list of times for every discriminator crossing on every DOM. These discriminator crossings can than be converted into supernova scalers using *SNi3ScalerWriter*.

Initially, a histogram with 1.6384 ms wide bins is created for every DOM such that each bin represents a scaler; see Section 4.7.2. This histogram is continuously filled with discriminator crossings that are separated by at least the user-specified supernova scaler deadtime (250 µs by default). Once all DOMs have a filled histogram of the desired size, these histograms are written to a binary file and become part of a "payload". A payload of *Type 16* is pDAQ's output format for supernova scalers; see Table 5.1 for details on the format. In data, each payload has on average a total of 625 scalers (or ∼1 s in lifetime) in data. In simulation, 625 bins or scalers is the default size of the histograms.

SNDAQ currently does not support the artificial payloads produced by *SNi3ScalerWriter* when written into a single file. This violates the assumptions that are being made inside of SNDAQ when parsing payloads. SNDAQ reads in 30000 payloads or until the end of the file. Once this action is complete, the absolute time variable is incremented according to the number of payloads parsed and their length. This will cause some payloads to be dropped in simulation because these payloads are considered to be too far in the past to be considered in the analysis. This requires the *SNi3ScalerWriter* to split the supernova scalers into smaller files than produced by pDAQ. The scalers are being split into files that have ∼4 s of scalers each too accommodate this behavior.

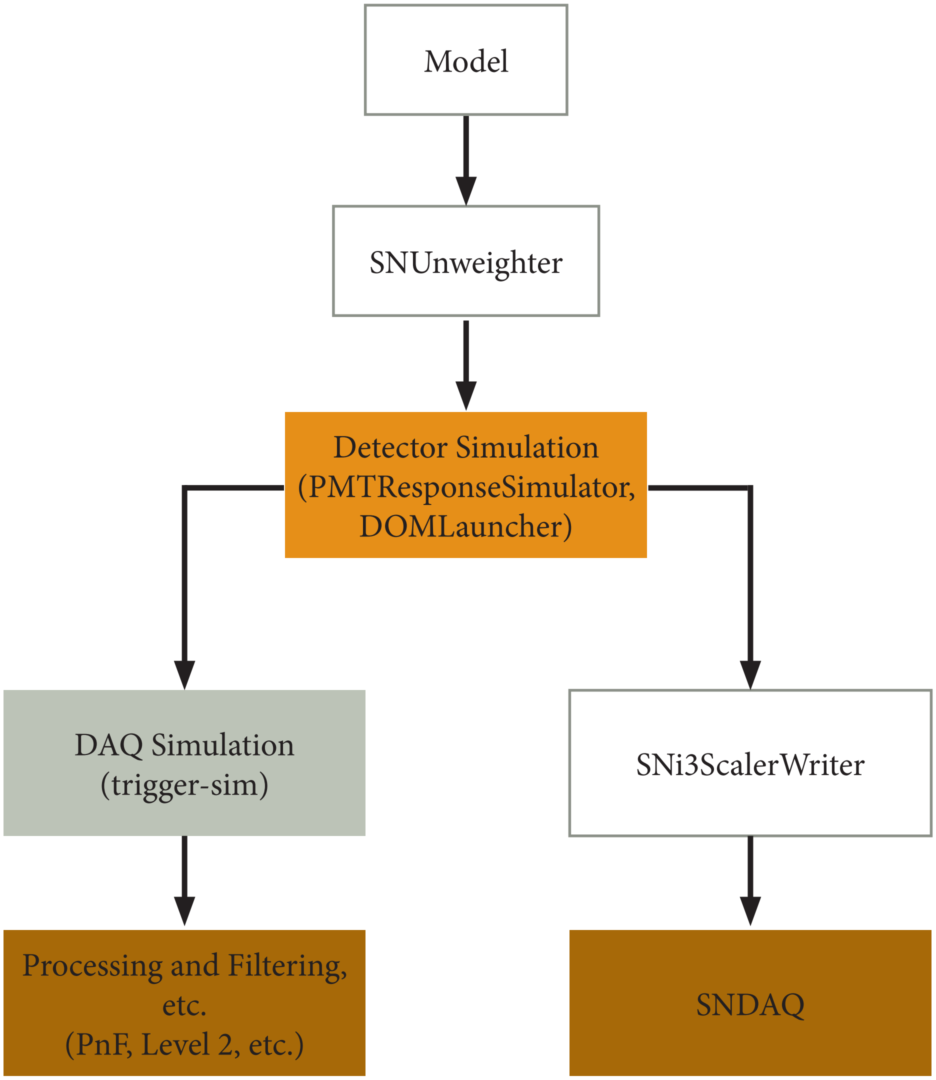

Figure 5.4: Summary of the SNDS simulation chain. The model generated from SNPS has to first be unweighted by running through *SNUnweighter*. The simulated electrical signal produced by the photoelectrons are digitized using *DOMLauncher*. The DAQ simulation will use the resulting DOM triggers into triggers and subsequently through the IceCube processing chain. Separately from the default IceCube chain, *DOMLauncher* produces timestamps for each discriminator crossings. These timestamps are then converted into supernova scalers and can be analyzed using SNDAQ.

Byte Offset	Size (Bytes)	Description
0	4	Total Length of Record
4	4	Payload Type (= 16)
8	8	Time in 0.1 ns since start of year
16	8	Mainboard ID
24	2	Scaler Record Length
26	2	Supernova Record ID (= 300)
28	6	6 least significant bits of DOM clock counter
34	$\mathrm{N}_{\mathrm{Scalers}}$	Supernova Scalers

Table 5.1: Binary file format for the supernova scaler payloads, *Type 16*, required by SNDAQ for processing. $\mathrm{N}_{\mathrm{Scalers}}$ the number of scalers for the given that are stored in this record and has a size of 1 byte each.

5.2.3 Background Simulation for sni3sim

As noted previously, the *IceSim* simulation framework does not readily support the production a continuous stream of background events. This section gives an overview of the modifications, mainly to the detector readout and event production, that were necessary to accommodate producing a continuous stream of data and the shortcomings of the background simulation in case of supernova neutrinos. The modification of the detector readout have been discussed previously in Section 5.2.2.2 with regard to an additional option in *DOMLauncher* in order to produce the timestamp for discriminator crossings on a per DOM basis.

It is currently not possible to use most of the CORSIKA or any of the *MuonGun* simulation produced for the collaboration as a whole for the background simulation in *sni3sim*. Most atmospheric muon background simulation uses weighted events. The weighting is needed for CORSIKA because CORSIKA samples the energies of its cosmic ray primaries from a power-law spectrum (E^{γ}). IceCube software, subsequently, calculates a weight for the events according to a desired cosmic ray model, hadronic interaction model, *etc.*, for examples see [36, 37, 264–267]. *MuonGun* operates in a similar fashion, as it injects muons from a given spectrum and then calculates a weight accordingly. The generated I3MCPEs are by this virtue weighted as well. The resulting weighted I3MCPEs cannot be translated into supernova scalers as the vast majority of events produce hits on more than one DOM, which violates the assumption made in *SNUnweighter*; see Section 5.2.2.2. Effects from seasonal changes to the atmospheric muon background are averaged throughout the year in current IceCube atmospheric muon background simulation ; see Figure 4.10. This makes it difficult to simulate a certain instance in time as needed to produce background for the SNDAQ analysis. IceCube simulation is typically biased towards producing events that are relatively rare and removes events that do not pass certain criteria, *i.e.* trigger threshold and preliminary data cuts. This means that a continuous stream of background cannot be produced from it.

IceCube has implemented a version of CORSIKA that allows the sampling of cosmic rays from certain cosmic ray models [264], dima-CORSIKA (dCORSIKA), named after Dmitry Chirkin [314]. This removes the need for weights when using CORSIKA background. This "natural" or unweighted spectrum can be currently used with *sni3sim*.

A coincident atmospheric background events can be produced using *I3PolyplopiaExp* from the *diplopia* project, which is used to produce background events for the search for non-relativistic magnetic monopoles, coincident atmospheric muon events, and coincident neutrino signal and atmospheric muon background events. A frame of coincident atmospheric muons with a certain lifetime is produced by accumulating unweighted atmospheric muon background that produce at least one DOM hit at a certain rate, R_μ^{Hit}. On average, $R_\mu^{\mathrm{Hit}} \approx 5.1$–$5.4\,\mathrm{kHz}$ [263] (the number varies with assumed optical properties of the ice, cosmic ray model [36, 37, 264–267], hadronic interaction model [315–318], *etc.*) as estimated from (d)CORSIKA simulation. The time differences between events is calculated according to exponential distribution with a time constant of $1/R_\mu^{\mathrm{Hit}}$.

To keep this within the computational constraints, the stream is spread across multiple frames of a given length; typically $\sim$100 ms. The atmospheric muons have to be correlated time, *i.e.* the time of the first atmospheric muon event in a frame was set by the time of the last atmospheric muon event in the previous frame. *I3PolyplopiaExp* was modified to support these correlated atmospheric muon events across frame boundaries and to produce frames with $\mathcal{O}(10$–$100\,\mathrm{ms})$.

The time window of the frame is not exactly the requested length. The window has to be extended to compensate for the detector readout effects; see Section 4.8. This makes it necessary to add 20 μs time padding and the time span of the last atmospheric muon in the frame at the end of the frame. If the extra time were not added the last atmospheric muon event would only be readout partially or not at all, as the DAQ simulation works on a per frame basis and not on a stream of data.

The improvements to the DOM noise simulation outlined in [253], *i.e.* addition of correlated noise, were crucial to be able to perform this simulation. The previous noise simulation, *noise-generator*, only produced Poisson noise with a rate given by the SLC rate and after-pulsing behavior for the DOM; see Figure 5.5. This would have over predicated the contribution of the DOM noise to the supernova scalers. The SLC rate for a DOM includes non-Poissonian behavior which is mostly removed by the supernova scaler deadtime; see Section 4.4.1 and Figure 4.4. Estimating the Poisson rate from the SLC rate of the DOMs would have over-predicated the Poisson noise rate and would have caused an unphysical increase in the relative contribution

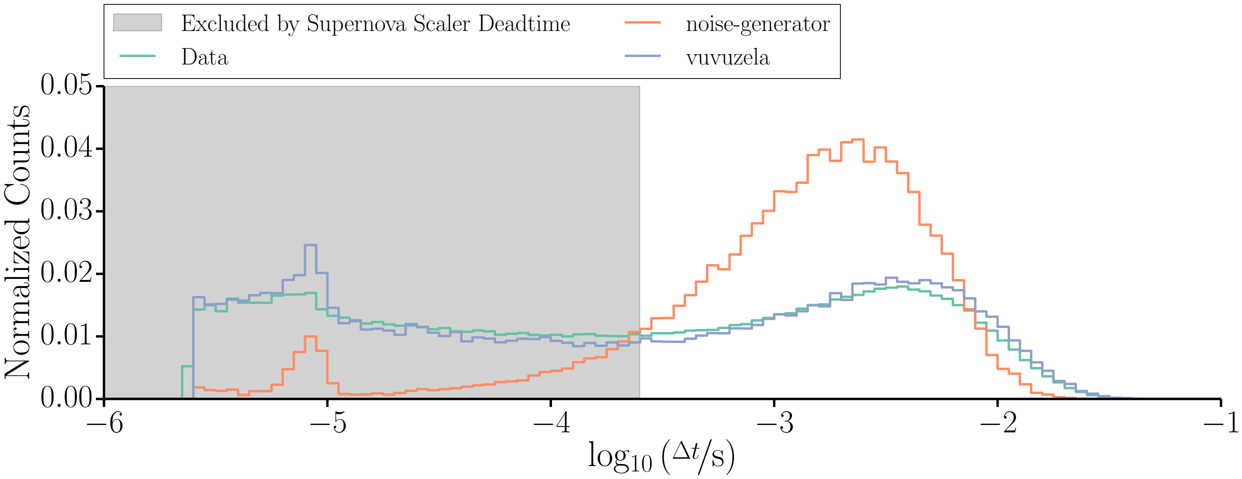

(a) Noise distribution in terms of the $\log_{10}(\Delta t)$ for DOM 21-01. *vuvuzela* is much closer representation of the data distribution compared to *noise-generator* for this DOM.

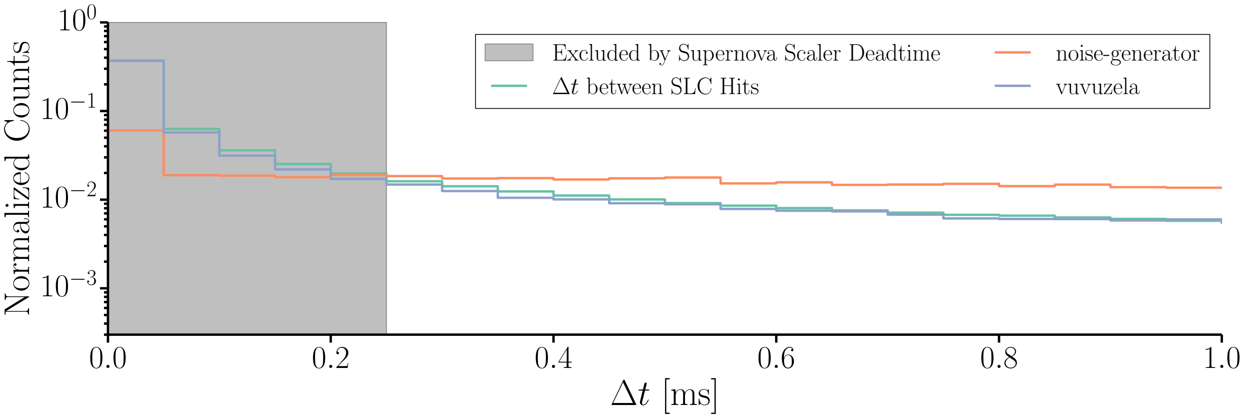

(b) Distribution of time differences, Δt, between in individual photoelectron detections for data and simulation on DOM 21-01 up to a difference in 1 ms. *noise-generator* does not produce any of the correlated noise behavior and would over-predict the contribution of DOM noise to the supernova scalers.

Figure 5.5: Comparison between data and different noise generation techniques. *vuvuzela* is much closer to the data for distribution compared to *noise-generator* for this DOM. Without the using *vuvuzela*, the DOM noise contribution to the supernova scaler rate would have been artificially increased. The non-Poisson behavior of the noise artificially increases the SLC rate used in *noise-generator*. The peak on the left side of the *noise-generator* is the after-pulsing behavior of DOMs. This simulation has been moved into *PMTResponseSimulator*. The top plot uses $\log_{10}(\Delta t)$ distribution instead of Δt used in Figure 4.4 and 5.5b to show the difference between the noise generation techniques over the whole range of Δt more clearly.

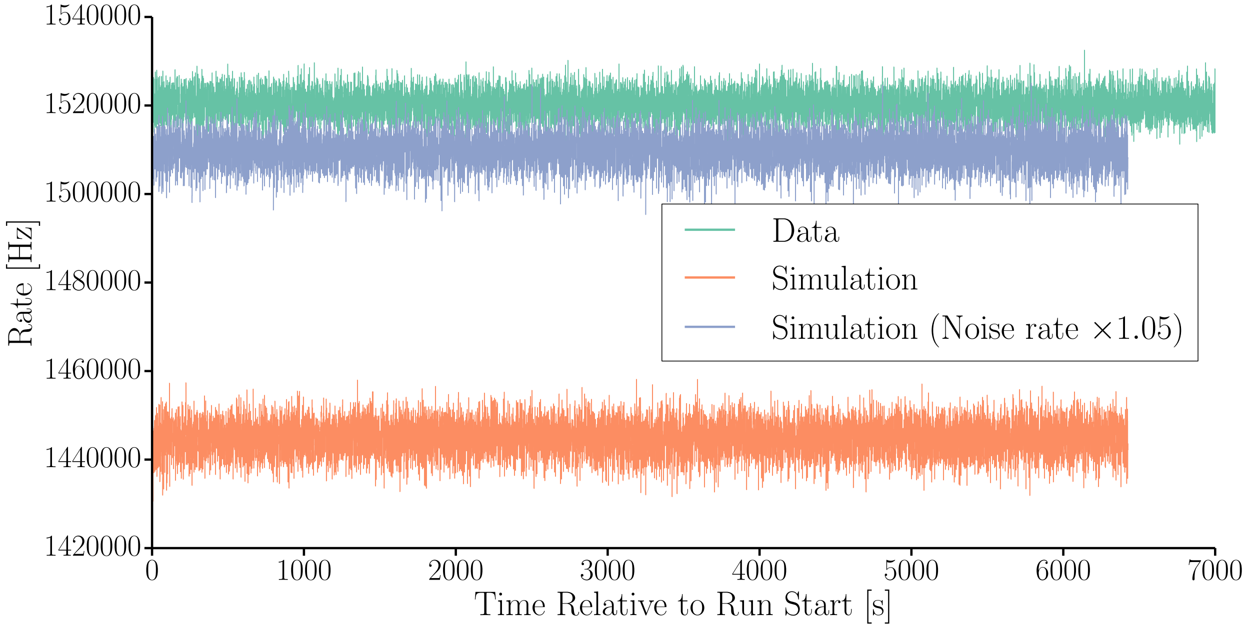

Figure 5.6: Comparison in the noise rates per SNDAQ analysis 0.5 s time bin between data and simulation. The noise rates have to be scaled by 1.05. *i.e.* 5%, to roughly match simulation and data. The distributions appear comparable otherwise.

of the DOM noise to the overall supernova scaler rate and decreased relative effect of atmospheric muons on the SNDAQ analysis.

The DOM noise produced by *vuvuzela* had to modified as well. Instead of providing noise photoelectrons in a timespan centered on an event, the noise is being produced from the start to the end of individual frames; making it a mostly continuous stream. It is not a perfectly continuous stream as the noise between frames is not statistically correlated, as it would be in reality. This does not have a measurable effect on the overall noise rate though. Additionally, the Poisson rate, *i.e.* rate of radioactive decays and thermal noise, had to be scaled by 5% in order to achieve a $< 1\%$ agreement between the average rate in data and simulation; see Figure 5.6. The remaining $< 1\%$ are due to DOMs that are being considered in the SNDAQ analysis, but not in simulation. The discrepancy is due to the difference in noise simulation and data, which trigger SNDAQ's quality cuts.

The detector simulation is reset at every frame transition. This means that the influence of large light deposition on individual DOMs is not fully considered. They can cause a $\mathcal{O}(1\,\mathrm{ms})$ recovery in the discriminator level. As these events are relatively rare and the effect on the overall simulation is negligible.

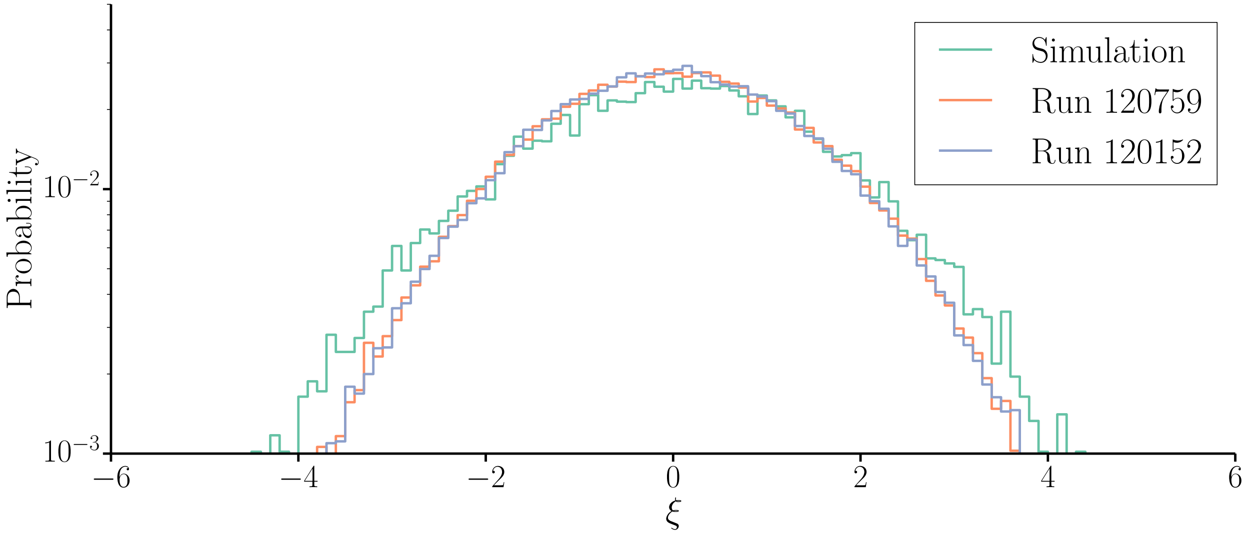

Figure 5.7: Comparison in the significance distribution between data and simulation. The width of the significance distribution indicates sensitivity to atmospheric muons; see Section 6.1. The distribution in simulation is significantly wider than in data, 1.63 versus 1.45, respectively. This means that the simulation is more sensitive to atmospheric muons. This is unexpected as the atmospheric muon trigger rate is generally lower by ∼10% in simulation compared to data. Separately, the distribution shows a trend towards under-fluctuations, as the widening is much more prominent on the left side of the distribution compared to the right side.

The simulated background appears to be more sensitive to the atmospheric muon background than data. This is indicated by a wider significance distribution in simulation compared to data in Figure 5.7; see Section 6.1 for the relationship between the significance distribution and the atmospheric muon background.

This higher sensitivity also appears in the relationship between the variance and the mean of DOM noise distribution in terms of the Fano factor, $F = \frac{\sigma^2}{\mu}$ [51]; see Figure 5.8. The data has a decreasing F as a function of depth. This is to be expected as the atmospheric muon flux decreases significantly as a function of depth; see Figure 5.9. The simulation shows a flatter trend in F with depth. This means that atmospheric muons have a more uniform contribution throughout the detector, which in turn causes the higher sensitivity to atmospheric muons at depth.

There are several possible explanations for why there is a discrepancy in between data and simulation. The most likely explanations are an artificially high atmospheric muon rate in simulation, the noise simulation relying on the atmospheric muon simulation to estimate the atmospheric muon contribution to the per-DOM

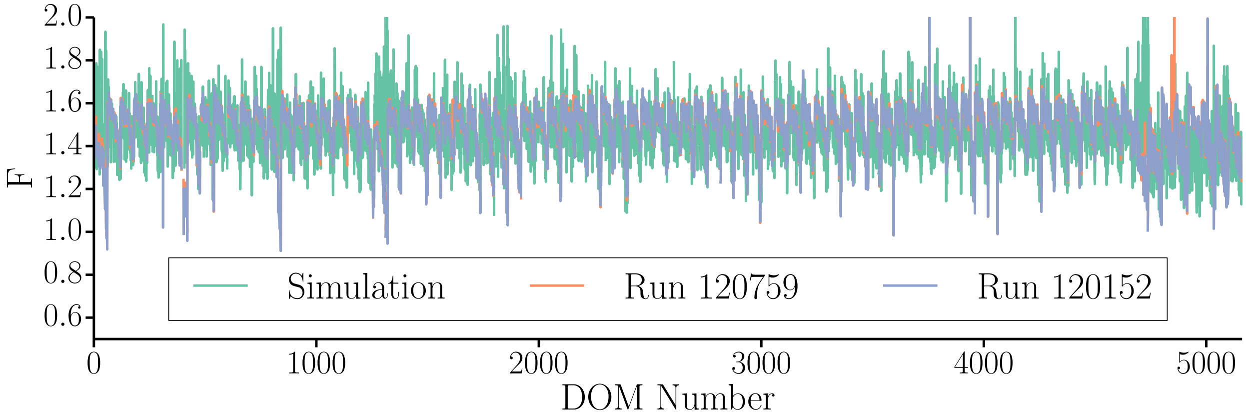

(a) Comparison of the Fano factor for all DOMs in the detector between data and simulation. Simulation shows a much larger spread in Fano factor across the whole detector. The depth effect seen in data is not as clearly represent in simulation.

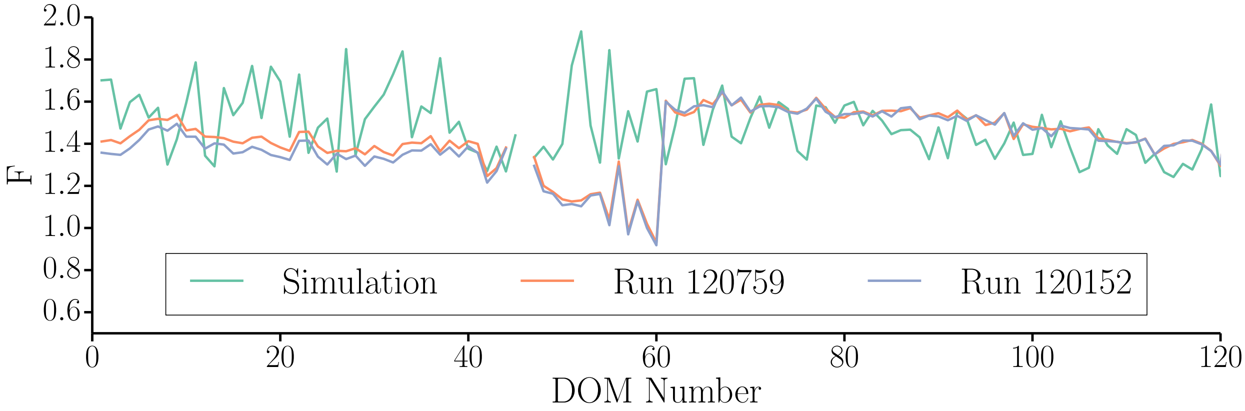

(b) Comparison of the Fano factor for the first 120 DOMs in the detector. The Fano factor does not show the same dependence in simulation as it does in data. The detector is apparently much more uniform in simulation. Alternatively, the DOM-by-DOM behavior shows more structure in simulation then it does in data.

Figure 5.8: Comparison of the Fano factor, $F = \frac{\sigma^2}{\mu}$, for all DOMs (top) and for the first 120 DOMs (bottom) in the detector between data and simulation. The DOM number is given by the location in the detector, such that DOM 1 on String 1 is DOM Number 1 and DOM 1 on String 2 is DOM Number 61. DOM 1 on every string is at the top at a depth ∼1450 m and DOM 60 at the bottom at depth of ∼2450 m. The Fano factor in simulation does not show the same depth dependence as data. The atmospheric muons appear to have a more uniform effect on the detector. This would explain why the significance distribution experiences a larger effect from atmospheric muons.

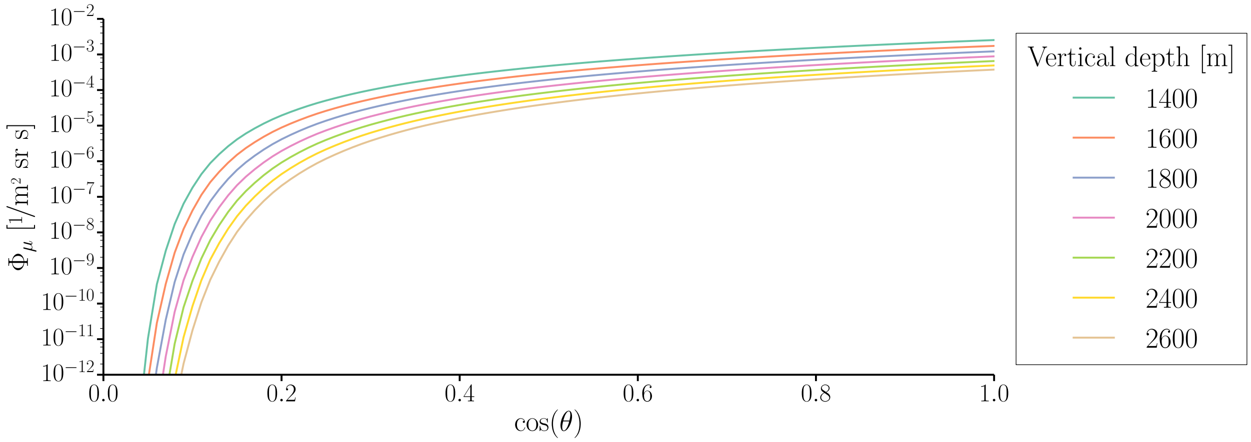

Figure 5.9: Single muon flux a function of the cosine of the zenith angle, θ, for various depths in ice as predicted by CORSIKA for a atmosphere in July. Credit: Jakob van Santen [48]

SLC rate and the detector simulation to estimate the atmospheric muon contribution, and that the noise simulation is not accurate at producing noise over such long time windows, *i.e.* $\mathcal{O}(100\,\mu\mathrm{s})$ versus $\mathcal{O}(100\,\mathrm{ms})$.

The atmospheric muons cannot cause this effect as the SMT8 trigger rate is 10–20% lower compared to data. This lower SMT8 trigger rate is expected as CORSIKA, the hadronic interaction model (SIBYLL [315]), and the cosmic ray model (Hörandel [264]) cannot fully describe the interaction of high energy cosmic rays that occur in the atmosphere needed to produce the atmospheric muons seen in IceCube. Additionally, only ∼1–10% of the per DOM rate can be attributed atmospheric muons. This means that the DOM noise simulation has a discrepancy that is mostly responsible for this effect. Similarly, the simulation was used for background estimates for the search for non-relativisitc monopoles and revealed a ∼40% lower trigger rate (8 Hz in simulation versus 13 Hz in data) in simulation compared to data.

As mentioned above, the atmospheric muon simulation is known to be inaccurate for the cosmic ray interactions detected by IceCube. This means that the atmospheric muon contribution to the noise rate is underestimated when determining the noise parameters. This is does not have a large on effect the noise rate itself, as only a small fraction of the noise rate can be attributed to atmospheric muons; see Section 6.1. It has a larger effect on the variance on noise rate, as the variance of the supernova scalers is ∼15% higher than expected from a Poisson process.

The current noise simulation assumes that the radioactive and thermal noise are both Poisson processes; see [253]. For short time windows, sampling from a Poisson distribution is necessary and sufficient. A Gaussian distribution, for example, would not describe the data properly, as there would be partial and/or a negative number of events. If the Poisson distribution is sampled more often the discrepancy with a Gaussian distribution becomes apparent. The supernova background simulation is sampling the noise distribution orders of magnitude more often than a typical IceCube background simulation. This means that difference in variance between Poisson and Gaussian become increasingly important.

To make a better comparison between data and simulation, SNDAQ-compatible scalers have to be produced from *Hit-spooling* data. These scalers are still artificial, as they are based off *DOMLaunch*es rather than discriminator crossings. The *DOMLaunch*es have a much smaller deadtime compared supernova scalers (∼2.5 µs versus 250 µs). This will only cause a ∼1% difference [297]. The scalers can then be compared to data directly, as there is no dependence on CORSIKA simulation and difference in the atmospheric muon flux because of different atmospheres.

It is also necessary to check whether the assumption of Poissonian noise is correct. To do so, the noise parameter fitting should be performed assuming a Gaussian or log-normal noise rate distribution. This may appear unphysical, as the underlying processes (thermal and radioactive noise) are known to be Poissonian in nature. The effect of atmospheric muons, correlated noise, PMT sensitivity, and possible effects due to noise photoelectron distribution, *i.e.* a noise photoelectron may not always be exactly one photoelectron, may distort the noise distribution measurably. Using a Gaussian or log-normal distribution may therefore provide a better description than a Poisson distribution.

An additional effect may be the time constraint that *vuvuzela* puts on the noise generation. Currently, *vuvuzela* does not produce noise hits with a Δt less than the SLC launch deadtime (∼2.5 µs). There are of course noise photoelectrons during that time period. These noise hits would have a small effect on the supernova scalers as the deadtime should remove them. There are currently attempts on the way to characterize and simulate these noise events.

In case the background simulation is still not comparable to data after further investigation, *Hit-spooling* data and supernova scaler can be used as a background. This does not provide the information or control, for example not being able to remove the atmospheric muon background, that simulation does. It does provide the largest amount of information available in data. Adding the supernova simulation to *Hit-spooling* data, does provide a mean to test the effect of background subtraction techniques on the supernova analysis. The scaler stream can be reproduced from the *Hit-spooling* data. The resulting data can be triggered, processed, and analyzed through the same steps as the normal data.

5.3 Comparison to Previous Simulations

As with any new simulation, the new expected detector response has to be compared to the one of the previous simulation. Given the changes to the cross-sections, lepton propagation, light propagation, ice models, detector sensitivity, and detector geometry, the simulations are expected to give results that are

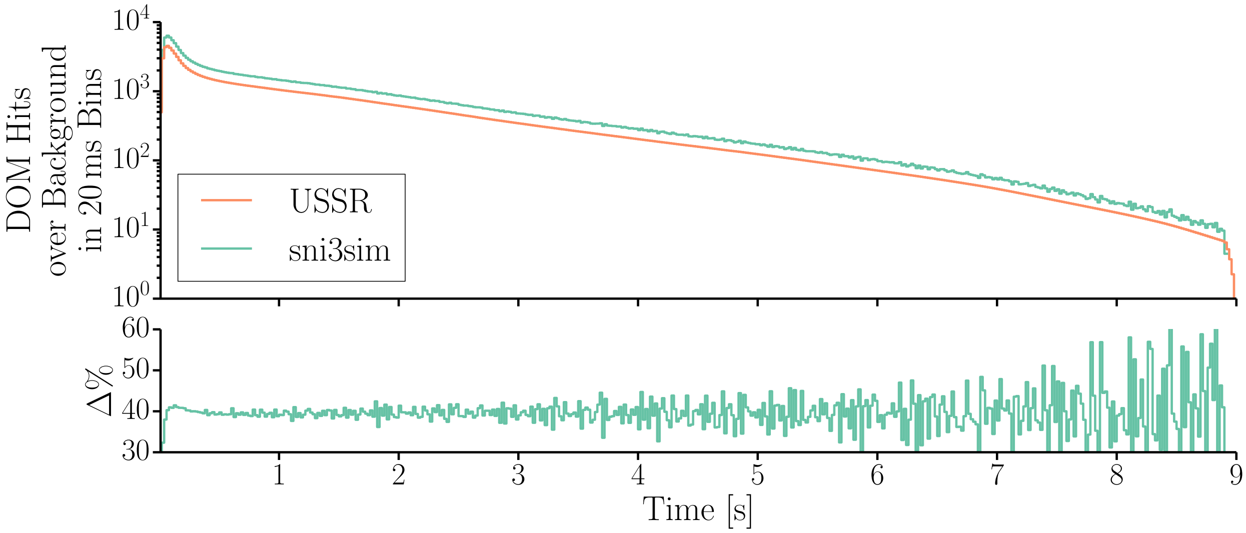

(a) Comparison between USSR and *sni3sim* results for a supernova according to the Garching model from Figure 3.8 and [24] at 10 kpc.

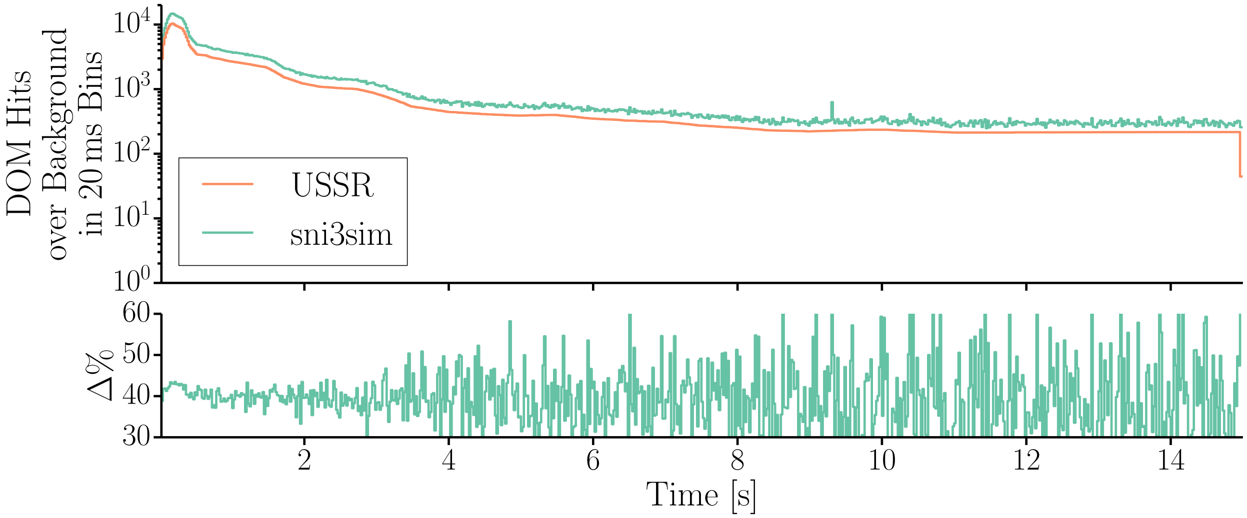

(b) Comparison between USSR and *sni3sim* results for a supernova according to the Lawrence-Livermore model from Figure 3.7 and [22] at 10 kpc.

Figure 5.10: Comparison between the expected signal over background as estimated from USSR and *sni3sim* for models given by [22] and [24] at 10 kpc. The plots shows the expected number of DOM hits over the background and the residual between the two methods, respectively. Since both models average out to a residual on the ∼40% level, the difference can be attributed to systematic difference between the simulations.

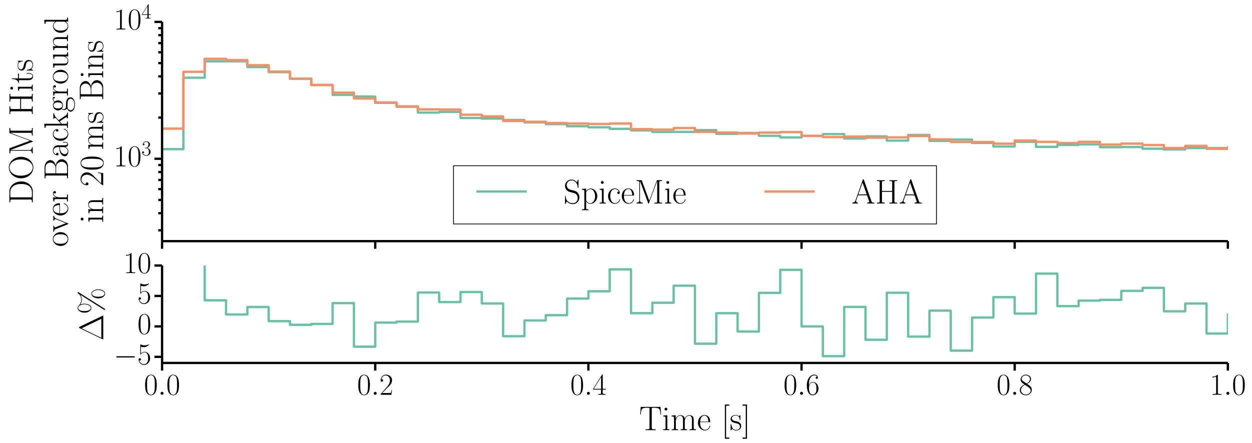

(a) Comparison between results for the event-based simulation for a supernova according to the Garching model from Figure 3.8 and [24] at 10 kpc using the Spice Mie and AHA ice models.

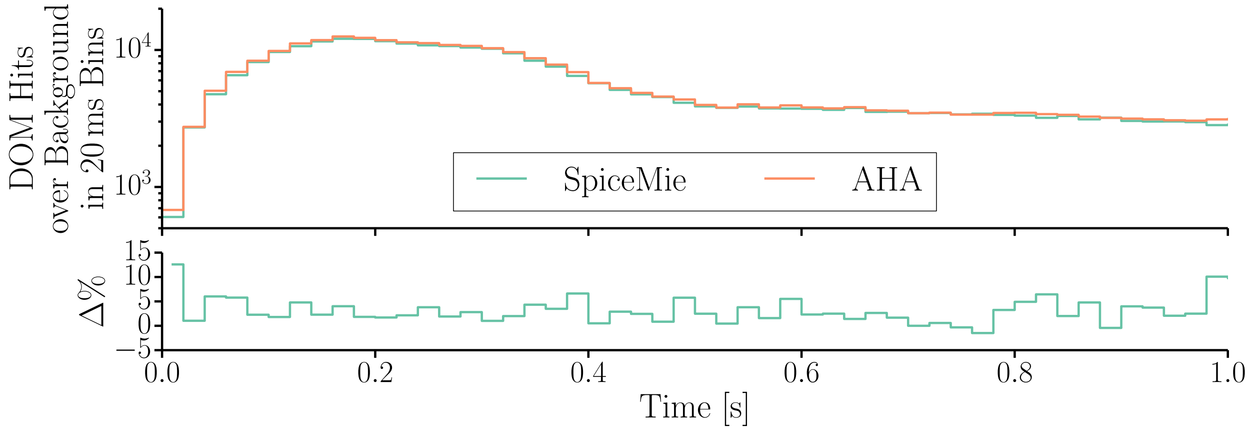

(b) Comparison between results for the event-based simulation for a supernova according to the Lawrence-Livermore model from Figure 3.7 and [22] at 10 kpc using the Spice Mie and AHA ice models.

Figure 5.11: Comparison of hits over background from Lawrence-Livermore and Garching model for an event-based simulation. The difference between residual between the two curves shows the effect of different ice models on the result of the simulation. On average the difference for either supernova model is ∼3%.

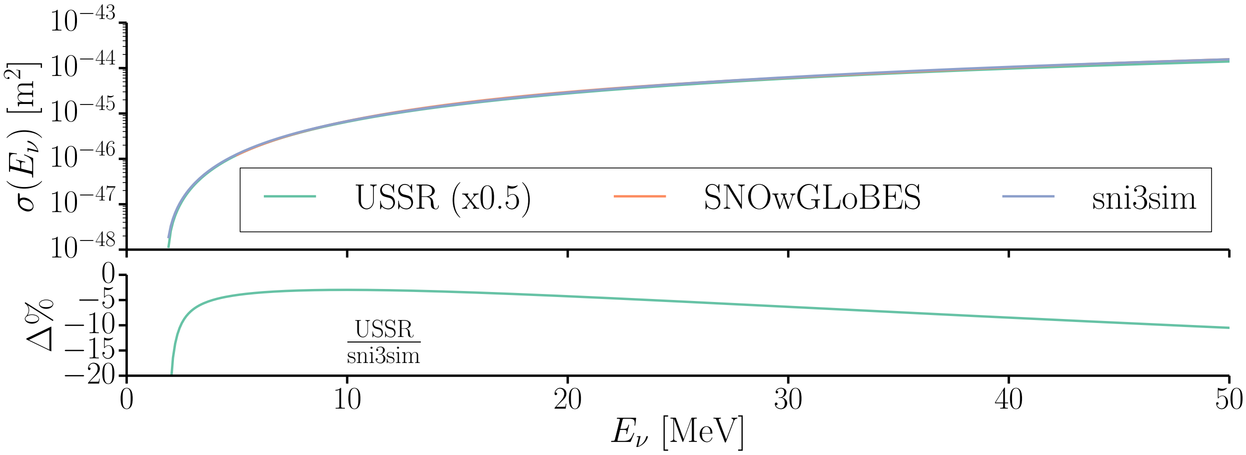

Figure 5.12: Comparison of the inverse β-decay cross-sections between USSR and *sni3sim*. The region of most interest (10 MeV–30 MeV) is different on the order of 5%. The difference between the two models is increasing with energy because of the different implementations of the two cross-sections calculations. For independent comparison the cross-sections used in supernova neutrino simulation package for future long-baseline neutrino oscillation experiments, code-named *SNOwGLoBES* were added to the plot; see [49].

offset by a certain percentage. Additionally, the parametric approach employed in the USSR removes some of the statistical features that are to be expected from such a large signal.

Overall, the differences between the two simulations for the tested models are at the level of ∼40%; see Figure 5.10. These models were selected because they represent a model based on SN1987A, one for a lower mass star, and both provide the cooling phase of the star. The difference arises mostly due to changes in the detector geometry, ice models as well as DOM sensitivity (∼3%), new inverse β-decay cross-sections (∼5%), no time interpolation of models and different definition of time (∼5%), removal of supernova scaler deadtime (∼10%), and different neutrino generation spectrum (∼20%).

The difference between ice models have already been explored before; see Section 4.6.1. In simulation the average difference is only ∼3%; see Figure 5.11. This is mostly because of changes in the geometry as the USSR does not simulate the location of DeepCore strings properly and the number of high quantum efficiency DOMs. These changes are model-dependent as closer spacing of DOMs and the increased interaction of neutrinos compensate each other. The large difference previously seen in Figure 4.17 were mostly due to effects in the dust layer and top of the detector.

The new cross-section implementation using the derivation in Section 4.5.1 produce a ∼5% effect. This difference arises mostly because USSR underestimates the cross-sections; see Figure 5.12. This will have

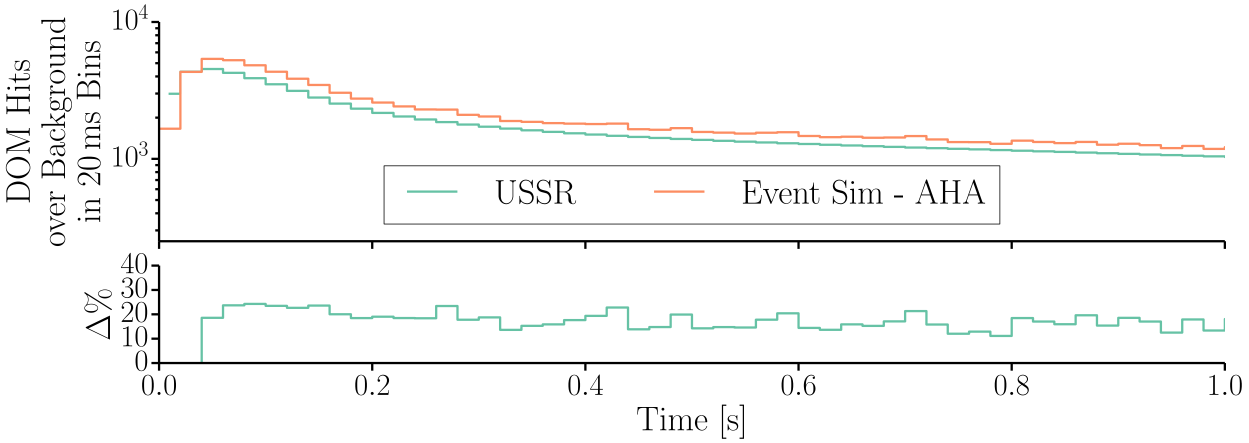

(a) Comparison between USSR and event-based simulation results for a supernova according to the Garching model from Figure 3.8 and [24] at 10 kpc.

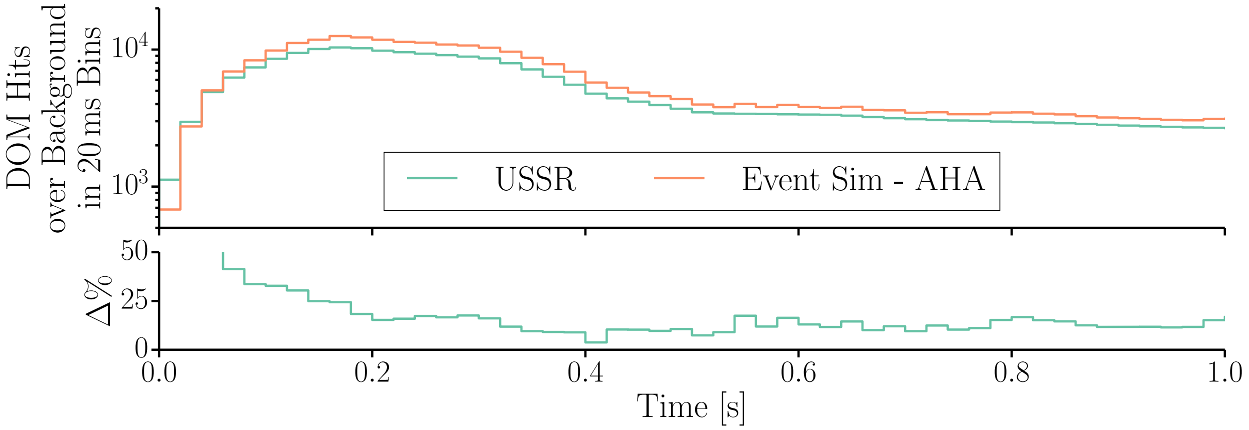

(b) Comparison between USSR and event-based simulation results for a supernova according to the Lawrence-Livermore model from Figure 3.7 and [22] at 10 kpc.

Figure 5.13: Comparison of hits over background from Lawrence-Livermore and Garching model for USSR and event-based simulation. The comparison shows the effect of the different photon propagation, lepton propagation, supernova scaler deadtime, and detector geometry. The effect for the Garching model is amplified because there is different definition of the start time of the model. This causes an aliasing effect, which can be especially seen in the first several bins of the model.

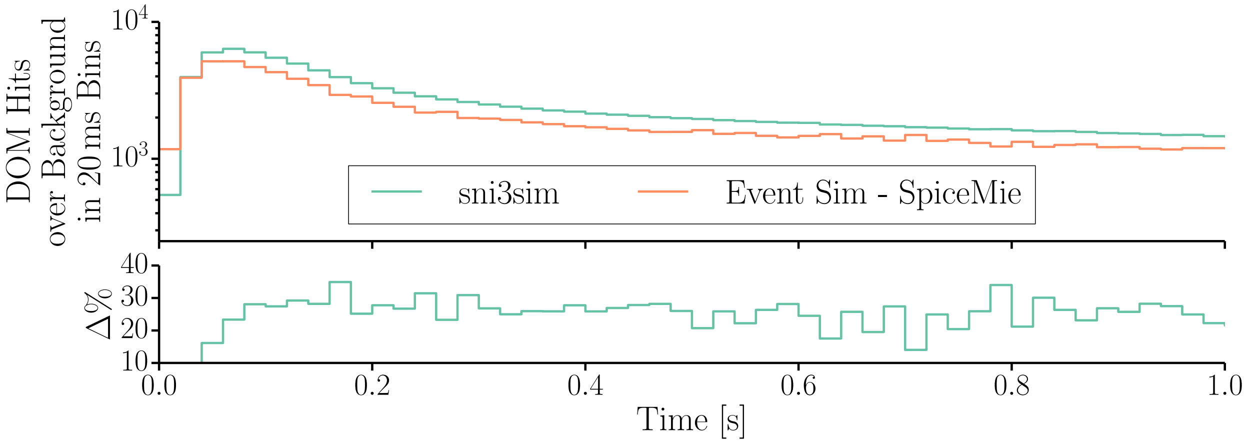

(a) Comparison between *sni3sim* and event-based simulation results for a supernova according to the Garching model from Figure 3.8 and [24] at 10 kpc using the Spice Mie ice model.

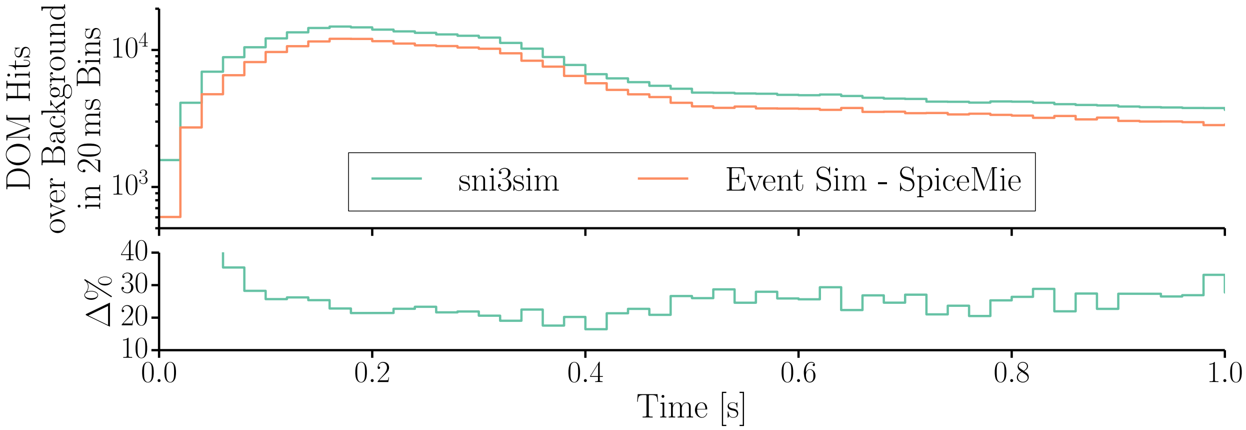

(b) Comparison between *sni3sim* and event-based results for a supernova according to the Lawrence-Livermore model from Figure 3.7 and [22] at 10 kpc using the Spice Mie ice model.

Figure 5.14: Comparison of hits over background from Lawrence-Livermore and O-Ne-Mg Garching model for an *sni3sim* and event-based simulation. The difference between the two approaches for both supernova models is ∼25%. This difference can be accounted for by the improved cross-sections; see Figure 5.12, and the change in the average energy of the spectrum ∼20%.

a direct effect on the number of events that are selected, as the number of interacted neutrinos is directly proportional to the cross-sections; see Equation 5.1.

A ∼5% effect is caused by the difference in time interpolation and different definition of time; see Figure 5.13. Time in the USSR is defined according to the start of the model, while *sni3sim* defines time as the start of the respective neutrino signal. USSR and *sni3sim* also use different interpolation schemes, which add to the overall effect.

USSR includes the supernova scaler deadtime in its estimate. This lowers the expected signal from USSR by ∼10%, as it depends on the size of the signal. *sni3sim* does not include the supernova scaler deadtime, as it is applied during scaler conversion; see Section 5.2.2.2. Additionally, to simulate the detector response outside of the supernova scalers this deadtime has to be removed.

One of the largest effects is due to the differences in the neutrino energy spectrum; see Figure 5.14. The difference of ∼20% is mostly due to a shift in the average energies, *i.e.* 12.5 MeV versus 15 MeV. This is necessary to accommodate a possible neutrino oscillation scenarios. For example for $\bar{\nu}_x$ to $\bar{\nu}_e$, the $\bar{\nu}_e$ flux will have a higher mean energy as they were produced as $\bar{\nu}_x$ inside the supernova and $\bar{\nu}_x$ have a higher average energy; see Figure 3.8. These oscillations will have the largest effect on the signal because of the dominance of inverse β-decay. The difference nearly directly translates into the difference in signal because of approximate proportionality between the product and neutrino energy; see Equation 4.9. This in turn means causes a proportional increase in the photon production yield and thereby increases the higher probability of detection; see Equation 4.20.

5.4 Possible Studies

sni3sim enables the study of signal and background under controlled conditions. Under these circumstances, one can expand upon the possible physics results from the search for supernova neutrinos in IceCube and explore new signals that the supernova analysis would be sensitive to.

5.4.1 Compact Object Mergers

Compact Object Mergers (CMOs) are the merger between two compact stellar objects, such as neutron stars or black holes. These mergers will produce an accretion disk that produces a neutrino flux with an energy of $\mathcal{O}(10\,\mathrm{MeV})$ and luminosity of $\mathcal{O}(1\text{–}10 \times 10^{53}\,{}^{\mathrm{ergs}}/_{\mathrm{s}})$ over $\mathcal{O}(10\text{–}100\,\mathrm{ms})$ timescales [319–322]. This is comparable to a very short burst of a galactic core-collapse supernova signal. Hence detecting such and event in our galaxy with IceCube is a strong possibility. Depending on the energy spectrum, IceCube's capabilities could go well beyond the galaxy ($\mathcal{O}(100\,\mathrm{kpc})$), as oxygen cross-sections begin to dominate at neutrino energies $\geq 60\,\mathrm{MeV}$; see Figure 4.13.

The possibility of detection such an event is minimal. The rate of these events is orders of magnitude lower then that of a core-collapse supernova [323–325]. Even with the low probability of detection, the largely unconstrained nature of the signal is worth studying in simulation and searching for in data. *sni3sim* is able to provide the means to study a possible detector response, as it includes the possibility to generate large samples of $\mathcal{O}(10\,\mathrm{MeV})$ with a given spectrum and adjust these according to theoretical models.

CMOs in the reach of IceCube and beyond ($\sim\mathcal{O}(100\,\mathrm{Mpc})$) would also produce detectable signatures in current and future gravitational wave observatories, such as the Laser Interferometer Gravitational-Wave Observatory (LIGO) and future Advanced LIGO [325–331]. This means that IceCube has an external trigger for these events. A similar approach was already used in [332]. Even if the average neutrino energy or flux were lower than predicted, IceCube still has a chance to observe these events and show a possible observation of these events using an external trigger

5.4.2 IceCube-specific Studies

Integrating the supernova simulation into *IceSim* opens the doors to answer multiple open questions: physics capabilities of *Hit-spooling*, exploring new background reduction techniques, and detector response in different data channels. Answering these questions will improve the understanding of the detector and IceCube's ability understand the supernova neutrino signal.

Hit-spooling was added as a means to store an untriggered waveform data stream for several hours; see [297] for details. The data is permanently stored in case of a high significance (currently $\xi \geq 7.65$) event in the supernova scaler stream. It still remains open how the extra information could be used besides the methods explored in [248] to find the average neutrino energy. *sni3sim* provides both the supernova scaler stream and waveform data stream, which make it possible to correlate the supernova scaler response to the waveform response. Work currently on the way will try to determine the neutrino mass from combining *sni3sim* simulation with available *Hit-spooling* data for background. Future work would also explore methods how to distinguish noise waveforms events from supernova events.

Atmospheric muons are one of the major backgrounds to the current online analysis; see Section 6.1. Current atmospheric muon background reduction methods outlined in [47, 298] rely on the assumption that the relatively short trigger and readout window of the SMT8 trigger does not remove a significant portion of the signal from the scaler stream; see Section 6.1 for more details. To first order this assumption appears to be valid as the probability of a supernova signal causing a SMT8 triggers or producing HLC hits is small. The question remains though how much of the signal could possibly be removed through this reduction method. This is especially of concern for close-by supernovae, as the signal scales with d^2; see Equation 4.1.

There are no means to test how much signal a new atmospheric muon background reduction method would remove from supernova scaler stream for a given supernova model. Separately, a study of the impact of current atmospheric muon background reduction techniques would yield a measure of response of trigger rates and properties, *i.e.* number of SLC and HLC hits in the trigger window, for a given supernova signal.

Hit-Spooling opens the doors to new online background techniques independent of triggers or other processing. A method to identify atmospheric muons below the trigger threshold is explored in [297]. To apply this method the online analysis would require testing this method on a simulated supernova signal.

The supernova scalers currently do not consider whether a discriminator crossing is associated with the HLC condition of a DOM. HLC was implemented as a means to reduce noise events in the detector and distinguish signal from noise. This means that one could produce a scaler stream with discriminator crossings that were associated with HLC hits removed, *i.e.* HLC-less supernova scalers. Supernova scaler-like output can be produced from *Hit-Spooling* as shown in [297]. These scalers were produced independent of whether a hit was HLC or SLC. By removing the HLC hits from the stream, one should be able to reduce the impact of atmospheric muons on the analysis. This method however requires a thorough study of the HLC rate behavior during an actual supernova signal.

Besides background reduction techniques, new or improved supernova search algorithms, especially using *Hit-spooling* data, could be explored using the simulation. One possible solution is to include a measure of inter-dependence between DOMs into the likelihood, *e.g.* HLC rate without random coincidences. This method would however require a study from data and simulation. Separately, one can explore the effects of non-paralyzing and paralyzing deadtime as well as different deadtimes on the background contamination and on the signal [14, 112, 120, 295].

Chapter 6

Analysis

6.1 Understanding the Increasing Number of False Positive Triggers

Over the course of the first three detector physics runs of the completed IceCube detectors (IC86-2011, IC86-2012, and IC86-2013), the frequency and supernova significance, ξ, of false positive supernova alerts has risen; see Figure 6.1 and Table 6.1. A similar trend had been previously observed by [47] for the 40-string through 79-string detector configurations (IC40, IC59, and IC79). The increasing effect of atmospheric muons for the partial detectors had been attributed to increased size of the detector, as the atmospheric muon sensitivity scales with detector size. The large differences between years of the completed detector has yet to be fully investigated, as the detector is assumed to be stable with time.

Atmospheric muons are considered the main cause of false triggers as ξ is correlated to the atmospheric muon hit rate as shown by [47]; see Figure 6.2a. On average, a higher number of atmospheric muon hits are registered during the time periods where a false positive alert occurs. A correction of this effect, as outlined in [47] and exemplified in Figure 6.2, produces an atmospheric muon-corrected significance, ξ', with the expected properties of ξ, *i.e.* Gaussian-distributed with $\mu = 0$ and $\sigma = 1$. There has been a more thorough investigation of one of the highest significance events in [333]. This work revealed that the noise rate increased fairly uniformly throughout the detector, there were no extremely high-energy muon events, and there was no particular direction for the atmospheric muon events.

An alternative method to remove the atmospheric muon contamination is to subtract the “NChannel”, an energy proxy for atmospheric muons using the number of channels that were associated with a triggered event, from the scalers as done in [298]. The atmospheric muon contamination is removed by repeatedly selecting a random DOM and subtracting one supernova scaler from the selected DOM until all atmospheric muon hits from the DST NChannel are accounted for. This means for an event with an DST NChannel of 12, 12 random DOMs will be selected and one scaler will be subtracted from each.

Atmospheric muons affect the analysis because the likelihood assumes that each DOM is independent; see Section 4.9. Atmospheric muons on average produce noise that is DOM-to-DOM correlated, *i.e.* a given muon produces hits on multiple DOMs as it travels through the detector. This DOM-to-DOM correlated

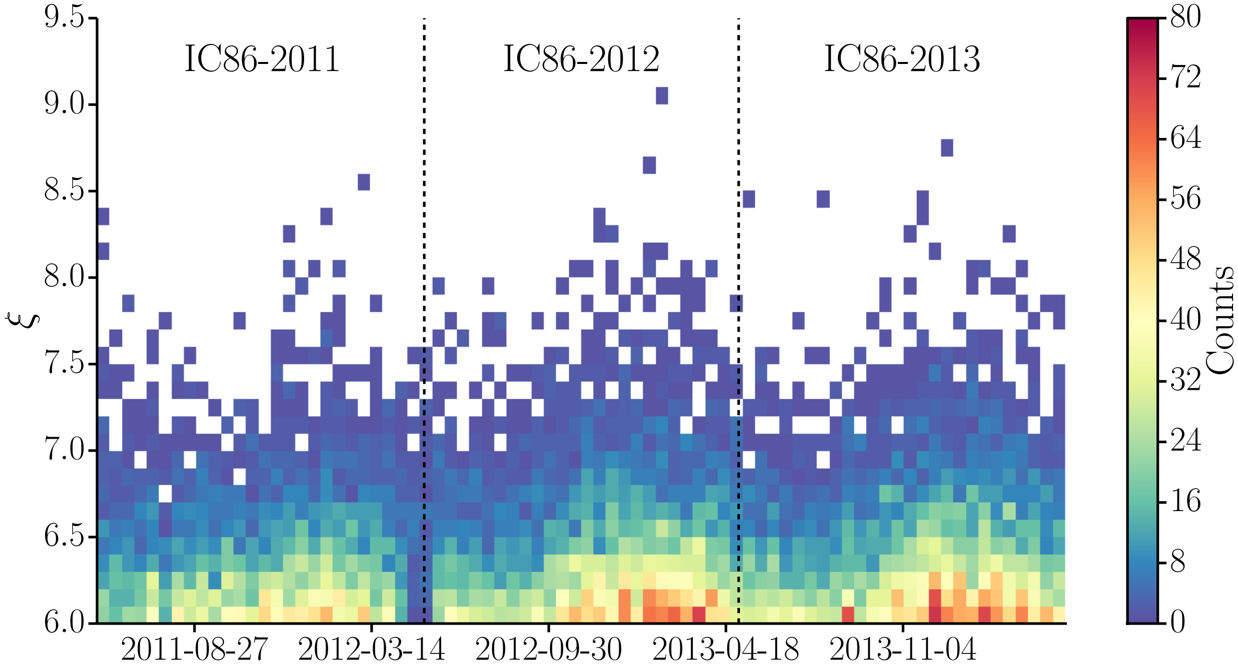

Figure 6.1: The number of events above trigger threshold for the SNDAQ analysis versus time for IC86-2011 through IC86-2013. The threshold is set to a supernova significance, ξ, ≥ 6.

noise will produce an higher then expected number of DOMs over a certain threshold, hence artificially increase $\Delta\mu$ in Equation 4.25; see Figure 6.3.

The seasonal variation of the atmospheric muons, will also produce a seasonal-dependence on sensitivity of the SNDAQ analysis; see Figure 4.10, 6.1, and 6.5. The seasonal variation in atmospheric muons is caused by a shift in the energy spectrum of atmospheric muon; see Figure 6.4. On average, more DOMs are involved in a given trigger. This means that the average DOM rate and the DOM-to-DOM correlation caused by the atmospheric muons will change with the seasons.

The two best explanations for the increase in the false positive trigger rate and significance are a long-term changes in either the nature of the atmospheric muon background or a systematic change in the detector noise baseline. IceCube has already observed both of these effects. The mean and median rate of SMT8 triggers changes from year-to-year and the change shape of periodic seasonal modulation of the atmospheric muon trigger rate; see Table 6.2 and Figure 6.6.

A significant decrease in the noise rate of newly deployed strings has been observed for DOMs for the first several months after deployment; see [47, 112, 269]. Other experiments have also observed a similar decrease in the PMT noise rate with time [334]. For these newly deployed DOMs, the water in the drill hole has

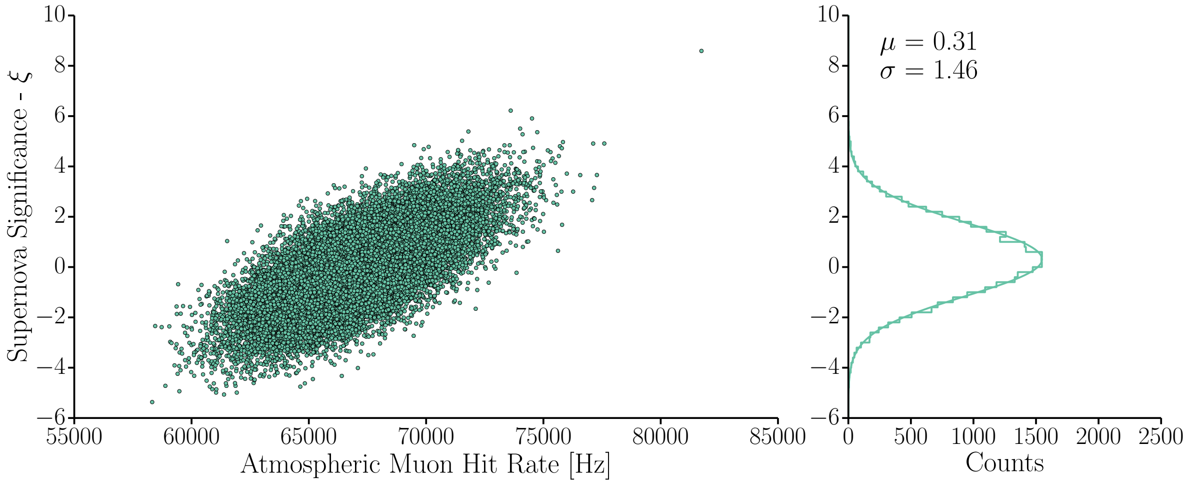

(a) Right: Supernova Significance, ξ, versus the atmospheric muon hit rate for Run 119716. Left: The distribution of ξ for Run 119716.

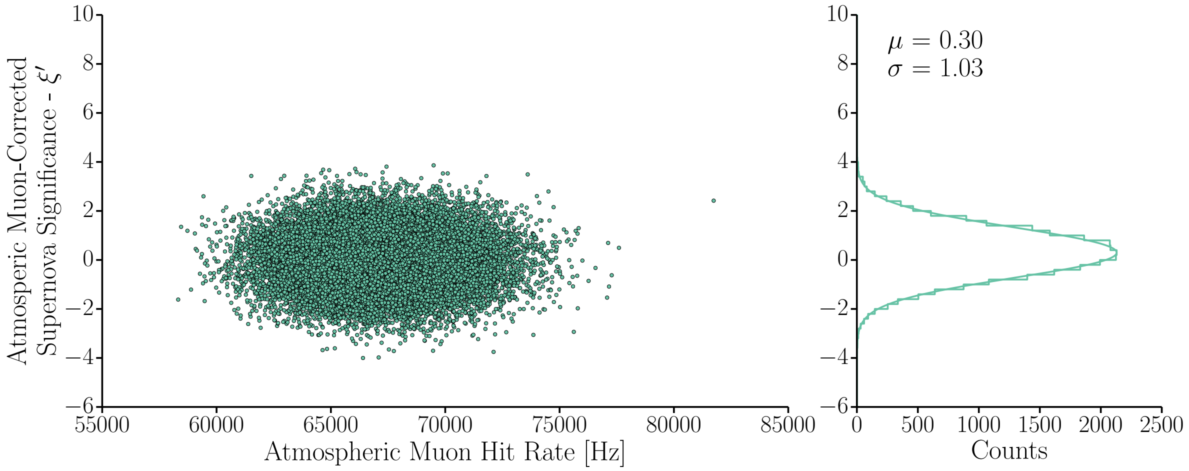

(b) Right: Atmospheric muon-corrected Supernova Significance, ξ', versus the atmospheric muon hit rate for Run 119716. Left: The distribution of ξ' for Run 119716.

Figure 6.2: Example of the atmospheric muon reduction method developed in [47]. The atmospheric muon hit rate is correlated to the supernova significance; see Figure 6.2a. The atmospheric muon hit rate is estimated from the DST NChannel, *i.e.* number of channels or DOMs that are attributed to a triggered atmospheric muon, distribution for SMT8 triggers integrated over the same time period as SNDAQ analysis bins. To remove the correlation, a linear regression is performed on the data in the lefthand plot in Figure 6.2a. The resulting relationship is subtracted from ξ to produce a atmospheric muon-corrected supernova significance, ξ'. The difference between ξ and ξ' can be seen in the righthand plots for both. Removing the contribution due to the atmospheric muons reduces the width of the significance distribution to the expected value.

Detector Year	Mean Number of False Positive Alerts [per day]	Δ% compared to IC86-2011
IC86-2011	10.07	0
IC86-2012	13.78	36.8
IC86-2013	14.43	43.3

(a) False positive SNDAQ trigger rate for IC86-2011 through IC86-2013 averaged over all analysis bins. A partial explanation for the increase is the introduction of an additional analysis bin, part way through IC86-2011; see second plot from the top in Figure 6.5.

Detector Year	Mean Number of False Positive Alerts [per day]	Δ% compared to IC86-2011
IC86-2011	3.22	0
IC86-2012	4.78	48.5
IC86-2013	5.02	55.6

(b) False positive SNDAQ trigger rate for IC86-2011 through IC86-2013 for the 0.5 s analysis bin.

Table 6.1: False positive trigger rate for IC86-2011 through IC86-2013 for all analysis bins (top) and the 0.5 s analysis bin (bottom). The change in the 0.5 s binning was added to give a better sense of the change because of the introduction of the 1.5 s analysis bin partway through IC86-2011; see Figure 6.5.

Detector Year	Mean SMT8 Rate (Hz)	Median SMT8 Rate (Hz)
IC86-2011	2088.13	2104.29
IC86-2012	2135.51	2166.76
IC86-2013	2121.91	2176.53

(a) Mean and median SMT8 rate for the first three years of the completed IceCube detector.

Detector Year	Mean Volume Trigger Rate (Hz)	Median Volume Trigger Rate (Hz)
IC86-2011	3685.87	3711.13
IC86-2012	3773.40	3827.99
IC86-2013	3750.66	3853.71

(b) Mean and median Volume Trigger rate for the first three years of the completed IceCube detector.

Table 6.2: Mean and median rate for SMT8 and Volume Trigger for the first three years of the completed IceCube detector. The volume trigger is shown for comparison purposes.

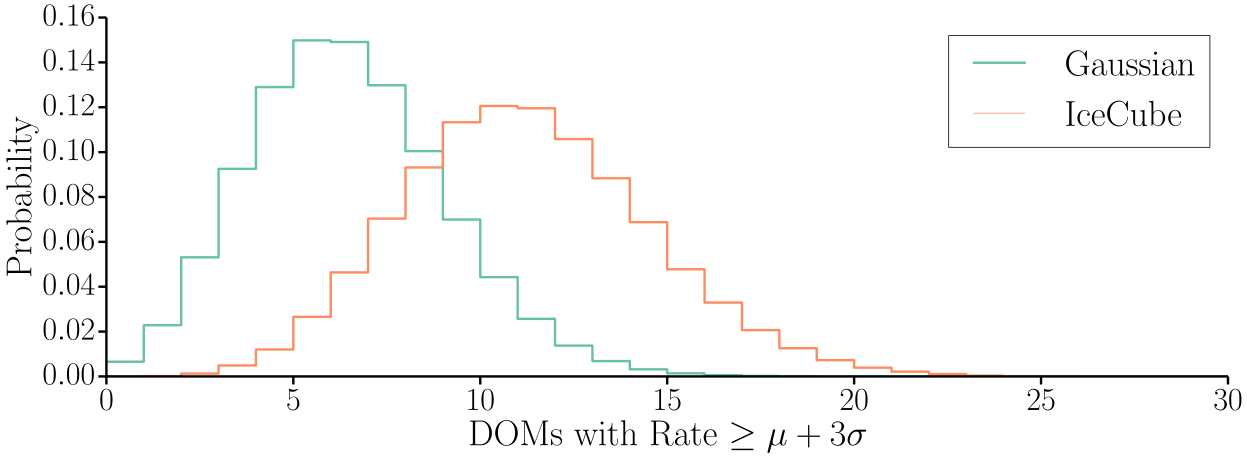

Figure 6.3: Illustration of the effect of atmospheric muons on the assumption of independently Gaussian-distributed DOM noise. The DOM-to-DOM correlate noise produced by atmospheric muons causes more DOMs to be above a certain threshold, in this case three standard deviations, σ, above the mean, μ. This will cause an artificial enhancement of increase in global DOM noise rate and hence and artificially large $\Delta\mu$.

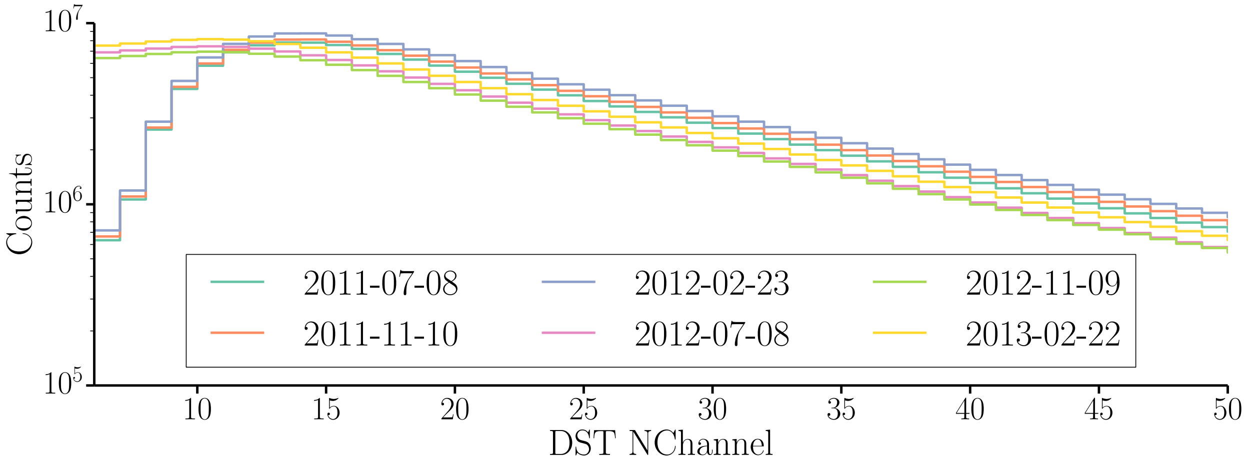

Figure 6.4: The DST NChannel that were attributed to a given SMT8 trigger for three different days during IC86-2011 and IC86-2012. The shift in the distribution can be attributed to the different atmospheric temperature and the subsequent change in the atmospheric muon flux. The difference in shape between IC86-2011 and IC86-2012 is due to changes in processing [50].

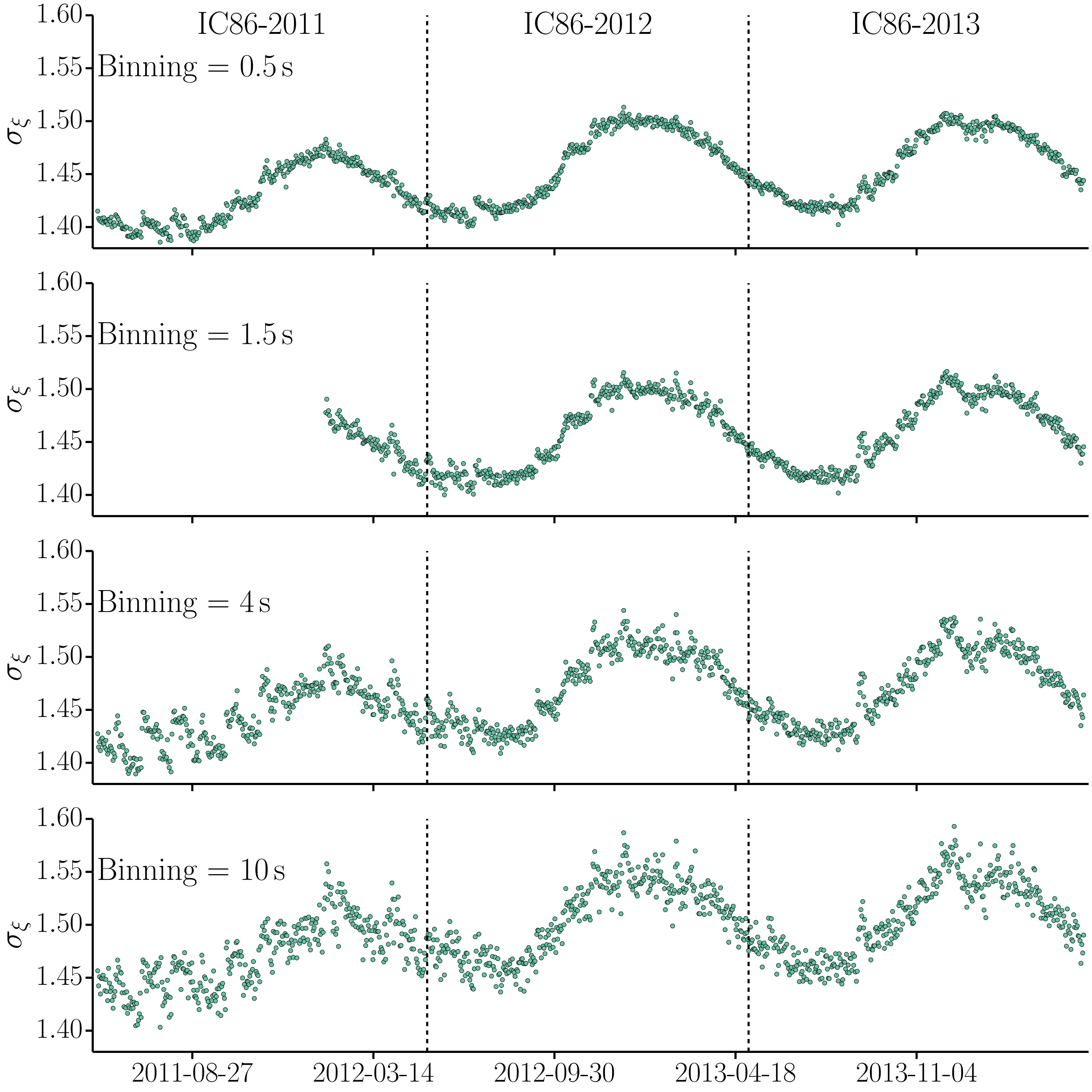

Figure 6.5: The standard deviation of the supernova significance distribution, σ_ξ, versus time for IC86-2011 to IC86-2013 for the four analysis binnings. The effect of the atmospheric muons in the austral summer is visible as the periodic behavior follows the seasons. The trend in all four analysis binnings is towards a wider significance distribution.

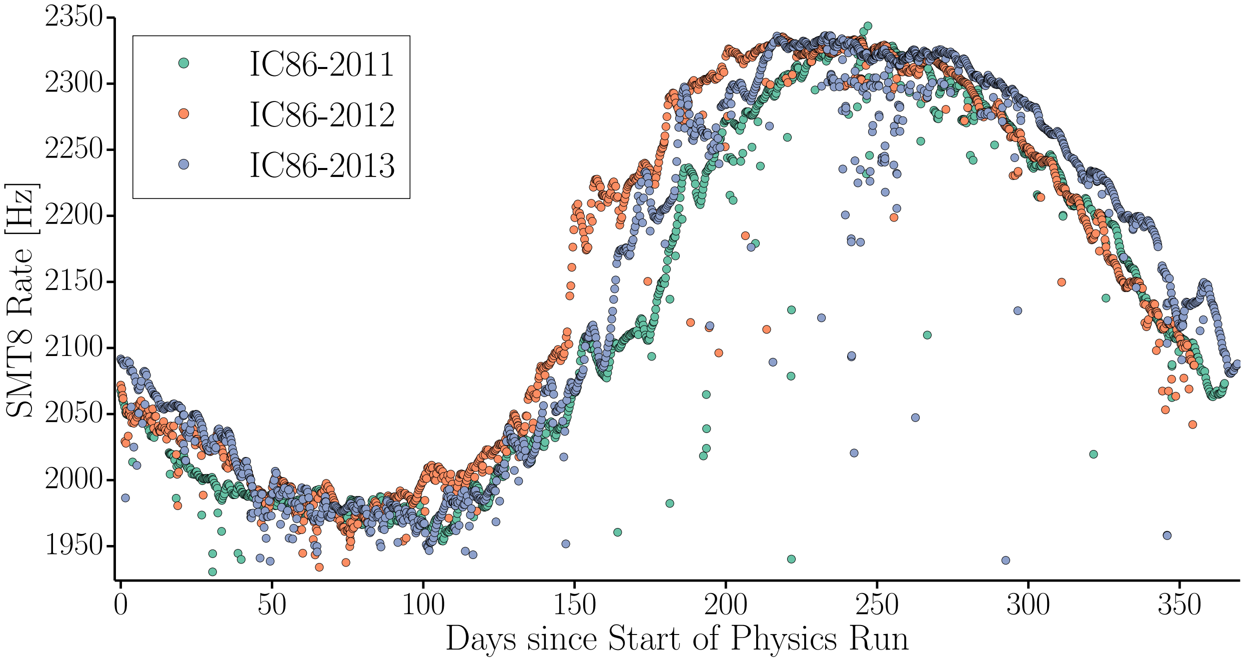

Figure 6.6: SMT8 rate versus days since the start of the respective physics runs. The periodic perturbation in the rate are due to changes in the atmospheric muon rate due to changes in the atmospheric temperature; see Figure 4.10. The overlay plot shows that the rate remains higher for longer periods of time, especially for IC86-2011 versus IC86-2012. The Pearson's r [39] for individual detector years is constant at ∼0.98; meaning that the atmospheric temperature and atmospheric muon rate are strongly correlated. NOTE: The dips in the rate during the austral summer in IC86-2013 are due to updates to the computing infrastructure at the South Pole.

not fully refrozen. To the best of the collaborations knowledge, the re-solidification or "freeze-in" process produces triboluminescences that is detected by the DOMs. It remains open whether the freeze-in process is still continuing, there is additional triboluminescence associated with the glacier's motion or construction, or there are detector aging effects that have to be taken in consideration.

The large change in the rate of false positive triggers seen in Figure 6.1 has to be mostly attributed to possible changes in the detector. The atmospheric muon trigger rate does not show a similar trend as the standard deviation of ξ, σ_ξ, and is correlated with the atmospheric effective temperature; see Figure 4.10, 4.12 and 6.7. The year-to-year changes in the mean and median rate as well as the shape of the periodic signal do have an effect on the false trigger rate; see Table 6.2 and Figure 6.6. These changes are not large enough to account for differences seen in Figure 6.1 and Table 6.1. A back-of-the-envelope calculation

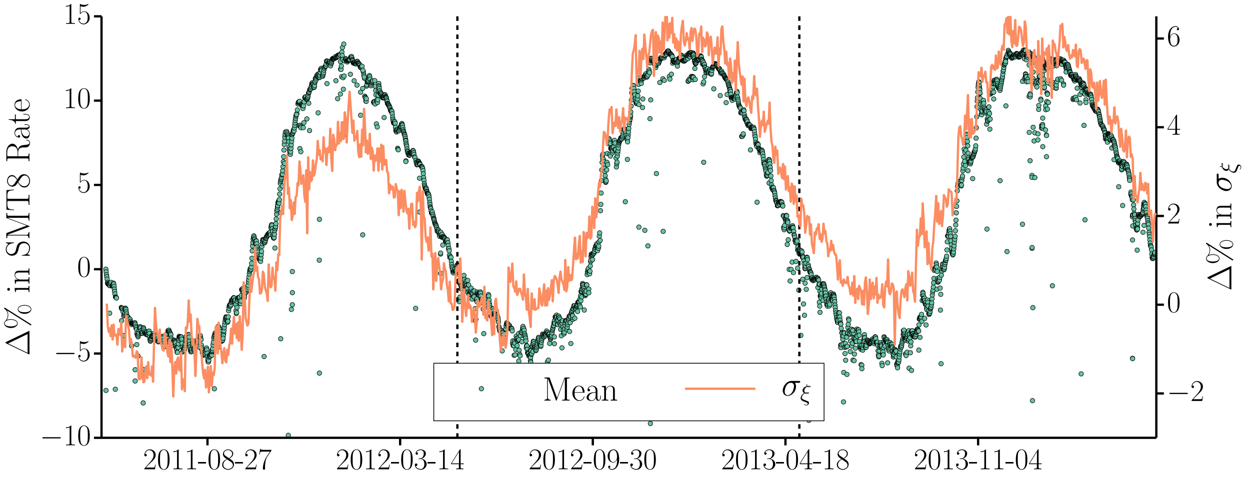

Figure 6.7: Comparison of trend in the SMT8 rate and σ_ξ over the course of the first three years of completed detector. The increasing sensitivity to atmospheric muons can be seen in the change of the peak-to-peak excursion of σ_ξ. The atmospheric muon rate changes by ~18% from peak-to-peak across all three years. The peak-to-peak change of σ_ξ changes from IC86-2011 to IC86-2012 by ~1% and stays roughly constant between IC86-2012 and IC86-2013. Overall, the change in σ_ξ is ~2% across three years.

supports this assessment. Assuming a detector with 5160 equivalent DOMs with purely Poisson noise with a rate of 300 Hz, a decrease in the noise rate of every DOM by 10 Hz will cause a $6\,\sigma$ signal to become $6.1\,\sigma$.

The subsequent sections will investigate whether the atmospheric muons effect is as small as expected, there are no other long-term trends in the atmospheric muon background, and the detector systematics are stable with time. The focus will be on possible changes in the atmospheric muon energy spectrum and the changes to the overall detector noise distribution.

6.1.1 Atmospheric Muon Background Stability

The increasing number of alerts could be attributed to difference in the atmospheric muon rate if the sensitivity of the atmospheric muons trigger IceCube is constant with time. In other words, for a given number of triggered atmospheric muons the number of false alerts should on average be constant between detector years. This holds if one assumes that the atmospheric muons for a given rate behave approximately the same. This can be measured using the Pearson's r correlation coefficient [39]. If the Pearson's r is constant with time, then there are either long-term trends in the atmospheric muon properties or in the detector itself.

Detector Year	Pearson's r SMT8 Trigger	Pearson's r Volume Trigger
IC86-2011	0.378	0.380
IC86-2012	0.560	0.565
IC86-2013	0.689	0.692

Table 6.3: Pearson's r for total number of triggers versus number of SNDAQ false positive triggers. Volume trigger is shown for comparison.

From Figure 6.8 and Table 6.3, one can see that the Pearson's r is increasing with time across IC86. This means the SNDAQ analysis is getting more sensitive to the effects of atmospheric muons. In conclusion, the year-to-year variations in the mean and median atmospheric muon rate can only explain a ∼3% increase in the false positive supernova triggers rate; see Table 6.2a and 6.2b.

The assumption that the atmospheric muon energy distribution for a given atmospheric temperature and SMT8 trigger rate is statistically speaking similar is valid to first order. The modulation of the atmospheric muon flux solely depends on the features of the atmosphere as the properties of the cosmic rays interacting in the atmosphere are on average constant with time [262]. Separately, the same atmospheric temperature typically yields comparable atmospheric properties as one can see from the strong correlation between atmospheric muons rate and atmospheric temperature; see Figure 4.10

In order to compare, the NChannel distribution for nearly all SMT8 triggers (there is a ∼10% overlap due to coincident events) is taken from IceCube's Data and Storage Tape (DST) data [335]. DST data is a minimalistic representation of data including, but not limited to, the NChannel, the direction from two independent reconstructions, and the trigger conditions that were met.

Comparing the DST NChannel distribution in Figure 6.9 between years, one sees that IC86-2012 and IC86-2013 are comparable. IC86-2011 has a slight trend towards higher NChannel. This is due to changes in the triggering and processing that were introduced in IC86-2011 and IC86-2012, respectively; see Figure 6.4. These changes were necessary because of the introduction of the slow particle trigger (SLOP) in IC86-2011, which can produce events that are $\mathcal{O}(0.1\,\mathrm{ms})$ long [5]. The SLOP trigger sweeps up multiple SMT8 and volume trigger events into one large event. To produce data that does not have these artificially long events, *trigger-splitter* was introduced to separate out other triggers from SLOP triggers [50].

To ensure that the assumption of similar DST NChannel for similar atmospheric temperatures is valid, the DST NChannel distribution from two days with roughly the same temperature and trigger rate were selected. To ensure data quality, the same preliminary data cuts as used by the cosmic ray anisotropy analysis are applied; see [335] for details. This is a trade off between having comparable trigger rates and temperatures. Any given day may have systematic detector effects that artificially decrease the detector rate

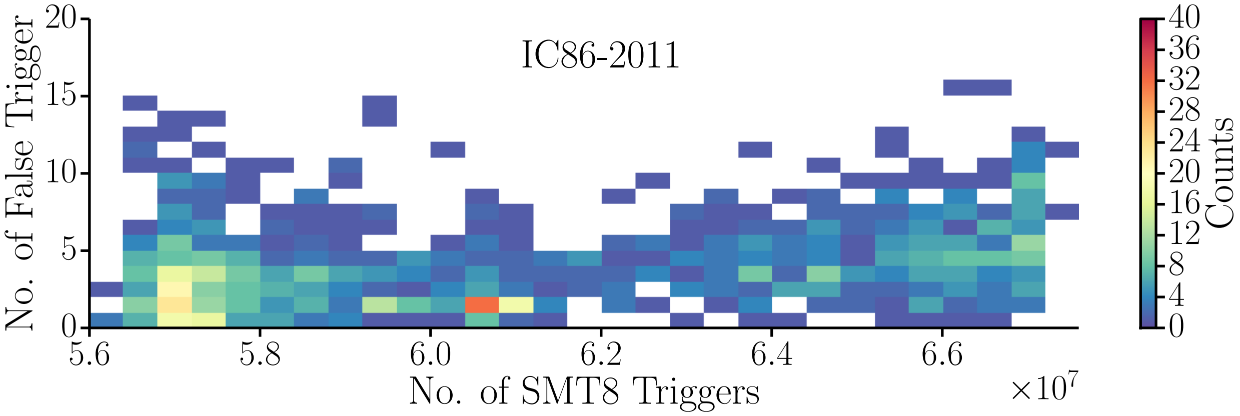

(a) Correlation between number of SMT8 triggers in a given run and the number of false triggers for IC86-2011

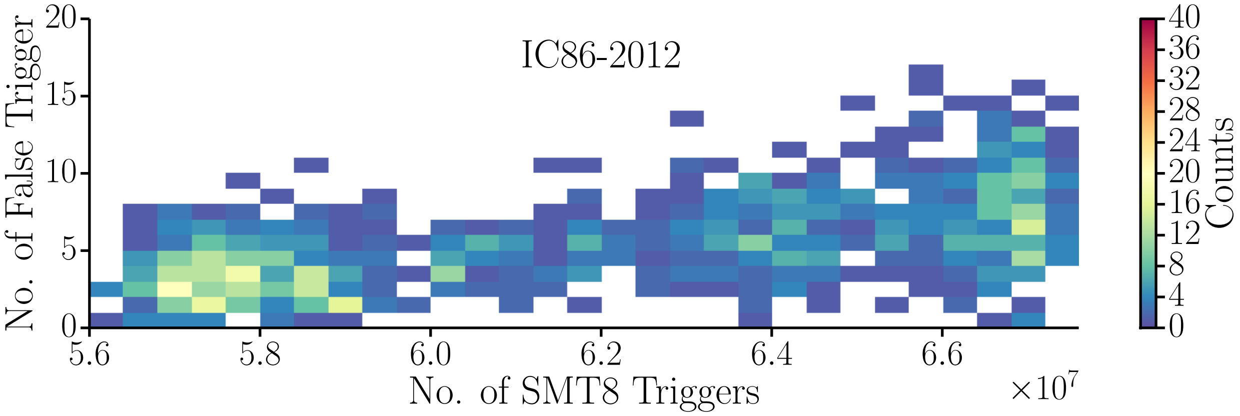

(b) Correlation between number of SMT8 triggers in a given run and the number of false triggers for IC86-2012

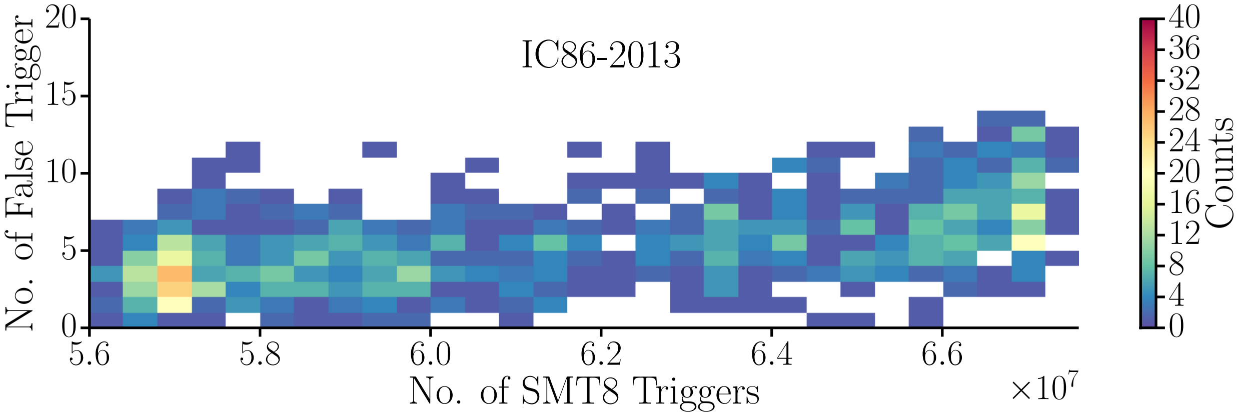

(c) Correlation between number of SMT8 triggers in a given run and the number of false triggers for IC86-2013

Figure 6.8: Correlation between number of SMT8 triggers in a given run and the number of false triggers for IC86-2011 through IC86-2013. A trend towards higher correlation can be seen especially when comparing IC86-2011 to IC86-2012.

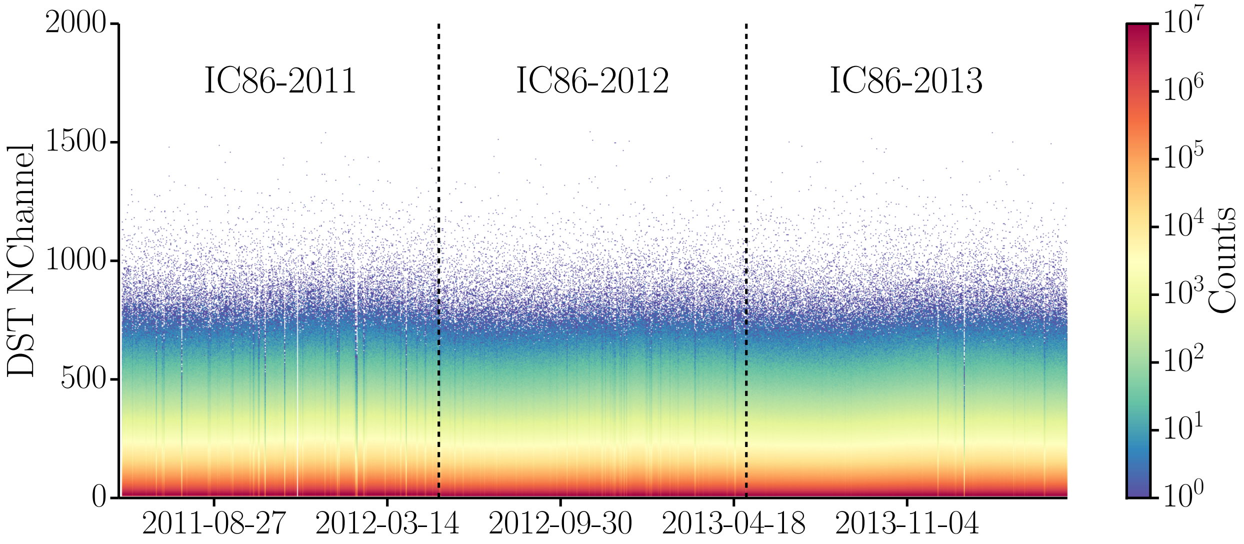

Figure 6.9: DST NChannel distribution versus time for IC86-2011 through IC86-2013. A slight shift in the austral summer due to the changes in the atmospheric temperature is visible in all three years. Otherwise the there are no recognizable trends. The difference between IC86-2011 and IC86-2012/-2013 is because of changes to the processing done at the South Pole [50].

and shift the DST NChannel distribution, for example both the NChannel and trigger rates are sensitive to the overall number of DOMs in the detector. For this study May 26 2012 and May 14 2013 were selected with effective atmospheric temperature of 199.86 K and 199.32 K and SMT8 trigger rate of 2061.79 Hz and 2051.06 Hz, respectively. Comparing the two distribution there is on average a ∼0.25–0.5% difference in the probability distribution functions (PDFs) between the two days; see Figure 6.10.

The Kolmogorov-Smirnov (K-S) [39] and χ^2 [336] test revealed that the two distributions are not the same PDFs. This result is not surprising, as the very high statistics (up to $\sim 1.8 \times 10^8$ events) makes either test sensitive to small systematic effects, such as DOMs being added or removed or systematic errors in the effective atmospheric temperature measurement.

The effect of systematics can be seen when testing a given day compared to all other days using the K-S test; see Figure 6.11. As expected, days surrounding the given day and days with roughly the same atmospheric temperature in a given detector years produce distributions that are comparable. When comparing the given day to days in the following detector year, in this case IC86-2012 to IC86-2013, one sees that there are still NChannel distributions that have a comparable PDFs. The effect of the systematic errors on the K-S test are also visible. Days that were expected to have the same distribution are incompatible and vice

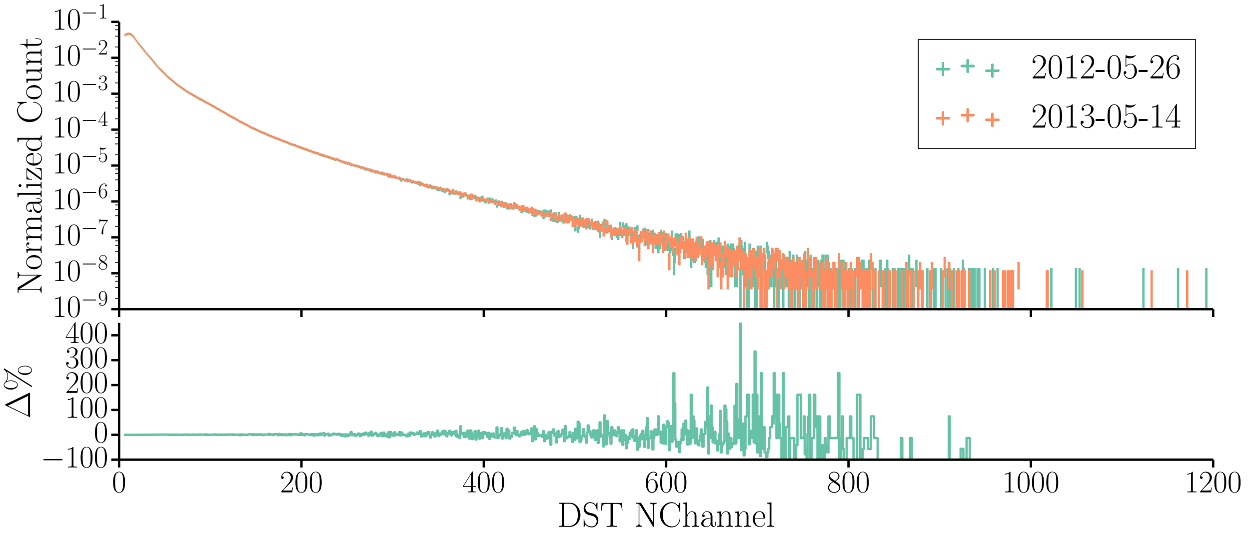

(a) Overlay (top) and the residual (bottom) of the NChannel PDFs from May 26 2012 and May 14 2013 with linear spaced bins. The residual indicates a small difference between the PDFs until the statistics are low for either PDF.

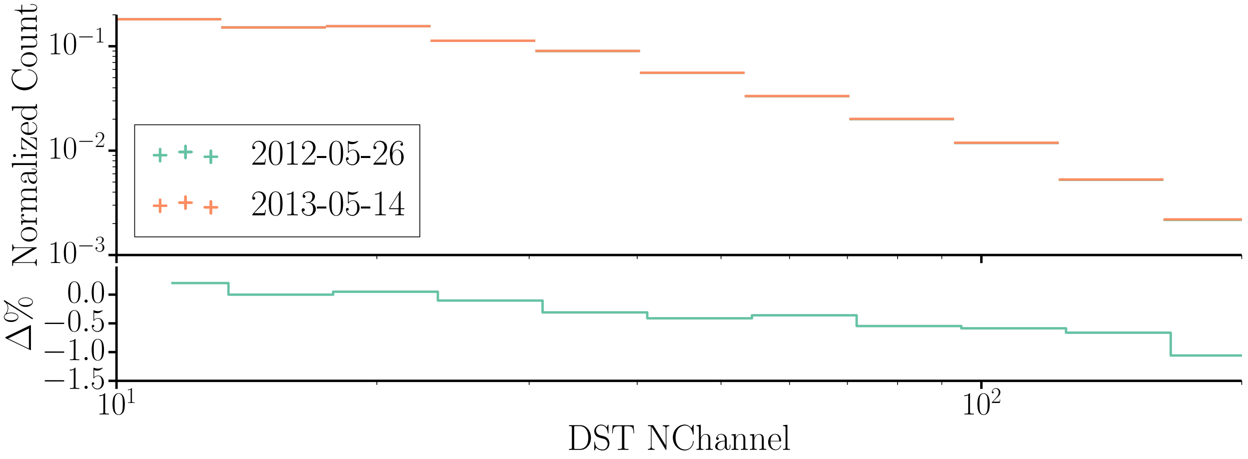

(b) Overlay (top) and the residual (bottom) of the NChannel PDFs from May 26 2012 and May 14 2013 for logarithmically spaced bins. The residual indicates a small difference between the PDFs and some of the noise that was seen in Figure 6.10a is mostly due to statistics in individual bins. NOTE: This only shows the bins until an NChannel of 200. This was done to show that the PDFs are comparable.

Figure 6.10: Overlay (top) and residual (bottom) plots for the NChannel PDFs from May 26 2012 and May 14 2013 in both linear- and logarithmic-sized bins. The PDFs are comparable in both binnings with an average residual of ∼0.25%.

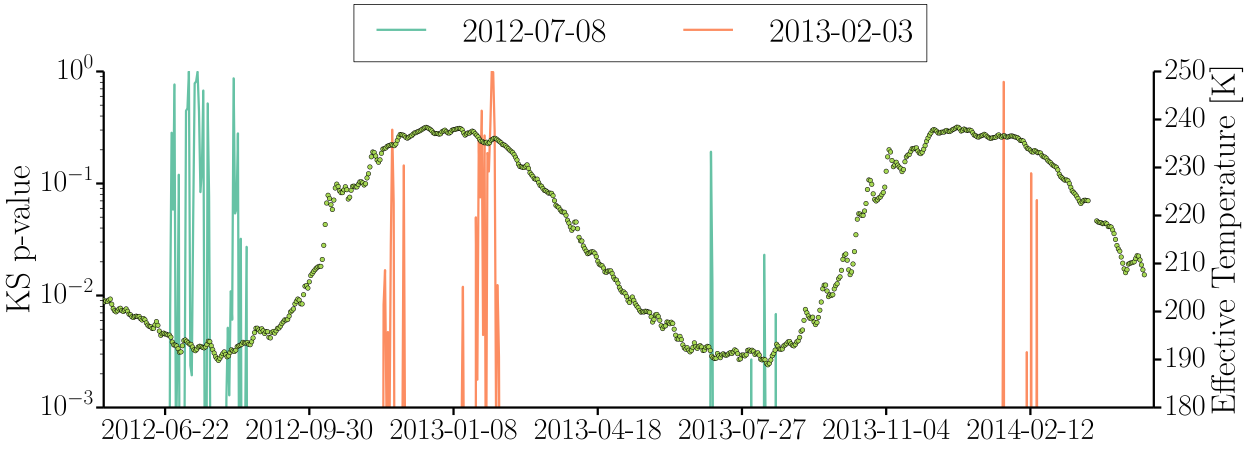

Figure 6.11: K-S test p-value when testing the DST NChannel distribution for July 08 2012 and February 03 2013 against the all other daily DST NChannel distributions for IC86-2012 and -2013. The response of the K-S test around the days being tested shows that days before and after with similar temperatures have statistically similar NChannel distributions. Days in different detector years also have statically similar distributions. These days do not necessarily have the same or comparable effective temperature. This means that the K-S test is sensitive to systematic effects in both the effective temperature and the detector. The effective atmospheric temperature for the same time range is added for reference.

versa. This can be due to systematic errors in the temperature measure (~5–10%) [337], in the number of active DOMs ($< 1\%$), or the settings of DOMs ($< 1\%$).

An additional factor could be the atmospheric muon zenith angle, θ, distribution. The zenith distribution could have an increasing number of events that are at a larger $\cos\theta$, *i.e.* more vertical. To do this the distributions in Figure 6.10b were weighted by $1/\cos\theta$ for events with a $\cos\theta \geq 0.5$. This angular threshold was chosen because at $\cos\theta < 0.5$ the atmospheric muon flux drops off sharply as the overburden increases significantly and the NChannel can no longer be corrected in this fashion corrected; see Figure 5.9. The resulting weighted NChannel distribution is seen in Figure 6.12. The PDFs are still ~0.25–0.5% apart, which means that the difference is solely due to the underlying unweighted NChannel distributions. This is not surprising as a vast majority of events are within a small zenith band centered on $\cos\theta = 1$.

A possible extension of this analysis is using SuperDST data [338]. It provides the full detector readout during a trigger, *i.e.* waveforms of every channel that had an SLC and HLC readout during a trigger. With this information, one could calculate a corrected NChannel distribution that accounts for detector size. The waveforms also allows to determine the total charge that was deposited by an event. This is a better measure

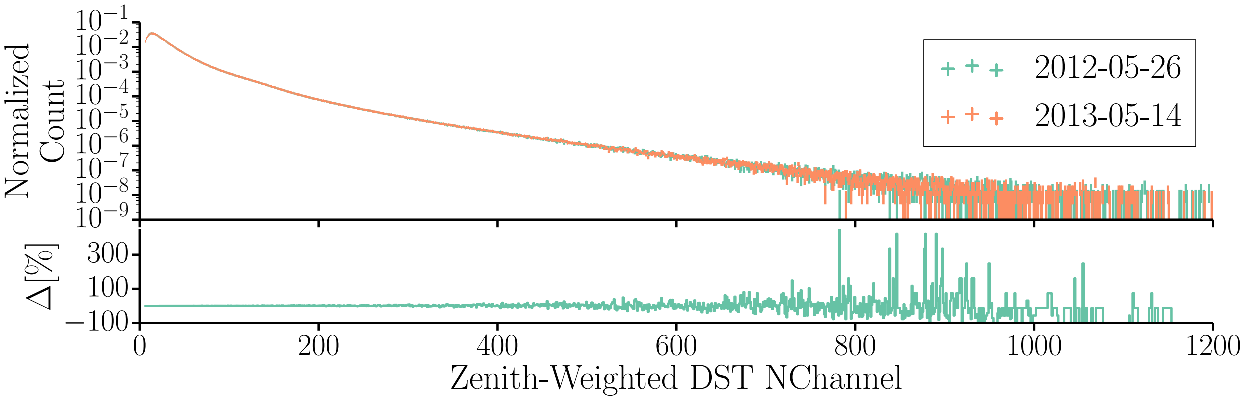

(a) Overlay and the residual of the zenith-weighted NChannel PDFs from May 26 2012 and May 14 2013 with linear-spaced bins. The residual indicates a small difference between the PDFs until the statistics are low for either PDF.

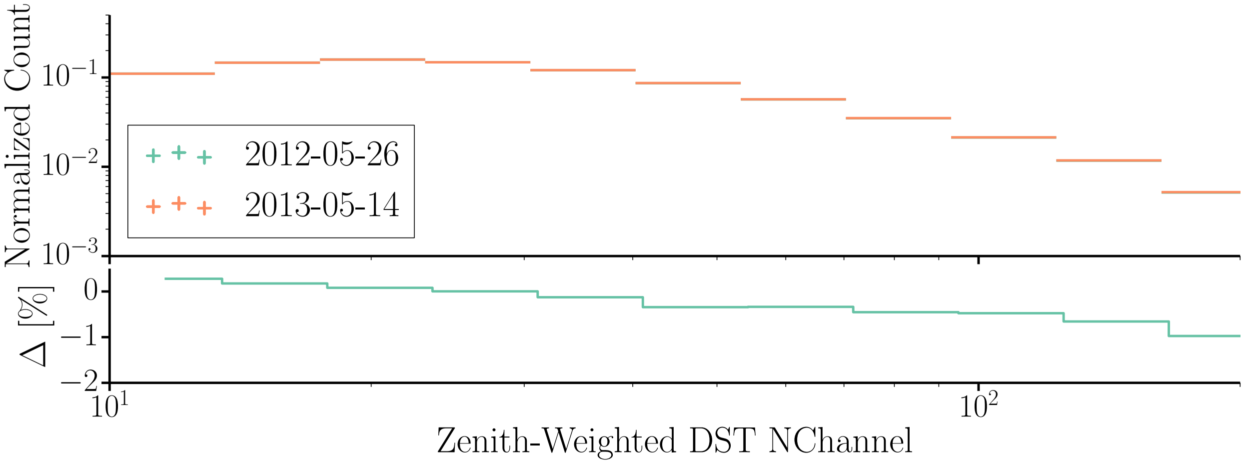

(b) Overlay and the residual of the zenith-weighted DST NChannel PDFs from May 26 2012 and May 14 2013 for logarithmically sized-spaced bins. The residual indicates a small difference between the PDFs and some of the noise that was seen in Figure 6.12a is mostly due to statistics in individual bins. NOTE: This only shows the bins until an NChannel of 200. This was done to show that the PDFs are comparable.

Figure 6.12: Overlay and residual plots for the zenith-weighted NChannel PDFs from May 26 2012 and May 14 2013 in both linear- and logarithmic-spaced bins. The zenith-weighting is applied by multiplying the NChannel by $^{1}/_{\cos\theta}$ to adjust for changes in overburden and relative size of the detector as a function of zenith angle. The PDFs are comparable in both binnings with an average residual of ∼0.25%, which means that the difference between the PDFs mostly arises from changes to the underlying NChannel distributions.

for the energy deposited in the detector than the number of channels that were involved in a trigger. The collected charge accounts for additional loss processes, *i.e.* bremsstrahlung, *etc.*, that occur for high energy atmospheric muons [12,247]. Using the total charge is not a better measure of the effect of atmospheric muons on the supernova scalers. The supernova scalers do not differentiate between individual photoelectrons and multiple photoelectrons.

In summary, one does expect a 3% increase in the number of faults alerts due to changes in the atmospheric properties. Additionally, the SNDAQ analysis is becoming more sensitive to muons by ∼2%; see Figure 6.7. Separately, under the consideration of possible detector systematic, *i.e.* active DOMs, the energy spectrum of atmospheric muons that trigger IceCube are comparable across two years of data. This means that the trend in the SNDAQ false positive alerts can not arise solely from changes to the atmospheric properties. The atmospheric muon rate and properties and the effective atmospheric temperature are correlated. This means that there are systematic detector effects that cause the bulk of the increase in false alerts.

6.1.2 Detector Noise Rate Stability

Section 6.1.1 showed that the year-to-year variations in the atmospheric muons background can only cause a small fraction of the increase in the false trigger rate seen in the supernova analysis. The supernova analysis remains subject to an increasing effect from atmospheric muons, *i.e.* the increased widening in the significance distribution with time observed in Figure 6.5.

Analysis of the detector noise rate stability for a single recently deployed string in [269] showed that there was significant rise in noise rate related to the deployment and position on a string. An exponential fall off in the noise rate of individual DOMs over long time periods was seen in [112]. A decay in the detector noise rate for partial detectors, 40-string through 79-string configuration, was seen in [30, 47].

For the completed detector, a similar effect is seen; see Figure 6.13. The detector mean rate decays mostly due to the DOMs that are newly added to the detector; see Figure 6.14a and 6.14b compared to Figure 6.14c. There is still a slight trend in the mean rate of DOMs in Figure 6.15a and 6.15b. This trend is much smaller than the trend seen in Figure 6.15c. As the decay progresses, the annual modulation of the atmospheric muon rate with temperature causes the mean DOM noise rate to have a periodic time dependence; see Figure 6.13b. This becomes the significant contribution to detector instability over the long-run and shows that there is increasing sensitivity to atmospheric muons with time.

The effect of the decreasing baseline noise rate on ξ can be seen in Figure 6.16. The significance increased ∼0.6% for a given signal, as the mean noise rate decreased by ∼3.5%. This in turn means that there is an increasing sensitivity to atmospheric muons. The increase is due to a larger fraction of supernova scalers being produced from atmospheric muons rather than from inherent DOM noise. This atmospheric muon

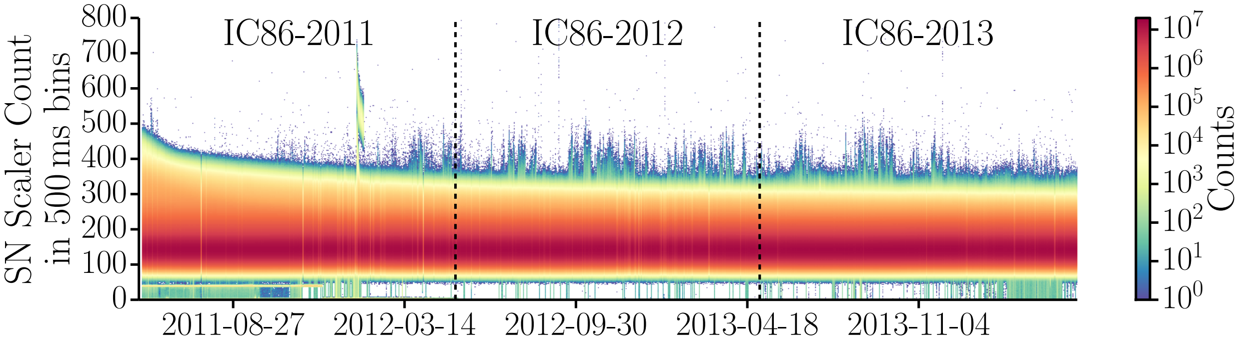

(a) Development of the supernova scaler distribution for the entire detector over the course of the first three years of the completed IceCube distribution

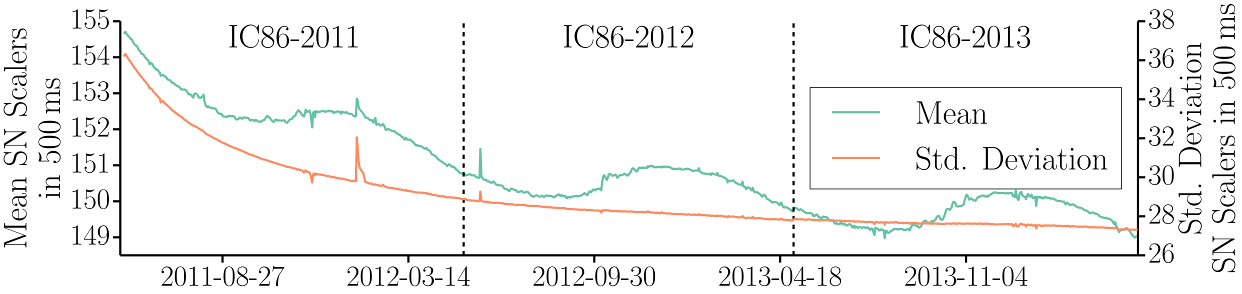

(b) Mean and variance of the supernova scaler distribution for the entire detector over the course of the first three years of the completed IceCube. There is a exponential decay over the course of the data set. This is especially recognizable in the standard deviation of the distribution. The standard deviation decreases by 25% over the course of the three years, and is not noticeably effect by the seasonal modulation. Changes in the mean is initially dominated by the decay component and later by the seasonal variation of the atmopsheric muons.

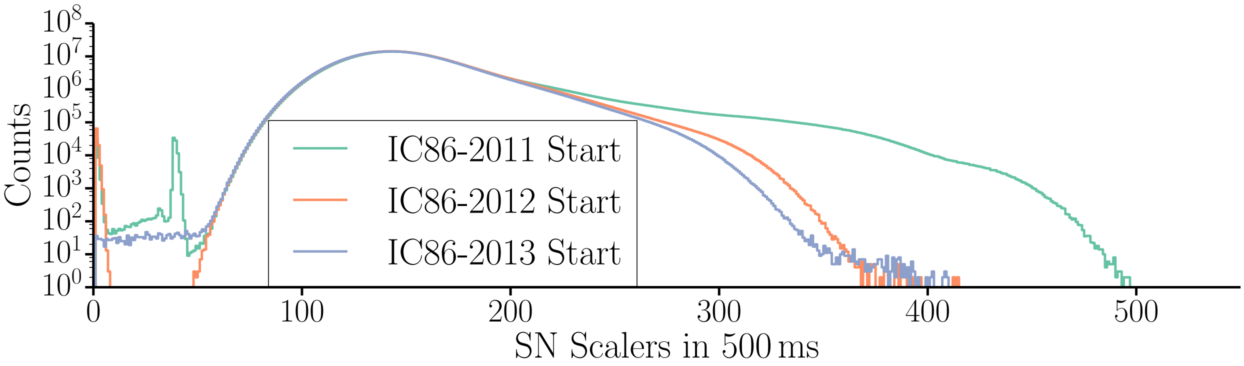

(c) Slices of the supernova distribution in Figure 6.13a at the start of physics runs in this data set. The decrease in righthand tail of the distribution is caused by the exponential decay. The lefthand side of the distribution changes as faulty DOMs are either taken out of the data taking or removed from the SNDAQ analysis.

Figure 6.13: Distribution of the supernova scaler and its statistical properties over the course of the first three years of the completed IceCube Detector.

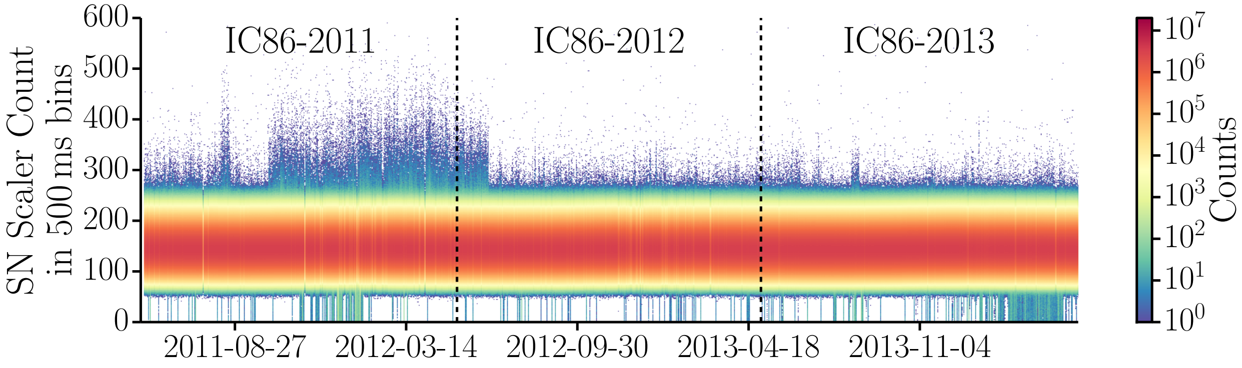

(a) Distribution of the scaler rate for strings deployed in the 2007/2008 austral summer season. String Number: 44, 45, 52, 53, 54, 55, 60, 61, 62, 63, 64, 68, 69, 70, 71, 75, 76, 77.

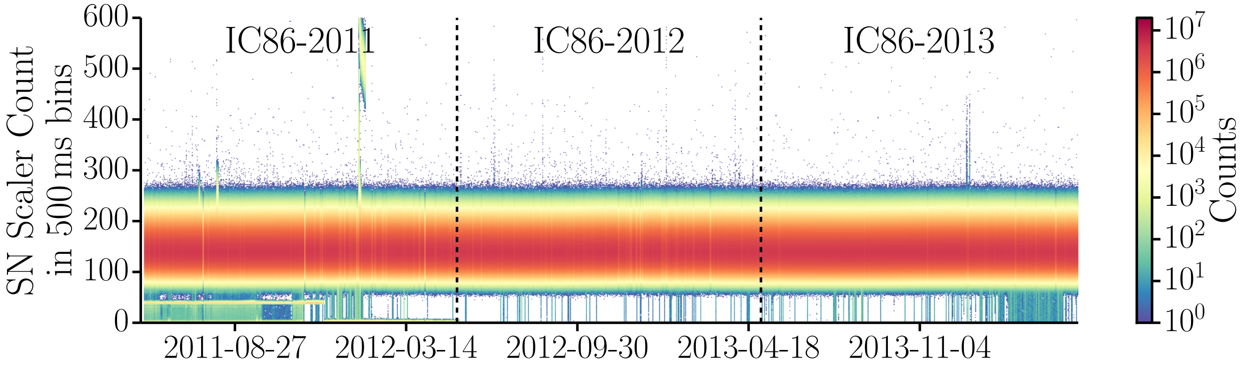

(b) Distribution of the scaler rate for strings deployed in the 2008/2009 austral summer season. String Number: 2, 3, 4, 5, 6, 10, 11, 12, 13, 18, 19, 20, 26, 27, 28, 36, 37, 83.

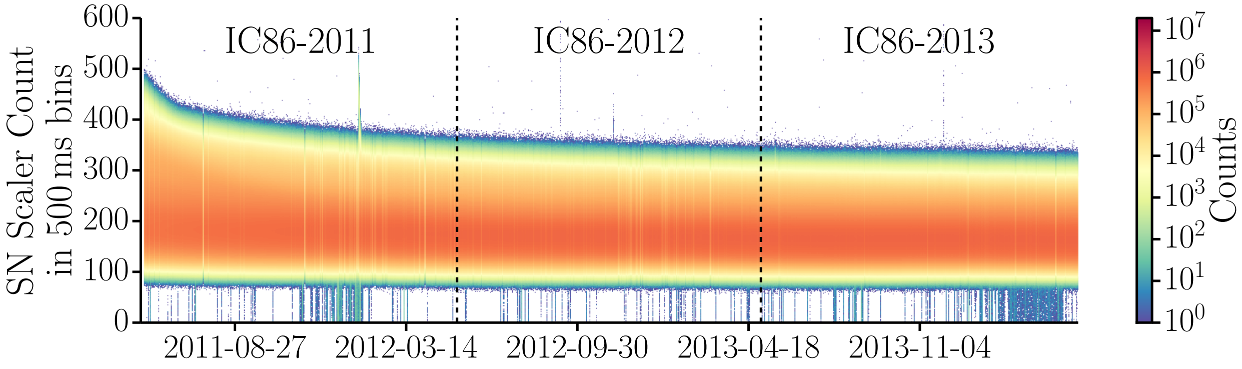

(c) Distribution of the scaler rate for strings deployed in the 2010/2011 austral summer season. String Number: 1, 7, 14, 22, 31, 79, 80.

Figure 6.14: Distribution of the supernova scaler over the course of the first three years of the completed IceCube Detector for sets of DOMs deployed during the 2007/2008, 2008/2009, and 2010/2011 austral summer season.

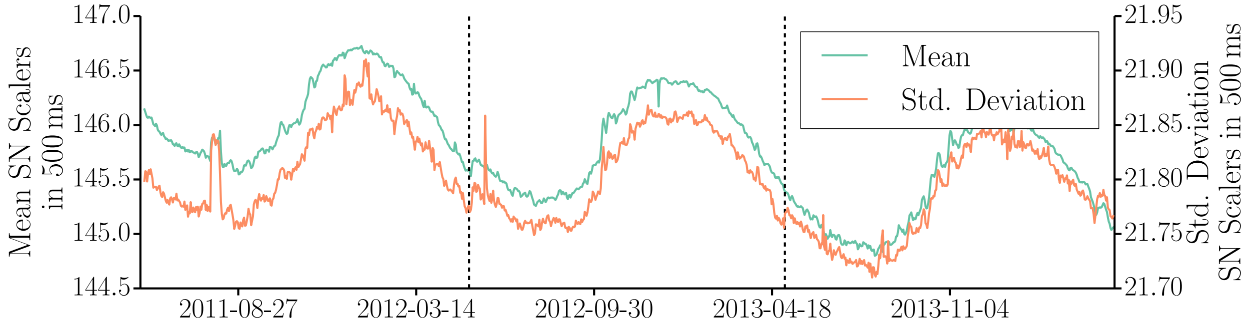

(a) Mean and standard deviation of the distribution of the scaler rate for strings deployed in the 2007/2008 austral summer season. String Number: 44, 45, 52, 53, 54, 55, 60, 61, 62, 63, 64, 68, 69, 70, 71, 75, 76, 77.

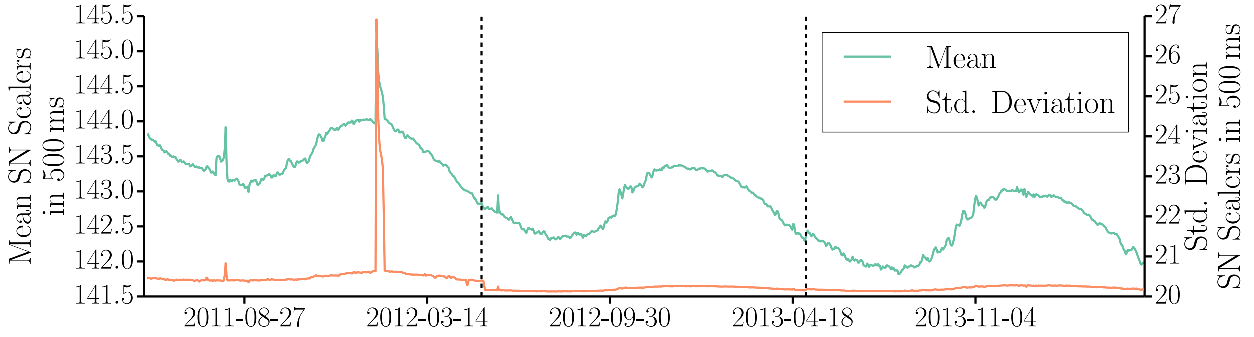

(b) Mean and standard deviation of the distribution of the scaler rate for strings deployed in the 2008/2009 austral summer season. String Number: 2, 3, 4, 5, 6, 10, 11, 12, 13, 18, 19, 20, 26, 27, 28, 36, 37, 83.

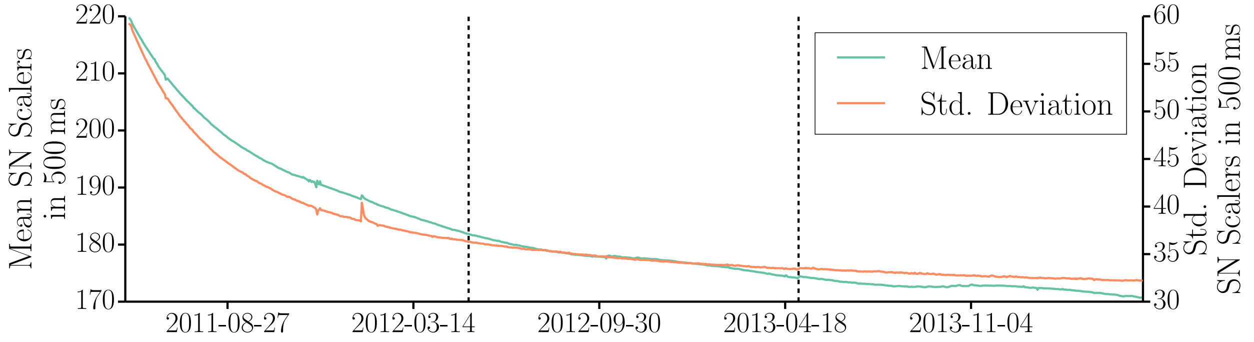

(c) Mean and standard deviation of the distribution of the scaler rate for strings deployed in the 2010/2011 austral summer season. String Number: 1, 7, 14, 22, 31, 79, 80.

Figure 6.15: Mean and standard deviation of the distribution of the supernova scaler over the course of the first three years of the completed IceCube Detector for sets of DOMs deployed during the 2007/2008, 2008/2009, and 2010/2011 austral summer season.

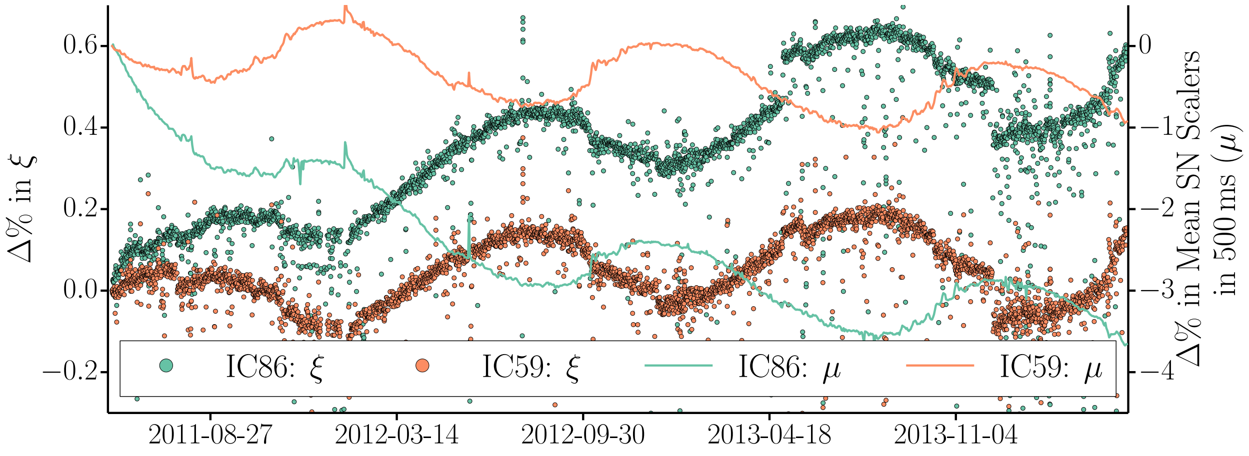

Figure 6.16: Comparison of trend in the mean DOM scaler count and the changes in the significance of a given signal. The significance is calculated using the prescription in Section 4.9. The background terms are the mean and standard deviation of the scaler count for every DOM during a run. The signal is a Poisson random number added to the mean drawn on a per DOM basis from a Poisson distribution with mean value of 2.5 Hz. Quality cuts are applied that such DOMs need an mean of at least 50 scaler counts and cannot have more 10000 scaler counts. The comparison to IC59, the 59-string configuration of IceCube, shows that a slower change in the mean rate causes a slower change in the significance. IC59 was chosen because most DOMs have been in the ice for at least 5 years and should have settled.

noise, as mentioned before, is correlated among DOMs. The assumption of DOMs being independent in the supernova analysis is becoming worse with time.

This effect can be seen in negative correlation between the σ_ξ and the mean detector rate with time; see Figure 6.17. The value of the σ_ξ is directly related to the atmospheric muon flux, as it is in phase with the seasonal variation of the atmospheric muon and correcting for their effect on the analysis produces an the expected value of σ_ξ; see Figure 6.2.

From simulation one can observe a proportional effect as well. Increasing the noise rate in simulation by ∼5% produces a ∼3.5% decrease in σ_ξ, similarly in data a decrease in noise rate by ∼3.5% produce an increase in σ_ξ by ∼2%. The increasing significance of the SNDAQ alerts can therefore be explained by a combination of increasing average atmospheric muon rate between years of operating the full IceCube detector and a decrease in the baseline noise rate that produces an increasing sensitivity to atmospheric muons.

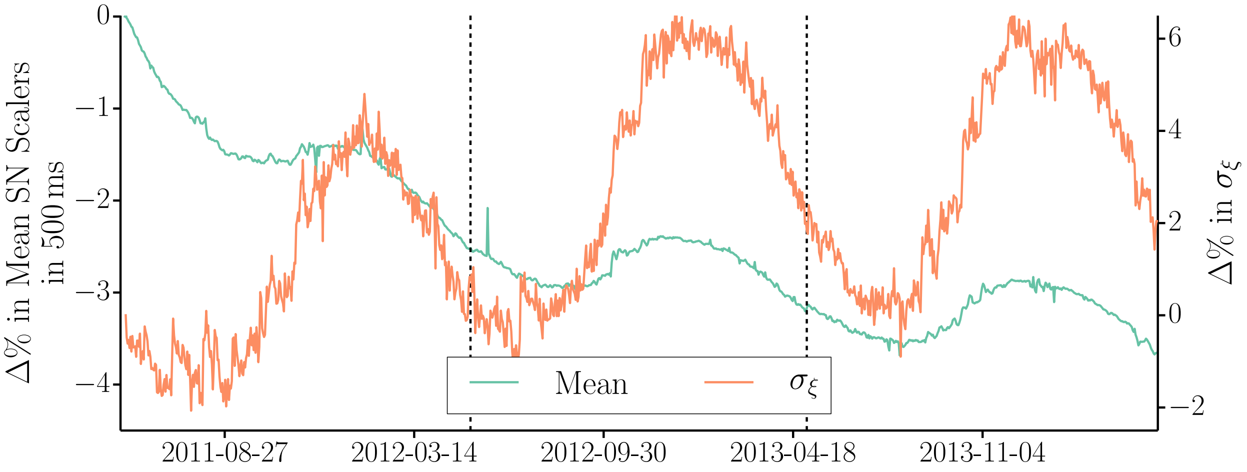

Figure 6.17: Comparison of trend in the mean DOM scaler count and σ_ξ. From this, one can see that a ∼3.5% change in the noise accounts for a ∼2%.

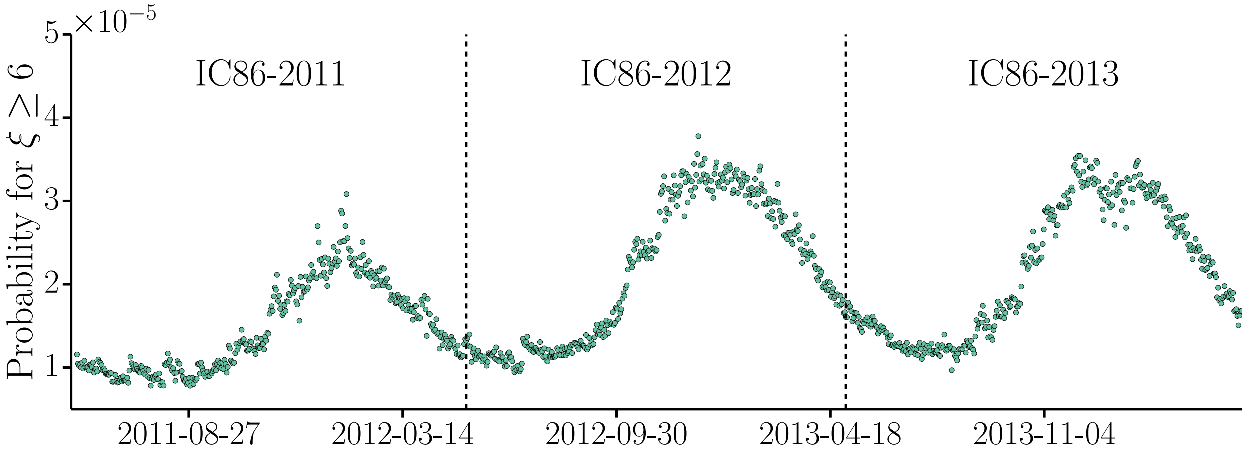

Figure 6.18: Probability to have an event with $\xi \geq 6$ over the course of IC86-2011 through IC86-2013 for the 0.5 s analysis binning.

The effect on the number of false alerts is large because the trigger threshold has been set at $\xi = 6$ for IC86-2011 through IC86-2013; see Table 6.1. The widening of ξ's distribution with time will cause more events to pass the threshold. The probability of having an event with $\xi \geq 6$ is directly related to σ_ξ; see Figure 6.18. The increase in average probability between IC86-2011 and IC86-2012 is 46.2%. The remaining ∼2% increase seen in data can be attributed to changes in uptime in SNDAQ and changes in the analysis;

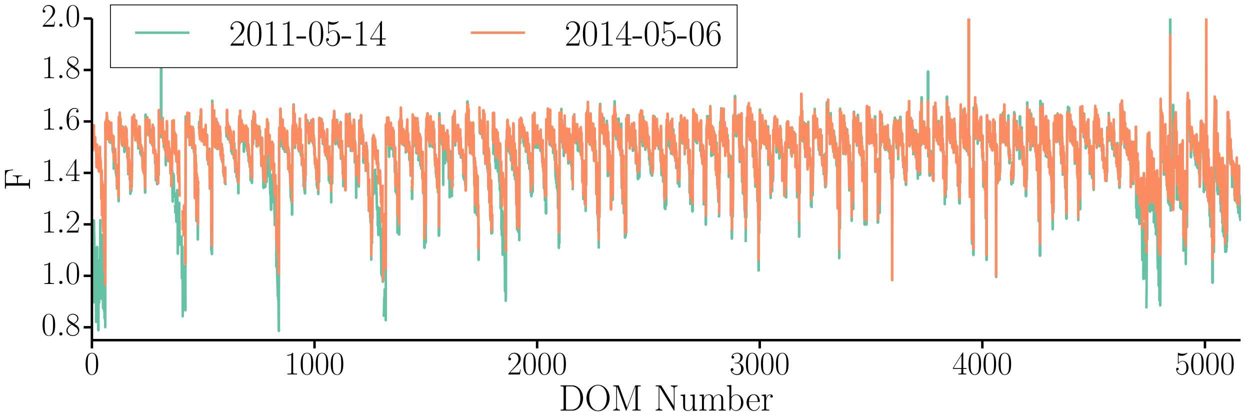

(a) Comparison in the Fano factor, F, per DOM for Run 118179 on May 14 2011 to Run 124700 on May 06 2014 for all DOMs.

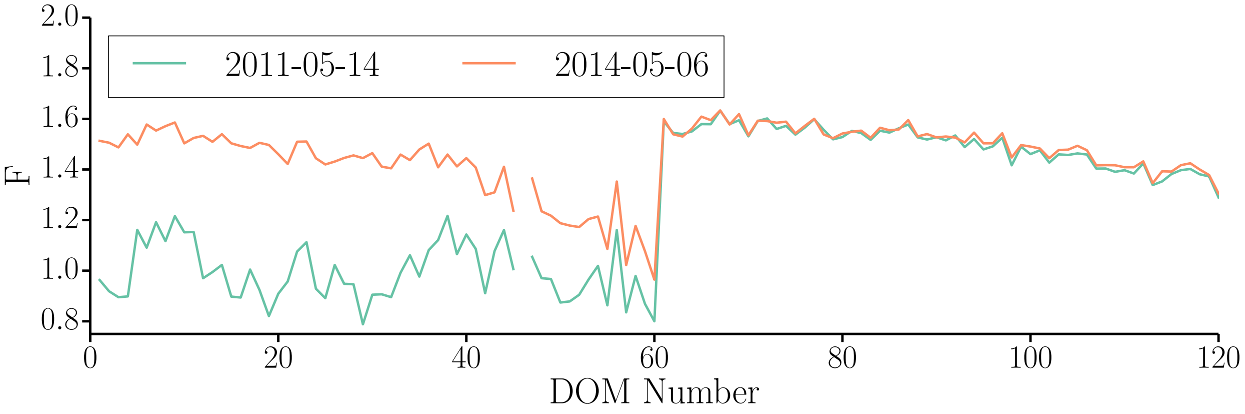

(b) Comparison in the Fano factor, F, per DOM for Run 118179 on May 14 2011 to Run 124700 on May 06 2014 for the first 120 DOMs. DOM 1 through 60 were added in 2010/2011. They exhibit a decaying mean rate and hence an increase in the Fano factor. DOM 61 through 120 show that DOMs have been in the ice longer are more stable with time.

Figure 6.19: Comparison of the Fano factor, F, per DOM for Run 118179 on May 14 2011 to Run 124700 on May 06 2014 for all DOMs (top) and the first 120 DOMs (bottom). The DOM number is given by the location in the detector; DOM 1 on String 1 is DOM Number 1 and DOM 1 on String 2 is DOM Number 61. DOM 1 on every string is at the top at a depth ∼1450 m and DOM 60 at the bottom at depth of ∼2450 m. The depth dependence is due to the influence from the atmospheric muon background. A change in the Fano factor over time are visible in the strings that were deployed in the final construction season in 2010/2011. The remaining DOMs appear to be constant with time. A decaying noise rate causes an increasing effect of the atmospheric muon background; indicated by the increasing Fano factor.

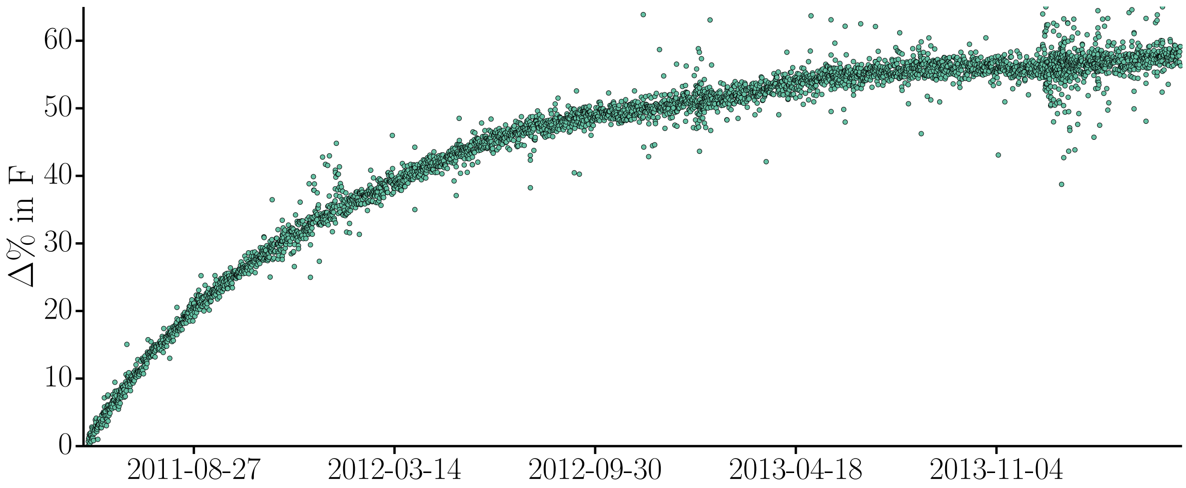

(a) Percentage change in the Fano factor, F, relative to start of IC86-2011, based on the average rate and standard deviation per run for DOM 1, top-most DOM, on String 1. An exponential rise is visible. The effect if the atmospheric muons that is seen in Figure 6.21a is subdominant to the noise rate.

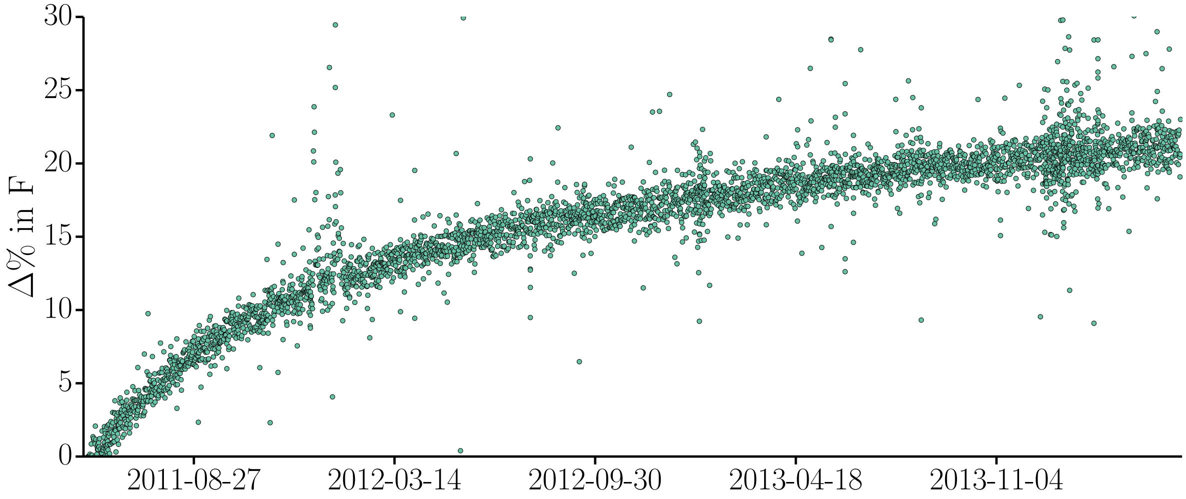

(b) Percentage change in the Fano factor, F, relative to start of IC86-2011, based on the average rate and standard deviation for DOM 60, bottom-most DOM, on String 1. A slower rise compared to Figure 6.20a is visible with no noticeable effect from atmospheric muons because of the additional overburden.

Figure 6.20: Percentage change in the Fano factor, $F = \frac{\sigma^2}{\mu}$ [51], relative to the start of IC86-2011, for top- and bottom-most DOM on String 1, one of the last deployed strings in December 2010. The increase in the Fano factor indicates that the ratio between the variance and the mean is increasing with time, *i.e.* the DOM noise is becoming more non-Poissonian with time; see Figure 6.19. This also shows that there is a increasing influence from atmospheric muons with time.

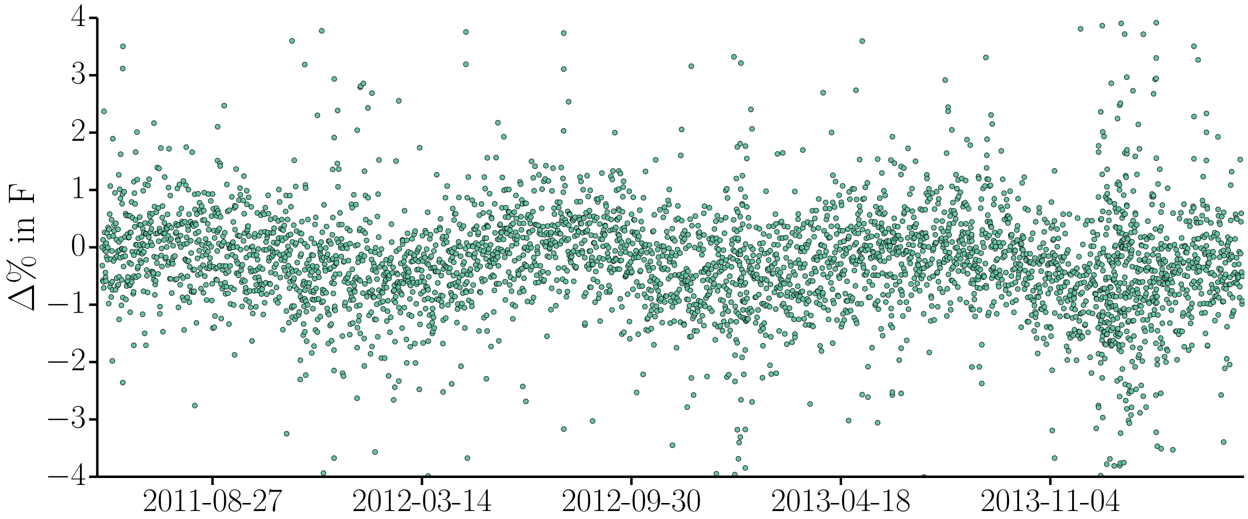

(a) Percentage change in the Fano factor, F, relative to start of IC86-2011, based on the average rate and standard deviation per run for DOM 1, top-most DOM, on String 21. The effect of the atmospheric muons is visible, but out of phase with the atmospheric muon signal. The signal predominately affects the mean and not the variance of the DOMs noise distribution.

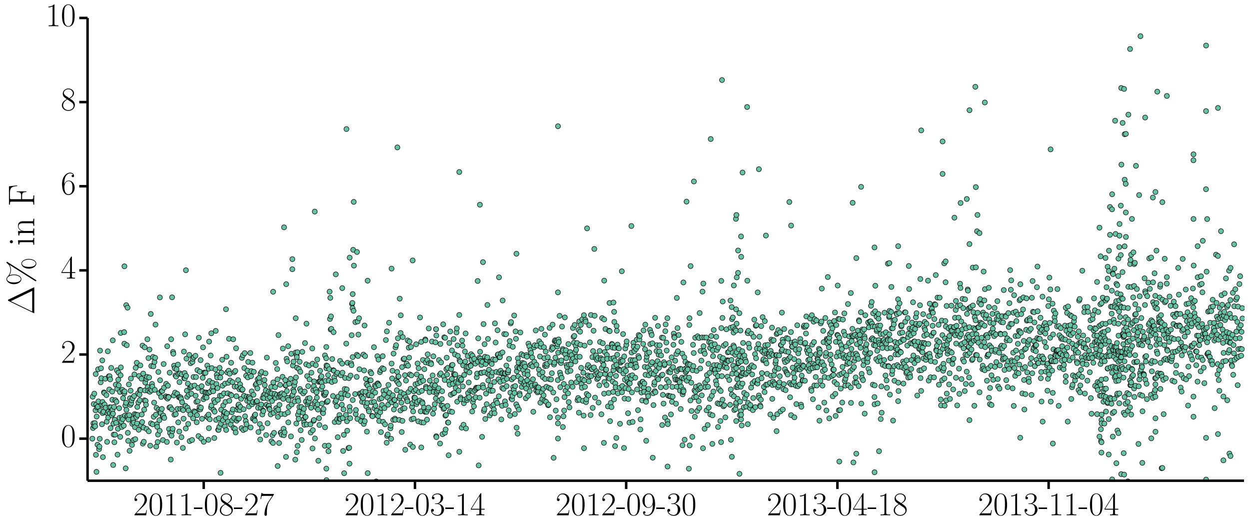

(b) Percentage change in the Fano factor, F, relative to start of IC86-2011,based on the average rate and standard deviation per run for DOM 60, bottom-most DOM, on String 21. A slight upward trend is visible. The effect of atmospheric muons is negligibly small because of the $\sim 1\,km$ additional overburden compared to DOM 1.

Figure 6.21: Percentage change in the Fano factor, $F = \frac{\sigma^2}{\mu}$ [51], relative to the start of IC86-2011, for top- and bottom-most DOM on String 21, the first IceCube string deployed in January 2005. The constant value indicates that the DOM's ratio between the variance and mean has settled. The effect of the atmospheric muons is noticeable especially in the top of the detector.

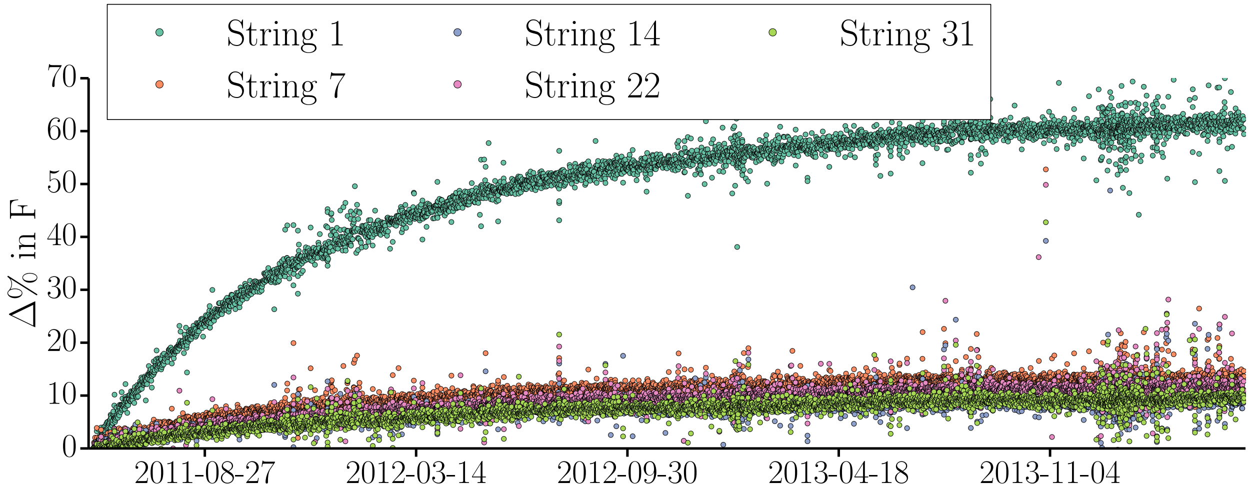

(a) Percentage change in the Fano factor, F, relative to start of IC86-2011, for DOMs deployed in the final season of construction, 2010/2011, at position 30.

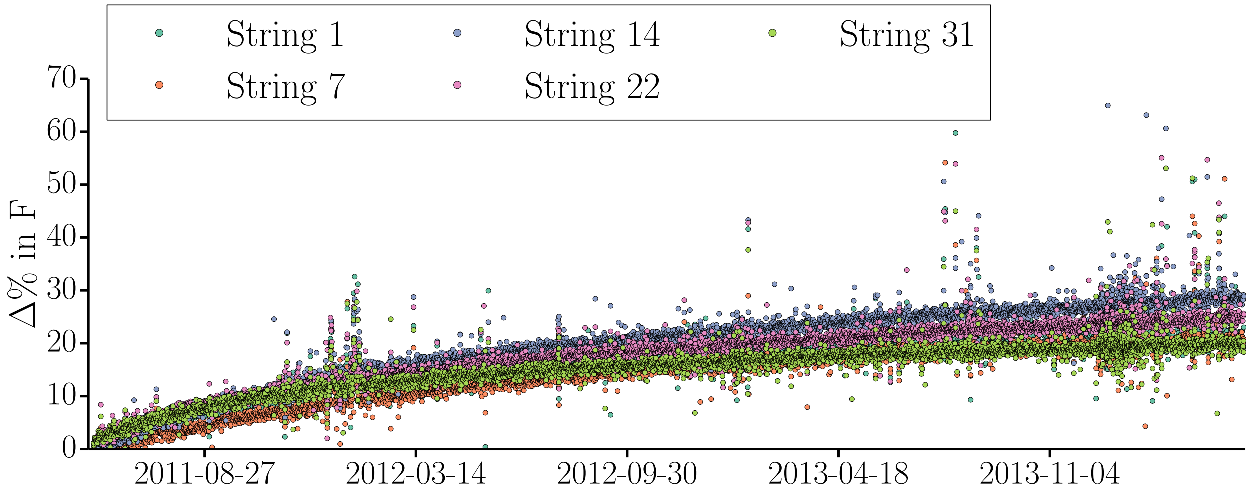

(b) Percentage change in the Fano factor, F, relative to start of IC86-2011, for DOMs deployed in the final season of construction, 2010/2011, at position 60.

Figure 6.22: Percentage change in the Fano factor, $F = \frac{\sigma^2}{\mu}$ [51], relative to the start of IC86-2011, DOMs deployed at position 30 and 60 for DOMs deployed in the final season of construction in the austral summer of 2010/2011. the trends indicate that the decay in the mean and variance of the DOM noise is related to the temperature and the condition of the bore hole surrounding the DOM.

see the transition between IC86-2011 and IC86-2012 in Figure 6.1 and smoothing out of σ_ξ in Figure 6.5 after the introduction of the 1.5 s analysis binning.

The effect of the atmospheric muons on individual DOMs can be seen in from the trend in the Fano factor [51] as a function of depth; see Figure 6.19. The DOMs at the top of the detector experience a higher flux of atmospheric muons; see Figure 5.9. This means that with an increasing atmospheric muon flux the Fano factor will increase.

The cause of the decay is still unknown. The decrease in rate appears to be related to the deployment date and the position in the detector. DOMs deployed at different locations in the detector, but at the same time have different decay constants; see Figure 6.20 and Figure 6.21. Alternatively, DOMs deployed in different seasons have already mostly settled and show similar decay trends between seasons; see Figure 6.14.

A drift in noise rate due to detector-related effects is unlikely, as the detector is calibrated yearly and the changes to the parameters for individual DOM causes discontinuity in the detector noise rate. These discontinuities are significantly smaller than the decay in the detector baseline noise rate, as can be seen by the transition between IC86-2012 and IC86-2013 in Figure 6.13b. A possible relationship between deployment date and position in the detector is hard to establish as every DOM appears to decay differently even at the same positions; see Figure 6.22. This trend does indicate that it is related to the properties of the ice surrounding the DOM. How the construction has affected the ice and how the ice behaves over long periods of time still remains an open question and is especially important for future extensions of IceCube [339, 340]. This is especially true for extensions focused on lower energies [339], as the DOM noise is a large effect in current neutrino oscillation analyses.

Overall, the ∼3.5% decrease in the baseline noise rate contributes to a ∼2% widening of the significance distribution and a ∼0.6% increase in the sensitivity to a given signal. This in turn means that the number of false alerts will increase significantly over time. The expected increase in the number of false alerts over time is inline with the measured increase in the number of false alerts for a given analysis bins. The source of the decrease of the noise rate cannot be fully established. It appears to be related to the freeze-in process and the newly formed ice settling over long time periods and the conditions of the surrounding ice.

6.2 Reducing Effects of Atmospheric Muons using the Volume Trigger

The atmospheric muon subtraction methods outlined in [47, 298] uses the events that include an SMT8 trigger in the DST data; see Section 4.8 and Table 4.3. Both these aspects have a few shortcomings. Atmospheric muons require ∼400 GeV at the glacier's surface to reach the top of IceCube. The energy threshold of the SMT8 trigger is ∼550 GeV. Assuming a power-law energy spectrum for these atmospheric muons, this means that a large flux of atmospheric muons cannot be tagged by this method. Separately, the DST data is a minimalistic representation of data. Not having the full information about individual triggers, *i.e.* which and when DOMs participated and how many times individual trigger conditions were met, makes it impossible to separate out coincident events and could possibly remove events that were associated with a supernova signal. The effect on the SNDAQ analysis of the background reduction technique has not been investigated.

A new online atmospheric muon subtraction method was introduced based on the method discussed in [47]. Instead of using the DST NChannel, the atmospheric muon contribution is estimated by integrated HLC hits in SMT8 trigger window. This does not take into account possible contribution of atmospheric muon SLC hits to the supernova scaler signal and has a shorter integration window (5 µs versus 6 µs [253]). This method has been implemented in the SNDAQ online analysis, which is not possible when using the DST NChannel. The amount of information used by SNDAQ is still minimal. The effect on the supernova signal has not been tested, and the energy threshold for muons to be considered is still higher than the energy threshold of IceCube itself.

Using the volume trigger in addition to the SMT8 trigger would lower the energy threshold for the currently used subtraction methods; see Section 4.8 and Table 4.3. In order to explore the effect of using the volume trigger, one will need to use the information encoded in either SuperDST or from a limited amount of *Hit-Spooling* data. This is necessary because individual events can meet both the volume and SMT8 trigger conditions; see Table 4.3. In DST data, it is impossible to separate out events that fulfill both the volume trigger and SMT8 and coincident events, one fulfilling the volume trigger and one the SMT8.

Currently, SuperDST is only available for event with an NChannel ≥ 25 or every fifth event and for IC86-2012. There are also efforts on the way to convert all triggered data from backup tapes into SuperDST. This conversion has not been completed yet. The NChannel cut removes ∼80% (∼450 Hz versus ∼2100 Hz) of the SMT8 triggers and only events with both a volume trigger and a SMT8 will pass; see Table 4.3. This makes it necessary to use the *Hit-Spooling* data.

Hit-Spooling data is limited because of the short readout window (∼105 s) and there have only been 20 events in SNDAQ that are above the readout threshold of $\xi \geq 7.65$ since *Hit-Spooling*'s introduction in January 2013 and the end of IC86-2013 in May 2014. The data is then triggered using pDAQ's *ReplayHubs*, an extension of pDAQ that can parse *Hit-Spooling* data and produce a data stream from it. This will provide the full information about detector readout and the triggers.

The rate for volume and SMT8 trigger and the respective number of hits in trigger windows are binned in same time bins as SNDAQ. Figure 6.23 shows that the rate for both triggers increases in the bin in which SNDAQ triggered. This effect is independent of the analysis bin size and is expected, as a higher hit rate should correspond a higher trigger rate. The sum of participating DOMs in these triggers, does increase as well for both triggers; see Figure 6.24. This effect appears to be caused solely by the increase in trigger rate in the signal time bin rather than a change in the HLC hit distribution; see Figure 6.25 and 6.26.

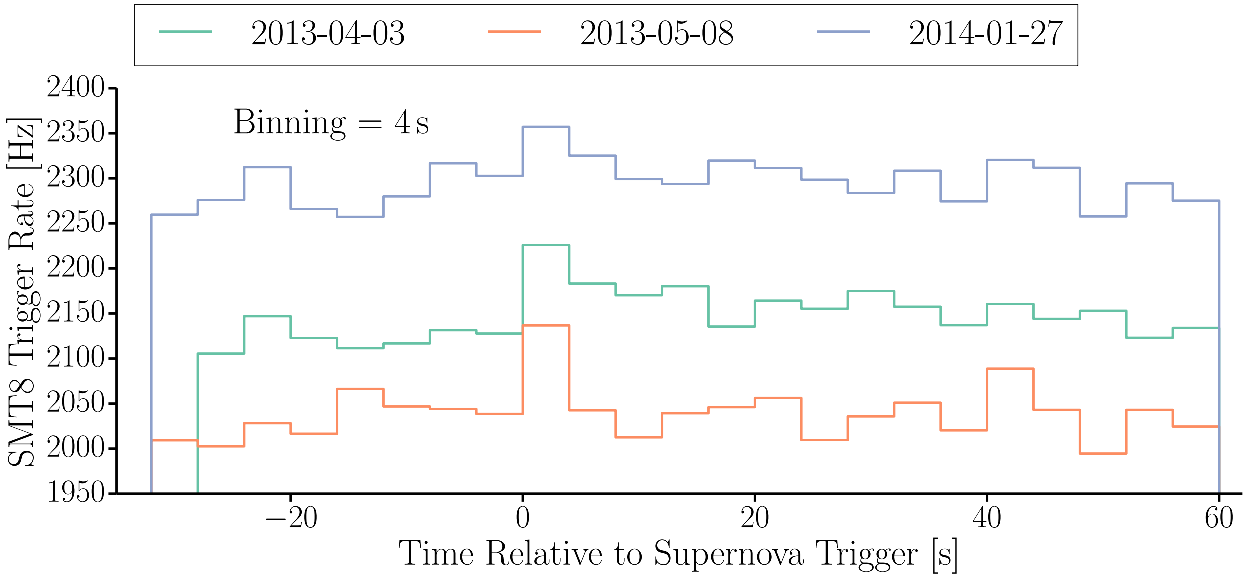

(a) SMT8 trigger rate for three significant alerts with $\xi \geq 7.65$ in the 4 s analysis binning. A peak in the bin that triggered the alert is clearly visible compared to remaining bin.

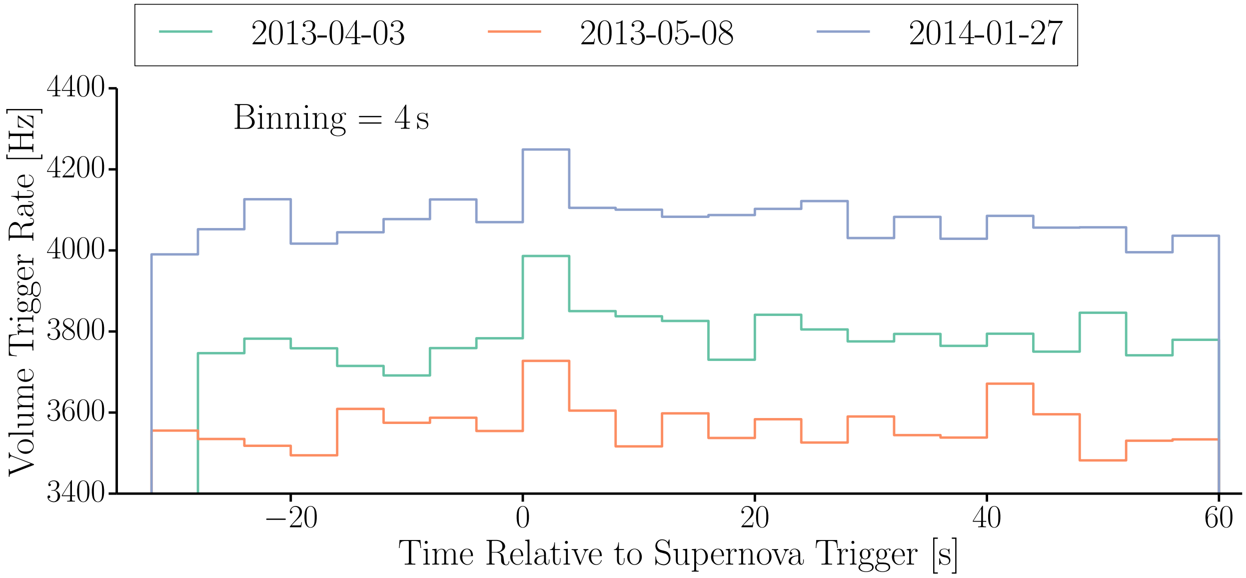

(b) Volume trigger (VT) rate for three significant alerts with $\xi \geq 7.65$ in the 4 s analysis binning. A peak in the bin that triggered the alert is clearly visible compared to remaining bin.

Figure 6.23: Trigger rates for the SMT8 and volume trigger for three significant alerts with $\xi \geq 7.65$ in the 4 s analysis binning. In all triggers a peak is clearly visible during the bin in which the triggered occurred. something here

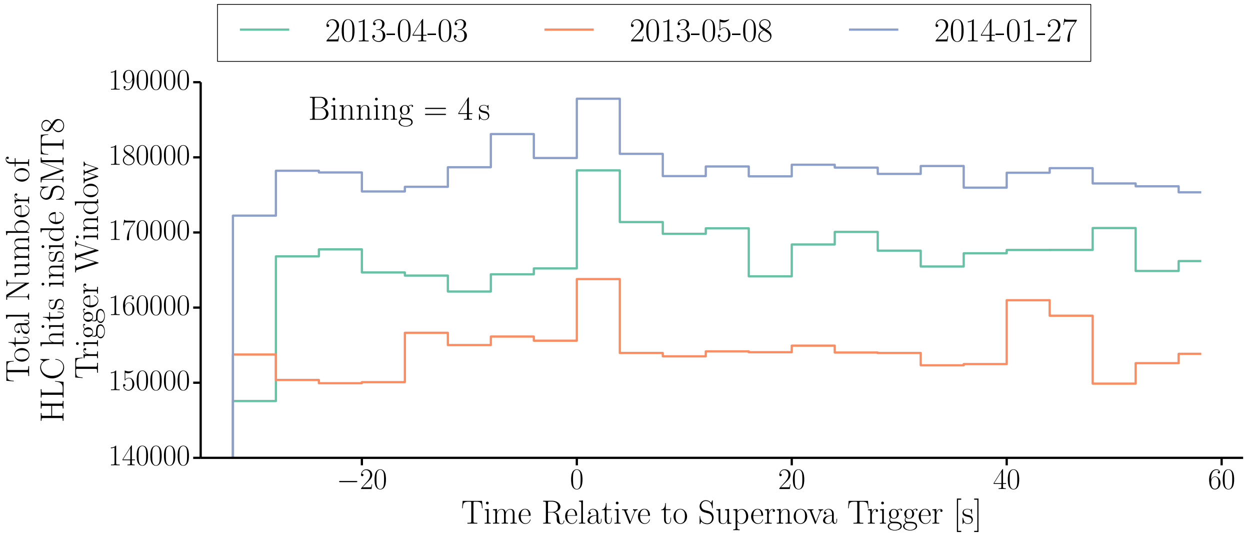

(a) Number of HLC hits inside the SMT8 trigger window for three supernova triggers with $\xi \geq 7.65$ in the 4 s analysis bin. A peak in the number of HLC hits inside the trigger window during the triggered bin is visible.

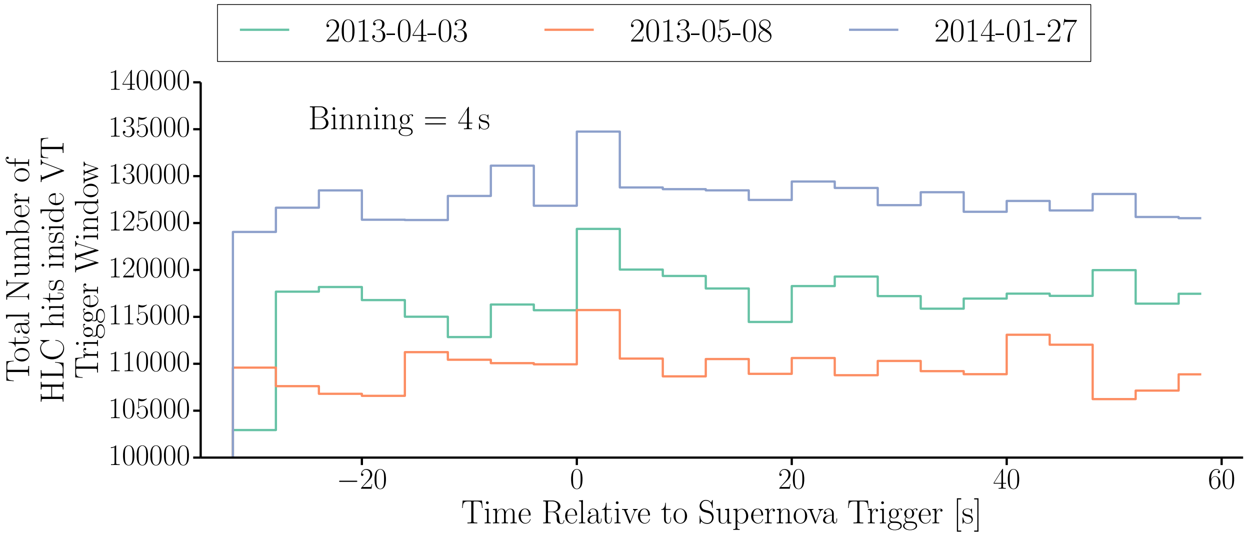

(b) Number of HLC hits inside the volume trigger window for three supernova triggers with $\xi \geq 7.65$ in the 4 s analysis bin. A peak in the number of HLC hits inside the trigger window during the triggered bin is visible.

Figure 6.24: Number of HLC hits inside the SMT8 (top) and volume trigger (bottom) trigger window for three supernova triggers with $\xi \geq 7.65$ in the 4 s analysis bin. A peak in the number of HLC hits inside the trigger window during the triggered bin is visible in both cases. SMT8 is a better measure of the atmospheric muon contribution, as it accounts for more hits inside the trigger window.

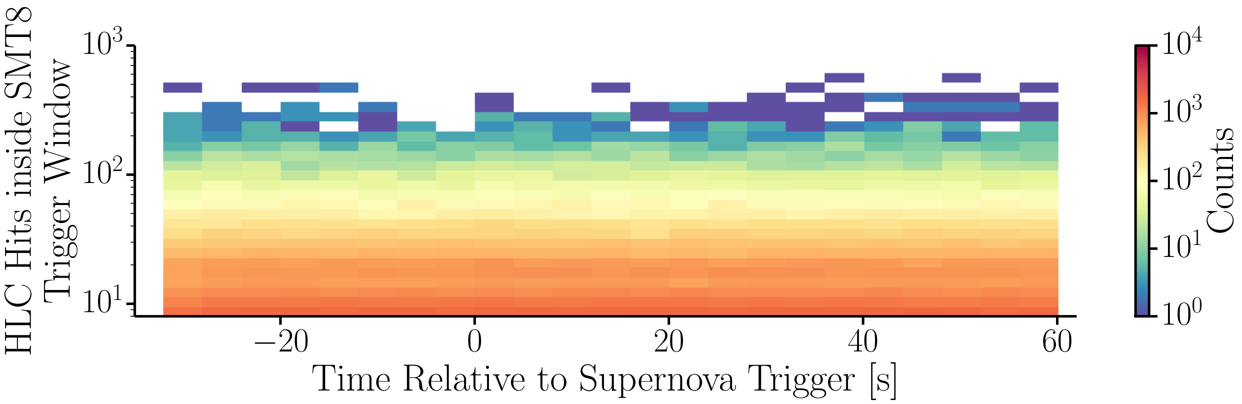

(a) NChannel distribution of the HLC hits inside SMT8 trigger window for the trigger on April 03 2013 in Figure 6.24a

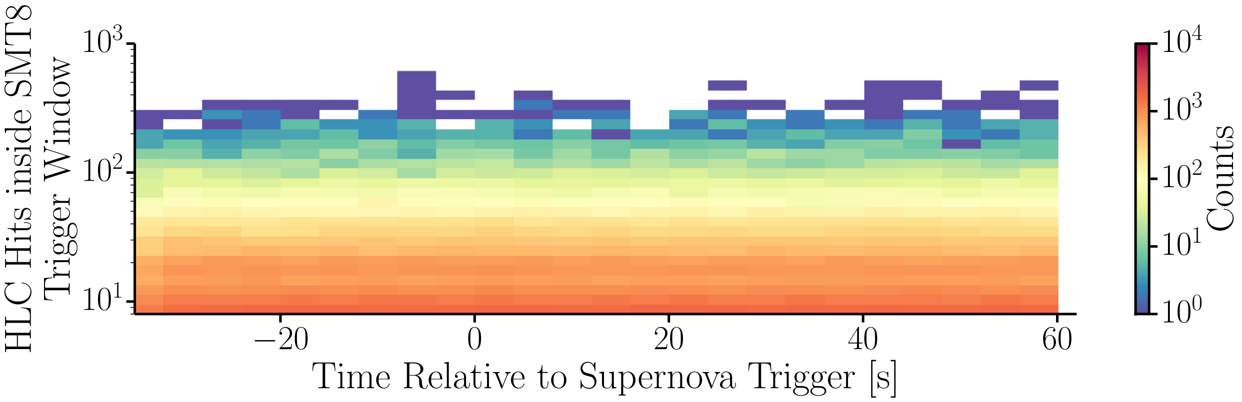

(b) NChannel distribution of the HLC hits inside SMT8 trigger window for the trigger on May 08 2013 in Figure 6.24a

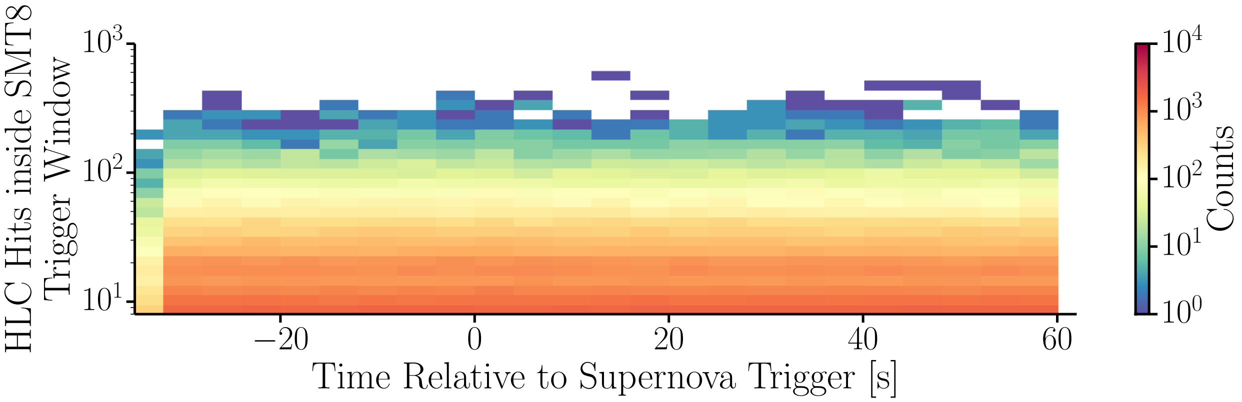

(c) NChannel distribution of the HLC hits inside SMT8 trigger window for the trigger on January 27 2014 in Figure 6.24a

Figure 6.25: NChannel distribution of the HLC hits inside SMT8 trigger window for the triggers shown in Figure 6.24a. There is no clear pattern in the signal bin visible. A closer look reveals that there is slightly higher rate in most NChannel the signal bin.

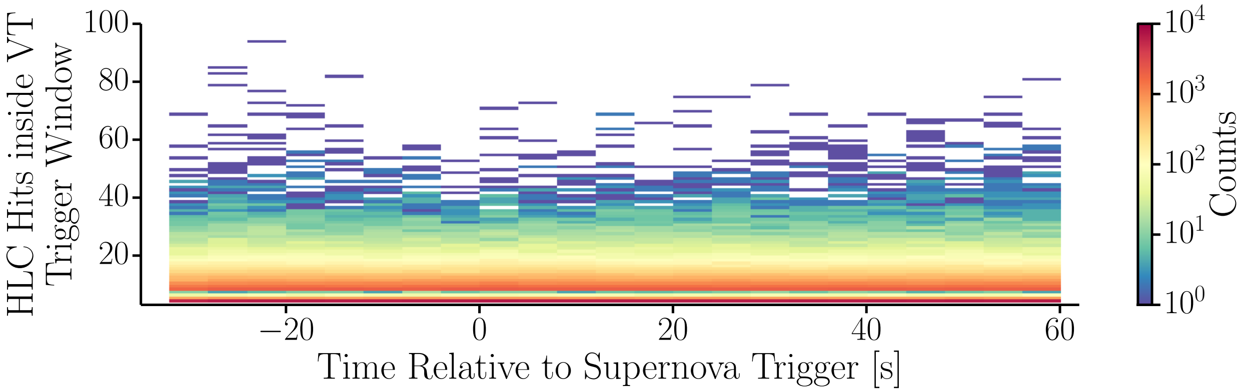

(a) NChannel distribution of the HLC hits inside volume trigger window for the trigger on April 03 2013 in Figure 6.24b

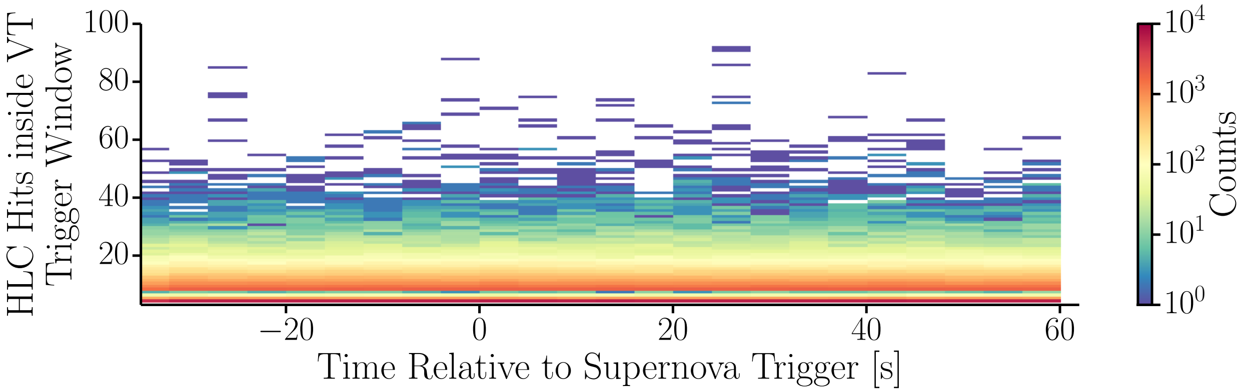

(b) NChannel distribution of the HLC hits inside volume trigger window for the trigger on May 08 2013 in Figure 6.24b

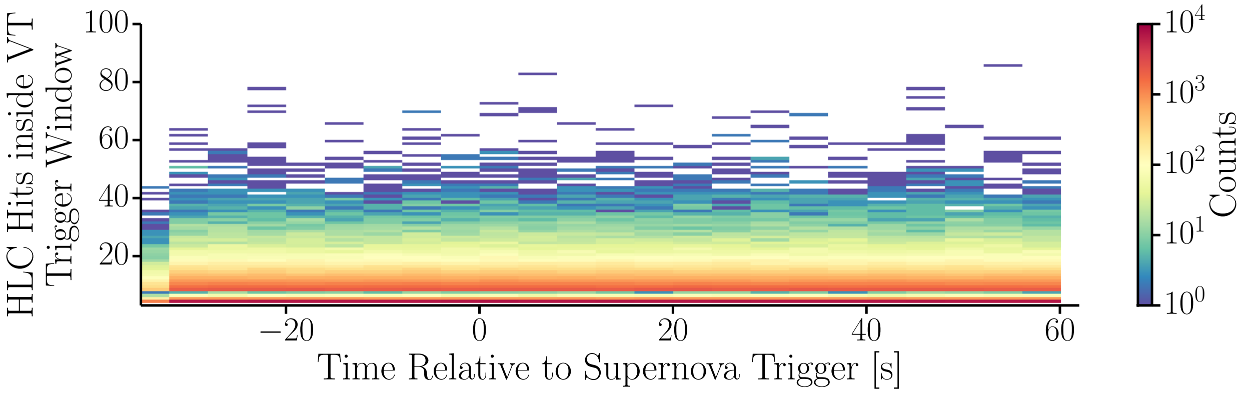

(c) NChannel distribution of the HLC hits inside volume trigger window for the trigger on January 27 2014 in Figure 6.24b

Figure 6.26: NChannel distribution of the HLC hits inside volume trigger trigger window for the triggers shown in Figure 6.24b. There is no clear pattern in the signal bin visible. A closer look reveals that there is slightly higher rate in most NChannel the signal bin.

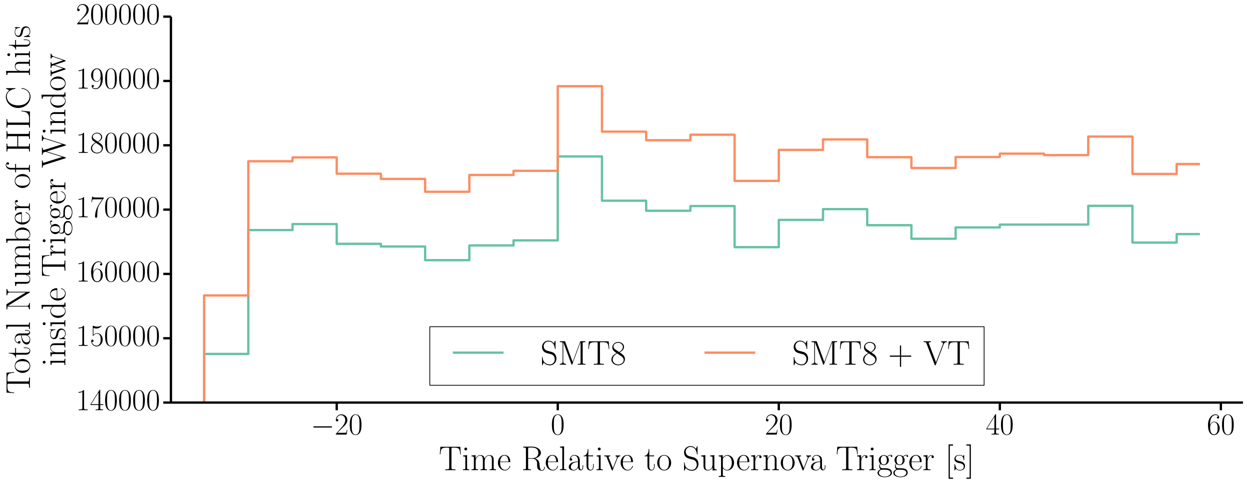

Figure 6.27: Number of HLC hits inside the SMT8 trigger window plus HLC hits inside the SMT8-less volume triggers for the trigger on April 03 2013 in Figure 6.24. One can see that adding the hits from the SMT8-less volume trigger simply shifts the number of hits in the HLC window upward. The shift in the peak is comparable to the shift in the surrounding bins.

Comparing Figure 6.24a and 6.24b, one sees that only using the volume trigger would be a worse measure of the atmospheric muon background compared to the SMT8 trigger. This is caused by much shorter integration window for the volume trigger versus SMT8, *i.e.* 1 µs versus 5 µs, respectively. Only about 18% of volume triggers do not have an SMT8 that is overlapping in time.

This means that certain events that satisfy the volume trigger will also satisfy the SMT8 trigger condition. The overlapping volume triggers are removed in order to avoid double counting hits. Figure 6.28 shows that the remaining triggers are all low energy muons with ≤ 7 participating DOMs.

After adding the hits in the SMT8-less volume triggers to the SMT8 hits, there is still an excess in the signal bin; see Figure 6.27. The excess can be attributed to the increase in SMT8 hits in the signal bin. The SMT8-less volume trigger does not have have a noticeable excess in the signal bin; see Figure 6.29. On average adding the volume trigger adds ∼6.5% more hits per time bin.

In the current hit subtraction method adding the volume trigger will therefore have little to no effect when accounting for double counting. The hit rate in Figure 6.2 will shift rightward by ∼6.5%, thus not altering the effect of the subtraction method. The method employed in [298] would be aided by this result as it is directly subtracting atmospheric muon hits. It can not be used. The DST does not allow for separating out volume triggers and SMT8 triggers in the same way *Hit-spooling* data does.

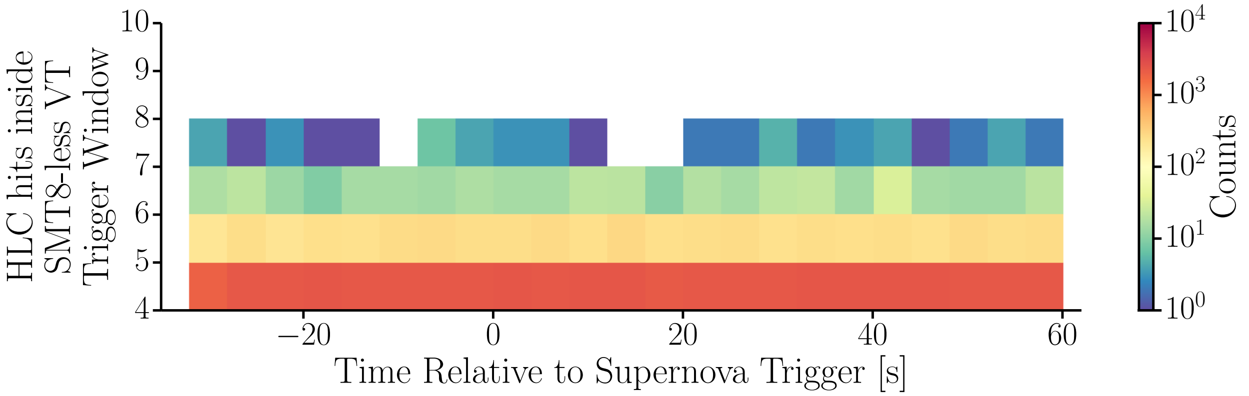

(a) NChannel distribution of the HLC hits inside SMT8-less volume trigger window for the trigger on April 03 2013.

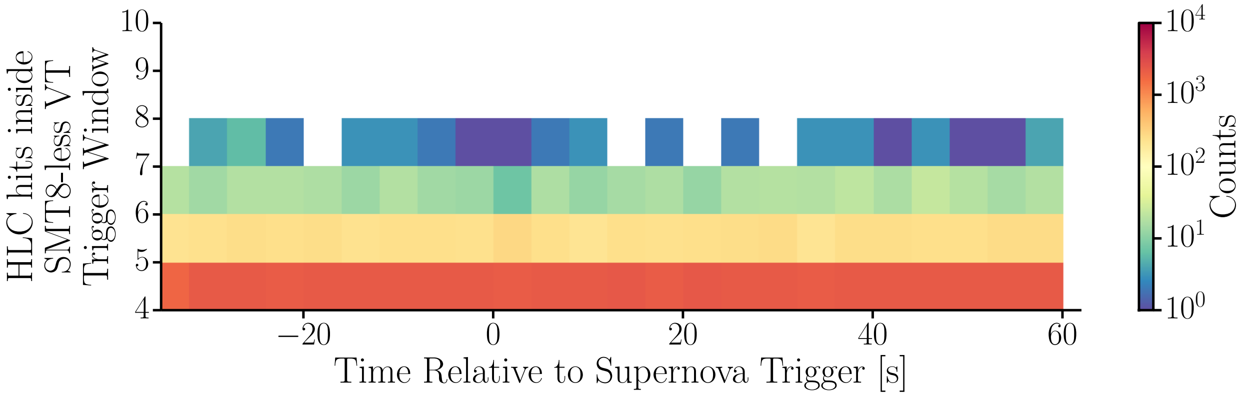

(b) NChannel distribution of the HLC hits inside SMT8-less volume trigger window for the trigger on May 08 2013.

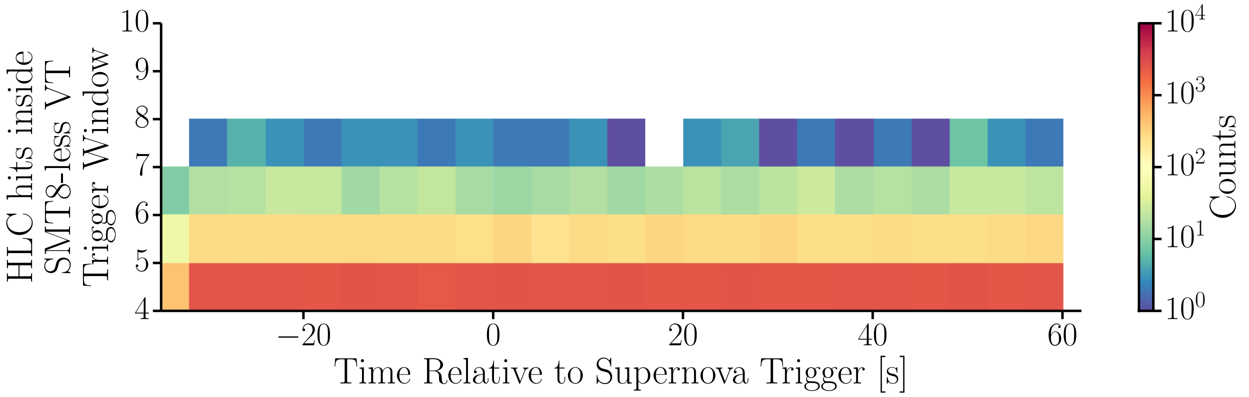

(c) NChannel distribution of the HLC hits inside SMT8-less volume trigger window for the trigger on January 27 2014.

Figure 6.28: NChannel distribution of the HLC hits inside SMT8-less volume trigger trigger window for the triggers shown in Figure 6.24b. There is no clear pattern in the signal bin visible. A closer look reveals that there is slightly higher rate in most NChannel bins the signal bin.

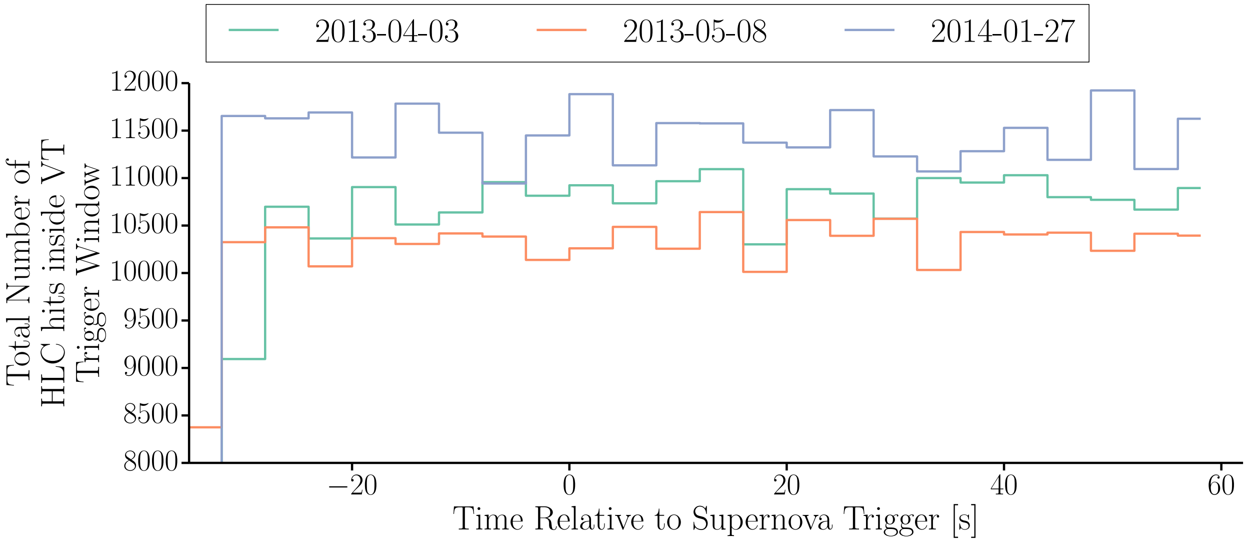

Figure 6.29: HLC hits inside the SMT8-less volume triggers for the triggers in Figure 6.24. As already mentioned in Figure 6.27, the signal bin does not have a measurable difference to the surrounding bins. This means that the SMT8-less volume triggers should not have an impact on current background reduction techniques.

This is not an unsurprising result. The SMT8-less volume trigger still does not fully account for the atmospheric muon flux below the SMT8 threshold. There are coincident events and the trigger conditions selects for atmospheric muon with a certain topology. Separately, given the large increase in hit rate observed for SNDAQ triggers with $\xi \geq 7.65$, one expects a large increase in events with high NChannel rather than a large rate increase in low energy muons.

A supporting trend can be observed when comparing the SMT8 DST data from the signal and background region for false positive supernova triggers from IC86-2012; see Figure 6.30. To do this, the DST data was split into the background and signal region as prescribed for the false positive supernova trigger analysis bin size; see Section 4.9. In the three ξ groupings (6-6.5, 6.5-7.5, and > 7.5) in Figure 6.30, a statistically significant excess is observed for DST NChannel distribution. Additionally, for DST NChannel $\gtrapprox 15$, the signal and background distribution begin to diverge increasingly with larger DST NChannel. This does not indicate whether the false alerts are caused by a large flux of coincident events or higher flux of high energy events. The most likely scenario is that there have to be coincident event with high DST NChannel in the signal bin. This can happen as the integration period for the SNDAQ analysis is significantly longer than that for individual triggers.The trend in Figure 6.30 also shows that no single event causes false positive triggers.

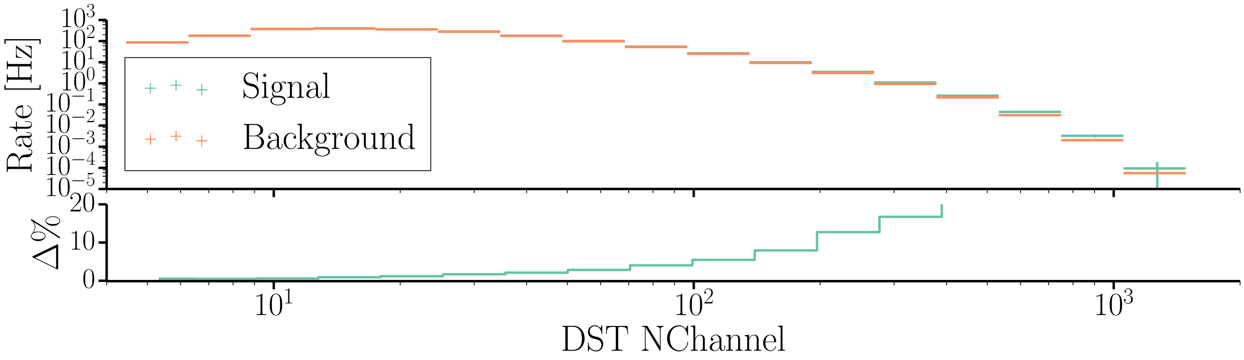

(a) DST NChannel distribution for signal and background regions for false positive supernova triggers from IC86-2012 with $6 \leq \xi < 6.5$

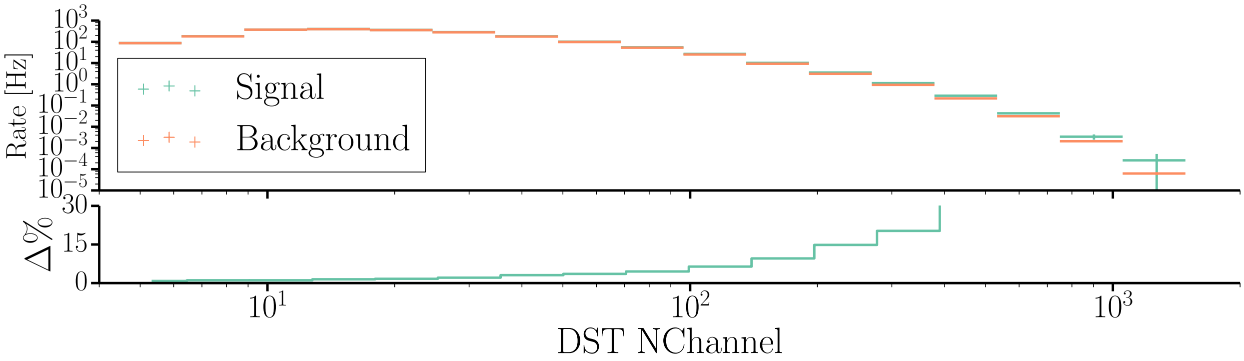

(b) DST NChannel distribution for signal and background regions for false positive supernova triggers from IC86-2012 with $6.5 \leq \xi < 7.5$

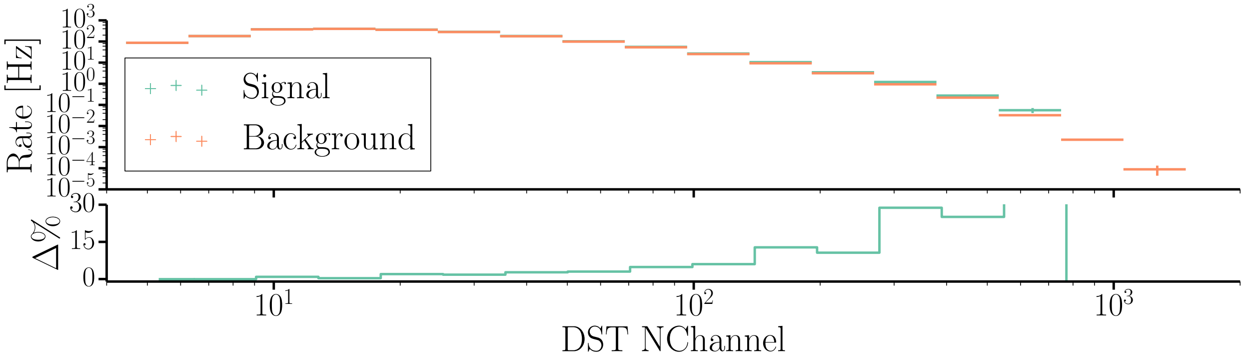

(c) DST NChannel distribution for signal and background regions for false positive supernova triggers from IC86-2012 with $\xi \geq 7.5$

Figure 6.30: DST NChannel distribution for signal and background regions for false positive supernova triggers from IC86-2012 in three different ξ groups: 6-6.5 (top), 6.5-7.5 (middle), and > 7.5 (bottom). This is done for better comparison. All three groups of alerts show similar trends, in which the signal and background distribution start diverging at NChannel.

The false positive false alerts are therefore caused by significant upward fluctuations in the atmospheric muon background.

In conclusion, the volume trigger by itself will not improve current background subtraction method employed in SNDAQ. Adding the hits from volume triggers to the hit rate as estimated by the SMT8 trigger does not significantly affect the hit rate in the signal bin compared to the background bins. Separately, this means that most false positive triggers are caused by having a statistically higher rate and number of events in with DST NChannel $\gtrapprox 15$. In case the hits were subtracted using SuperDST data without the NChannel cut, the volume trigger would help in reducing the effect of atmospheric muons.

Chapter 7

Conclusion and Outlook

So eine Arbeit wird eigentlich nie fertig.
Man muss sie als fertig erklären,
wenn man nach Zeit und
Umständen das Mögliche getan hat.
–Johann Wolfgang von Goethe
Italienische Reise, 1786

7.1 Summary of Results

This work has shown that the simulation of supernova neutrinos in the IceCube Neutrino Observatory's simulation framework can be performed in a computationally feasible manner. The simulation represents a new tool in studying the detector response to supernova neutrino signals. Making it possible to study the response in most detailed manner yet possible. Additionally, this method is applicable to future proposed extensions of IceCube [339, 340] or new proposed large volume neutrino detectors, especially in the Antarctic ice shelf [341, 342]. The background simulation has shown that there are large disagreements between data and simulation. These disagreements stem from discrepancies in the DOM noise and the atmospheric muon simulation that have to be explored further.

Besides the simulation framework, the long standing issue of the increasing sensitivity to the atmospheric muon background of the supernova online analysis in the completed IceCube detector has been explained. The exponential decay in the mean detector noise rate by ∼3.5% over the course of three years of data taking with the completed detector has produced has increased the sensitivity to atmospheric muons by ∼2%. This produces a ∼0.6% increase in the sensitivity to supernova neutrino signals and a 48% increase in the false positive triggers.

Finally, a preliminary look at the impact of the volume trigger on atmospheric muon background subtraction techniques from *Hit-spooling* data is taken. Using this trigger, one is able to tag ∼6.5% more atmospheric muon hits compared to just using the SMT8 trigger. In the background reduction scheme developed in [47] this has little to no effect. The method in [298] would be aided by this method as atmospheric muon hits are subtracted from the stream.

7.2 Outlook

This section will provide an outlook on the possible improvements and extensions to the new simulation framework and the data sets used and discussed in the analysis in Chapter 6. Future versions of the supernova online analysis and proposed extensions and new neutrino detectors are discussed as well.

7.2.1 Simulation

The new simulation tool makes it possible to study new techniques for analysis of supernova neutrino signals and to reduce the impact of the atmospheric muon background. At the forefront of future work in the area of supernova neutrinos in IceCube, is reducing the impact of atmospheric muons on the online analysis and studying the impact of current techniques on the supernova analysis. It has not been established what fraction of the signal is removed by current background reduction technique or what the impact on the overall IceCube trigger rate is. This has been discussed in Section 5.4.

The new framework will also help in exploring new techniques in understanding the supernova neutrino signal and extracting information from other data streams, mainly SuperDST, DST, and *Hit-Spooling*, in IceCube. Besides the already mentioned efforts to determine the average energy of the neutrinos, there is work going on to determine the neutrino mass and hierarchy using theoretical signals. Being able to study the signal in detail using all IceCube data channels will be especially helpful in future endeavors of this kind.

New analysis techniques for the SNDAQ analysis can now be explored in a controlled environment. This provides the means to use future improvements to pDAQ and the online processing to be incorporated into the SNDAQ analysis or for SNDAQ to be incorporated into the online processing. Additionally, open questions about the stability of pDAQ for close-by supernova, *i.e.* $\leq 1\,\mathrm{kpc}$, could be answered once a conversion from the IceTray format to the DAQ-compatible *Hit-spooling* format has been completed.

The physics capabilities of future proposed detector extensions, such as the Precision IceCube Next Generation Upgrade (PINGU) and High Energy Extension (HEX), have yet to be fully explored. Once the detector geometries and hardware have been finalized, future studies are needed. This is especially necessary considering the effects of atmospheric muons increase with detector size; see Section 6.1 and [47]. This is especially true for future detectors that are build for proton decay studies and search for $\mathcal{O}(1\text{–}10\,\mathrm{MeV})$ neutrinos in the Antarctic ice shelf.

Improvements can be made to any software. In this case, some major improvements would be the better overall handling of ν–e^- scattering and ν–O interaction cross-sections and combing several cross-section simulation together. These are not well tested, especially, the energy of the products of the interaction.

They cannot be compared to the ones used in the USSR, as they are differently implemented. In case neutrino oscillations are not being considered, the generation weight will have to be adjusted for the energy bias that introduced by the ensemble. The oscillation weight will also have to be improved to show the effect from other oscillation scenarios.

The structure of the code can also be improved. This means to break up the code further, *i.e.* moving functions and functionality outside of the modules mentioned in Section 5.2.2.1 and 5.2.2.2 into dedicated functions. Additional improvements are accessing internal function from Python besides C++ and removing dependencies on other parts of *IceSim*.

7.2.2 Supernova Scaler, Monitoring, DST, and SuperDST data sets

The data sets used to determine the effect of the detector decay on the SNDAQ analysis offers a variety of additional possibilities. The supernova scalers, as per their design, provide the means to perform a long-term study of trends in the detector noise rate. The detector noise has significant impact on the neutrino oscillation analyses in IceCube. A long-term trend in the baseline noise rate has to considered in future analyses of DeepCore data that use data taking during IC79, IC86-2011, IC86-2012, and IC86-2013. The sensitivity of these analyses and especially the contamination of the signal due to detector noise will change over time. In order to correct for this effect, one would have to estimate the decay for every DOM independently.

Various methods to determine the decay were explored during the completion of this work. One of the major obstacles to determining the per-DOM decay constant is parametrizing the per-DOM periodic contribution from atmospheric muons with time. The most promising method to reduce this background is to use the per-DOM HLC rate as an estimate for the atmospheric muon contribution to a given DOM supernova scaler signal or SLC rate. The long-term trend of both the per-DOM SLC and HLC rate can be determined from the monitoring files provided by pDAQ; see Figure 4.21 and 4.22. A fit can then be performed using

$$R_{\text{SLC/SN Scaler}} = R^{\text{Base}}_{\text{SLC/SN Scaler}} + A \cdot (R_{\text{HLC}} - \langle R_{\text{HLC}} \rangle - R^{\text{Coincidence}}_{\text{HLC}}) + B \cdot \exp(-t \cdot \tau) \tag{7.1}$$

where $R_{\text{SLC/SN Scaler}}$ is the total SLC or supernova scaler rate for a given DOM, $R^{\text{Base}}_{\text{SLC/SN Scaler}}$ is the baseline SLC or supernova scaler rate, A is a scale factor to compensate for the difference rate of SLC or supernova scaler hits to HLC hits from atmospheric muons, R_{HLC} is the HLC rate, $\langle R_{\text{HLC}} \rangle$ is the average HLC rate for the given DOM over the course of one detector year, $R^{\text{Coincidence}}_{\text{HLC}}$ is the HLC rate due to random coincidence between DOMs estimated from *vuvuzela*, and $B \cdot \exp(-t \cdot \tau)$ is the exponential decay component of the noise.

New background reduction technique for the search for supernova neutrinos in IceCube should use of SuperDST data instead of DST data. SuperDST stores the information from the individual DOMs that were being readout out during a triggered event. This is a clear advantage to the data stored in the DST format. This allows for a much better rejection of atmospheric muon events. DOM triggers produced by the event can be subtracted from the supernova scalers from DOMs that contributed rather than employing a statistical methods correct for the effect of atmospheric muons or subtracting the DOMs triggers from randomly selected DOMs in the detectors. In case of a supernova, this data would also allow one to discern between hits produced by atmospheric muons and the supernova, especially in case the SMT8 trigger rate or the HLC rate were affected by the supernova neutrino signal.

Hit-Spooling data could also be employed for future background reduction techniques. A possible method will be proposed in [297]. To be able to do so further study is needed, especially of the effect of the supernova signal on the *Hit-Spooling* readout.

The sun follows a ∼11 year activity cycle [343,344]. The next maximum will be reached in late 2014. This means that during the last three years of IceCube's operation the solar activity has steadily increased. Such an increase in solar activity could causes changes to the solar irradiation of the upper atmosphere and in turn changes in atmospheric properties [345]. This could cause an increasing atmospheric muon flux observed by IceCube. During the last three years a trend towards higher median rate and longer periods at higher rates have been observed; see Section 6.1.1. This trend could be indicative of a change atmospheric properties due to the solar cycle. At least three additional years of trigger rate and DST data with a thorough study of possible systematics that could effect this trend are needed to support this hypothesis.

Cosmic ray interactions in the solar atmosphere can produce produce $\mathcal{O}(0.5\text{–}10\,\text{GeV})$ neutrinos [346–349]. These interactions could cause a sub-threshold signal in IceCube, which would be detectable as fluctuations in the noise rate. Similarly, the solar flares can produce a large flux of charged particles and neutrinos [350,351]. These flares are typically associated with sunspots or areas of high activity [352]. The number of sunspots follows the solar cycle [353]. This means that the flux of these sub-threshold neutrinos would modulate with the solar cycle and may be detectable in the supernova scaler stream.

Searches for neutrinos coincident with Fast Radio Brusts [354, 355] are currently being performed across large energy range, including sub-threshold neutrinos at energies of $\mathcal{O}(\text{MeV-GeV})$. The supernova scalers are needed as they provide an untriggered stream,and should sensitive to a large flux of sub-threshold neutrinos.

7.2.3 The Future of Supernova DAQ

The current SNDAQ implementation is based on a version that was deployed starting with 40-string configuration. The improvements made since then have focused on code structure, communications with other systems in IceCube, and introduced an online atmospheric muon subtraction method based the methods introduced in [47] and described in Chapter 6.

These are steps forward. Some inherent flaws remain. Using SNDAQ, may it be reading its output files, compiling the code, or simply running it, requires expert knowledge and a specifically setup system. This circumstance makes it extraordinarily hard for non-expert members of the collaboration to use it or the data for that matter. An additional concern is the future addition of more individual modules to IceCube, which will increase the sensitivity of the analysis to atmospheric muons, and potential changes in DOM electronics that are being considered for future extensions [339]. Future versions of SNDAQ will have to handle data from the current and future hardware.

This requires that SNDAQ be re-implemented focusing on these concerns. To open the analysis and data up to a wider community, SNDAQ should be moved into the IceCube software framework, *IceTray*. This would move the data into the *IceTray* file format and could therefore be used by other members of the collaboration. Separately, the software is maintained within the collaboration, there is significant amount of experience in using the framework. The framework also already implements and maintains most of the necessary software to handle IceCube-specific attributes of the data, for example the conversion from DOM mainboard ID to a human-readable format as well as handle standard IceCube data.

At the moment, the offline atmospheric muon subtraction method requires the conversion of *IceTray* files into ROOT files [356] in order for SNDAQ to parse the data. This transition would also make it possible to easily integrate the supernova data stream with the triggered stream online instead of having to rely an *a posterior* online subtraction.

7.2.4 Future Supernova Neutrino Detectors

The holy grail of supernova neutrino astronomy is being able to produce a catalog of supernovae. This means that at least one supernova per year would have to be detected with neutrinos. Building the required detector or detectors is still far in the future, as it would require detectors with a fiducial mass of $\mathcal{O}(1\text{–}100\,\text{Mtons})$ depending on the detection technology [357].

There are multiple proposal for the next generation of neutrino detectors that are sensitive to supernova neutrinos and would improve our understanding of the signal. The most promising of these are upgrades to existing detectors, such as IceCube with PINGU [339] and HEX [340] and gadolinium-doping SuperK (Gadolinium Antineutrino Detector Zealously Outperforming Old Kamiokande, Super!–GADZOOKS!) [358–361]. There are also multiple proposal for future neutrino detectors using a wide-range of technologies: water Cherenkov (Hyper-Kamiokande (Hyper-K) [362] and Multi-Megaton Ice Cherenkov Array (MICA) [342, 363, 364]), liquid argon (Long-Baseline Neutrino Experiment (LBNE)[1] [366]) and liquid scintillator (Low Energy Neutrino Astronomy (LENA) [367]).

Upgrades to existing facilities would only push the sensitivity to supernovae a little bit further out in terms of distance, the possible physics research of individual experiments is extend significantly. With the

---

[1] The LBNE collaboration has since been dissolved and reformed as the Long-Baseline Neutrino Facility (LBNF) collaboration in accordance with the Particle Physics Project Prioritization Panel report [365]. Since detector technology for LBNF has not been decided, LBNE is used as an example for a future large liquid argon neutrino detector.

future PINGU upgrade, IceCube would be able to perform more in depth studies of the neutrino properties, specifically the average neutrino energy [339]. HEX would increase the overall statistics of the signal. GADZOOKS! would improve Super-K's sensitivity to ν_e, which would be an important in identifying the deleptonization peak and neutrino trapping, and directional reconstruction.

Hyper-K will be able to detect $\mathcal{O}(10)$ neutrinos from supernovae as far as out as Andromeda. This a significant improvement on SuperK. The reach still false short for building a catalog. The main advantage of HyperK is the high statistics measurement of the neutrino energy spectrum and improvements of the timing resolution. This will provide information about the evolution of the energy spectrum or possible oscillation scenarios that can change with time. Hyper-K does have a very high cost because of the large excavation work needed to accommodate the new detector.

MICA is a proposed future neutrino detector in the Antarctic ice shelf focused on proton decay, solar neutrinos, supernova neutrinos. It will deploy pressure vessels with smaller multiple PMTs or wavelength shifting light guides in the ice shelf that will be able to resolve the Cherenkov ring [364]. With its proposed design it will be one of the first detectors that could detect supernova neutrinos from $\mathcal{O}(1\,\mathrm{Mpc})$.

LBNE is the next generation accelerator-based neutrino oscillation experiment. With a proposed fiducial mass of 34 ktons of liquid argon, LBNE would have the highest sensitivity to ν_e from a supernova of all currently operating detectors. This would help in identifying features of the supernova neutrino time and energy spectrum that are only present in the ν_e flux; see Section 3.4 and [366, 368]. The detector would also be extraordinarily sensitive to oscillations scenarios involving neutrino-neutrino interactions. A possible spectral feature that water-based detectors can hardly identify. LBNE would only be able to detect supernova neutrinos from within our galaxy, but provide an invaluable addition to the current supernova neutrino experiments.

Future large liquid scintillator experiments, such as the proposed LENA, will complement future neutrino detectors such as LBNE. The sensitivity compared to current liquid scintillator-based and even water based experiments would be increase by at least a factor ≥ 2. This does not make detection from outside the galaxy feasible. The calorimetric, higher sensitivity, especially compared to SuperK, and pointing would add another invaluable piece to the puzzle.

Future neutrino experiments will take a step towards increasing the physics reach of detecting neutrinos from a galactic supernova. The detection of extra-galactic supernova neutrinos is still decades in the future. There are steps being taken to move this to become a reality than just an idea.

LIST OF REFERENCES

[1] G. L. Fogli et al. Global analysis of neutrino masses, mixings, and phases: Entering the era of leptonic CP violation searches. *Physical Review D*, 86(1):013012, July 2012. `arXiv:1205.5254`, `doi:10.1103/PhysRevD.86.013012`.

[2] F. Capozzi et al. Status of three-neutrino oscillation parameters, circa 2013. *Physical Review D*, 89(9):093018, May 2014. `arXiv:1312.2878`, `doi:10.1103/PhysRevD.89.093018`.

[3] R. Tomàs et al. Supernova pointing with low- and high-energy neutrino detectors. *Physical Review D*, 68:093013, Nov 2003. URL: `http://link.aps.org/doi/10.1103/PhysRevD.68.093013`, `doi:10.1103/PhysRevD.68.093013`.

[4] Lukas Schulte. Supernova Detection in a future Extension of the IceCube Neutrino Telescope. Master's thesis, Johannes Gutenberg-Universität Mainz, Mainz, June 2011.

[5] John Kelley. Event Triggering in the IceCube Data Acquisition System. In *Proceedings of the VLVnT 2013 Workshop (Stockholm, Sweden)*, AIP Conference Proceedings, to be published.

[6] David Glowacki. Personal Communication.

[7] Gösta Kroll. Personal Communication.

[8] Anglo-Australian Observatory, 2014 (accessed Sept. 7 2014). URL: `http://www.aao.gov.au/`.

[9] Quark Stars, 2014 (accessed Sept. 7 2014). URL: `http://universe-review.ca/F08-star15.htm`.

[10] M.S. Gordon et al. Alpha-Particle Emission Energy Spectra From Materials Used for Solder Bumps. *Nuclear Science, IEEE Transactions on*, 57(6):3251–3256, Dec 2010. `doi:10.1109/TNS.2010.2085015`.

[11] T2K Collaboration. A Brief History Of Neutrinos, 2013 (accessed August 25 2014). URL: `http://t2k-experiment.org/neutrinos/a-brief-history/`.

[12] J. Beringer et al. Review of Particle Physics. *Physical Review D*, 86:010001, Jul 2012. URL: `http://link.aps.org/doi/10.1103/PhysRevD.86.010001`, `doi:10.1103/PhysRevD.86.010001`.

[13] David Galbraith and Carsten Burgard. Standard Model Standard Infographic, August 2012. URL: `http://davidgalbraith.org/portfolio/ux-standard-model-of-the-standard-model/`.

[14] Thomas Kowarik. *Supernova Neutrinos in AMANDA and IceCube*. PhD thesis, Johannes Gutenberg-Universität Mainz, November 2010. URL: `http://ubm.opus.hbz-nrw.de/volltexte/2010/2466/pdf/doc.pdf`.

[15] M. Herant, S. Colgate, W. Benz, and C. Fryer. Neutrinos and Supernovae. *Los Alamos Science*, 25:64–79, November 1997. URL: `http://library.lanl.gov/cgi-bin/getfile?25-14.pdf`.

[16] European Southern Observatory. Hertzsprung-Russel Diagram, 2012 (accessed June 16 2012). URL: `https://www.eso.org/public/images/`.

[17] European Southern Observatory. Hertzsprung-Russel Diagram, 2012 (accessed Sept. 19 2014). URL: `https://en.wikipedia.org/wiki/File:Hertzsprung-Russel_StarData.png`.

[18] J. Jeff Hester. The Crab Nebula: An Astrophysical Chimera. *Annual Review of Astronomy and Astrophysics*, 46(1):127–155, 2008. URL: `http://dx.doi.org/10.1146/annurev.astro.45.051806.110608`, `doi:10.1146/annurev.astro.45.051806.110608`.

[19] NASA, ESA, J. Hester, and Loll A. A Giant Hubble Mosaic of the Crab Nebula, December 2005. URL: `http://hubblesite.org/newscenter/archive/releases/2005/37/image/a/`.

[20] NASA, ESA, JPL-Caltech, CXC, J. Hester, A. Loll, and R. Gehrz. NASA's Great Observatories' View of the Crab Nebula, November 2009. URL: `http://www.spitzer.caltech.edu/images/2857-sig09-009-NASA-s-Great-Observatories-View-of-the-Crab-Nebula`.

[21] Takashi Kunugise and Koichi Iwamoto. Neutrino Emission from Type Ia Supernovae. *Publications of the Astronomical Society of Japan*, 59:L57, December 2007. URL: `http://adsabs.harvard.edu/cgi-bin/nph-data_query?bibcode=2007PASJ...59L..57K&link_type=ABSTRACT`.

[22] T. Totani, K. Sato, H.E. Dalhed, and J.R. Wilson. Future detection of supernova neutrino burst and explosion mechanism. *Astrophysical Journal*, 496:216–225, 1998. `arXiv:astro-ph/9710203`, `doi:10.1086/305364`.

[23] H.-T. Janka et al. Theory of core-collapse supernovae. *Physics Reports*, 442(1):38–74, 2007. URL: `http://adsabs.harvard.edu/cgi-bin/nph-data_query?bibcode=2007PhR...442...38J&link_type=ABSTRACT`, `arXiv:astro-ph/0612072`.

[24] L. Hüdepohl et al. Neutrino Signal of Electron-Capture Supernovae from Core Collapse to Cooling. *Physical Review Letters*, 104(25):251101, June 2010. `arXiv:0912.0260`, `doi:10.1103/PhysRevLett.104.251101`.

[25] H. Shen, H. Toki, K. Oyamatsu, and K. Sumiyoshi. Relativistic equation of state of nuclear matter for supernova and neutron star. *Nuclear Physics A*, 637(3):435 – 450, 1998. URL: `http://www.sciencedirect.com/science/article/pii/S037594749800236X`, `doi:10.1016/S0375-9474(98)00236-X`.

[26] H.-T. Janka. Explosion Mechanisms of Core-Collapse Supernovae. *Annual Review of Nuclear and Particle Science*, 62:407–451, November 2012. `arXiv:1206.2503`, `doi:10.1146/annurev-nucl-102711-094901`.

[27] F. S. Kitaura, H.-T. Janka, and W. Hillebrandt. Explosions of O-Ne-Mg cores, the Crab supernova, and subluminous type II-P supernovae. *Astronomy and Astrophysics*, 450:345–350, April 2006. `arXiv:astro-ph/0512065`, `doi:10.1051/0004-6361:20054703`.

[28] K. Sumiyoshi, S. Yamada, and H. Suzuki. Dynamics and neutrino signal of black hole formation in non-rotating failed supernovae. 1. EOS dependence. *Astrophysical Journal*, 667:382–394, 2007. `arXiv:0706.3762`, `doi:10.1086/520876`.

[29] J. N. Bahcall and T. Piran. Stellar collapses in the galaxy. *Astrophysical Journal Letters*, 267:L77–L81, April 1983. `doi:10.1086/184007`.

[30] R. Abbasi et al. IceCube sensitivity for low-energy neutrinos from nearby supernovae. *Astronomy and Astrophysics*, 535:A109, November 2011. `doi:10.1051/0004-6361/201117810`.

[31] Carlo Giunti and Chung Wook Kim. *Fundamentals of neutrino physics and astrophysics*. Oxford University Press, USA, May 2007. URL: `http://books.google.com/books?id=2faTXKIDnfgC&printsec=frontcover&dq=Fundamentals+of+Neutrino+Physics+and+Astrophysics&cd=1&source=gbs_api`.

[32] M.G. Aartsen et al. Evidence for High-Energy Extraterrestrial Neutrinos at the IceCube Detector. *Science*, 342:1242856, 2013. `arXiv:1311.5238`, `doi:10.1126/science.1242856`.

[33] Thomas K. Gaisser. *Cosmic Rays and Particle Physics*. Cambridge University Press, 1990.

[34] James J. Beatty and Stefan Westerhoff. The Highest-Energy Cosmic Rays. *Annual Review of Nuclear and Particle Science*, 59:319–345, 2009. `doi:10.1146/annurev.nucl.58.110707.171154`.

[35] B. Louis et al. *Los Alamos Science*, 25, November 1997. URL: `http://library.lanl.gov/cgi-bin/getfile?25-09.pdf`.

[36] M. Thunman, G. Ingelman, and P. Gondolo. Charm production and high energy atmospheric muon and neutrino fluxes. *Astroparticle Physics*, 5:309–332, October 1996. `arXiv:hep-ph/9505417`, `doi:10.1016/0927-6505(96)00033-3`.

[37] M. Honda, T. Kajita, K. Kasahara, and S. Midorikawa. New calculation of the atmospheric neutrino flux in a three-dimensional scheme. *Physical Review D*, 70(4):043008, August 2004. `arXiv:astro-ph/0404457`, `doi:10.1103/PhysRevD.70.043008`.

[38] National Weather Service. Standardized Temperature Profile, 2013 (accessed Sept. 12 2014). URL: `http://www.srh.noaa.gov/jetstream/atmos/atmprofile.htm`.

[39] F. James. *Statistical Methods in Experimental Physics*. World Scientific, 2006. URL: `http://books.google.com/books?id=S8N_QgAACAAJ`.

[40] Jakob van Santen. Markov-Chain Monte-Carlo Reconstruction for Cascade-like Events in IceCube. Master's thesis, Humboldt-Universität zu Berlin, January 2010. URL: `http://icecube.wisc.edu/~jvansanten/lit/jvs_diplom.pdf`.

[41] Kurt Woschnagg. New ice model, May 2008. URL: `https://wiki.icecube.wisc.edu/index.php/Aha#Naming_the_new_ice_model`.

[42] M.G. Aartsen et al. Measurement of South Pole ice transparency with the IceCube LED calibration system. *Nuclear Instruments and Methods in Physics Research A*, 711(0):73 – 89, 2013. URL: `http://www.sciencedirect.com/science/article/pii/S0168900213001460`, `arXiv:1301.5361`, `doi:10.1016/j.nima.2013.01.054`.

[43] Johan Lundberg et al. Light tracking for glaciers and oceans: Scattering and absorption in heterogeneous media with Photonics. *Nuclear Instruments and Methods in Physics Research A*, A581:619–631, 2007. `arXiv:astro-ph/0702108`, `doi:10.1016/j.nima.2007.07.143`.

[44] Claudio Kopper. *Performance Studies for the KM3NeT Neutrino Telescope*. PhD thesis, Universität Erlangen-Nürnberg, Erlangen Centre for Astroparticle Physics, 2010.

[45] IceCube Collaboration and NSF. Instrumentation DOM, October 2014. URL: `http://wipac.wisc.edu/wipac/static/images/instruments-dom.jpg`.

[46] IceCube Collaboration, NSF, and Physical Sciences Lab. Digital Optical Modules, October 2014. URL: `http://www.psl.wisc.edu/wp-content/themes/default/images/projects/dom.jpg`.

[47] Volker Baum. Verbesserung der Supernova-Detektion mit dem IceCube-Neutrinoteleskop. Master's thesis, Johannes Gutenberg-Universität Mainz, November 2011.

[48] Jakob van Santen. A parametrization of the atmospheric muon flux in the deep ice, 2013 (accessed Sept. 12 2014). URL: `http://icecube.wisc.edu/~jvansanten/docs/muon_flux_parametrization/index.html`.

[49] Kate Scholberg. SNOwGLoBES: SuperNova Observatories with GLoBES, 2014 (accessed Sept. 3 2014). URL: `http://www.phy.duke.edu/~schol/snowglobes/`.

[50] Naoko Kurahashi Neilson. Personal Communication.

[51] U. Fano. Ionization Yield of Radiations. II. The Fluctuations of the Number of Ions. *Physical Review*, 72:26–29, July 1947. `doi:10.1103/PhysRev.72.26`.

[52] Richard Stothers. Is the Supernova of A.D. 185 Recorded in Ancient Roman Literature? *Isis*, 68(3):pp. 443–447, 1977. URL: `http://www.jstor.org/stable/231322`.

[53] P. Murdin and L. Murdin. *Supernovae*. Cambridge University Press, 1985. URL: `http://books.google.com/books?id=2zTnw4fR17YC`.

[54] O. Krause et al. Tycho Brahe's 1572 supernova as a standard typeIa as revealed by its light-echo spectrum. *Nature*, 456:617–619, December 2008. `arXiv:0810.5106`, `doi:10.1038/nature07608`.

[55] W. P. Blair, K. S. Long, and O. Vancura. A detailed optical study of Kepler's supernova remnant. *Astrophysical Journal*, 366:484–494, January 1991. `doi:10.1086/169583`.

[56] Riccardo Giacconi. Nobel Lecture: The dawn of x-ray astronomy. *Reviews of Modern Physics*, 75:995–1010, Aug 2003. URL: `http://link.aps.org/doi/10.1103/RevModPhys.75.995`, `doi:10.1103/RevModPhys.75.995`.

[57] J. Krebs and W. Hillebrandt. The interaction of supernova shockfronts and nearby interstellar clouds. *Astronomy and Astrophysics*, 128:411–419, December 1983.

[58] Thomas Preibisch and Hans Zinnecker. Triggered star formation in the scorpius-centaurus ob association (sco ob2). 2000. `arXiv:astro-ph/0008013`.

[59] M. Ackermann et al. Detection of the Characteristic Pion-Decay Signature in Supernova Remnants. *Science*, 339:807, 2013. `arXiv:1302.3307`, `doi:10.1126/science.1231160`.

[60] W. Baade and F. Zwicky. On Super-novae. *Proceedings of the National Academy of Science*, 20:254–259, May 1934. `doi:10.1073/pnas.20.5.254`.

[61] N.E. Sanders et al. PS1-12sk is a Peculiar Supernova From a He-rich Progenitor System in a Brightest Cluster Galaxy Environment. *Astrophysical Journal*, 769:39, 2013. `arXiv:1303.1818`, `doi:10.1088/0004-637X/769/1/39`.

[62] E. Margaret Burbidge, G. R. Burbidge, William A. Fowler, and F. Hoyle. Synthesis of the Elements in Stars. *Reviews of Modern Physics*, 29:547–650, Oct 1957. URL: `http://link.aps.org/doi/10.1103/RevModPhys.29.547`, `doi:10.1103/RevModPhys.29.547`.

[63] K. Hirata et al. Observation of a neutrino burst from the supernova SN1987A. *Physical Review Letters*, 58:1490–1493, Apr 1987. URL: `http://link.aps.org/doi/10.1103/PhysRevLett.58.1490`, `doi:10.1103/PhysRevLett.58.1490`.

[64] R. M. Bionta et al. Observation of a neutrino burst in coincidence with supernova 1987A in the Large Magellanic Cloud. *Physical Review Letters*, 58:1494–1496, Apr 1987. URL: `http://link.aps.org/doi/10.1103/PhysRevLett.58.1494`, `doi:10.1103/PhysRevLett.58.1494`.

[65] W.D. Arnett, J.N. Bahcall, R.P. Kirshner, and S.E. Woosley. SUPERNOVA 1987A. *Annual Review of Astronomy and Astrophysics*, 27:629–700, 1989. `doi:10.1146/annurev.aa.27.090189.003213`.

[66] E. N. Alekseev, L. N. Alekseeva, I. V. Krivosheina, and V. I. Volchenko. Properties of the Supernova 1987A Neutrino Signal Recorded by the Baksan Underground Scintillation Telescope. *Soviet Astronomy Letters*, 14:41, February 1988.

[67] Pietro Antonioli et al. SNEWS: The Supernova Early Warning System. *New Journal of Physics*, 6:114, 2004. `arXiv:astro-ph/0406214`, `doi:10.1088/1367-2630/6/1/114`.

[68] U. F. Katz and C. Spiering. High-energy neutrino astrophysics: Status and perspectives. *Progress in Particle and Nuclear Physics*, 67:651–704, July 2012. `arXiv:1111.0507`, `doi:10.1016/j.ppnp.2011.12.001`.

[69] Mario Vietri. On the acceleration of ultrahigh-energy cosmic rays in gamma-ray bursts. *Astrophysical Journal*, 453:883–889, 1995. `arXiv:astro-ph/9506081`, `doi:10.1086/176448`.

[70] Eli Waxman. Cosmological Gamma-Ray Bursts and the Highest Energy Cosmic Rays. *Phys. Rev. Lett.*, 75:386–389, Jul 1995. URL: `http://link.aps.org/doi/10.1103/PhysRevLett.75.386`, `doi:10.1103/PhysRevLett.75.386`.

[71] H.-T. Janka et al. Core-collapse supernovae: Reflections and directions. *Progress of Theoretical and Experimental Physics*, 2012(1):1A309–0, January 2012. URL: `http://ptep.oxfordjournals.org/cgi/doi/10.1093/ptep/pts067`, `doi:10.1093/ptep/pts067`.

[72] Adam Burrows. Colloquium: Perspectives on core-collapse supernova theory. *Reviews of Modern Physics*, 85(1):245–261, January 2013. URL: `http://adsabs.harvard.edu/cgi-bin/nph-data_query?bibcode=2013RvMP...85..245B&link_type=ABSTRACT`, `doi:10.1103/RevModPhys.85.245`.

[73] Per Askebjer et al. Optical properties of deep ice at the South Pole: Absorption. *Applied Optics*, 36(18):4168–4180, 1997.

[74] DM-Ice Collaboration:, J. Cherwinka, et al. First data from DM-Ice17. *ArXiv e-prints*, January 2014. `arXiv:1401.4804`.

[75] K. Winter. *Neutrino Physics*. Cambridge Studies in Historical Geography. Cambridge University Press, 1991. URL: `http://books.google.com/books?id=IhjDQgAACAAJ`.

[76] J. Chadwick. The intensity distribution in the magnetic spectrum of beta particles from radium (B + C). *Verh.Phys.Gesell.*, 16:383–391, 1914.

[77] E. Fermi. Versuch einer Theorie der β-Strahlen. I. *Zeitschrift fur Physik*, 88:161–177, March 1934. `doi:10.1007/BF01351864`.

[78] C.L. Cowan et al. Detection of the free neutrino: A Confirmation. *Science*, 124:103–104, 1956. `doi:10.1126/science.124.3212.103`.

[79] T. D. Lee and C. N. Yang. Theoretical Discussions on Possible High-Energy Neutrino Experiments. *Phys. Rev. Lett.*, 4:307–311, Mar 1960. URL: `http://link.aps.org/doi/10.1103/PhysRevLett.4.307`, `doi:10.1103/PhysRevLett.4.307`.

[80] G. Danby et al. Observation of High-Energy Neutrino Reactions and the Existence of Two Kinds of Neutrinos. *Physical Review Letters*, 9:36–44, Jul 1962. URL: `http://link.aps.org/doi/10.1103/PhysRevLett.9.36`, `doi:10.1103/PhysRevLett.9.36`.

[81] LEP Collaborations. A Combination of Preliminary Electroweak Measurements and Constraints on the Standard Model. *CERN Document PPE/96-183*, pages 96–183, 1996.

[82] K. Kodama et al. Observation of tau neutrino interactions. *Physics Letters B*, 504:218–224, 2001. `arXiv:hep-ex/0012035`, `doi:10.1016/S0370-2693(01)00307-0`.

[83] N. Agafonova et al. Observation of a first ν_τ candidate in the OPERA experiment in the CNGS beam. *Phys.Lett.*, B691:138–145, 2010. `arXiv:1006.1623`, `doi:10.1016/j.physletb.2010.06.022`.

[84] T. D. Lee and C. N. Yang. Parity Nonconservation and a Two-Component Theory of the Neutrino. *Physical Review*, 105:1671–1675, March 1957. `doi:10.1103/PhysRev.105.1671`.

[85] Martin L. Perl et al. Evidence for Anomalous Lepton Production in $e^+ - e^-$ Annihilation. *Physical Review Letters*, 35:1489–1492, 1975. `doi:10.1103/PhysRevLett.35.1489`.

[86] Raymond Davis. Nobel Lecture: A half-century with solar neutrinos. *Reviews of Modern Physics*, 75:985, 2003.

[87] B. Pontecorvo. Mesonium and anti-mesonium. *Soviet Journal of Experimental and Theoretical Physics*, 6:429, 1957.

[88] B. Pontecorvo. Neutrino Experiments and the Problem of Conservation of Leptonic Charge. *Soviet Journal of Experimental and Theoretical Physics*, 26:984, May 1968.

[89] Q.R. Ahmad et al. Measurement of the rate of $\nu_e + d \to p + p + e^-$ interactions produced by ^8B solar neutrinos at the Sudbury Neutrino Observatory. *Physical Review Letters*, 87:071301, 2001. `arXiv:nucl-ex/0106015`, `doi:10.1103/PhysRevLett.87.071301`.

[90] A. de Gouvea et al. Working Group Report: Neutrinos. 2013. `arXiv:1310.4340`.

[91] T. D. Lee and C. N. Yang. Question of Parity Conservation in Weak Interactions. *Physical Review*, 104:254–258, October 1956. `doi:10.1103/PhysRev.104.254`.

[92] C. S. Wu et al. Experimental Test of Parity Conservation in Beta Decay. *Physical Review*, 105:1413–1415, Feb 1957. URL: `http://link.aps.org/doi/10.1103/PhysRev.105.1413`, `doi:10.1103/PhysRev.105.1413`.

[93] M. Goldhaber, L. Grodzins, and A.W. Sunyar. Helicity of Neutrinos. *Physical Review*, 109:1015–1017, 1958. `doi:10.1103/PhysRev.109.1015`.

[94] R.N. Mohapatra and P.B. Pal. *Massive Neutrinos in Physics and Astrophysics*. Lecture Notes in Physics Series. World Scientific, 2004. URL: `http://books.google.com/books?id=qOnPnQEACAAJ`.

[95] M. Fukugita and T. Yanagida. *Physics of Neutrinos: And Applications to Astrophysics*. Physics and astronomy online library. Springer, 2003. URL: `http://books.google.com/books?id=El8R8nC5QegC`.

[96] M. Drewes. The Phenomenology of Right Handed Neutrinos. *International Journal of Modern Physics E*, 22:30019, August 2013. `arXiv:1303.6912`, `doi:10.1142/S0218301313300191`.

[97] R.N. Mohapatra and P.B. Pal. Massive neutrinos in physics and astrophysics. Second edition. *World Sci.Lect.Notes Phys.*, 60:1–397, 1998.

[98] P. A. M. Dirac. The Quantum Theory of the Electron. *Proceedings of the Royal Society of London. Series A*, 117(778):610–624, 1928. URL: `http://rspa.royalsocietypublishing.org/content/117/778/610.short`, `arXiv:http://rspa.royalsocietypublishing.org/content/117/778/610.full.pdf+html`, `doi:10.1098/rspa.1928.0023`.

[99] Ettore Majorana. Theory of the Symmetry of Electrons and Positrons. *Nuovo Cim.*, 14:171–184, 1937. `doi:10.1007/BF02961314`.

[100] J. Schechter and J. W. F. Valle. Neutrinoless double-β decay in SU(2)×U(1) theories. *Physical Review D*, 25:2951–2954, June 1982. `doi:10.1103/PhysRevD.25.2951`.

[101] F. Halzen and A.D. Martin. *Quarks and Leptons: An Introductory Course in Modern Particle Physics*. Wiley, 1984. URL: `http://books.google.com/books?id=zwDvAAAAMAAJ`.

[102] D. Griffiths. *Introduction to Elementary Particles*. Physics textbook. Wiley, 2008. URL: `http://books.google.com/books?id=Wb9DYrjcoKAC`.

[103] R. Slansky et al. The Oscillating Neutrino–An Introduction to Neutrino Masses and Mixings. *Los Alamos Science*, 25, November 1997. URL: `http://library.lanl.gov/cgi-bin/getfile?25-03.pdf`.

[104] S. Raby. Family Mixing and the Origin of Mass. *Los Alamos Science*, 25, November 1997. URL: `http://library.lanl.gov/cgi-bin/getfile?25-05.pdf`.

[105] Z. Maki, M. Nakagawa, and S. Sakata. Remarks on the Unified Model of Elementary Particles. *Progress of Theoretical Physics*, 28:870–880, November 1962. URL: `http://adsabs.harvard.edu/cgi-bin/nph-data_query?bibcode=1962PThPh..28..870M&link_type=ABSTRACT`, `doi:10.1143/PTP.28.870`.

[106] Planck Collaboration, P. A. R. Ade, et al. Planck 2013 results. XVI. Cosmological parameters. *ArXiv e-prints*, March 2013. `arXiv:1303.5076`.

[107] V.N. Aseev et al. An upper limit on electron antineutrino mass from Troitsk experiment. *Physical Review D*, 84:112003, 2011. `arXiv:1108.5034`, `doi:10.1103/PhysRevD.84.112003`.

[108] K. Assamagan et al. Upper limit of the muon-neutrino mass and charged-pion mass from momentum analysis of a surface muon beam. *Physical Review D*, 53:6065–6077, Jun 1996. URL: `http://link.aps.org/doi/10.1103/PhysRevD.53.6065`, `doi:10.1103/PhysRevD.53.6065`.

[109] R. Barate et al. An upper limit on the τ neutrino mass from three- and five-prong tau decays. *The European Physical Journal C - Particles and Fields*, 2(3):395–406, 1998. URL: `http://dx.doi.org/10.1007/s100529800850`, `doi:10.1007/s100529800850`.

[110] T. K. Kuo and James Pantaleone. Neutrino oscillations in matter. *Reviews of Modern Physics*, 61:937–979, Oct 1989. URL: `http://link.aps.org/doi/10.1103/RevModPhys.61.937`, `doi:10.1103/RevModPhys.61.937`.

[111] Kei Kotake, Katsuhiko Sato, and Keitaro Takahashi. Explosion mechanism, neutrino burst and gravitational wave in core-collapse supernovae. *Reports on Progress in Physics*, 69(4):971–1143, April 2006. URL: `http://adsabs.harvard.edu/cgi-bin/nph-data_query?bibcode=2006RPPh...69..971K&link_type=ABSTRACT`, `doi:10.1088/0034-4885/69/4/R03`.

[112] Alexander Piégsa. *Supernova-Detektion mit dem IceCube-Neutrinoteleskop*. PhD thesis, Johannes Gutenberg-Universität Mainz, December 2009. URL: `http://icecube.wisc.edu/~rmaruyama/temp/riedel/phd_thesis__alexander_piegsa__german.pdf`.

[113] Yayun Ding et al. A new gadolinium-loaded liquid scintillator for reactor neutrino detection. *Nuclear Instruments and Methods in Physics Research A*, 584:238–243, 2008. `doi:10.1016/j.nima.2007.09.044`.

[114] M. Yeh, A. Garnov, and Richard L. Hahn. Gadolinium-loaded liquid scintillator for high-precision measurements of antineutrino oscillations and the mixing angle, $\Theta(13)$. *Nuclear Instruments and Methods in Physics Research A*, 578:329–339, 2007. `doi:10.1016/j.nima.2007.03.029`.

[115] L Wolfenstein. Neutrino oscillations in matter. *Physical Review D*, 17(9):2369–2374, May 1978. URL: `http://link.aps.org/doi/10.1103/PhysRevD.17.2369`, `doi:10.1103/PhysRevD.17.2369`.

[116] S. P. Mikheev and A. Iu. Smirnov. Resonant amplification of neutrino oscillations in matter and solar-neutrino spectroscopy. *Nuovo Cimento C*, 9:17–26, February 1986. URL: `http://adsabs.harvard.edu/cgi-bin/nph-data_query?bibcode=1986NCimC...9...17M&link_type=ABSTRACT`, `doi:10.1007/BF02508049`.

[117] M.L. Goldberger and K.M. Watson. *Collision Theory*. Dover books on physics. Dover Publications, 2004. URL: `http://books.google.com/books?id=4JUCFZiZOHgC`.

[118] P. Langacker, S. T. Petcov, G. Steigman, and S. Toshev. Implications of the Mikheyev-Smirnov-Wolfenstein (MSW) mechanism of amplification of neutrino oscillations in matter. *Nuclear Physics B*, 282:589–609, 1987. `doi:10.1016/0550-3213(87)90699-7`.

[119] A.S. Dighe and A.Y. Smirnov. Identifying the neutrino mass spectrum from a supernova neutrino burst. *Physical Review D*, 62(3):033007, 2000. URL: `http://adsabs.harvard.edu/cgi-bin/nph-data_query?bibcode=2000PhRvD..62c3007D&link_type=ABSTRACT`, `arXiv:hep-ph/9907423`.

[120] Timo Greisel. *Optimierung des Nachweises von Supernovae in IceCube*. PhD thesis, Johannes Gutenberg-Universität Mainz, December 2010. URL: `http://ubm.opus.hbz-nrw.de/volltexte/2010/2479/pdf/doc.pdf`.

[121] T. K. Kuo and James Pantaleone. Nonadiabatic neutrino oscillations in matter. *Physical Review D*, 39:1930–1939, Apr 1989. URL: `http://link.aps.org/doi/10.1103/PhysRevD.39.1930`, `doi:10.1103/PhysRevD.39.1930`.

[122] G. L. Fogli, E. Lisi, D. Montanino, and A. Palazzo. Supernova neutrino oscillations: A simple analytical approach. *Physical Review D*, 65(7):073008, April 2002. `arXiv:hep-ph/0111199`, `doi:10.1103/PhysRevD.65.073008`.

[123] F.P. An et al. Observation of electron-antineutrino disappearance at Daya Bay. *Physical Review Letters*, 108:171803, 2012. `arXiv:1203.1669`, `doi:10.1103/PhysRevLett.108.171803`.

[124] K. Takahashi, K. Sato, H. E. Dalhed, and J. R. Wilson. Shock propagation and neutrino oscillation in supernova. *Astroparticle Physics*, 20:189–193, November 2003. `arXiv:astro-ph/0212195`, `doi:10.1016/S0927-6505(03)00175-0`.

[125] R. Tomàs et al. Neutrino signatures of supernova forward and reverse shock propagation. *Journal of Cosmology and Astroparticle Physics*, 9:15, September 2004. `arXiv:astro-ph/0407132`, `doi:10.1088/1475-7516/2004/09/015`.

[126] H. -Thomas Janka and E. Mueller. The First Second of a Type-II Supernova: Convection, Accretion, and Shock Propagation. *ArXiv Astrophysics e-prints*, March 1995. `arXiv:astro-ph/9503015`.

[127] H. Duan, G. M. Fuller, and Y.-Z. Qian. Collective neutrino flavor transformation in supernovae. *Physical Review D*, 74(12):123004, December 2006. `arXiv:astro-ph/0511275`, `doi:10.1103/PhysRevD.74.123004`.

[128] H. Duan, G. M. Fuller, J. Carlson, and Y.-Z. Qian. Simulation of coherent nonlinear neutrino flavor transformation in the supernova environment: Correlated neutrino trajectories. *Physical Review D*, 74(10):105014, November 2006. `arXiv:astro-ph/0606616`, `doi:10.1103/PhysRevD.74.105014`.

[129] H. Duan, G. M. Fuller, J. Carlson, and Y.-Z. Qian. Coherent Development of Neutrino Flavor in the Supernova Environment. *Physical Review Letters*, 97(24):241101, December 2006. `arXiv:astro-ph/0608050`, `doi:10.1103/PhysRevLett.97.241101`.

[130] Huaiyu Duan, George M. Fuller, and J. Carlson. Simulating nonlinear neutrino flavor evolution. *Comput.Sci.Dis.*, 1:015007, 2008. `arXiv:0803.3650`, `doi:10.1088/1749-4699/1/1/015007`.

[131] H. Duan and J. P. Kneller. TOPICAL REVIEW: Neutrino flavour transformation in supernovae. *Journal of Physics G Nuclear Physics*, 36(11):113201, November 2009. `arXiv:0904.0974`, `doi:10.1088/0954-3899/36/11/113201`.

[132] Huaiyu Duan, George M. Fuller, and Yong-Zhong Qian. Collective Neutrino Oscillations. *Ann.Rev.Nucl.Part.Sci.*, 60:569–594, 2010. `arXiv:1001.2799`, `doi:10.1146/annurev.nucl.012809.104524`.

[133] J. F. Cherry et al. Density fluctuation effects on collective neutrino oscillations in O-Ne-Mg core-collapse supernovae. *Physical Review D*, 84(10):105034, November 2011. `arXiv:1108.4064`, `doi:10.1103/PhysRevD.84.105034`.

[134] John F Cherry. *Neutrino Flavor Transformation in Core-Collapse Supernovae*. PhD thesis, University of California, San Diego, November 2012. URL: `http://128.48.120.176/uc/item/9p60h8bw#`.

[135] G. Laughlin, P. Bodenheimer, and F. C. Adams. The End of the Main Sequence. *Astrophysical Journal*, 482:420–432, June 1997.

[136] D. Vanbeveren, C. De Loore, and W. Van Rensbergen. Massive stars. *Astronomy and Astrophysics Reviews*, 9:63–152, 1998. `doi:10.1007/s001590050015`.

[137] D. Prialnik. *An Introduction to the Theory of Stellar Structure and Evolution*. Cambridge University Press, 2000. URL: `http://books.google.com/books?id=TGyzlVbgkiMC`.

[138] A. C. Maury and E. C. Pickering. Spectra of bright stars photographed with the 11-inch Draper Telescope as part of the Henry Draper Memorial. *Annals of Harvard College Observatory*, 28:1–128, 1897.

[139] E. Hertzsprung. Über die Sterne der Unterabteilungen c und ac nach der Spektralklassifikation von Antonia C. Maury. *Astronomische Nachrichten*, 179:373, January 1909.

[140] H. N. Russell. Relations Between the Spectra and Other Characteristics of the Stars. *Popular Astronomy*, 22:275–294, May 1914.

[141] F.H. Shu, F.C. Adams, and S. Lizano. Star Formation in Molecular Clouds - Observation and Theory. *Annual Review of Astronomy and Astrophysics*, 25:23–81, 1987. `doi:{10.1146/annurev.aa.25.090187.000323}`.

[142] C.J. Hansen, S.D. Kawaler, and V. Trimble. *Stellar Interiors: Physical Principles, Structure, and Evolution*. Astronomy and Astrophysics Library. Springer New York, 2004. URL: `http://books.google.com/books?id=NnBq7ROM4UgC`.

[143] Irving. Langmuir and G. M. J. Mackay. THE DISSOCIATION OF HYDROGEN INTO ATOMS. Part I. Experimental. *Journal of the American Chemical Society*, 36(8):1708–1722, 1914. URL: `http://dx.doi.org/10.1021/ja02185a011`, `arXiv:http://dx.doi.org/10.1021/ja02185a011`, `doi:10.1021/ja02185a011`.

[144] R. B. Larson. Numerical calculations of the dynamics of collapsing proto-star. *Monthly Notices of the RAS*, 145:271, 1969.

[145] M. N. Saha. On a Physical Theory of Stellar Spectra. *Royal Society of London Proceedings Series A*, 99:135–153, May 1921. `doi:10.1098/rspa.1921.0029`.

[146] Megh Nad Saha. LIII. Ionization in the solar chromosphere. *Philosophical Magazine Series 6*, 40(238):472–488, 1920. URL: `http://dx.doi.org/10.1080/14786441008636148`, `arXiv:http://dx.doi.org/10.1080/14786441008636148`, `doi:10.1080/14786441008636148`.

[147] K. H. Kingdon and I. Langmuir. The Removal of Thorium from the Surface of a Thoriated Tungsten Filament by Positive Ion Bombardment. *Physical Review*, 22:148–160, August 1923. `doi:10.1103/PhysRev.22.148`.

[148] E.G. Adelberger et al. Solar fusion cross sections II: The pp chain and CNO cycles. *Reviews of Modern Physics*, 83:195, 2011. `arXiv:1004.2318`, `doi:10.1103/RevModPhys.83.195`.

[149] J. Liebert. White dwarf stars. *Annual Review of Astronomy and Astrophysics*, 18:363–398, 1980. `doi:10.1146/annurev.aa.18.090180.002051`.

[150] I.-J. Sackmann, A. I. Boothroyd, and K. E. Kraemer. Our Sun. III. Present and Future. *Astrophysical Journal*, 418:457, November 1993. `doi:10.1086/173407`.

[151] C. L. Fryer. Black-hole formation from stellar collapse. *Classical and Quantum Gravity*, 20:73, May 2003. `doi:10.1088/0264-9381/20/10/309`.

[152] J. R. Oppenheimer and G. M. Volkoff. On Massive Neutron Cores. *Physical Review*, 55:374–381, February 1939. `doi:10.1103/PhysRev.55.374`.

[153] R. C. Tolman. Static Solutions of Einstein's Field Equations for Spheres of Fluid. *Physical Review*, 55:364–373, February 1939. `doi:10.1103/PhysRev.55.364`.

[154] I. Bombaci. The maximum mass of a neutron star. *Astronomy and Astrophysics*, 305:871, January 1996.

[155] S. Chandrasekhar. *An Introduction to the Study of Stellar Structure*. Dover Books on Astronomy Series. Dover Publications, Incorporated, 2012. URL: `http://books.google.com/books?id=joWn8s2BF04C`.

[156] F. X. Timmes, S. E. Woosley, and T. A. Weaver. The Neutron Star and Black Hole Initial Mass Function. *Astrophysical Journal*, 457:834, February 1996. `arXiv:astro-ph/9510136`, `doi:10.1086/176778`.

[157] L. A. L. da Silva. The classification of supernovae. *Astrophysics and Space Science*, 202:215–236, April 1993. `doi:10.1007/BF00626878`.

[158] E. Cappellaro and M. Turatto. Supernova Types and Rates. In D. Vanbeveren, editor, *The Influence of Binaries on Stellar Population Studies*, volume 264 of *Astrophysics and Space Science Library*, page 199, 2001. `arXiv:astro-ph/0012455`.

[159] J. B. Doggett and D. Branch. A comparative study of supernova light curves. *Astronomical Journal*, 90:2303–2311, November 1985. `doi:10.1086/113934`.

[160] A. V. Filippenko. Optical Spectra of Supernovae. *Annual Review of Astronomy and Astrophysics*, 35:309–355, 1997. `doi:10.1146/annurev.astro.35.1.309`.

[161] V. P. Utrobin. Nonthermal ionization and excitation in Type IIb supernova 1993J. *Astronomy and Astrophysics*, 306:219, February 1996.

[162] W. Hillebrandt and J. C. Niemeyer. Type IA Supernova Explosion Models. *Annual Review of Astronomy and Astrophysics*, 38:191–230, 2000. `arXiv:astro-ph/0006305`, `doi:10.1146/annurev.astro.38.1.191`.

[163] P. A. Mazzali, F. K. Röpke, S. Benetti, and W. Hillebrandt. A Common Explosion Mechanism for Type Ia Supernovae. *Science*, 315:825–, February 2007. `arXiv:astro-ph/0702351`, `doi:10.1126/science.1136259`.

[164] S. A. Colgate and R. H. White. The Hydrodynamic Behavior of Supernovae Explosions. *Astrophysical Journal*, 143:626, March 1966. `doi:10.1086/148549`.

[165] H. A. Bethe and J. R. Wilson. Revival of a stalled supernova shock by neutrino heating. *Astrophysical Journal*, 295:14–23, August 1985. `doi:10.1086/163343`.

[166] Stan Woosley and Thomas Janka. The physics of core-collapse supernovae. *Nature Physics*, 2006. `arXiv:astro-ph/0601261`.

[167] H.-T. Janka. Conditions for shock revival by neutrino heating in core-collapse supernovae. *Astronomy and Astrophysics*, 368:527–560, March 2001. `arXiv:astro-ph/0008432`, `doi:10.1051/0004-6361:20010012`.

[168] A. Burrows and J. M. Lattimer. The birth of neutron stars. *Astrophysical Journal*, 307:178–196, August 1986. `doi:10.1086/164405`.

[169] J. A. Pons, S. Reddy, M. Prakash, J. M. Lattimer, and J. A. Miralles. Evolution of Proto-Neutron Stars. *Astrophysical Journal*, 513:780–804, March 1999. `arXiv:astro-ph/9807040`, `doi:10.1086/306889`.

[170] R. Buras, M. Rampp, H.-T. Janka, and K. Kifonidis. Two-dimensional hydrodynamic core-collapse supernova simulations with spectral neutrino transport. I. Numerical method and results for a 15 $M_\odot$ star. *Astronomy and Astrophysics*, 447:1049–1092, March 2006. `arXiv:astro-ph/0507135`, `doi:10.1051/0004-6361:20053783`.

[171] R. Buras, H.-T. Janka, M. Rampp, and K. Kifonidis. Two-dimensional hydrodynamic core-collapse supernova simulations with spectral neutrino transport. II. Models for different progenitor stars. *Astronomy and Astrophysics*, 457:281–308, October 2006. `arXiv:astro-ph/0512189`, `doi:10.1051/0004-6361:20054654`.

[172] T. Foglizzo, L. Scheck, and H.-T. Janka. Neutrino-driven Convection versus Advection in Core-Collapse Supernovae. *Astrophysical Journal*, 652:1436–1450, December 2006. `arXiv:astro-ph/0507636`, `doi:10.1086/508443`.

[173] T. Foglizzo, P. Galletti, L. Scheck, and H.-T. Janka. Instability of a Stalled Accretion Shock: Evidence for the Advective-Acoustic Cycle. *Astrophysical Journal*, 654:1006–1021, January 2007. `arXiv:astro-ph/0606640`, `doi:10.1086/509612`.

[174] A. Marek and H.-T. Janka. Delayed Neutrino-Driven Supernova Explosions Aided by the Standing Accretion-Shock Instability. *Astrophysical Journal*, 694:664–696, March 2009. `arXiv:0708.3372`, `doi:10.1088/0004-637X/694/1/664`.

[175] F. Hanke, A. Marek, B. Müller, and H.-T. Janka. Is Strong SASI Activity the Key to Successful Neutrino-driven Supernova Explosions? *Astrophysical Journal*, 755:138, August 2012. `arXiv:1108.4355`, `doi:10.1088/0004-637X/755/2/138`.

[176] F. Hanke et al. SASI Activity in Three-dimensional Neutrino-hydrodynamics Simulations of Supernova Cores. *Astrophysical Journal*, 770:66, June 2013. `arXiv:1303.6269`, `doi:10.1088/0004-637X/770/1/66`.

[177] Christian D. Ott, Adam Burrows, Luc Dessart, and Eli Livne. 2D Multi-Angle, Multi-Group Neutrino Radiation-Hydrodynamic Simulations of Postbounce Supernova Cores. *Astrophysical Journal*, 685:1069–1088, 2008. `arXiv:0804.0239`, `doi:10.1086/591440`.

[178] E. Abdikamalov et al. A New Monte Carlo Method for Time-dependent Neutrino Radiation Transport. *Astrophysical Journal*, 755:111, August 2012. `arXiv:1203.2915`, `doi:10.1088/0004-637X/755/2/111`.

[179] E. O'Connor and C. D. Ott. The Progenitor Dependence of the Pre-explosion Neutrino Emission in Core-collapse Supernovae. *Astrophysical Journal*, 762:126, January 2013. `arXiv:1207.1100`, `doi:10.1088/0004-637X/762/2/126`.

[180] P. Mösta et al. Magnetorotational Core-collapse Supernovae in Three Dimensions. *Astrophysical Journal Letters*, 785:L29, April 2014. `arXiv:1403.1230`, `doi:10.1088/2041-8205/785/2/L29`.

[181] E. Livne et al. Two-dimensional, Time-dependent, Multigroup, Multiangle Radiation Hydrodynamics Test Simulation in the Core-Collapse Supernova Context. *Astrophysical Journal*, 609:277–287, July 2004. `arXiv:astro-ph/0312633`, `doi:10.1086/421012`.

[182] A. Burrows et al. Features of the Acoustic Mechanism of Core-Collapse Supernova Explosions. *Astrophysical Journal*, 655:416–433, January 2007. `arXiv:astro-ph/0610175`, `doi:10.1086/509773`.

[183] A. Burrows et al. Simulations of Magnetically Driven Supernova and Hypernova Explosions in the Context of Rapid Rotation. *Astrophysical Journal*, 664:416–434, July 2007. `arXiv:astro-ph/0702539`, `doi:10.1086/519161`.

[184] T. D. Brandt, A. Burrows, C. D. Ott, and E. Livne. Results from Core-collapse Simulations with Multi-dimensional, Multi-angle Neutrino Transport. *Astrophysical Journal*, 728:8, February 2011. `arXiv:1009.4654`, `doi:10.1088/0004-637X/728/1/8`.

[185] A. Mezzacappa and S.W. Bruenn. A numerical method for solving the neutrino Boltzmann equation coupled to spherically symmetric stellar core collapse. *Astrophysical Journal*, 405:669–684, 1993. `doi:10.1086/172395`.

[186] Matthias Liebendoerfer et al. Probing the gravitational well: no supernova explosion in spherical symmetry with general relativistic boltzmann neutrino transport. *Physical Review D*, 63:103004, 2001. `arXiv:astro-ph/0006418`, `doi:10.1103/PhysRevD.63.103004`.

[187] Anthony Mezzacappa et al. The Simulation of a spherically symmetric supernova of a 13 $M_\odot$ star with Boltzmann neutrino transport, and its implications for the supernova mechanism. *Physical Review Letters*, 86:1935–1938, 2001. `arXiv:astro-ph/0005366`, `doi:10.1103/PhysRevLett.86.1935`.

[188] J. M. Blondin, A. Mezzacappa, and C. DeMarino. Stability of Standing Accretion Shocks, with an Eye toward Core-Collapse Supernovae. *Astrophysical Journal*, 584:971–980, February 2003. `arXiv:astro-ph/0210634`, `doi:10.1086/345812`.

[189] T. Fischer et al. Protoneutron star evolution and the neutrino-driven wind in general relativistic neutrino radiation hydrodynamics simulations. *Astronomy and Astrophysics*, 517:A80, July 2010. `arXiv:0908.1871`, `doi:10.1051/0004-6361/200913106`.

[190] A. Mezzacappa et al. Two- and Three-Dimensional Multi-Physics Simulations of Core Collapse Supernovae: A Brief Status Report and Summary of Results from the "Oak Ridge" Group. *ArXiv e-prints*, May 2014. `arXiv:1405.7075`.

[191] K. Kotake, N. Ohnishi, S. Yamada, and K. Sato. Multigroup Flux-limited Diffusion Neutrino Transport Simulations for Magnetized and Rotating Core-Collapse Supernovae. In S. Kubono, W. Aoki, T. Kajino, T. Motobayashi, and K. Nomoto, editors, *Origin of Matter and Evolution of Galaxies*, volume 847 of *American Institute of Physics Conference Series*, pages 421–423, July 2006. `doi:10.1063/1.2234445`.

[192] H. Mikami, Y. Sato, T. Matsumoto, and T. Hanawa. Three-dimensional Magnetohydrodynamical Simulations of a Core-Collapse Supernova. *Astrophysical Journal*, 683:357–374, August 2008. `arXiv:0804.3700`, `doi:10.1086/589759`.

[193] T. Takiwaki, K. Kotake, and Y. Suwa. Three-dimensional Hydrodynamic Core-collapse Supernova Simulations for an 11.2 $\mathrm{M}_\odot$ Star with Spectral Neutrino Transport. *Astrophysical Journal*, 749:98, April 2012. `arXiv:1108.3989`, `doi:10.1088/0004-637X/749/2/98`.

[194] K. Kotake et al. Core-collapse supernovae as supercomputing science: A status report toward six-dimensional simulations with exact Boltzmann neutrino transport in full general relativity. *Progress of Theoretical and Experimental Physics*, 2012(1):010000, August 2012. `arXiv:1205.6284`, `doi:10.1093/ptep/pts009`.

[195] K. Sumiyoshi and S. Yamada. Neutrino Transfer in Three Dimensions for Core-collapse Supernovae. I. Static Configurations. *Astrophysical Journal Supplements*, 199:17, March 2012. `arXiv:1201.2244`, `doi:10.1088/0067-0049/199/1/17`.

[196] A. Marek, M. Rampp, F. Hanke, and H.-T. Janka. Towards Petaflops Capability of the VERTEX Supernova Code. *ArXiv e-prints*, April 2014. `arXiv:1404.1719`.

[197] Kate Scholberg. Supernova neutrino detection in water Cherenkov detectors. *Journal of Physics: Conference Series*, 309:012028, 2011. `doi:10.1088/1742-6596/309/1/012028`.

[198] S. E. Woosley and T. A. Weaver. The Evolution and Explosion of Massive Stars. II. Explosive Hydrodynamics and Nucleosynthesis. *Astrophysical Journal Supplements*, 101:181, November 1995. `doi:10.1086/192237`.

[199] I. Tamborra et al. Neutrino Signature of Supernova Hydrodynamical Instabilities in Three Dimensions. *Physical Review Letters*, 111(12):121104, September 2013. `arXiv:1307.7936`, `doi:10.1103/PhysRevLett.111.121104`.

[200] C. D. Ott et al. Correlated gravitational wave and neutrino signals from general-relativistic rapidly rotating iron core collapse. *Physical Review D*, 86(2):024026, July 2012. `arXiv:1204.0512`, `doi:10.1103/PhysRevD.86.024026`.

[201] M. T. Keil, G. G. Raffelt, and H.-T. Janka. Monte Carlo Study of Supernova Neutrino Spectra Formation. *Astrophysical Journal*, 590:971–991, June 2003. `arXiv:astro-ph/0208035`, `doi:10.1086/375130`.

[202] Mathias Thorsten Keil. *Supernova Neutrino Spectra and Applications to Flavor Oscillations*. PhD thesis, Technischen Universität München, June 2003. URL: `http://arxiv.org/pdf/astro-ph/0308228v1.pdf`.

[203] T. A. Thompson, A. Burrows, and P. A. Pinto. Shock Breakout in Core-Collapse Supernovae and Its Neutrino Signature. *Astrophysical Journal*, 592:434–456, July 2003. `arXiv:astro-ph/0211194`, `doi:10.1086/375701`.

[204] G. Cresci, F. Mannucci, M. Della Valle, and R. Maiolino. A NICMOS search for obscured supernovae in starburst galaxies. *Astronomy and Astrophysics*, 462:927–931, February 2007. `arXiv:astro-ph/0610783`, `doi:10.1051/0004-6361:20065364`.

[205] Georg G. Raffelt. Physics with supernovae . *Nuclear Physics B - Proceedings Supplements*, 110(0):254 – 267, 2002. URL: `http://www.sciencedirect.com/science/article/pii/S0920563202014895`, `doi:10.1016/S0920-5632(02)01489-5`.

[206] Louis E. Strigari. The Type Ia Supernova rate in the local Universe. *New Astronomy Reviews*, 50(78):566 – 569, 2006. Astronomy with Radioactivities. V 5th International Conference on Astronomy with Radioactivities, and annual Workshop of the Clemson/Washington Universities on Isotopic Anomalies in Meteorites. URL: `http://www.sciencedirect.com/science/article/pii/S1387647306001515`, `doi:10.1016/j.newar.2006.06.043`.

[207] Roland Diehl. Measuring 26Al and 60Fe in the Galaxy. *New Astronomy Reviews*, 50(78):534 – 539, 2006. Astronomy with Radioactivities. V 5th International Conference on Astronomy with Radioactivities, and Annual Workshop of the Clemson/Washington Universities on Isotopic Anomalies in Meteorites. URL: `http://www.sciencedirect.com/science/article/pii/S1387647306001576`, `doi:10.1016/j.newar.2006.06.082`.

[208] Roland Diehl and iothers. Radioactive Al-26 and massive stars in the galaxy. *Nature*, 439:45–47, 2006. `arXiv:astro-ph/0601015`, `doi:10.1038/nature04364`.

[209] Mark F. Theiling and Mark D. Leising. Investigation of 44Ti decay X-ray lines in CasA. *New Astronomy Reviews*, 50(78):544 – 547, 2006. Astronomy with Radioactivities. V 5th International Conference on Astronomy with Radioactivities, and Annual Workshop of the Clemson/Washington Universities on Isotopic Anomalies in Meteorites. URL: `http://www.sciencedirect.com/science/article/pii/S1387647306001606`, `doi:10.1016/j.newar.2006.06.054`.

[210] Peter Hflich, Christopher L. Gerardy, Howie Marion, and Robert Quimby. Signatures of isotopes in thermonuclear supernovae. *New Astronomy Reviews*, 50(78):470 – 473, 2006. Astronomy with Radioactivities. V 5th International Conference on Astronomy with Radioactivities, and Annual Workshop of the Clemson/Washington Universities on Isotopic Anomalies in Meteorites. URL: `http://www.sciencedirect.com/science/article/pii/S1387647306001254`, `doi:10.1016/j.newar.2006.06.074`.

[211] Alessandro Mirizzi, G.G. Raffelt, and P.D. Serpico. Earth matter effects in supernova neutrinos: Optimal detector locations. *Journal of Cosmology and Astroparticle Physics*, 0605:012, 2006. `arXiv:astro-ph/0604300`, `doi:10.1088/1475-7516/2006/05/012`.

[212] K. M. Ferrière. The interstellar environment of our galaxy. *Reviews of Modern Physics*, 73:1031–1066, October 2001. `arXiv:astro-ph/0106359`, `doi:10.1103/RevModPhys.73.1031`.

[213] G. A. Tammann, W. Loeffler, and A. Schroeder. The Galactic supernova rate. *Astrophysical Journal Supplements*, 92:487–493, June 1994. `doi:10.1086/192002`.

[214] E.N. Alekseev and L.N. Alekseeva. Twenty years of Galactic observations in searching for bursts of collapse neutrinos with the Baksan Underground Scintillation Telescope. *J.Exp.Theor.Phys.*, 95:5–10, 2002. `arXiv:astro-ph/0212499`, `doi:10.1134/1.1499896`.

[215] L. O'Connor Drury. Origin of Cosmic Rays. *Astroparticle Physics*, 39:52–60, December 2012. `arXiv:1203.3681`, `doi:10.1016/j.astropartphys.2012.02.006`.

[216] C.A. Duba et al. HALO: The helium and lead observatory for supernova neutrinos. *J.Phys.Conf.Ser.*, 136:042077, 2008. URL: `http://iopscience.iop.org/1742-6596/136/4/042077/media/077_NEUT08p.pdf`, `doi:10.1088/1742-6596/136/4/042077`.

[217] M. Ikeda et al. Search for Supernova Neutrino Bursts at Super-Kamiokande. *Astrophysical Journal*, 669:519–524, 2007. `arXiv:0706.2283`, `doi:10.1086/521547`.

[218] L. Cadonati, F.P. Calaprice, and M.C. Chen. Supernova neutrino detection in Borexino. *Astronomy and Astrophysics*, 16:361–372, 2002. `arXiv:hep-ph/0012082`, `doi:10.1016/S0927-6505(01)00129-3`.

[219] D. Väänänen and C. Volpe. The neutrino signal at HALO: learning about the primary supernova neutrino fluxes and neutrino properties. *Journal of Cosmology and Astroparticle Physics*, 10:19, October 2011. `arXiv:1105.6225`, `doi:10.1088/1475-7516/2011/10/019`.

[220] N. Yu. Agafonova et al. Study of the effect of neutrino oscillations on the supernova neutrino signal in the LVD detector. *Astronomy and Astrophysics*, 27:254–270, 2007. `arXiv:hep-ph/0609305`, `doi:10.1016/j.astropartphys.2006.11.004`.

[221] N. Yu. Agafonova et al. On-line recognition of supernova neutrino bursts in the LVD detector. *Astronomy and Astrophysics*, 28:516–522, 2008. `arXiv:0710.0259`, `doi:10.1016/j.astropartphys.2007.09.005`.

[222] S. Amerio et al. Design, construction and tests of the {ICARUS} {T600} detector. *Nuclear Instruments and Methods in Physics Research A*, 527(3):329 – 410, 2004. URL: `http://www.sciencedirect.com/science/article/pii/S0168900204004966`, `doi:10.1016/j.nima.2004.02.044`.

[223] A. Bueno, I. Gil-Botella, and A. Rubbia. Supernova Neutrino Detection in a liquid Argon TPC. *ArXiv High Energy Physics - Phenomenology e-prints*, July 2003. `arXiv:hep-ph/0307222`.

[224] B. Bekman, J. Holeczek, and J. Kisiel. Detection of Supernova Neutrinos. *Acta Physica Polonica B*, 35:1215, March 2004. `arXiv:hep-ph/0403117`.

[225] M.A. Schumaker. Supernova Detection with SNO+. *Nuclear Physics B - Proceedings Supplements*, 229232(0):547 –, 2012. Neutrino 2010. URL: `http://www.sciencedirect.com/science/article/pii/S092056321200401X`, `doi:10.1016/j.nuclphysbps.2012.09.184`.

[226] Y. Fukuda et al. Evidence for oscillation of atmospheric neutrinos. *Physical Review Letters*, 81:1562–1567, 1998. `arXiv:hep-ex/9807003`, `doi:10.1103/PhysRevLett.81.1562`.

[227] T2K Collaboration, K. Abe, et al. The T2K experiment. *Nuclear Instruments and Methods in Physics Research A*, 659:106–135, December 2011. `arXiv:1106.1238`, `doi:10.1016/j.nima.2011.06.067`.

[228] Y. Fukuda et al. Study of the atmospheric neutrino flux in the multi-GeV energy range. *Phys.Lett.*, B436:33–41, 1998. `arXiv:hep-ex/9805006`, `doi:10.1016/S0370-2693(98)00876-4`.

[229] Y. Fukuda et al. Measurements of the Solar Neutrino Flux from Super-Kamiokande's First 300 Days. *Phys. Rev. Lett.*, 81:1158–1162, Aug 1998. URL: `http://link.aps.org/doi/10.1103/PhysRevLett.81.1158`, `doi:10.1103/PhysRevLett.81.1158`.

[230] J. Yoo et al. A Search for periodic modulations of the solar neutrino flux in Super-Kamiokande I. *Physical Review*, D68:092002, 2003. `arXiv:hep-ex/0307070`, `doi:10.1103/PhysRevD.68.092002`.

[231] H. Nishino et al. Search for Proton Decay via $p \rightarrow e^+ + \pi^0$ and $p \rightarrow \mu^+ + \pi^0$ in a Large Water Cherenkov Detector. *Physical Review Letters*, 102:141801, 2009. `arXiv:0903.0676`, `doi:10.1103/PhysRevLett.102.141801`.

[232] John F. Beacom and P. Vogel. Can a supernova be located by its neutrinos? *Physical Review*, D60:033007, 1999. `arXiv:astro-ph/9811350`, `doi:10.1103/PhysRevD.60.033007`.

[233] M. Aglietta et al. Muon "depth-intensity" relation measured by the LVD underground experiment and cosmic-ray muon spectrum at sea level. *Physical Review D*, 58(9):092005, November 1998. `arXiv:hep-ex/9806001`, `doi:10.1103/PhysRevD.58.092005`.

[234] N.Yu. Agafonova et al. Analysis of seasonal variations of the cosmic ray muon flux and neutrons produced by muons in the LVD detector. *Bulletin of the Russian Academy of Sciences: Physics*, 75(3):427–430, 2011. URL: `http://dx.doi.org/10.3103/S1062873811030063`, `doi:10.3103/S1062873811030063`.

[235] L. Ludhova et al. Solar neutrino physics with Borexino I. 2012. `arXiv:1205.2989`.

[236] G. Bellini et al. Neutrinos from the primary protonproton fusion process in the Sun. *Nature*, 512(7515):383–386, 2014. `doi:10.1038/nature13702`.

[237] J. Hartnell and SNO+ Collaboration. Neutrinoless Double Beta Decay with SNO+. *Journal of Physics Conference Series*, 375(4):042015, July 2012. `arXiv:1201.6169`, `doi:10.1088/1742-6596/375/1/042015`.

[238] V Lozza. Neutrinoless double beta decay search with SNO+. In *EPJ Web of Conferences*, volume 65, page 01003. EDP Sciences, 2014. URL: `http://www.epj-conferences.org/articles/epjconf/pdf/2014/02/epjconf_rpsc2013_01003.pdf`.

[239] B. Aharmim et al. An Independent Measurement of the Total Active B-8 Solar Neutrino Flux Using an Array of He-3 Proportional Counters at the Sudbury Neutrino Observatory. *Physical Review Letters*, 101:111301, 2008. `arXiv:0806.0989`, `doi:10.1103/PhysRevLett.101.111301`.

[240] C. Rubbia. The Liquid Argon Time Projection Chamber: A New Concept for Neutrino Detectors. 1977.

[241] C. Rubbia et al. Underground operation of the ICARUS T600 LAr-TPC: first results. *Journal of Instrumentation*, 6:7011, July 2011. `arXiv:1106.0975`, `doi:10.1088/1748-0221/6/07/P07011`.

[242] R. Abbasi et al. Calibration and characterization of the IceCube photomultiplier tube. *Nuclear Instruments and Methods in Physics Research A*, 618:139–152, June 2010. `arXiv:1002.2442`, `doi:10.1016/j.nima.2010.03.102`.

[243] R. Abbasi et al. The IceCube data acquisition system: Signal capture, digitization, and timestamping. *Nuclear Instruments and Methods in Physics Research A*, 601(3):294 – 316, 2009. URL: `http://www.sciencedirect.com/science/article/pii/S0168900209000084`, `doi:10.1016/j.nima.2009.01.001`.

[244] A. Achterberg et al. First Year Performance of The IceCube Neutrino Telescope. *Astronomy and Astrophysics*, 26:155–173, 2006. `arXiv:astro-ph/0604450`, `doi:10.1016/j.astropartphys.2006.06.007`.

[245] R. Abbasi et al. The design and performance of IceCube DeepCore. *Astroparticle Physics*, 35(10):615 – 624, 2012. URL: `http://www.sciencedirect.com/science/article/pii/S0927650512000254`, `arXiv:1109.6096`, `doi:10.1016/j.astropartphys.2012.01.004`.

[246] R. Abbasi et al. IceTop: The surface component of IceCube. *Nuclear Instruments and Methods in Physics Research A*, 700:188–220, 2013. `arXiv:1207.6326`, `doi:10.1016/j.nima.2012.10.067`.

[247] M.G. Aartsen et al. Energy Reconstruction Methods in the IceCube Neutrino Telescope. *JINST*, 9:P03009, 2014. `arXiv:1311.4767`, `doi:10.1088/1748-0221/9/03/P03009`.

[248] M. Salathe, M. Ribordy, and L. Demirörs. Novel technique for supernova detection with IceCube. *Astroparticle Physics*, 35:485–494, March 2012. `arXiv:1106.1937`, `doi:10.1016/j.astropartphys.2011.10.012`.

[249] Amol S. Dighe, Mathias T. Keil, and Georg G. Raffelt. Detecting the neutrino mass hierarchy with a supernova at IceCube. *Journal of Cosmology and Astroparticle Physics*, 0306:005, 2003. `arXiv:hep-ph/0303210`, `doi:10.1088/1475-7516/2003/06/005`.

[250] H. Nyquist. Thermal Agitation of Electric Charge in Conductors. *Physical Review*, 32:110–113, Jul 1928. URL: `http://link.aps.org/doi/10.1103/PhysRev.32.110`, `doi:10.1103/PhysRev.32.110`.

[251] J. B. Johnson. Thermal Agitation of Electricity in Conductors. *Physical Review*, 32:97–109, Jul 1928. URL: `http://link.aps.org/doi/10.1103/PhysRev.32.97`, `doi:10.1103/PhysRev.32.97`.

[252] O.W. Richardson. *Thermionic Emission from Hot Bodies*. Lightning Source Incorporated, 2003. URL: `http://books.google.com/books?id=vbcQngEACAAJ`.

[253] Michael Larson. Simulation and Identification of Non-Poissonian Noise Triggers in the IceCube Neutrino Detector. Master's thesis, University of Alabama, 2013. URL: `https://docushare.icecube.wisc.edu/dsweb/Get/Document-68303/LarsonThesis_final.pdf`.

[254] H.O. Meyer. Dark Rate of a Photomultiplier at Cryogenic Temperatures. 2008. `arXiv:0805.0771`.

[255] A. Ankowski et al. Characterization of ETL 9357FLA photomultiplier tubes for cryogenic temperature applications. 556(1):146 – 157, 2006. URL: `http://www.sciencedirect.com/science/article/pii/S0168900205020851`, `doi:10.1016/j.nima.2005.10.108`.

[256] Klaus Helbing et al. Light emission in AMANDA pressure spheres-The cause of noise in OMs and its correlation. Internal report, Johannes Gutenberg-Universität Mainz, 2003. URL: `http://butler.physik.uni-mainz.de/~amauser/download/afterscint.pdf`.

[257] Hamamatsu Photonics. Photomultiplier Tubes and Assemblies for Scintillation Counting High Energy physics. Brochure, 2004. URL: `http://neutron.physics.ucsb.edu/docs/High_energy_PMT_TPMO0007E01.pdf`.

[258] Hamamatsu Photonics. Photomultiplier Tubes: Basics and Application. Brochure, 2007. URL: `https://www.hamamatsu.com/resources/pdf/etd/PMT_handbook_v3aE.pdf`.

[259] K. D. Ianakiev, B. S. Alexandrov, P. B. Littlewood, and M. C. Browne. Temperature behavior of NaI(Tl) scintillation detectors. *Nuclear Instruments and Methods in Physics Research A*, 607:432–438, August 2009. `arXiv:physics/0605248`, `doi:10.1016/j.nima.2009.02.019`.

[260] C. Sailer, B. Lubsandorzhiev, C. Strandhagen, and J. Jochum. Low temperature light yield measurements in NaI and NaI(Tl). *European Physical Journal C*, 72:2061, June 2012. `arXiv:1203.1172`, `doi:10.1140/epjc/s10052-012-2061-7`.

[261] A.H. Sommer. *Photoemissive materials: preparation, properties, and uses.* Wiley, 1968. URL: `http://books.google.com/books?id=c_4iHo0cNgMC`.

[262] R. Abbasi et al. The IceCube Neutrino Observatory III: Cosmic Rays. *ArXiv e-prints*, November 2011. `arXiv:1111.2735`.

[263] Juan Carlos Díaz Vélez. Personal Communication.

[264] J. R. Hörandel. On the knee in the energy spectrum of cosmic rays. *Astroparticle Physics*, 19:193–220, May 2003. `arXiv:astro-ph/0210453`, `doi:10.1016/S0927-6505(02)00198-6`.

[265] Anthony M. Hillas. Cosmic Rays: Recent Progress and some Current Questions. 2006. `arXiv:astro-ph/0607109`.

[266] T. K. Gaisser. Spectrum of cosmic-ray nucleons, kaon production, and the atmospheric muon charge ratio. *Astroparticle Physics*, 35:801–806, July 2012. `arXiv:1111.6675`, `doi:10.1016/j.astropartphys.2012.02.010`.

[267] Thomas K. Gaisser, Todor Stanev, and Serap Tilav. Cosmic Ray Energy Spectrum from Measurements of Air Showers. *Front.Phys.China*, 8:748–758, 2013. `arXiv:1303.3565`, `doi:10.1007/s11467-013-0319-7`.

[268] P.V. Hobbs. *Ice Physics*. Oxford Classic Texts in the Physical Sciences. OUP Oxford, 2010. URL: `http://books.google.com/books?id=7Is6AwAAQBAJ`.

[269] Mark Krasberg. Low-Level Commissioning, 2006 (accessed Sept. 7 2014). Slides from 2006 IceCube Collaboration Meeting, Baton Rouge, La. URL: `http://icecube.wisc.edu/~krasberg/Talks/060412-BatonRougeCommissioning.ppt`.

[270] Per Olof Hulth. Personal Communication.

[271] J.A. Formaggio and G.P. Zeller. From eV to EeV: Neutrino Cross Sections Across Energy Scales. *Reviews of Modern Physics*, 84:1307, 2012. `arXiv:1305.7513`, `doi:10.1103/RevModPhys.84.1307`.

[272] A. Strumia and F. Vissani. Precise quasielastic neutrino/nucleon cross-section. *Physics Letters B*, 564:42–54, July 2003. `arXiv:astro-ph/0302055`, `doi:10.1016/S0370-2693(03)00616-6`.

[273] P. Vogel and J. F. Beacom. Angular distribution of neutron inverse beta decay, $\bar{\nu}_e + p \rightarrow e^+ + n$. *Physical Review D*, 60:053003, Jul 1999. URL: `http://link.aps.org/doi/10.1103/PhysRevD.60.053003`, `doi:10.1103/PhysRevD.60.053003`.

[274] Varley F. Sears. Neutron scattering lengths and cross sections. *Neutron News*, 3(3):26–37, 1992. URL: `http://www.tandfonline.com/doi/abs/10.1080/10448639208218770`, `arXiv:http://www.tandfonline.com/doi/pdf/10.1080/10448639208218770`, `doi:10.1080/10448639208218770`.

[275] National Institute of Standards and Technology. Neutron scattering lengths and cross sections, 2013 (accessed Sept. 18 2014). URL: `http://www.ncnr.nist.gov/resources/n-lengths/`.

[276] H. M. Childers and J. D. Graves. Bipartition Angles for Compton Scattering by Free Electrons. *Physical Review*, 99:343–345, Jul 1955. URL: `http://link.aps.org/doi/10.1103/PhysRev.99.343`, `doi:10.1103/PhysRev.99.343`.

[277] William J. Marciano and Zohreh Parsa. Neutrino electron scattering theory. *J.Phys.*, G29:2629–2645, 2003. `arXiv:hep-ph/0403168`, `doi:10.1088/0954-3899/29/11/013`.

[278] W. C. Haxton. Nuclear response of water Cherenkov detectors to supernova and solar neutrinos. *Physical Review D*, 36:2283–2292, Oct 1987. URL: `http://link.aps.org/doi/10.1103/PhysRevD.36.2283`, `doi:10.1103/PhysRevD.36.2283`.

[279] W. C. Haxton and R. G. H. Robertson. Solar neutrino interactions with ^{18}O in the SuperKamiokande water Cerenkov detector. *Physical Review C*, 59:515–519, Jan 1999. URL: `http://link.aps.org/doi/10.1103/PhysRevC.59.515`, `doi:10.1103/PhysRevC.59.515`.

[280] E. Kolbe, K. Langanke, and P. Vogel. Estimates of weak and electromagnetic nuclear decay signatures for neutrino reactions in Super-Kamiokande. *Physical Review D*, 66:013007, Jul 2002. URL: `http://link.aps.org/doi/10.1103/PhysRevD.66.013007`, `doi:10.1103/PhysRevD.66.013007`.

[281] S. Agostinelli et al. GEANT4: A Simulation toolkit. *Nuclear Instruments and Methods in Physics Research A*, A506:250–303, 2003. `doi:10.1016/S0168-9002(03)01368-8`.

[282] J. Allison et al. Geant4 developments and applications. *Nuclear Science, IEEE Transactions on*, 53(1):270–278, Feb 2006. `doi:10.1109/TNS.2006.869826`.

[283] P. A. Cherenkov. Visible emission of clean liquids by action of gamma radiation. *Doklady Akademii Nauk SSSR*, 2:451+, 1934. URL: `http://ufn.ru/en/articles/2007/4/g/`.

[284] Boris M Bolotovskii. Vavilov Cherenkov radiation: its discovery and application. *Physics-Uspekhi*, 52(11):1099, 2009. URL: `http://stacks.iop.org/1063-7869/52/i=11/a=R03`.

[285] Ig. Tamm. Radiation Emitted by Uniformly Moving Electrons. In Boris M. Bolotovskii, Victor Ya. Frenkel, and Rudolf Peierls, editors, *Selected Papers*, pages 37–53. Springer Berlin Heidelberg, 1991. URL: `http://dx.doi.org/10.1007/978-3-642-74626-0_3`, `doi:10.1007/978-3-642-74626-0_3`.

[286] K. Abe et al. Calibration of the Super-Kamiokande detector. *Nuclear Instruments and Methods in Physics Research A*, 737:253–272, February 2014. `arXiv:1307.0162`, `doi:10.1016/j.nima.2013.11.081`.

[287] Borexino collaboration, H. Back, et al. Borexino calibrations: Hardware, Methods, and Results. *ArXiv e-prints*, July 2012. `arXiv:1207.4816`.

[288] R. C. Bay, R. A. Rohde, P. B. Price, and N. E. Bramall. South Pole paleowind from automated synthesis of ice core records. *Journal of Geophysical Research: Atmospheres*, 115(D14):n/a–n/a, 2010. URL: `http://dx.doi.org/10.1029/2009JD013741`, `doi:10.1029/2009JD013741`.

[289] Jacob Feintzeig. *Searches for Point-like Sources of Astrophysical Neutrinos with the IceCube Neutrino Observatory*. PhD thesis, University of Wisconsin–Madison, in prep.

[290] M.G. Aartsen et al. South Pole glacial climate reconstruction from multi-borehole laser particulate stratigraphy. *Journal of Glaciology*, 59(218):1117–1128, 2013-12-01T00:00:00. URL: `http://www.ingentaconnect.com/content/igsoc/jog/2013/00000059/00000218/art00011`, `doi:doi:10.3189/2013JoG13J068`.

[291] N. E. Bramall et al. A deep high-resolution optical log of dust, ash, and stratigraphy in South Pole glacial ice. *Geophysical Research Letters*, 32(21):n/a–n/a, 2005. URL: `http://dx.doi.org/10.1029/2005GL024236`, `doi:10.1029/2005GL024236`.

[292] R. C. Bay et al. Globally synchronous ice core volcanic tracers and abrupt cooling during the last glacial period. *Journal of Geophysical Research: Atmospheres*, 111(D11):n/a–n/a, 2006. URL: `http://dx.doi.org/10.1029/2005JD006306`, `doi:10.1029/2005JD006306`.

[293] M.G. Aartsen et al. Search for a diffuse flux of astrophysical muon neutrinos with the IceCube 59-string configuration. *Physical Review D*, 89:062007, 2014. `arXiv:1311.7048`, `doi:10.1103/PhysRevD.89.062007`.

[294] Anne Schukraft. *Search for a diffuse flux of extragalactic neutrinos with the IceCube Neutrino Observatory*. PhD thesis, Rheinisch-Westfälische Technische Hochschule Aachen, 2013. URL: `http://internal.icecube.wisc.edu/reports/data/icecube/2013/08/001/icecube_201308001_v1-clean.pdf`.

[295] W.R. Leo. *Techniques for Nuclear and Particle Physics Experiments: A How-To Approach*. U.S. Government Printing Office, 1994. URL: `http://books.google.com/books?id=8VufE4SD-AkC`.

[296] M.G. Aartsen et al. The IceCube Neutrino Observatory Part V: Neutrino Oscillations and Supernova Searches. 2013. `arXiv:1309.7008`.

[297] David Heereman von Zuydtwyck. *Hit-Spooling: An Improvement for the Supernova Detection System in IceCube*. PhD thesis, Université Libres de Bruxelles, in prep.

[298] Gösta Kroll. *Galactic supernova detection with IceCube*. PhD thesis, Johannes Gutenberg-Universität Mainz, in prep.

[299] M. Ahlers, P. Mertsch, and S. Sarkar. Cosmic ray acceleration in supernova remnants and the FERMI/PAMELA data. *Physical Review D*, 80(12):123017, December 2009. `arXiv:0909.4060`, `doi:10.1103/PhysRevD.80.123017`.

[300] Marco Salathe. Novel Search Methodology for Supernovae with IceCube. Master's thesis, Ecole Polytechnique Fédérale de Lausanne, February 2011. URL: `http://www-lphe.epfl.ch/publications/diplomas/ms.master.pdf`.

[301] D. Heck, Forschungszentrum Karlsruhe, and Forschungszentrum (Karlsruhe). *CORSIKA: A Monte Carlo Code to Simulate Extensive Air Showers*. FZKA–6019. FZKA, 1998. URL: `http://books.google.nl/books?id=65sfHAAACAAJ`.

[302] D. Heck. Extensive air shower simulations with CORSIKA and the influence of highenergy hadronic interaction models. pages 252–259, 2000. `arXiv:astro-ph/0103073`.

[303] Jakob van Santen. *Neutrino Interactions in IceCube above 1 TeV: Constraints on atmospheric charmed-meson production and investigation of the astrophysical neutrino flux with 2 years of IceCube data.* PhD thesis, University of Wisconsin–Madison, in prep.

[304] Askhat Gazizov and Marek P. Kowalski. ANIS: High energy neutrino generator for neutrino telescopes. *Comput.Phys.Commun.*, 172:203–213, 2005. `arXiv:astro-ph/0406439`, `doi:10.1016/j.cpc.2005.03.113`.

[305] Y. Becherini, A. Margiotta, M. Sioli, and M. Spurio. A parameterisation of single and multiple muons in the deep water or ice. *Astroparticle Physics*, 25(1):1 – 13, 2006. URL: `http://www.sciencedirect.com/science/article/pii/S092765050500157X`, `doi:10.1016/j.astropartphys.2005.10.005`.

[306] C. Andreopoulos et al. The GENIE neutrino Monte Carlo generator. *Nuclear Instruments and Methods in Physics Research A*, 614(1):87 – 104, 2010. URL: `http://www.sciencedirect.com/science/article/pii/S0168900209023043`, `doi:10.1016/j.nima.2009.12.009`.

[307] T. Yang et al. A hadronization model for few-GeV neutrino interactions. *The European Physical Journal C*, 63(1):1–10, 2009. URL: `http://dx.doi.org/10.1140/epjc/s10052-009-1094-z`, `doi:10.1140/epjc/s10052-009-1094-z`.

[308] GENIE Collaboration. GENIE Neutrino Monte Carlo Generator, 2014 (accessed Sept. 7 2014). URL: `http://www.genie-mc.org/`.

[309] GENIE Collaboration. GENIE Neutrino Monte Carlo Generator–Very Low Energy, 2014 (accessed Sept. 7 2014). URL: `https://genie.hepforge.org/trac/browser/trunk/src/VLE`.

[310] Dmitry Chirkin and Wolfgang Rhode. Muon Monte Carlo: A High-precision tool for muon propagation through matter. 2004. `arXiv:hep-ph/0407075`.

[311] J.-H. Koehne et al. PROPOSAL: A tool for propagation of charged leptons. *Computer Physics Communications*, 184(9):2070 – 2090, 2013. URL: `http://www.sciencedirect.com/science/article/pii/S0010465513001355`, `doi:10.1016/j.cpc.2013.04.001`.

[312] Dmitry Chirkin. Photon tracking with GPUs in IceCube. *Nuclear Instruments and Methods in Physics Research A*, 725(0):141 – 143, 2013. VLVνT 11, Erlangen, Germany, 12 - 14 October, 2011 5th International Workshop on Very Large Volume Neutrino Telescopes, The future of high-energy neutrino astronomy. URL: `http://www.sciencedirect.com/science/article/pii/S0168900212015173`, `doi:10.1016/j.nima.2012.11.170`.

[313] M. G. Aartsen et al. Search for non-relativistic magnetic monopoles with IceCube. *European Physical Journal C*, 74:2938, July 2014. `arXiv:1402.3460`, `doi:10.1140/epjc/s10052-014-2938-8`.

[314] D. Chirkin. Fluxes of Atmospheric Leptons at 600 GeV - 60 TeV. *ArXiv High Energy Physics - Phenomenology e-prints*, July 2004. `arXiv:hep-ph/0407078`.

[315] R. S. Fletcher, T. K. Gaisser, Paolo Lipari, and Todor Stanev. SIBYLL: An Event generator for simulation of high-energy cosmic ray cascades. *Physical Review D*, 50:5710–5731, Nov 1994. URL: `http://link.aps.org/doi/10.1103/PhysRevD.50.5710`, `doi:10.1103/PhysRevD.50.5710`.

[316] S. Roesler, R. Engel, and J. Ranft. *The Monte Carlo Event Generator DPMJET-III*, page 1033. 2001. `doi:10.1007/978-3-642-18211-2_166`.

[317] S. Ostapchenko. QGSJET-II: results for extensive air showers. *Nuclear Physics B Proceedings Supplements*, 151:147–150, January 2006. `arXiv:astro-ph/0412591`, `doi:10.1016/j.nuclphysbps.2005.07.027`.

[318] T. Pierog and K. Werner. EPOS Model and Ultra High Energy Cosmic Rays. *Nuclear Physics B Proceedings Supplements*, 196:102–105, December 2009. `arXiv:0905.1198`, `doi:10.1016/j.nuclphysbps.2009.09.017`.

[319] L. Dessart et al. Neutrino Signatures and the Neutrino-Driven Wind in Binary Neutron Star Mergers. *Astrophysical Journal*, 690:1681–1705, January 2009. `arXiv:0806.4380`, `doi:10.1088/0004-637X/690/2/1681`.

[320] O. L. Caballero, G. C. McLaughlin, and R. Surman. Detecting neutrinos from black hole-neutron star mergers. *Physical Review D*, 80(12):123004, December 2009. `arXiv:0910.1385`, `doi:10.1103/PhysRevD.80.123004`.

[321] M. B. Deaton et al. Black Hole-Neutron Star Mergers with a Hot Nuclear Equation of State: Outflow and Neutrino-cooled Disk for a Low-mass, High-spin Case. *Astrophysical Journal*, 776:47, October 2013. `arXiv:1304.3384`, `doi:10.1088/0004-637X/776/1/47`.

[322] F. Foucart et al. Neutron star-black hole mergers with a nuclear equation of state and neutrino cooling: Dependence in the binary parameters. *Physical Review D*, 90(2):024026, July 2014. `arXiv:1405.1121`, `doi:10.1103/PhysRevD.90.024026`.

[323] Aleksander Sadowski et al. The Total Merger Rate of Compact Object Binaries In The Local Universe. *Astrophysical Journal*, 2007. `arXiv:0710.0878`.

[324] Michal Dominik et al. Double Compact Objects II: Cosmological Merger Rates. *Astrophysical Journal*, 779:72, 2013. `arXiv:1308.1546`, `doi:10.1088/0004-637X/779/1/72`.

[325] J. Abadie et al. Search for gravitational waves from binary black hole inspiral, merger and ringdown. *Physical Review D*, 83:122005, 2011. `arXiv:1102.3781`, `doi:10.1103/PhysRevD.86.069903, 10.1103/PhysRevD.85.089904,10.1103/PhysRevD.83.122005`.

[326] Alex Abramovici et al. LIGO: The Laser interferometer gravitational wave observatory. *Science*, 256:325–333, 1992. `doi:10.1126/science.256.5055.325`.

[327] P. D. D'Eath and P. N. Payne. Gravitational radiation in black-hole collisions at the speed of light. I. Perturbation treatment of the axisymmetric collision. *Physical Review D*, 46:658–674, Jul 1992. URL: `http://link.aps.org/doi/10.1103/PhysRevD.46.658`, `doi:10.1103/PhysRevD.46.658`.

[328] Gregory M. Harry. Advanced LIGO: The next generation of gravitational wave detectors. *Class.Quant.Grav.*, 27:084006, 2010. `doi:10.1088/0264-9381/27/8/084006`.

[329] J. Abadie et al. Topical Review: Predictions for the rates of compact binary coalescences observable by ground-based gravitational-wave detectors. *Classical and Quantum Gravity*, 27(17):173001, September 2010. `arXiv:1003.2480`, `doi:10.1088/0264-9381/27/17/173001`.

[330] J. Abadie et al. Search for Gravitational Waves from Low Mass Compact Binary Coalescence in LIGO's Sixth Science Run and Virgo's Science Runs 2 and 3. *Physical Review D*, 85:082002, 2012. `arXiv:1111.7314`, `doi:10.1103/PhysRevD.85.082002`.

[331] N. Mennekens and D. Vanbeveren. Massive double compact object mergers: gravitational wave sources and r-process element production sites. *Astronomy and Astrophysics*, 564:A134, April 2014. `arXiv:1307.0959`, `doi:10.1051/0004-6361/201322198`.

[332] M.G. Aartsen et al. Multimessenger Search for Sources of Gravitational Waves and High-Energy Neutrinos: Results for Initial LIGO-Virgo and IceCube. 2014. `arXiv:1407.1042`.

[333] Simon Olofsson and Erik Setterquist. Investigation into the anomalous trigger rates in the IceCube Neutrino Observatory on Feburary 5th 2013. Internal report, Uppsala Universitet, 2013. URL: `http://internal.icecube.wisc.edu/reports/data/icecube/2013/07/001/icecube_201307001_v1-clean.pdf`.

[334] Aksel Hallin and Neil McCauley. Personal Communication.

[335] Juan Marcos Santander. *Observation of Cosmic-Ray Anisotropy at TeV and PeV Energies in the Southern Sky*. PhD thesis, University of Wisconsin–Madison, 2013.

[336] N. D. Gagunashvili. Comparison of weighted and unweighted histograms. *ArXiv Physics e-prints*, May 2006. `arXiv:physics/0605123`.

[337] Paolo Desiati. Personal Communication.

[338] Jakob van Santen. SuperDST Format Details, 2014 (accessed Sept. 12 2014). URL: `http://software.icecube.wisc.edu/icerec_trunk/projects/superdst/index.html#format-details`.

[339] M.G. Aartsen et al. Letter of Intent: The Precision IceCube Next Generation Upgrade (PINGU). 2014. `arXiv:1401.2046`.

[340] Albrecht Karle. A Next Generation IceCube, 2014 (accessed Sept. 7 2014). Slides from Neutrinos Beyond IceCube, April 24 2014, Arlington, Va. URL: `https://docushare.icecube.wisc.edu/dsweb/Get/Document-69617/4-Karle_NGIC_Arlington.pdf`.

[341] S. Böser et al. Detecting extra-galactic supernova neutrinos in the Antarctic ice. *ArXiv e-prints*, April 2013. `arXiv:1304.2553`.

[342] Elisa Resconi. The stepping stones to proton decay: IceCube PINGU MICA, 2013 (accessed Sept. 7 2014). Slides from New Directions in Neutrino Physics, Aspen, CO. URL: `https://indico.cern.ch/event/224351/contribution/33/material/slides/0.pdf`.

[343] R. C. Willson and H. S. Hudson. Solar luminosity variations in solar cycle 21. *Nature*, 332:810–812, April 1988. `doi:10.1038/332810a0`.

[344] R. C. Willson and H. S. Hudson. The sun's luminosity over a complete solar cycle. *Nature*, 351:42–44, May 1991. `doi:10.1038/351042a0`.

[345] S. K. Solanki and N. A. Krivova. Can solar variability explain global warming since 1970? *Journal of Geophysical Research: Space Physics*, 108(A5):n/a–n/a, 2003. URL: `http://dx.doi.org/10.1029/2002JA009753`, `doi:10.1029/2002JA009753`.

[346] D. Seckel, T. Stanev, and T. K. Gaisser. Signatures of cosmic-ray interactions on the solar surface. *Astrophysical Journal*, 382:652–666, December 1991. `doi:10.1086/170753`.

[347] I. V. Moskalenko and S. Karakula. Very high energy neutrinos from the Sun. *Journal of Physics G Nuclear Physics*, 19:1399–1406, 1993. `doi:10.1088/0954-3899/19/9/019`.

[348] G. Ingelman and M. Thunman. High energy neutrino production by cosmic ray interactions in the Sun. *Physical Review D*, 54:4385–4392, October 1996. `arXiv:hep-ph/9604288`, `doi:10.1103/PhysRevD.54.4385`.

[349] J. G. Learned and K. Mannheim. High-Energy Neutrino Astrophysics. *Annual Review of Nuclear and Particle Science*, 50:679–749, 2000. `doi:10.1146/annurev.nucl.50.1.679`.

[350] J. N. Bahcall. Solar flares and neutrino detectors. *Physical Review Letters*, 61:2650–2652, December 1988. `doi:10.1103/PhysRevLett.61.2650`.

[351] D. Fargion. Neutrino Solar Flare detection for a saving alert system of satellites and astronauts. *International Cosmic Ray Conference*, 6:309, 2011. `arXiv:1106.3750`, `doi:10.7529/ICRC2011/V06/1140`.

[352] E. Tandberg-Hanssen and A.G. Emslie. *The Physics of Solar Flares*. Cambridge Tracts in Mathematics. Cambridge University Press, 1988. URL: `http://books.google.com/books?id=wcF0bnSqVVIC`.

[353] Douglas V. Hoyt and Kenneth H. Schatten. Group Sunspot Numbers: A New Solar Activity Reconstruction. *Solar Physics*, 179(1):189–219, 1998. URL: `http://dx.doi.org/10.1023/A%3A1005007527816`, `doi:10.1023/A:1005007527816`.

[354] D. R. Lorimer et al. A Bright Millisecond Radio Burst of Extragalactic Origin. *Science*, 318:777–, November 2007. `arXiv:0709.4301`, `doi:10.1126/science.1147532`.

[355] D. Thornton et al. A Population of Fast Radio Bursts at Cosmological Distances. *Science*, 341:53–56, July 2013. `arXiv:1307.1628`, `doi:10.1126/science.1236789`.

[356] I. Antcheva et al. ROOT - A C++ framework for petabyte data storage, statistical analysis and visualization. *Computer Physics Communications*, 180(12):2499 – 2512, 2009. 40 Years of CPC: A celebratory issue focused on quality software for high performance, grid and novel computing architectures. URL: `http://www.sciencedirect.com/science/article/pii/S0010465509002550`, `doi:10.1016/j.cpc.2009.08.005`.

[357] M. D. Kistler et al. Core-collapse astrophysics with a five-megaton neutrino detector. *Physical Review D*, 83(12):123008, June 2011. `arXiv:0810.1959`, `doi:10.1103/PhysRevD.83.123008`.

[358] J. F. Beacom and M. R. Vagins. Antineutrino Spectroscopy with Large Water Čerenkov Detectors. *Physical Review Letters*, 93(17):171101, October 2004. `arXiv:hep-ph/0309300`, `doi:10.1103/PhysRevLett.93.171101`.

[359] H. Watanabe et al. First Study of Neutron Tagging with a Water Cherenkov Detector. *Astronomy and Astrophysics*, 31:320–328, 2009. `arXiv:0811.0735`, `doi:10.1016/j.astropartphys.2009.03.002`.

[360] Takaaki Mori. Status of the Super-Kamiokande gadolinium project. *Nuclear Instruments and Methods in Physics Research A*, 732(0):316 – 319, 2013. Vienna Conference on Instrumentation 2013. URL: `http://www.sciencedirect.com/science/article/pii/S0168900213009078`, `doi:10.1016/j.nima.2013.06.074`.

[361] Ranjan Laha and John F. Beacom. Gadolinium in water Cherenkov detectors improves detection of supernova ν_e. *Physical Review D*, 89:063007, 2014. `arXiv:1311.6407`, `doi:10.1103/PhysRevD.89.063007`.

[362] K. Abe et al. Letter of Intent: The Hyper-Kamiokande Experiment — Detector Design and Physics Potential —. *ArXiv e-prints*, September 2011. `arXiv:1109.3262`.

[363] Uli Katz. PINGU An IceCube extension for low-energy neutrinos, 2012 (accessed Sept. 7 2014). Slides from European Strategy for Neutrino Oscillation Physics II, CERN. URL: `http://ecap.nat.uni-erlangen.de/members/katz/talks/UliKatz_cern12.pdf`.

[364] D. Jason Koskinen. Megaton Ice Cherenkov Array, 2014 (accessed Sept. 12 2014). Slides from Astroparticle Neutrino Physics in Antarctica Workshop. URL: `https://indico.nbi.ku.dk/getFile.py/access?contribId=10&resId=0&materialId=slides&confId=620`.

[365] Particle Physics Project Prioritization Panel. Building for Discovery–Strategic Plan for U.S. Particle Physics in the Global Context. Report, 2014. URL: `http://science.energy.gov/~/media/hep/hepap/pdf/May%202014/FINAL_P5_Report_Interactive_060214.pdf`.

[366] LBNE Collaboration, C. Adams, et al. The Long-Baseline Neutrino Experiment: Exploring Fundamental Symmetries of the Universe. *ArXiv e-prints*, July 2013. `arXiv:1307.7335`.

[367] M. Wurm et al. The next-generation liquid-scintillator neutrino observatory LENA. *Astroparticle Physics*, 35:685–732, June 2012. `arXiv:1104.5620`, `doi:10.1016/j.astropartphys.2012.02.011`.

[368] David Webber. Determining the neutrino hierarchy from a galactic supernova using a next-generation detector, 2011 (accessed Sept. 29 2014). Slides from American Physical Society April Meeting 2011, Anaheim, CA and `http://meetings.aps.org/link/BAPS.2011.APR.Y7.8`. URL: `http://www.hep.wisc.edu/~dwebber/SNB_APS_April2011/Webber%20APS.pdf`.